



Institute of Spintronics and Quantum Information
Faculty of Physics
Adam Mickiewicz University in Poznań

Shilan Abo

**Control of quantum correlations
in dissipative systems:
New quantum effects, and novel
theoretical and experimental methods**

PhD thesis

Supervisor: Prof. Dr. Hab. Adam Miranowicz
Assistant Supervisor: Dr. Hab. Ravindra Chhajlany, Prof. UAM

February 2024

Declaration

Declaration of the author of this dissertation: I hereby declare that except where specific reference is made to the work of others, the contents of this dissertation are original and have not been submitted in whole or in part for consideration for any other degree or qualification in this, or any other university. This dissertation is my own work and all the contents of the dissertation have been obtained by legal means.

Shilan Abo
.....

M.Sc. Shilan Abo

Declarations of the thesis Supervisors:

This dissertation is ready to be reviewed.

A. Miranowicz
.....

Prof. Dr. Hab. Adam Miranowicz

R. W. Chhajlany
.....

Dr. Hab. Ravindra Chhajlany, Prof. UAM

Shilan Abo
February 2024

Acknowledgements

I am immensely grateful for the completion of my Ph.D. journey, which was filled with countless exploration, learning, and personal growth. I owe this to the continued support of numerous individuals who have played a pivotal role in shaping my path.

First and foremost, I would like to thank my supervisor, Prof. Adam Miranowicz, for his invaluable guidance and mentorship throughout my doctoral degree. Prof. Miranowicz gave me the chance to explore the fascinating field of quantum optics and quantum information and inspired me with his patience, encouragement, and direction. He helped me overcome the challenges and difficulties of my research and pursued my interests and passions. I acknowledge his great effort to help me begin and continue my Ph.D. journey, taught me how to explore the topic wisely from different perspectives, and made my thesis work more accurate, intelligible, and thorough.

I would also like to express my sincere gratitude to my second supervisor, Prof. Ravindra Chhajlany, for the opportunity to work with him, and his insightful discussions on my Ph.D. research that truly enriched my knowledge and understanding of the field.

I am grateful to my dissertation advisory committee and all the people who supported this work, including my colleagues and co-authors: Prof. Anna Kowalewska-Kudłaszyk, Prof. Karol Bartkiewicz, Dr. Grzegorz Chimczak, and M.Sc. Patrycja Tulewicz, along with my supervisors from Nonlinear Optics Division of Adam Mickiewicz University for their valuable involvement and feedback. I would like to express my sincere gratitude for their support and care during these years in Poznań. They have created an environment that truly felt like home to me and have helped me in several ways.

I would also like to thank Prof. Salvatore Savasta and his great group for their insightful discussions and continuous support during my long-term internship at the University of Messina. I am especially grateful for the welcoming and supportive environment that Prof. Omar Di Stefano and Prof. Savasta provided for me. I also

appreciate the chance to explore physics in the ultra-strong-coupling regime with my colleagues and co-authors, Alberto Mercurio, Fabio Mauceri, Vincenzo Macrì, Enrico Russo, and Roberto Stassi. This was a very rewarding and enjoyable part of my Ph.D. journey.

I extend my gratitude to our collaborators in the Joint Laboratory of Optics at Palacký University in Olomouc, including Prof. Karel Lemr, Prof. Jan Soubusta, Dr. Antonin Černoch, Dr. Katerina Jiráková, and especially to Prof. Jan Peřina Jr. for our productive collaboration and fruitful discussions.

I also warmly acknowledge collaborations with Prof. Franco Nori from RIKEN Center for Emergent Matter Science in Wako-shi and Prof. Şahin K. Özdemir from Pennsylvania State University.

I am grateful to my friends, especially Sanam Ghamarsoorat and Shraddha Wadurkar, for their encouragement and positive vibes throughout this journey.

I acknowledge the financial support of the Polish National Science Centre (NCN) under the Maestro Grant No. DEC-2019/34/A/ST2/00081 and grant No. POWER.03.05.00-00-Z303/17 within the University of Tomorrow Project of Adam Mickiewicz University to stay at the University of Messina for my internship.

I am deeply grateful to my loving family for always cheering me on my journey. Their constant support and encouragement helped me overcome my challenges and pursue my goals. I especially thank my wonderful, brilliant mother Sabriya Atrushi, who inspired me with her limitless support and enthusiasm for my future endeavors.

I am deeply grateful for the privilege of pursuing my Ph.D. in a supportive and stimulating environment. I could not have done so without the help and encouragement of all these wonderful people.

That was a pleasant adventure.

Abstract

The thesis on “Control of quantum correlations in dissipative systems: New quantum effects, and novel theoretical and experimental methods” concentrates on developing and applying quantum techniques to generate, enhance, control, and detect nonclassical correlations in dissipative systems. The methods enabled me to predict new quantum effects, such as hybrid photon-phonon blockade or two-photon blockade induced by light squeezing. The research is based on five articles co-authored by me. Below I show the motivation behind my studies and briefly summarize the main reported results.

Quantum correlations, such as quantum entanglement, Einstein-Podolsky-Rosen (EPR) steering (also known as quantum steering), Bell nonlocality, squeezing of light, and photon antibunching are critical resources for quantum technologies, including quantum information processing and quantum metrology. Unfortunately, quantum states are very fragile to the environmental noise, which causes their amplitude and phase damping. As a result, it is critical to develop methods for controlling and preserving quantum correlations in dissipative systems. In my thesis, I described and applied various approaches which offer promising routes to a better quantum control of dissipative systems and also to generate various novel effects useful for quantum technologies (including new single-photon and single-phonon sources).

Quantum entanglement, EPR steering, and Bell nonlocality reduce to the same effect for two-qubit systems in pure states; however, system dissipation can reveal their fundamental differences. I studied theoretically the hierarchy of these effects on the examples of the Werner states, which are the mixtures of the singlet state and the maximally mixed state (i.e., white noise). I also studied a refined hierarchy of quantum correlations of generalized Werner states, which are defined as white-noise-affected arbitrary two-qubit pure states. And more importantly, I reported the results of our experiments demonstrating the hierarchy of these quantum correlations for the Werner states without full quantum state tomography (QST) [Sci. Rep. **13**, 8564 (2023)]. Previous experimental studies were based on applying complete QST methods.

Moreover, I studied nonclassical phenomena, such as various types of photon blockade and photon-induced tunneling, and their phononic analogues. In particular, I discussed in [Sci. Rep. **12**, 17655 (2022)] a novel type of blockade, referred to as hybrid photon-phonon blockade, which is the blockade of excitations in a hybrid mode generated by linear coupling of purely photonic and phononic modes. I demonstrated how this effect can be generated in an optomechanical system and described in experimental setups, which can enable measuring this novel effect. Furthermore, I discussed the possibility to observe unconventional single- and multi-photon blockade effects, which can be generated in a linear system coupled to a squeezed reservoir, as reported in [Phys. Rev. A **100**, 053857 (2019)]. In that case, the nonlinearity required to observe photon blockade in a linear quantum system is induced by its linear coupling to a nonlinear quantum environment.

The physics of open quantum light-matter systems in the ultrastrong and deep-strong coupling regimes is also discussed in the thesis. I have paid a special attention to pure dephasing, which is an essential factor deteriorating quantum-information processing. I explained the impact of pure dephasing of either light or matter within the ultrastrong and deep-strong coupling regimes by applying generalized master equations for two well-known models of light-matter interactions beyond the rotating-wave approximation, i.e.: (i) the quantum Rabi model describing a two-level system coupled to a single cavity mode, and (ii) the Hopfield model describing collective (bosonic) matter excitations interacting with a single-mode light field. I explained that the form of the noise Hamiltonians for the components of a light-matter system can be affected by light-matter interactions and can, thus, be gauge relative. However, if the changes induced by the interaction as well as gauge transformations are correctly described, then the correct gauge-invariant rates can be obtained as explained in [Phys. Rev. Lett. **130**, 123601 (2023)]. The dephasing rates induced by the states of the interacting light-matter systems and including fluctuations in either the light or matter degrees of freedom are calculated and the results are analyzed in detail.

Under ideal physical conditions, one typically considers Hermitian systems assuming their complete isolation from their environment, whereas non-Hermitian systems account for non-unitary evolutions in more realistic physical models. The dynamics of a realistic system is described by a master equation, which describe how energy, coherence, and quantum information are lost to its environment. The master equation (in the standard form of Gorini, Kossakowski, Sudarshan, and Lindblad) consists of a Hermitian-Hamiltonian term that describes a unitary evolution of a

given system and a non-Hermitian part, given by the so-called Lindblad dissipators, describing a non-unitary evolution. According to the quantum-trajectory (or quantum-jump) interpretation of master equations, these dissipators can be separated into two terms depending whether they are affected or unaffected by quantum jumps. Thus, a Hermitian Hamiltonian can be transformed into a non-Hermitian one, which describes the system dissipating coherently and non-unitarily without quantum jumps. The second part of the Lindblad dissipators describes a given system evolution induced by quantum jumps, which result from continuous measurements of the system by its environment. Quantum jumps are usually critical for accurately describing microscopic open quantum systems and obtaining results consistent with quantum measurement theories. The quantum-jump-free evolution, which is described by small perturbations to a given non-Hermitian Hamiltonian, can exhibit distinct and novel types of behavior. One example of such a novel behavior is the appearance of exceptional points, where some eigenvalues of a non-Hermitian Hamiltonian become degenerate and the corresponding eigenvectors coalesce. In my thesis I discuss quantum Liouvillian exceptional points (LEPs), which are defined as the eigenvalue and eigenvectors degeneracies of a quantum Liouvillian (which includes the effect of quantum jumps), instead of those of the corresponding non-Hermitian Hamiltonian (which ignores quantum jumps). In order to confirm these theoretical predictions, I performed cloud quantum experiments on an IBM quantum processor [e-print arXiv:2401.14993 (2024)]. These results have unequivocally demonstrated the experimental capabilities of generating, controlling, and detecting quantum exceptional points in systems with a small number of qubits based on quantum process tomography.

Streszczenie

W dysertacji pt. „Kontrola korelacji kwantowych w układach dyssypatywnych: Nowe zjawiska kwantowe oraz nowatorskie metody teoretyczne i eksperymentalne” opracowano i zastosowano metody kwantowe do generacji, wzmacniania, kontrolowania i detekcji nieklasycznych korelacji w układach dyssypatywnych. Metody te umożliwiły mi przewidzenie nowych efektów kwantowych takich jak hybrydowa blokada fotonowo-fononowa czy też blokada dwufotonowa uzyskana poprzez ściskanie światła. Wyniki tych badań zostały opisane w pięciu artykułach, których jestem współautorem. Poniżej przedstawione są cele tych badań i podsumowane główne wyniki rozprawy.

Korelacje kwantowe, takie jak splątanie kwantowe, sterowanie kwantowe (zwane też sterowaniem Einsteina-Podolsky’ego-Rosena, EPR), Nielokalność Bella, ściskanie światła, czy też antygrupowanie fotonowe są krytycznymi zasobami technologii kwantowych, w szczególności mają kluczowe znaczenie w kwantowym przetwarzaniu informacji i metrologii kwantowej. Niestety stany kwantowe są wyjątkowo wrażliwe na szumy środowiskowe, które powodują tłumienie ich amplitudy i fazy. Dlatego też, kwestią niezwykle ważną jest opracowanie metod kontroli i przechowywania korelacji kwantowych w układach dyssypatywnych. W rozprawie opisano i zastosowano różne metody, które umożliwiają lepszą kontrolę kwantowych układów dyssypatywnych, a także umożliwiają generację i detekcję nowych zjawisk kwantowych przydatnych w technologiach kwantowych, m.in. jako nowe źródła pojedynczych fotonów i fononów.

Splątanie kwantowe, sterowanie EPR i Nielokalność Bella redukują się do tego samego typu korelacji kwantowych w układach dwukubitowych w stanach czystych; jednak dyssypacja takich układów dwukubitowych może ujawnić ich fundamentalne różnice. Zbadano numerycznie i analitycznie hierarchię tych efektów na przykładach stanów Wernera, które są mieszaninami stanu singletowego (tj. dwukubitowego stanu maksymalnie splątanego) i (separowalnego) stanu maksymalnie zmieszanego (tj. białego szumu). Ponadto zbadano bardziej złożoną hierarchię uogólnionych stanów Wernera, zdefiniowanych jako dowolne dwukubitowe stany

czyste zaszumione białym szumem. Co ważniejsze, przedstawiano wyniki naszych eksperymentów demonstrujących hierarchię tych korelacji kwantowych dla stanów Wernera bez zastosowania pełnej tomografii stanów kwantowych (QST) [Sci. Rep. **13**, 8564 (2023)]. Wcześniejsze badania doświadczalne opierały się na pomiarach odpowiadających wyłącznie pełnej tomografii stanów.

Ponadto w rozprawie opisano zjawiska nieklasyczne, takie jak różne rodzaje blokad fotonowych i tunelowania indukowanego fotonami oraz ich odpowiedniki fononowe. W szczególności, w pracy [Sci. Rep. **12**, 17655 (2022)] opisano nowy rodzaj blokady, który nazwaliśmy hybrydową blokadą fotonowo-fononową. Zjawisko to polega na blokowaniu wzbudzeń w modzie hybrydowym generowanym w wyniku liniowego sprzężenia modów optycznych i fononowych. Zademonstrowano w jaki sposób efekt ten można wywołać w kwantowym układzie optomechanicznym i opisano układy eksperymentalne, w których generacja i obserwacja tego nowego zjawiska jest możliwa. Ponadto omówiono możliwość zaobserwowania niekonwencjonalnych jedno- i wielofotonowych blokad, które mogą być wywołane w układzie liniowym sprzężonym ze ściśniętym rezerwuarem, jak to opisano w pracy [Phys. Rev. A **100**, 053857 (2019)]. W tym przypadku nieliniowość, która jest odpowiedzialna za generację blokady fotonowej w liniowym układzie kwantowym jest indukowana przez jego liniowe sprzężenie z nieliniowym rezerwuarem kwantowym.

Fizyka otwartych kwantowych układów w przypadkach ultrasłabego i tzw. głęboko-słabego sprzężenia światła z materią jest również omawiana w rozprawie. Szczegółowo zbadano zjawisko rozfazowania układów kwantowych będące głównym czynnikiem utrudniającym implementację algorytmów kwantowych i tym samym rozwój praktycznych technologii kwantowych. Wyjaśniano wpływ czystego rozfazowania światła i materii, w przypadkach ultrasłabego i głęboko-słabego sprzężenia, stosując uogólnione równania podstawowe dla dwóch dobrze znanych modeli oddziaływan światła z materią bez zastosowania przybliżenia rotującej fali, tj.: (i) kwantowego modelu Rabiego opisującego układ dwupoziomowy sprzężony z pojedynczym modem wnęki rezonansowej oraz (ii) modelu Hopfielda opisującego kolektywne (bozonowe) wzbudzenia materii oddziałującej z jednomodowym polem wnęki. Wyjaśniono w rozprawie, że postać Hamiltonianu szumu dla składników takich układów może zależeć od oddziaływania światła z materią, a zatem może zależeć od zastosowanego cechowania. Jednakże, jeśli zmiany wywołane przez oddziaływania, jak również transformacje cechowania są poprawnie zastosowane, wówczas można uzyskać prawidłowe współczynniki niezmiennicze względem ce-

chowania, tak jak opisano to w pracy [Phys. Rev. Lett. **130**, 123601 (2023)]. W rozprawie policzono i szczegółowo omówiono współczynniki rozfazowania zależne od stanów oddziałujących układów światła z materią przy uwzględnieniu fluktuacji w stopniach swobody światła lub w stopniach swobody materii.

W idealnych warunkach fizycznych można rozważać unitarną ewolucję układów hermitowskich zakładając ich całkowitą izolację od otoczenia, podczas gdy układy niehermitowskie w bardziej realistycznych modelach fizycznych ewoluują (zwykle) w sposób nieunitarny. Dynamika realistycznego układu jest opisana przez równanie podstawowe, które opisuje, w jaki sposób energia, spójność i informacja kwantowa są tracone do środowiska. Równanie podstawowe w standardowej postaci Goriniego, Kossakowskiego, Sudarshana i Lindblada składa się z członu uwzględniającego hamiltonian hermitowski, który opisuje unitarną ewolucję układu, oraz z członu niehermitowskiego określonego przez tak zwane dyssypatory Lindblada opisujące nieunitarną ewolucję układu. Zgodnie z metodą trajektorii kwantowych (zwaną też metodą skoków kwantowych), umożliwiającą rozwiązywanie i intuicyjną interpretację równań podstawowych, te dyssypatory mogą być rozdzielone na dwa człony: zależne i niezależne od skoków kwantowych. W ten sposób hermitowski hamiltonian może być przekształcony w hamiltonian niehermitowski, który opisuje układ, który ulega dyssypacji bez skoków kwantowych. Drugi człon dyssypatorów Lindblada opisuje ewolucję układu wywołaną skokami kwantowymi, które wynikają z ciągłych pomiarów układu wykonywanych przez otoczenie. Skoki kwantowe są zwykle istotne dla dokładnego opisu mikroskopijnych otwartych układów kwantowych i uzyskania wyników zgodnych z teorią pomiarów kwantowych. Ewolucja bez skoków kwantowych, która jest określona przez małe perturbacje w układzie opisanym przez hamiltonian niehermitowski, może prowadzić do nowych fundamentalnych typów ewolucji. Jednym z ciekawych przykładów takiego nowego zachowania w niehermitowskiej mechanice Carla Bendera jest pojawienie się (półklasycznych) punktów wyjątkowych, w których niektóre wartości i wektory własne niehermitowskiego hamiltonianu stają się zdegenerowane. W rozprawie omówione kwantowe punkty wyjątkowe Liouvillianów (LEP), które są zdefiniowane jako degeneracje wartości i wektorów własnych kwantowego Liouvillianu (przy uwzględnieniu efektu skoków kwantowych), zamiast rozważania półklasycznych punktów wyjątkowych odpowiadających degeneracjom niehermitowskiego hamiltonianu (z pominięciem skoków kwantowych). W rozprawie wykazano teoretycznie i eksperymentalnie, że można zaobserwować kwantowe punkty wyjątkowe stosując tomografię procesów kwantowych (QPT). Celem potwierdzenia tych przewidywań

teoretycznych, przeprowadziłam eksperymenty kwantowe w chmurze na procesorze kwantowym IBMQ [e-print arXiv:2401.14993 (2024)]. Wyniki te jednoznacznie pokazały możliwości eksperymentalne generowania, kontroli i detekcji kwantowych punktów wyjątkowych w układach o małej liczbie kubitów z wykorzystaniem kwantowej tomografii procesów.

Contents

1	Experimental hierarchy of two-qubit quantum correlations without state tomography	5
1.1	Chapter outline	5
1.1.1	Popular introduction	5
1.1.2	Motivation	7
1.1.3	Main results	7
1.1.4	My contribution and importance of the work	10
1.2	Reprint of article [P1]	11
2	Hybrid Photon-Phonon Blockade	25
2.1	Chapter outline	25
2.1.1	Popular introduction	25
2.1.2	Motivation	28
2.1.3	Main results	29
2.1.4	My contribution and importance of the work	31
2.2	Reprint of article [P2]	32
3	Two-photon blockade via squeezing	57
3.1	Chapter outline	57
3.1.1	Popular introduction to multi photon blockade (multi-PB)	57
3.1.2	Motivation	58
3.1.3	Main results	59
3.1.4	My contribution and importance of the work	61
3.2	Reprint of article [P3]	62
4	Pure dephasing in the ultrastrong coupling regime	81
4.1	Chapter outline	81
4.1.1	Popular introduction	81

4.1.2	Motivation	83
4.1.3	Main results	83
4.1.4	My contribution and importance of the work	86
4.2	Reprint of article [P4]	87
5	Quantum exceptional points of non-Hermitian systems via quantum process tomography	101
5.1	Chapter outline	101
5.1.1	Popular introduction	101
5.1.2	Motivation	104
5.1.3	Summary of the main results	104
5.1.4	More details on the applied methods	105
5.1.5	My contribution and importance of the work	107
5.2	Preprint of article [P5]	108
6	Conclusion	135
	Appendix A List of publications	139
	Appendix B Statements about the contributions to the publications	141
	Appendix C Abbreviations	147

Preface

This thesis comprises a collection of five articles that delve into the fascinating world of controlling and preserving quantum correlations in dissipative systems, shedding light on how dissipation can result in novel phenomena and effects in the quantum world.

Quantum correlations, including entanglement, quantum steering, Bell nonlocality, quadrature squeezing, photon antibunching, and sub-Poissonian photon number statistics, are vital for quantum technologies such as quantum information processing and metrology. However, these correlations are fragile and are susceptible to environmental noise and dissipation. Therefore, it is crucial to develop methods for controlling and preserving quantum correlations in dissipative systems.

My research journey was fueled by this quest to understand and manipulate quantum correlations in the presence of noise. In article [P1] (chapter 1) I explain how the presence of system dissipation can uncover a fundamental distinction between quantum entanglement, EPR steering, and Bell nonlocality for two-qubit systems.

In the initial stages of my research, my focus was on engineering nonlinear quantum optics systems and exploring the nonclassical effects that could be anticipated within different systems, including cavity-quantum electrodynamics (QED) and circuit QED. Specifically, I have delved into the possibilities of observing photon blockade and photon-induced tunneling phenomena. To accomplish this, I employed existing criteria and proposed novel criteria to predict and ascertain these effects within our proposed systems in chapters 2 and 3.

In this thesis, I also study the physics of open quantum light-matter systems in the ultrastrong and deep-strong coupling regimes, focusing on pure dephasing, which is a major source of quantum information loss. Pure dephasing can limit the performance of quantum devices and protocols that rely on coherence. In article [P4] (chapter 4), we applied generalized master equations and calculated the dephasing rates induced by fluctuations in either the light or matter degrees-of-freedom.

Another research topic that our group is focused on for dissipative quantum engineering are exceptional points (EPs), which are singularities in the spectrum of a non-Hermitian Hamiltonian. In article [P5] (chapter 5), we studied quantum Liouvillian exceptional points (LEPs) as degeneracies of quantum Liouvillians. LEPs are natural generalizations of standard semiclassical Hamiltonian EPs, by including the effect of quantum jumps. We suggested and experimentally implemented quantum process tomography (QPT) to reveal LEPs in a chosen system.

This thesis is composed of five chapters, where each chapter presents the research conducted during my studies related to the topic of the dissertation. Each chapter provides an overview of a given paper. It comprises a short general introduction to the topic considered, as well as motivation for the stated problem, followed by a summary of the obtained results. It also include the statement of my contribution.

For the convenience of cross-reference within the dissertation, I index these publications with the letter **P**.

Chapter 1 is titled *Experimental hierarchy of two-qubit quantum correlations without state tomography* [P1].

This chapter is devoted to the theoretical study of the hierarchy of quantum correlations on the example of two-qubit pure states mixed with white noise, which are referred to as Werner states or generalized Werner states (GWSs). Moreover, the experimental results are reported demonstrating these quantum correlations for the Werner states without full quantum state tomography (QST).

Chapter 2 is titled *Hybrid photon-phonon blockade* [P2].

This chapter introduces the phenomenon of photon-phonon blockade in a hybrid optomechanical system, in which a cavity mode is coupled to both a mechanical mode and a qubit. This is a novel type of a blockade effect. It is demonstrated how the interplay between photon and phonon interactions can lead to strong nonlinearity effects and nonclassical correlations.

Chapter 3 is titled *Two-photon blockade and photon-induced tunneling generated by squeezing* [P3].

This chapter discusses the generation of two-photon blockade and photon-induced tunneling in a cavity QED system with squeezed light. It is demonstrated how to control the transition between different regimes of photon statistics and quantum interference by properly tuning the squeezing parameter.

Chapter 4 is titled *Pure Dephasing of Light-Matter Systems in the ultrastrong and deep-Strong coupling regimes* [P4].

The chapter is devoted to the dephasing problem in a two well-studied models of light-matter interactions, i.e.: the quantum Rabi model and the Hopfield model in the ultra-strong and deep-strong coupling regimes. In these regimes the light-matter interaction becomes comparable to the bare resonance frequencies of the subsystems. It is shown how the choice of gauge transformation affects the noise Hamiltonians and dephasing rates.

Chapter 5 is titled *Quantum exceptional points of non-Hermitian systems via quantum process tomography* [P5].

This chapter discusses how non-Hermitian Hamiltonians can describe open quantum systems and how their degeneracies, known as exceptional points, affect quantum dynamics and measurements. Here, a novel method and its experimental implementation for detecting and characterizing exceptional points using quantum process tomography is described.

Appendix A contains the list of my publications which are discussed in this thesis.

The interrelations between my papers are summarized in the Table below.

Appendix B includes statements about the contributions of other co-authors to publications [P1]–[P5].

Appendix C comprises the list of abbreviations utilized in my thesis, including those in my publications.

It is my sincere hope that this thesis not only enriches the current knowledge, but also inspires further research in the fascinating field of quantum optics.

Research fields & topics	Articles				
	[P1]	[P2]	[P3]	[P4]	[P5]
Nonlinear optics	—	yes	yes	yes	—
Linear optics	yes	—	—	—	—
Circuit-QED	—	—	—	—	yes
Optomechanics	—	yes	—	—	—
Quantum information processing	yes	—	—	—	yes
Non-Hermitian systems	yes	yes	yes	yes	yes
Non-Hermitian Hamiltonians	—	yes	—	—	yes
White noise	yes	—	—	—	yes
Master equations (MEs)	—	yes	yes	yes	yes
Generalized MEs	—	—	yes	yes	—
Exceptional points	—	—	—	—	yes
Photon correlations	yes	yes	yes	yes	—
Correlations of qubits	yes	yes	—	—	yes
Entanglement	yes	yes	yes	yes	—
Photon antibunching	—	yes	yes	—	—
Quantum tomography	yes	yes	—	—	yes
Experiments	yes	—	—	—	yes

Table 1 Research areas and topics (including quantum effects and quantum methods) covered by my papers and thesis.

Chapter 1

Experimental hierarchy of two-qubit quantum correlations without state tomography

1.1 Chapter outline

This chapter explores various types of quantum correlations, such as quantum entanglement, EPR steering, and Bell nonlocality, for two-qubit pure states affected by white noise, which are called Werner or generalized Werner states (GWSs) and discussed in my article [P1]. Specifically, Werner states [8]¹ are the mixtures of a maximally entangled state and a maximally mixed state corresponding to white noise. Moreover, I studied GWSs which are defined as an arbitrary two-qubit pure state mixed with white noise. They exhibit quantum correlations which are even more counterintuitive than those of the standard Werner states (see, e.g., [9] and references therein).

I present the main results of article [P1] that clarify the significance and impact of our results in the field of quantum information and technology.

1.1.1 Popular introduction

Quantum correlations stand as a fundamental feature of quantum physics, setting them apart from classical physics. They encompass various forms, such as quantum entanglement [2], EPR steering [3,4], and Bell nonlocality [5]. Comprehending and

¹This and other references in this chapter correspond to those cited in article [P1].

quantifying various properties of quantum correlations is crucial for advancing the development of quantum information protocols and their practical applications.

From a cryptographic standpoint, distinguishing the three types of two-party quantum correlations involves assessing the reliability of detectors employed by the involved parties, typically referred to as Alice and Bob. In reference to [6], the distinctions are as follows: (i) Quantum entanglement signifies nonlocal quantum correlations detectable when both parties possess reliable detectors; (ii) EPR steering denotes nonlocal quantum correlations verifiable when one party has a reliable detector and the other an unreliable one; and (iii) Bell nonlocality represents nonlocal quantum correlations observable when both parties have unreliable detectors.

Although quantum entanglement, EPR steering, and Bell nonlocality are indistinguishable for pure two-qubit states, they may exhibit different characteristics when dealing with mixed two-qubit states that contain noise. Thus, by introducing noise into a pure state, a hierarchy of these types of quantum correlations emerges.

The Werner states exemplify this hierarchy, because they demonstrate that the singlet state when is influenced to a precisely defined extent by white noise can exhibit, e.g., entanglement without displaying Bell nonlocality, as first demonstrated by Werner in 1989 [8]. Further explorations of the Werner states revealed that different regimes of entanglement, EPR steerability, and Bell nonlocality can arise, depending on the level of white noise. Thus, special states of the Werner states can be: (i) Bell nonlocal and thus entangled and steerable, (ii) Bell local but steerable and thus entangled, (iii) unsteerable (and thus Bell local) but entangled, or (iv) separable (and thus unsteerable and Bell local). Note that steering and its measures can be defined in various measurement scenarios. Then a more nuanced and profound insight into the hierarchy of quantum correlations can be revealed. Article [P1] focuses on generating and detecting these correlations, with a particular emphasis on the Werner and Werner-like states.

The objective of article [P1] is to investigate the hierarchy of quantum correlations, including entanglement, steering, and Bell nonlocality, for two-qubit mixed states. Detecting and quantifying quantum correlations experimentally can be challenging because traditional methods such as quantum state tomography (QST) or specific witnesses are often inefficient or limited in scope. Therefore, our aim was to establish a versatile and practical experimental setup capable of measuring various types of quantum correlations without relying on a full QST. To achieve this, we reviewed the existing methods and indicators of quantum correlations in the literature and compare them with our proposed approach.

We introduced a convenient tool for determining the density matrix of a two-qubit system using only six elements of a correlation matrix R , which are linear combinations of two-qubit Stokes parameters. Experimental determination of these elements of R allowed us to unveil the hierarchy of ‘good’ measures of entanglement, steering, and Bell nonlocality for the Werner states. Furthermore, we demonstrated that our experimental setup can reveal the hierarchy of these quantum correlations also for the GWSs. Crucially, our method eliminates the necessity for employing complete QST methods, thereby significantly reducing experimental complexity and potential errors.

1.1.2 Motivation

The main motivation for this work is to investigate and understand the hierarchy of quantum correlations, such as entanglement, steering, and nonlocality, in two-qubit mixed states. We aim to explore these correlations in the context of quantum information processing and quantum technologies, as they play a crucial role in these fields. The detection and quantification of quantum correlations are challenging tasks, and existing methods, such as QST and specific witnesses, have limitations in terms of efficiency and scope. To our knowledge former experimental demonstration of such hierarchies based on ‘good’ measures of quantum correlations were based on performing full QST (see [9] and references therein) or full quantum process tomography (see [23,24] and references therein).

Therefore, we motivated to develop a versatile and practical experimental setup that can measure various types of quantum correlations without the need for full quantum state tomography. By proposing a new approach using correlation matrices and measuring specific elements, we seek to provide an efficient way to estimate quantum correlation measures and gain insights into the nature and structure of quantum correlation in two-qubit systems.

1.1.3 Main results

Understanding the distinctions between entanglement, steering, and Bell nonlocality is crucial in exploring and quantifying quantum correlations. Each concept provides valuable insights into the nature of quantum systems and offers different perspectives on the characterization and verification of quantum correlations.

The study of quantum correlations emphasizes the importance of understanding their hierarchical relationship. We use an experimental approach in this study to

investigate this aspect by measuring six elements of the correlation matrix $R = T^T T$, where the matrix elements of T are defined by $T_{ij} = \text{Tr}[\rho(\sigma_i \otimes \sigma_j)]$, which represent the average values of the Pauli matrices σ_i ($i = 1, 2, 3$), and are often referred in optics to as two-qubit Stokes parameters. Here the superscript T denotes transposition. Furthermore, we demonstrated that our experimental setup could reveal the hierarchy of these quantum correlations of the Werner state and GWSs.

Below, I explain how through article [P1] we used these concepts to show the hierarchy of quantum correlations of the Werner state and GWSs.

First, we calculated the matrix R for these two states. I should note that we have prepared experimentally the polarization Werner states by mixing the singlet Bell state with white noise.

The entanglement measure we used is the fully entangled fraction (FEF) which is dependent solely on the R matrix and, therefore, cannot be considered a universal witness of two-qubit entanglement. However, it remains a ‘good’ measure for quantifying the entanglement of the Werner states and GWSs, for which it reduces to the same function as the commonly used measures of entanglement: the Wootters’ concurrence [27] and the Zyczkowski et al.’s negativity [28]. We identified the range of the mixing (white-noise) parameter, in which the GWSs are entangled. Concerning quantifying EPR steering, we assumed simple measurement scenarios (MSs) based on two- (2MS) and three (3MS) measurements. Specifically, these scenarios involve measuring two and three Pauli operators in the qubits of both parties. For this, we used the Costa-Angelo steering measures [61], which we have rewritten in terms of the correlation matrix R . These measures quantify the degree of the violation of the steering inequality derived by Cavalcanti, Jones, Wiseman, and Reid (CJWR) [60].

We stressed that the Costa-Angelo measures, because their invariance under qubit swapping, are unable to capture the directional nature of EPR steering. It means that these measures do not account for the possibility that one qubit can be steerable by another, while the reverse may not hold. Specifically, the steering measures in the 2MS and 3MS depend on the eigenvalues of the correlation matrix R while, swapping qubits A and B leads to a modified correlation matrix $R' = T T^T$, which, however, shares the same eigenvalues as R . Consequently, the steering measures remain unchanged under qubit swapping and describe only two-way symmetric steering for any two-qubit states.

Moreover, we used the fact that the Bell nonlocality of a two-qubit state can be checked by the violation of the Bell inequality in the Clauser-Horne-Shimony-Holt (CHSH) form. We applied a rescaled Bell nonlocality measure of Horodecki

et al. [58] in a way that it takes values in the range $[0,1]$ for easier comparison with other measures employed in the article. We found the range of white noise that can be added to a given pure state, for which the resulting theoretical and experimental GWSs are Bell nonlocal. It should be stressed that the steering effect defined via the violation of the CJWR inequality in the 2MS exactly corresponds to Bell nonlocality defined via the violation of the CHSH inequality. Indeed, the Costa-Angelo steering measure in the 2MS is one-to-one related to the Horodecki et al.'s nonlocality measure.

The hierarchy of quantum correlations of the GWSs is analyzed theoretically in the article. More importantly in article [P1] we demonstrate this hierarchy experimentally by measuring only six elements of a correlation matrix. The experiment described in the study is conducted using a linear optics platform. In this setup, qubits are encoded into polarization states of discrete photons, which are generated through spontaneous parametric down-conversion (SPDC). We tested the experimental Werner-like states generated in our setup and compared experimental results with our theoretical predictions for the ideal Werner states demonstrating a very good agreement.

We calculated experimentally the correlation matrix elements R_{ij} for the Bell singlet state $R_{|\psi^-\rangle}$ and the maximally mixed state R_I corresponding to white noise. In this way the correlation matrix R_{ρ_W} of the Werner states for selected values of the mixing parameter p can be calculated as

$$R_W(P) = p^2 R_{|\psi^-\rangle} + (1 - p^2) R_I. \quad (1.1)$$

Given the experimental correlation matrix for the Werner states, we could apply the R -dependent measures of quantum correlations introduced in the theoretical part of article [P1]. These include the above mentioned measures of Bell nonlocality, steering, and entanglement solely based on the correlation matrix R .

We showed that the feasibility of our method based on measuring only six elements of the correlation matrix R for a given state ρ instead of measuring all (i.e., 15 or 16) elements of ρ as required for full QST. We tested this method on the example of the Werner states with different amounts of white noise that we were able to determine various measures of quantum entanglement, steerability, and Bell nonlocality. The method can readily be applied also for the GWSs, as we predicted theoretically, but we have not performed such experiments.

1.1.4 My contribution and importance of the work

To the best of our knowledge, prior to the publication of article [P1], there were no experimental demonstrations showcasing the hierarchy of quantum entanglement, steering, and Bell nonlocality using their respective ‘good’ measures, all achieved without resorting to full QST.

Thus, we believe that our experimental approach, which avoids the need for full QST, provides significant advantages compared to standard methods. By measuring only six elements of a correlation matrix instead of measuring all (15 or 16) elements of a density matrix required for a complete two-qubit QST, we could determine various measures of entanglement, steering, and Bell nonlocality for some classes of two-qubit states, including the studied Werner states and GWSs.

From a general perspective, we believe, that exploring the hierarchy of quantum correlation measures has potential applications such as testing complimentary relations, estimating one measure based on another without full QST, and quantifying nonclassicality in single-qubit systems using the potentials of quantum correlations. Recent experiments, such as those detailed in *Opt. Express* **32**, 2333-2346 (2024), along with preprints arXiv:2401.15995 and arXiv:2312.01055 from the experimental group led by Prof. Karel Lemr at Palack’y University in Olomouc, Czech Republic, have further validated the usefulness of our approach, as developed in [P1], and its generalizations.

I and Jan Soubusta have performed all numerical and analytical calculations. I prepared the first draft of the theoretical part of the article (i.e., its first six pages). It is important to emphasize that while I was not involved in designing the experimental setup or conducting the experiment, my contribution was significant in comparing the experimental data with the theoretical framework.

1.2 Reprint of article [P1]

On the subsequent pages, we append a reprint with permission:



[P1] Shilan Abo, Jan Soubusta, Katerina Jiráková, Karol Bartkiewicz,
Antonin Černoč, Karel Lemr, Adam Miranowicz,
*Experimental hierarchy of two-qubit quantum correlations
without state tomography*,
Scientific Reports **13**, 8564 (2023).
<http://dx.doi.org/10.1038/s41598-023-35015-9>
Copyright (2023) is retained by the authors.²

²“Copyright on any research article in open access (OA) journals published by Springer Nature is retained by the author(s). Authors grant Springer Nature a license to publish the article and identify itself as the original publisher. Authors also grant any third party the right to use the article freely as long as its integrity is maintained and its original authors, citation details and publisher are identified. OA articles in Springer Nature journals are predominantly published under Creative Commons Attribution v4.0 International licence (CC BY).” according to Global Open Research Support.



OPEN

Experimental hierarchy of two-qubit quantum correlations without state tomography

Shilan Abo¹, Jan Soubusta², Kateřina Jiráková², Karol Bartkiewicz^{1,2}, Antonín Černoč³, Karel Lemr² & Adam Miranowicz¹

A Werner state, which is the singlet Bell state affected by white noise, is a prototype example of states, which can reveal a hierarchy of quantum entanglement, steering, and Bell nonlocality by controlling the amount of noise. However, experimental demonstrations of this hierarchy in a sufficient and necessary way (i.e., by applying measures or universal witnesses of these quantum correlations) have been mainly based on full quantum state tomography, corresponding to measuring at least 15 real parameters of two-qubit states. Here we report an experimental demonstration of this hierarchy by measuring only six elements of a correlation matrix depending on linear combinations of two-qubit Stokes parameters. We show that our experimental setup can also reveal the hierarchy of these quantum correlations of generalized Werner states, which are any two-qubit pure states affected by white noise.

Quantum correlations reveal not only the strangeness of quantum mechanics, but are the main resources for quantum technologies, including quantum sensing and quantum information processing¹. Thus, the detection, control, and quantification of these resources are of paramount importance.

Among different types of quantum correlations, a special interest has been paid to quantum entanglement², Einstein–Podolsky–Rosen (EPR) steering (also called quantum steering)^{3,4}, and Bell nonlocality that can be revealed by testing the violation of a Bell inequality⁵. These types of correlations coincide for two-qubit pure states, but can be different for mixed states. Probably, the most intuitive distinction between these three types of quantum correlations for two systems (parties) can be given from a cryptographic perspective with the use of trusted and untrusted detectors. Specifically, according to Refs.^{6,7}: (i) quantum entanglement can be revealed if both parties use only trusted detectors, (ii) EPR steering can be tested if one party uses trusted detectors and the other untrusted ones, and (iii) Bell nonlocality can be demonstrated if both parties use untrusted detectors. We experimentally determined and compared measures of these correlations for Werner states.

It is theoretically well known that by gradually adding noise to a pure state, one can reveal a hierarchy of different types of quantum correlations, including quantum entanglement, EPR steering, and Bell nonlocality. These effects are equivalent for two-qubit pure states, however they are in general different for mixed states. Werner⁸ found in 1989 that the singlet Bell state affected by white noise can be entangled without exhibiting Bell nonlocality, i.e., without violating any Bell inequality. It was further found that Werner states with a proper amount of white noise can be entangled but unsteerable, or steerable without exhibiting Bell nonlocality, in addition to the trivial cases when a given state is Bell nonlocal (so also steerable and entangled) or separable (so also unsteerable and Bell local). Even a more refined hierarchy can be revealed by considering generalized Werner states, defined as mixtures of an arbitrary two-qubit pure states and white noise⁹. Thus, the Werner and Werner-like states can be considered prototype examples of states indicating such a hierarchy. Their generation and the detection of their quantum correlations are a central topic of this paper.

Here we study a hierarchy of quantum correlations via their measures. We note that various other hierarchies of non-universal witnesses of quantum correlations have been investigated in detail. These include studies of sufficient conditions (i.e., nonuniversal witnesses) for observing specific types of correlations via matrices of moments of, e.g., the annihilation, creation, position, momentum, or Pauli operators. For example: (i) hierarchies of various witnesses of spatial¹⁰ and spatiotemporal^{11,12} correlations of bosonic systems revealing their

¹Institute of Spintronics and Quantum Information, Faculty of Physics, Adam Mickiewicz University, 61-614 Poznań, Poland. ²Palacký University Olomouc, Faculty of Science, Joint Laboratory of Optics of PU and IP CAS, 17. listopadu 1192/12, 779 00 Olomouc, Czech Republic. ³Institute of Physics of the Czech Academy of Sciences, Joint Laboratory of Optics of PU and IP CAS, 17. listopadu 1154/50a, 779 00 Olomouc, Czech Republic. ✉email: jan.soubusta@upol.cz; miran@amu.edu.pl

nonclassicality via a nonpositive Glauber–Sudarshan P function; (ii) a hierarchy of entanglement witnesses^{13,14} based on the Peres–Horodecki partial transposition criterion or their generalizations¹⁵ using contraction maps (e.g., realignment) and positive maps (e.g., those of Kossakowski, Choi, and Breuer); (iii) a hierarchy of necessary conditions for the correlations that arise when performing local measurements on separate quantum systems, which enabled finding a hierarchy of upper bounds on Bell nonlocality^{16,17} (iv) a hierarchy of EPR steering witnesses¹⁸ based on entanglement criteria with the constraint that measurement devices of one party cannot be trusted. Especially powerful methods for finding infinite hierarchies of quantum-correlation criteria are those formulated as semidefinite programs^{16–20}. Note that semidefinite programming has been found very effective in calculating not only nonuniversal witnesses but also measures (or universal witnesses) of quantum steering^{3,21,22}, Bellnonlocality⁵, and entanglement². It could also be noted that a hierarchy of quantum nonbreaking channels, which is closely related to a hierarchy of temporal²³ and spatial quantum correlations, has been studied very recently both theoretically and experimentally in Ref.²⁴, where the effects of white noise (or, equivalently, of a qubit-depolarizing channel) on quantum memory, temporal steerability^{25,26}, and nonmacrorealism were revealed by applying a *full* quantum process tomography.

The use of measures or universal witnesses of these quantum correlations, however, is required to demonstrate experimentally such hierarchies in a sufficient and necessary manner. For example, to our knowledge, no experiment has been performed to determine standard entanglement measures of a general two-qubit mixed state without full quantum state tomography (QST). These measures include the concurrence²⁷, which is a measure of the entanglement of formation, the negativity²⁸ related to the Peres–Horodecki entanglement criterion, and the relative entropy of entanglement²⁹. Thus, a QST-based approach to study a hierarchy of quantum correlations was applied in our former related study⁹, which was based on measuring 16 real parameters for two-qubit Werner states.

A hierarchy of quantum-correlation measures enables efficient estimations of one measure for a given value of another. More specifically, the estimations of a measure of a given type of quantum correlation for a certain value of a measure (or bounds) of another type of quantum correlations were reported for arbitrary or specific classes of two-qubit states. These estimations include various comparisons of: (i) entanglement and Bell nonlocality^{30–33}, (ii) steering and Bell nonlocality³⁴, as well as (iii) entanglement and steering³⁵. Note that such estimations can also be applied to compare non-equivalent measures describing the same type of correlations, including two-qubit entanglement^{36,37} or single-qubit nonclassicality³⁸. Explorations of the relationships between measures of entanglement, steering, and Bell nonlocality for specific types of two-qubit states have also been attracting a considerable interest. Recent studies include, e.g., theoretical analyses of two-qubit X -states³⁹ and two-mode Gaussian states⁴⁰. Experimental QST-based hierarchies of quantum entanglement, steering, and Bell nonlocality for specific classes of two-qubit states in relation to the above-mentioned estimations were also reported, which include experiments with mixtures of partially entangled two-qubit pure states⁴¹ and GWSs based on full QST⁹ or full quantum process tomography²⁴. Such a hierarchy for the Werner states is also experimentally studied here but *without* applying a full QST.

We note that an experimental method for testing polarization entanglement without QST of general two qubit states was proposed in Ref.⁴² based on measuring a collective universal witness of Ref.⁴³. However, the method, to our knowledge, has not been implemented experimentally yet. Another experimental approach to determine entanglement of a given state without QST can be based on measuring a bipartite Schmidt number, which satisfies various conditions of a good entanglement measure^{44,45} and can be determined experimentally via a witnessing approach⁴⁶. However, it is not clear how the same method can also be used to experimentally determine steering and nonlocality measures. Note that we want to apply a versatile experimental setup, which can be used to determine various measures of all the three types of quantum correlations.

Multiple indicators of quantum steering have been demonstrated experimentally (for a review see Ref.⁴). We note a very recent Ref.⁴⁷, where it was shown experimentally that a critical steering radius is the most powerful among practical steering indicators. Its scaling property allows classifying as steerable or non-steerable various families of quantum states. This approach is useful in testing theoretical concepts of the critical radius in real experiments prone to unavoidable noise. The authors used a setup introducing losses and measured elements of a correlation matrix to determine the steering indicators. Similar quantifiers, but describing nonlocality and entanglement, were measured in Ref.⁴⁸ using the parameters M and F , which are also applied in this paper.

Here, we report the first (to our knowledge) experimental demonstration of the hierarchy of measures of entanglement, steering, and Bell nonlocality without applying full QST, i.e., by measuring only six elements of a correlation matrix R (corresponding to linear combinations of two-qubit Stokes parameters) for the Werner states. Moreover, we show that the generalized Werner states (GWSs), which are mixtures of an arbitrary two-qubit pure state and white noise, can reveal a more refined hierarchy of the quantum-correlation measures using our experimental setup.

We note that the setup applied in this work was also used earlier in Refs.^{48–51}, but for conceptually different tasks, e.g., measuring collective nonlinear witnesses of entanglement^{52,53}, Bell nonlocality measure⁵⁴, or diagnosing an entanglement-swapping protocol. Moreover, the setup enables entanglement swapping and measuring multicopy entanglement witnesses as inspired by Refs.^{55,56}.

The setup also bears some similarities with a previously proposed and implemented scheme by Bovino et al.⁵⁶. Our experimental method of measuring R for general two qubit states is conceptually similar to that reported in Ref.⁵⁶ for measuring a nonlinear entropic witness. We find that the witness, defined in the next section, can actually be interpreted as the three-measurement steering measure S . However, the advantage of our method is that it is more versatile. As shown in Ref.⁴⁸, one can perform a full tomography of all the elements of the R matrix rather than only determining its trace. Thus, from the set of six numbers (determining a correlation matrix R) we can learn much more about quantum correlations compared to the original method of Ref.⁵⁶. In addition to that, our design provides several practical benefits with respect to Ref.⁵⁶. Namely from the experimental point of view,

it only requires a single Hong–Ou–Mandel interferometer instead of two. Moreover, our design shares the same geometry with the entanglement-swapping protocol⁴⁸. As a result, it can be deployed in future teleportation-based quantum networks to acquire various entanglement measures of distributed quantum states.

This experimental method of measuring the R matrix enables us a complete determination of not only steering measures, but also a fully entangled fraction (FEF)⁵⁷ and Bell nonlocality measures⁵⁸. We note that for the GWSs, the FEF is exactly equal to the two most popular measures of entanglement, i.e., the negativity and concurrence². Thus, the hierarchy of the three measures can be experimentally determined from the R matrix for the Werner states, which is the main goal of this paper.

Correlation matrix R for Werner and Werner-like states

We study quantum effects in two qubits by means of the 3×3 correlation matrix $R = T^T T$, which is defined by the matrix T composed of the two-qubit Stokes parameters $T_{ij} = \text{Tr}[\rho(\sigma_i \otimes \sigma_j)]$, which are the mean values of the Pauli matrices σ_i ($i = 1, 2, 3$). Superscript T denotes transposition. The standard Bloch representation of a general two-qubit state ρ can be given by the elements T_{ij} together with the single-qubit Stokes parameters $u_i = \text{Tr}[\rho(\sigma_i \otimes I_2)]$ and $v_i = \text{Tr}[\rho(I_2 \otimes \sigma_i)]$ as

$$\rho = \frac{1}{4} \left(I_4 + \mathbf{u} \cdot \boldsymbol{\sigma} \otimes I_2 + I_2 \otimes \mathbf{v} \cdot \boldsymbol{\sigma} + \sum_{i,j=1}^3 T_{ij} \sigma_i \otimes \sigma_j \right), \tag{1}$$

where $\mathbf{u} = [u_1, u_2, u_3]$ and $\mathbf{v} = [v_1, v_2, v_3]$ denote the Bloch vectors of the first and second qubits, respectively. Moreover, $\boldsymbol{\sigma} = [\sigma_1, \sigma_2, \sigma_3] \equiv [X, Y, Z]$, and I_n is the n -dimensional identity operator.

We analyze in detail a special type of the general states given in Eq. (1). Specifically, we have experimentally generated the polarization Werner states by mixing the singlet Bell state, $|\psi^-\rangle = (|HV\rangle - |VH\rangle)/\sqrt{2}$, with white noise (i.e., the maximally mixed state)⁸:

$$\rho_W = p|\psi^-\rangle\langle\psi^-| + \frac{1-p}{4} I_4, \tag{2}$$

assuming various values of the mixing (noise) parameter $p \in [0, 1]$. Here, $|H\rangle$ and $|V\rangle$ denote horizontal and vertical polarization states, respectively. The correlation matrix R for the Werner states simplifies to $R(\rho_W) = p^2 I_3$.

We also theoretically analyze GWSs, which can be defined by replacing the singlet state $|\psi^-\rangle$ in Eq. (2) by a pure state $|\psi_q\rangle = \sqrt{q}|HV\rangle - \sqrt{1-q}|VH\rangle$ with a superposition parameter $q \in [0, 1]$, i.e.,

$$\rho_{GW}(p, q) = p|\psi_q\rangle\langle\psi_q| + \frac{1-p}{4} I_4. \tag{3}$$

The state can also be obtained by transmitting a photon in the state $|\psi_q\rangle$ through a depolarizing channel. Note that GWSs is often defined slightly differently, i.e., $\rho'_{GW}(p, q) = p|\phi_q\rangle\langle\phi_q| + (1-p)I_4/4$, where $|\phi_q\rangle = \sqrt{q}|HH\rangle + \sqrt{1-q}|VV\rangle$ instead of $|\psi_q\rangle$ in Eq. (3), as experimentally studied in, e.g., Ref.⁹. A special case of such states, i.e., a modified Werner state, when $|\psi^-\rangle$ is replaced by $|\phi_{q=1/2}\rangle$, is referred to as an isotropic state. Such modifications of the Werner states or the GWSs do not affect their quantum correlation measures.

The correlation matrix R for the GWSs, given in Eq. (3), is diagonal and reads

$$R[\rho_{GW}(p, q)] = \begin{pmatrix} 4p^2q(1-q) & 0 & 0 \\ 0 & 4p^2q(1-q) & 0 \\ 0 & 0 & p^2 \end{pmatrix}. \tag{4}$$

We note that the correlation matrices T and R are in general nondiagonal (including the non-perfect Werner state measured by us experimentally), although they are diagonal for the perfect GWSs states given in Eq. (3). Anyway, as shown in Ref.⁵⁹, an arbitrary state ρ described by a nondiagonal T , can be transformed (via a singular-value decomposition) into a state with a diagonal T by local unitary operations, thus, without changing its quantum correlations, including those studied below.

Measures of quantum correlations for Werner and Werner-like states

Fully entangled fraction and entanglement measures. The FEF⁵⁷ for an arbitrary two-qubit state ρ in Eq. (1) can be defined as⁴⁸:

$$\text{FEF}(\rho) = \frac{1}{2} \theta(\text{Tr}\sqrt{R} - 1), \tag{5}$$

given in terms the function $\theta(x) = \max(x, 0)$. In general, the FEF is only a witness of entanglement; however, for some special classes of two-qubit states, including the GWSs, the FEF becomes a good entanglement measure, and it reduces to the concurrence and negativity:

$$\text{FEF}[\rho_{GW}(p, q)] = N(\rho_{GW}) = C(\rho_{GW}) = \frac{1}{2} \theta \left\{ p[1 + 4\sqrt{q(1-q)}] - 1 \right\}. \tag{6}$$

For completeness, we recall that the concurrence $C(\rho)$ of an arbitrary two-qubit state ρ is defined as²⁷: $C(\rho) = \theta(\sqrt{\lambda_1} - \sqrt{\lambda_2} - \sqrt{\lambda_3} - \sqrt{\lambda_4})$, where $\lambda_1 \geq \lambda_2 \geq \lambda_3 \geq \lambda_4$ are the eigenvalues of $\rho(\sigma_2 \otimes \sigma_2)\rho^*(\sigma_2 \otimes \sigma_2)$, the superscript $*$ denotes complex conjugation, and σ_2 is the second Pauli matrix. Moreover, we recall the definition of the negativity N of a two-qubit state ρ , which reads²⁸: $N(\rho) = \theta(-2\mu_{\min})$ with μ_{\min} denoting the smallest

eigenvalue of ρ^Γ , i.e., $\min[\text{eig}(\rho^\Gamma)]$, where the superscript Γ indicates partial transposition. It is seen that the negativity, concurrence, and FEF reduce to the same function for the GWSs.

Let $p_E(q)$ denote the largest value of the mixing parameter p as a function of the superposition parameter q for which $\rho_{\text{GW}}(p, q)$ is separable. This can be obtained by solving $\text{FEF}(\rho_{\text{GW}}) = 0$ resulting in:

$$p_E(q) = 1/[1 + 4\sqrt{q(1-q)}], \quad (7)$$

which means that $\rho_{\text{GW}}(p, q)$ is entangled iff $p \in (p_E(q), 1]$. In the special case of the standard Werner states, Eq. (6) simplifies to

$$\text{FEF}[\rho_W(p)] = N[\rho_W(p)] = C[\rho_W(p)] = \theta(3p - 1)/2, \quad (8)$$

which implies the well known fact⁸ that a given Werner state is separable iff its mixing parameter is $p \in [0, 1/3]$.

It should be noted that entanglement measures for general states, given in Eq. (1), depend not only on the correlation matrix R , but also on the single-qubit Stokes parameters (σ_n^i) for $n = 1, 2, 3$ and $i = 1, 2$. It is seen that the FEF is not a universal witness of two-qubit entanglement, because it solely depends on the R matrix. Nevertheless, the FEF is a good measure of the entanglement of the GWSs.

Quantum steering measures. The effect of quantum steering of a two-qubit state refers to the possibility to affect at a distance one qubit (say subsystem B of Bob) via local measurements performed on the other qubit (say subsystem A of Alice). The quantum steerability of a given two-qubit state ρ can be experimentally tested, assuming that each party is allowed to measure n observables in their sites (qubit), by the inequality derived by Cavalcanti, Jones, Wiseman, and Reid (CJWR), which reads⁶⁰:

$$F_n(\rho, \mathbf{r}) = \frac{1}{\sqrt{n}} \left| \sum_{i=1}^n \langle A_i \otimes B_i \rangle \right| \leq 1, \quad (9)$$

where $\mathbf{r} = \{\hat{r}_1^A, \dots, \hat{r}_n^A, \hat{r}_1^B, \dots, \hat{r}_n^B\}$ is the set of measurement directions with $\hat{r}_i^A, \hat{r}_i^B \in \mathbb{R}^3$ (for $i = 1, \dots, n$) denoting unit and orthonormal vectors, respectively. According to Ref.⁶¹, the orthogonality of the vectors \hat{r}_i^A is not required, which allows for non-orthogonal measurements to be carried out on the subsystem A . Moreover, $A_i = \hat{r}_i^A \cdot \boldsymbol{\sigma}$, $B_i = \hat{r}_i^B \cdot \boldsymbol{\sigma}$, and $\langle A_i \otimes B_i \rangle = \text{Tr}(\rho A_i \otimes B_i)$. A measure of steering can be obtained by maximizing $F_n(\rho, \mathbf{r})$ over the set of measurement directions, i.e., $F_n(\rho) = \max_{\mathbf{r}} F_n(\rho, \mathbf{r})$. More specifically, Costa and Angelo⁶¹ suggested the following steering measures depending on the number n of measurements per qubit:

$$S_n(\rho) = \mathcal{N}_n \theta[F_n(\rho) - 1], \quad (10)$$

where $\mathcal{N}_n = [\max_{\rho} F_n(\rho) - 1]^{-1}$ is the normalization constant such that $S_n(\rho) \in [0, 1]$ for any two-qubit ρ . Hereafter, we focus on analyzing the steering measures S_2 and S_3 (and related quantifiers) in the two- and three-measurement scenarios, denoted as 2MS and 3MS, which correspond respectively to measuring two and three Pauli operators on qubits of both parties. Costa and Angelo found that these two-qubit steering measures can be compactly written as⁶¹:

$$S_3(\rho) = \frac{\theta(c-1)}{\sqrt{3}-1}, \quad S_2(\rho) = \frac{\theta(\sqrt{c^2 - c_{\min}^2} - 1)}{\sqrt{2}-1}, \quad (11)$$

respectively, given in terms of $c = \sqrt{c_1^2 + c_2^2 + c_3^2}$ and $c_{\min} = \min |c_i|$, where $\{c_i\} = \text{svd}(T)$ are singular values of T . Note that the original formulas for S_2 and S_3 in Ref.⁶¹ were given assuming the diagonal form of the matrix T , so c_i were simply given by T_{ii} . The steering measures given in (11) can be rewritten in terms of the correlation matrix R as follows:

$$S_3(\rho) = \frac{\theta(\sqrt{\text{Tr}R} - 1)}{\sqrt{3}-1}, \quad (12)$$

$$S_2(\rho) = \frac{\theta\{\sqrt{\text{Tr}R - \min[\text{eig}(R)]} - 1\}}{\sqrt{2}-1}. \quad (13)$$

The Costa–Angelo measure S_3 of steering in the 3MS is sometimes modified as (see, e.g., Refs.^{35,41}):

$$S(\rho) = \sqrt{\frac{1}{2}\theta(\text{Tr}R - 1)}, \quad (14)$$

and we also apply this measure in the following, because of a useful property that S reduces to the negativity and concurrence for any two-qubit pure states. Note that $S, S_3 \in [0, 1]$ and they are monotonically related to each other for any two-qubit states:

$$S_3(\rho) = \frac{\sqrt{2S^2(\rho) + 1} - 1}{\sqrt{3}-1} \leq S(\rho). \quad (15)$$

For the GWSs, described by the correlation matrix R given in Eq. (4), we find

$$S[\rho_{\text{GW}}(p, q)] = \sqrt{\frac{1}{2}\theta[8p^2q(1 - q) + p^2 - 1]}, \tag{16}$$

$$S_3[\rho_{\text{GW}}(p, q)] = \frac{\theta[p\sqrt{1 + 8q(1 - q)} - 1]}{\sqrt{3} - 1}. \tag{17}$$

Let $p_S(q)$ denote the largest value of the mixing parameter p for a given value of the superposition parameter q for which $\rho_{\text{GW}}(p, q)$ is unsteerable. Thus, by solving $S(\rho_{\text{GW}}) = 0$, we have:

$$p_S(q) = [1 + 8q(1 - q)]^{-1/2}, \tag{18}$$

which means that a given GWS, $\rho_{\text{GW}}(p)$, is steerable assuming three measurements per qubit iff the mixing parameter $p \in (p_S(q), 1]$. In the special case of the Werner states, Eq. (16) simplifies to the formulas:

$$S[\rho_W(p)] = \sqrt{\frac{1}{2}\theta(3p^2 - 1)}, \quad S_3[\rho_W(p)] = \frac{\theta(\sqrt{3}p - 1)}{\sqrt{3} - 1}, \tag{19}$$

which imply that $\rho_W(p)$ is unsteerable in the 3MS iff $p \in [0, 1/\sqrt{3}]$.

Quantum steerability in the 2MS, as based on S_2 or related measures, corresponds to Bell nonlocality and it is discussed in detail in the next section.

We note that to quantify steering, assuming three measurements on both Alice' and Bob's qubits, we can interchangeably use: S_3 , defined in Eq. (12), S , given in Eq. (14), as well the steerable weight²¹ (as applied in our closely related paper⁹), or the steering robustness²² in the 3MS. Indeed, if one of the steering measures vanishes, then all the other measures vanish too. However, the steering measure S_2 , as defined in Eq. (13) in the 2MS, although it is equivalent to the Bell nonlocality measure B , but it is fundamentally different from another steering measure S_2 (for clarity denoted here as S'_2) studied by us in Ref.⁹, because it corresponds to the case when Alice (Bob) performs two (three) measurements on her (his) qubit. Thus, $S_2(\rho) = 0$ (corresponding to vanishing Bell nonlocality of a given state ρ) does not imply that also $S'_2(\rho) = 0$, which was shown experimentally in Ref.⁹. This is possible because an extra measurement performed by Bob on his qubit, which is allowed in the S'_2 scenario, can reveal the steerability of ρ .

Finally, it is important to stress that the applied Costa–Angelo measures, because of their invariance under qubit swapping, cannot reflect the directional property of EPR steering that one qubit might be steerable by another, but not vice versa. Specifically, the steering measures S_2 and S_3 are the functions of some eigenvalues of the correlation matrix $R = T^T T$. By swapping qubits A and B , one obtains a modified correlation matrix $R' = T T^T$, which, however, has the same eigenvalues as those of R . This means that the steering measures are invariant under the qubit-swapping operation, and, thus, describe only two-way-symmetric steering for arbitrary two-qubit states.

However, two-way steering with an asymmetry in the steering strengths⁶² and one-way steering⁶³ can be revealed, by some strengthened criteria or measures, including the steering measure S_{LUR} based on local uncertainty relations (LUR), as introduced in Ref.⁶⁴. Note that S_{LUR} cannot be determined from R , because its definition requires, in general, the knowledge of not only the correlation matrix T (or R), but also the vectors \mathbf{u} and \mathbf{v} for a given density state ρ .

The ideal Werner states $\rho_W(p)$ and the GWSs $\rho'_{\text{GW}}(p, q)$, for any $p, q \in [0, 1]$, are unchanged under qubit swapping operation (say U_{SWAP}). Although, the GWSs $\rho_{\text{GW}}(p, q)$, given in Eq. (3), change under qubit swapping, but still can be transformed into a swapping-invariant $\rho'_{\text{GW}}(p, q)$ by local unitary operations. Thus, any steering measures are symmetric (including those based on the LUR) for $\rho_W(p)$, $\rho'_{\text{GW}}(p, q)$, and $\rho_{\text{GW}}(p, q)$ with arbitrary p, q . Of course, this steering-strength symmetry can be slightly broken for experimental states, as we have revealed for the experimental Werner states ρ_W^{exp} reported in Ref.⁹. Note that those states were generated in a setup fundamentally different from that applied in the present paper and reconstructed by a full state tomography. Thus, one can calculate the steering difference $\Delta S_j = |S_{\text{LUR}}(\rho_{j,W}^{\text{exp}}) - S_{\text{LUR}}(U_{\text{SWAP}}\rho_{j,W}^{\text{exp}}U_{\text{SWAP}})|$ to reveal a potential asymmetry in the LUR-based steering measure from qubit A to B compared to that from qubit B to A , where j labels the generated eleven states. Thus, the maximum steering difference for the experimental states of Ref.⁹ can be found to be $\max_j \Delta S_j = 0.0016$, which is practically negligible and much less than the corresponding error bars. More importantly, none of those experimental states exhibited one-way steering. As explained above, S_{LUR} cannot be calculated, in general, from R , so one cannot calculate ΔS_j for the experimental data reported here, but one can reasonably assume that ΔS_j would be negligible as those for the experimental states reported in Ref.⁹.

Bell nonlocality measures. The Bell nonlocality of a given two-qubit state ρ can be tested by the violation of the Bell inequality in the Clauser–Horne–Shimony–Holt (CHSH) form⁶⁵

$$|\langle \mathcal{B} \rangle_\rho| \equiv |\langle \mathbf{a} \cdot \boldsymbol{\sigma} \otimes (\mathbf{b} + \mathbf{b}') \cdot \boldsymbol{\sigma} + \mathbf{a}' \cdot \boldsymbol{\sigma} \otimes (\mathbf{b} - \mathbf{b}') \cdot \boldsymbol{\sigma} \rangle_\rho| \leq 2, \tag{20}$$

where $\mathbf{a}, \mathbf{a}', \mathbf{b}, \mathbf{b}' \in \mathbb{R}^3$ are unit vectors describing measurement settings, and \mathcal{B} is referred to as the Bell-CHSH operator. Bell nonlocality can be quantified by the maximum possible violation of the CHSH inequality in Eq. (20) over all measurement settings, which lead Horodecki et al. to the following analytical formula⁶⁸

$$\max_{\mathcal{B}} \langle \mathcal{B} \rangle_{\rho} = 2\sqrt{M(\rho)}, \quad (21)$$

where the nonnegative quantity $M(\rho)$ is the sum of the two largest eigenvalues of $R(\rho)$. The CHSH inequality in (20) is satisfied iff $M(\rho) \leq 1$. For a better comparison with other measures of quantum correlations defined in the range $[0,1]$, the Bell nonlocality measure of Horodecki et al.⁵⁸ can be given by (see, e.g.,^{41,48,66})

$$B(\rho) = \sqrt{\theta[M-1]} = \sqrt{\theta\{\text{Tr}R - \min[\text{eig}(R)] - 1\}}, \quad (22)$$

or, equivalently, as⁶¹

$$B'(\rho) = \frac{\theta[\sqrt{M}-1]}{\sqrt{2}-1} = \frac{\theta(\sqrt{\text{Tr}R - \min[\text{eig}(R)]} - 1)}{\sqrt{2}-1} = S_2(\rho), \quad (23)$$

which guarantee that $B, B' \in [0, 1]$. It is seen that B' is exactly equal to the steering measure S_2 , given in Eq. (13), in the 2MS.

Hereafter, we apply both nonlocality measures because their specific advantages. In particular, as shown explicitly below, B' depends linearly on the mixing parameter p of the Werner states and GWSs, thus its experimental estimation results in smaller error bars compared to those of B . On the other hand, B is equal to the negativity and concurrence^{37,66}, but also to the steering measure S and the FEF:

$$B(|\psi\rangle) = S(|\psi\rangle) = \text{FEF}(|\psi\rangle) = C(|\psi\rangle) = N(|\psi\rangle) = 2|ad - bc|, \quad (24)$$

for an arbitrary two-qubit pure state $|\psi\rangle = a|HH\rangle + b|HV\rangle + c|VH\rangle + d|VV\rangle$, where a, b, c, d are the normalized complex amplitudes. This useful property of B is not satisfied for B' . We also study B to enable a more explicit comparison of our present experimental results with those in our former closely related papers^{9,48}. Anyway, B and B' are monotonically related to each other:

$$B'(\rho) = \frac{\sqrt{B^2(\rho) + 1} - 1}{\sqrt{2} - 1} \leq B(\rho). \quad (25)$$

The Bell nonlocality measures B and B' for the Werner states read

$$B[\rho_W(p)] = \sqrt{\theta(2p^2 - 1)}, \quad B'[\rho_W(p)] = \frac{\theta(\sqrt{2}p - 1)}{\sqrt{2} - 1}, \quad (26)$$

which explicitly shows that the states are nonlocal iff $p > 1/\sqrt{2}$. By comparing Eq. (26) with Eq. (8), it is clearly seen that the Werner states for the mixing parameter $p \in (1/3, 1/\sqrt{2})$ are entangled, although they do not violate the CHSH inequality, as was first predicted in Ref.⁸. For the GWSs, formulas in Eq. (26) generalize to:

$$B[\rho_{\text{GW}}(p, q)] = \sqrt{\theta\{p^2[1 + 4q(1 - q)] - 1\}}, \quad (27)$$

$$B'[\rho_{\text{GW}}(p, q)] = \frac{\theta[p\sqrt{1 + 4q(1 - q)} - 1]}{\sqrt{2} - 1}, \quad (28)$$

Let $p_B(q)$ denote the largest value of the mixing parameter p for a given value the superposition parameter q for which $\rho_{\text{GW}}(p, q)$ is Bell local. Thus, by solving $B(\rho_{\text{GW}}) = 0$ one finds:

$$p_B(q) = [1 + 4q(1 - q)]^{-1/2}, \quad (29)$$

which means that $\rho_{\text{GW}}(p, q)$ is Bell nonlocal if $p \in (p_B(q), 1]$. This function reduces for $q = 1/2$ to the well-known result that the Werner state violates the CHSH inequality iff the mixing parameter $p \in (1/\sqrt{2}, 1]$ ⁸.

Hierarchy of quantum correlations. The following hierarchy of the discussed quantum correlation measures hold for a general two-qubit state ρ :

$$B(\rho) \leq S(\rho) \leq \text{FEF}(\rho) \leq N(\rho) \leq C(\rho), \quad (30)$$

or, equivalently,

$$S_2(\rho) \leq S_3(\rho) \leq \text{FEF}(\rho) \leq N(\rho) \leq C(\rho), \quad (31)$$

We also note that $S_2(\rho) \leq B(\rho)$ and $S_3(\rho) \leq S(\rho)$. The inequalities in (30) for the GWSs reduce to

$$B(\rho_{\text{GW}}) \leq S(\rho_{\text{GW}}) \leq \text{FEF}(\rho_{\text{GW}}) = N(\rho_{\text{GW}}) = C(\rho_{\text{GW}}). \quad (32)$$

To visualize this hierarchy, we define the following hierarchy parameter of quantum correlations for the GWSs,

$$H(\rho_{\text{GW}}) = \chi[B(\rho_{\text{GW}})] + \chi[S(\rho_{\text{GW}})] + \chi[\text{FEF}(\rho_{\text{GW}})] = \chi[S_2(\rho_{\text{GW}})] + \chi[S_3(\rho_{\text{GW}})] + \chi[\text{FEF}(\rho_{\text{GW}})], \quad (33)$$

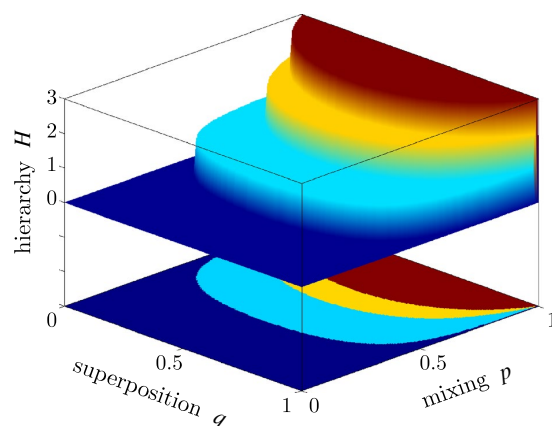


Figure 1. Hierarchy of quantum correlations of the generalized Werner states: The hierarchy parameter $H[\rho_{GW}(p, q)]$, defined in Eq. (33), versus the superposition (q) and mixing (p) parameters. A given GWS, $\rho_{GW}(p, q)$, is separable if $H(\rho_{GW}) = 0$, entangled if $H(\rho_{GW}) \geq 1$, steerable in the 3MS if $H(\rho_{GW}) \geq 2$, and Bell nonlocal (and steerable in the 2MS) if $H(\rho_{GW}) = 3$.

which is given in terms of the Heaviside function $\chi(x)$ equal to 1 for $x > 0$ and zero for $x \leq 0$. This parameter is plotted in Fig. 1 as a function of the parameters p and q uniquely specifying $\rho_{GW}(p, q)$.

Methods

The experiment is implemented on the platform of linear optics with qubits encoded into polarization states of discrete photons. These photons are generated in the process of spontaneous parametric down-conversion occurring in a cascade of two Type-I BBO crystals in the Kwiat et al. configuration⁶⁷. A femtosecond fundamental laser pulse is frequency doubled to 413 nm and pumps the crystal cascade on its way there and back (as depicted in Fig. 2). Each time the pulse impinges on the crystals, a pair of photons can be generated in the polarization singlet Bell state. To achieve a high degree of entanglement, the pumping pulse is diagonally polarized (by the half-wave plate HWP_A) and subject to a polarization dispersion line⁶⁸. In our case, this dispersion line is implemented by two beam displacers (BDs) enveloping HWP_B . The photons generated, while the pulse propagates forward are labelled 1 and 2 while the photons generated in the pulses second-time travel through the crystals are denoted 3 and 4.

The investigated state is encoded both into photons 1 and 2 (the first copy) and into photons 3 and 4 (the second copy). A collective measurement on both copies is then performed by projecting photons 2 and 4 onto the singlet Bell state using a fiber beam splitter (FBS) followed by post-selection onto coincidence detection on

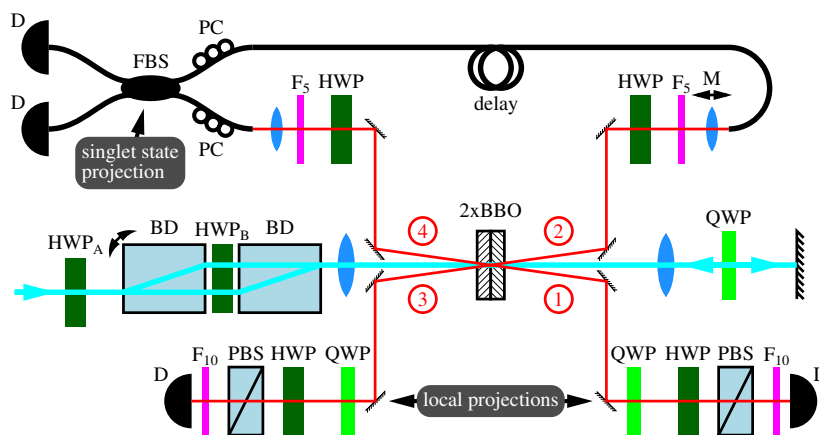


Figure 2. Schematic depiction of the experimental setup. Individual components are labelled as follows: HWP half-wave plate, QWP quarter-wave plate, D detector, BD beam displacer, PBS polarizing beam splitter, BBO β -barium-borate crystals, M motorized translation, $F_{5,10}$ 5, 10 nm-wide bandpass filters, FBS fiber beam splitter, PC polarization controller. Photons generated during the forward (backward) propagation of pump photons through the BBO crystals are labelled as 1 and 2 (3 and 4).

its output ports. The remaining photons 1 and 3 are projected locally by means of the sets of quarter and half-wave plates (QWPs and HWPs) and polarizing beam splitters (PBSs). We recorded the number of four-fold coincidence detections for various settings of the wave plates; namely, for all combinations of the projections onto the horizontal, vertical, diagonal, anti-diagonal, and both circular polarization states. We have subsequently calculated the expectation values of the Pauli matrices, that is $A_{ij} = \text{Tr}[\rho_1 \rho_2 \Pi \sigma_i \sigma_j]$, where $\Pi = -4|\psi^-\rangle\langle\psi^-|$. Note that this formula is almost identical to the one in our previous paper⁴⁸, except that in the paper instead of the Π projection, the $1 - \Pi$ projection was applied there.

When adjusting the setup to generate the requested Bell state (or the maximally mixed state), we have tuned the polarization of the pump beam, so that locally the generated photons have equal probabilities to be horizontally and vertically polarized. (The probability for a single photon being horizontally polarized is $p_H = 0.50 \pm 0.03$.) Balancing these probabilities for the horizontal and vertical polarizations implies also balancing in any single-photon polarization basis. Note that the single-photon state is fully incoherent, because the other photon from a pair is ignored and, hence, mathematically one traces over its state. As a consequence, we can consider $B_{ij} = \text{Tr}[\rho_1 \rho_2 I_4 \sigma_i \sigma_j] \approx 0$. With respect to that we conclude that the prepared two copies of the Bell state are balanced enough to warrant the replacement of $1 - \Pi$ by Π . This is also supported by the fact that the numerically closest Bell state producing the observed values for the three measures has its parameter $q = 0.474$ – see Eq. (38) and comments in the surrounding paragraph.

Despite narrow frequency filtering on all photons (see the parameters of the bandpass filters in Fig. 2) and a relatively thin crystal cascade of twice 1 mm, there is a generation-time jitter, which causes the visibility of two-photon interference on the FBS to decrease. We have performed a calibration measurement that reveals that 56.7% of the photons do not interfere on FBS. Moreover, the laser power fluctuates over time yielding variable rates of photon-pairs generation. In order to compensate for these two effects, we have performed all the measurements in the two regimes with a temporal delay between photons 2 and 4: (a) tuned for interference and (b) detuned (controlled by the motorized translation M). These two measurements together with the calibration measurement allow us to estimate the net probability of the two copies of the investigated state to pass simultaneously the Bell-state projection on the FBS, as well as the local polarization projections resulting in a four-fold detection event. With the repetition rate of the laser pulse of 80 MHz, we achieve about 1 such an event per 5 minutes.

While the crystals generate two copies of the singlet Bell state, we can readily modify the detection electronics to effectively perform the measurement on the two copies of a maximally mixed state. So far the coincidence window, i.e., the time within all photons must be detected to be considered a coincidence event, had to be very narrow (5 ns) to assure detection of photon pairs originating from a single laser pulse. By considerably widening that window by several orders of magnitude, we effectively aggregate also detections that are completely unrelated and mutually random. This way, the observed state becomes effectively white noise.

Having all the measurements performed on a pure entangled state (two copies of the singlet Bell states) as well as on the maximally mixed state (i.e., the two copies of the maximally mixed state), we can easily interpolate the results for any Werner state with mixing parameter p . In order to do so, we make use of the fact that when two polarization states of single photons interact on a beam splitter and one of them is being a maximally mixed state, the resulting probability of coincidence detection is independent of the state of the other photon. As a result, we interpolate the measurement for any Werner state by combining with probability p^2 the outcomes observed on two copies of maximally entangled states and with probability of $1 - p^2$ the results observed on a maximally mixed state.

Note that, contrary to reconstructing the R matrix, there is no experimental advantage of reconstructing the 3×3 matrix $T \equiv T_3$ compared to a full QST of a two qubit state ρ , which corresponds to reconstructing the 4×4 matrix $T_4 = [(\sigma_n \otimes \sigma_m)]$ for $n, m = 0, \dots, 3$, where $\sigma_0 = I_2$ is the qubit identity operator. It might look that reconstructing all the 9 elements of T_3 is much simpler than reconstructing 16 (or 15) elements of T_4 . But this is not the case, because the required types of measurements are the same in both reconstructions. Note that the optical reconstruction T_3 for a given two-qubit polarization state ρ is usually based on projecting ρ on all the eigenstates of the three Pauli operators for each qubit, i.e., projections onto the six polarization single-qubit states (so 36 two-qubit states): diagonal ($|D\rangle$), antidiagonal ($|A\rangle$), right- ($|R\rangle$) and left-circular ($|L\rangle$), horizontal ($|H\rangle$), and vertical ($|V\rangle$). Analogously, a standard QST of ρ also corresponds to reconstructing T_4 via the same 36 projections as those for T_3 , and the single-qubit identity operator is given by $I_2 = |H\rangle\langle H| + |V\rangle\langle V|$. So, the required measurements for reconstructing T_3 and T_4 are the same, but only their numerical reconstructions are different, although can be based on exactly the same measured data.

Results

In this section we test the experimental Werner states generated in the setup described in the former section and compare experimental results with theoretical predictions for ideal Werner states. One can calculate the correlation matrix elements R_{ij} following the derivations⁴⁸:

$$R_{ij} = A_{ij} + B_{ij} = \text{Tr}(\rho_1 \rho_2 \Pi \sigma_i \sigma_j) + \text{Tr}(\rho_1 \rho_2 I_4 \sigma_i \sigma_j), \quad (34)$$

noting that A_{ij} and B_{ij} can be experimentally determined. As a result, the physical correlation matrices R_{ij} of the singlet Bell state and the maximally mixed state were obtained using a maximum likelihood method. First we derive the correlation matrix $R_{|\psi^-\rangle}$ for the singlet Bell state.

$$R_{|\psi^-\rangle} = \begin{pmatrix} 0.971 & 0.073 & 0.010 \\ 0.073 & 0.966 & -0.009 \\ 0.010 & -0.009 & 0.941 \end{pmatrix}. \tag{35}$$

Then we evaluated also the correlation matrix for the maximally mixed state corresponding to white noise,

$$R_I = \begin{pmatrix} 0.017 & 0.006 & -0.007 \\ 0.006 & 0.013 & 0.016 \\ -0.007 & 0.016 & 0.006 \end{pmatrix}. \tag{36}$$

Using definition (2) we can derive the correlation matrix $R_W(p)$ of the Werner states for selected values of the mixing parameter p as follows,

$$R_W(p) = p^2 R_{|\psi^-\rangle} + (1 - p^2) R_I. \tag{37}$$

Now we apply the above-described definitions of the quantifiers of quantum correlations including the defined measures of Bell nonlocality (B and $B' = S_2$), steering in the 3MS (S and S_3), and entanglement (FEF) based on this correlation matrix.

Our experimental results are summarized in Tables 1 and 2 and marked by symbols in Figs. 3 and 4. The error bars were derived using a Monte Carlo method following the normal distribution of the correlation matrix components with variance corresponding to the number of detected photocounts. The asymmetry of estimated error bars results from presence of the θ function in the formulas for the estimated quantities as well as from

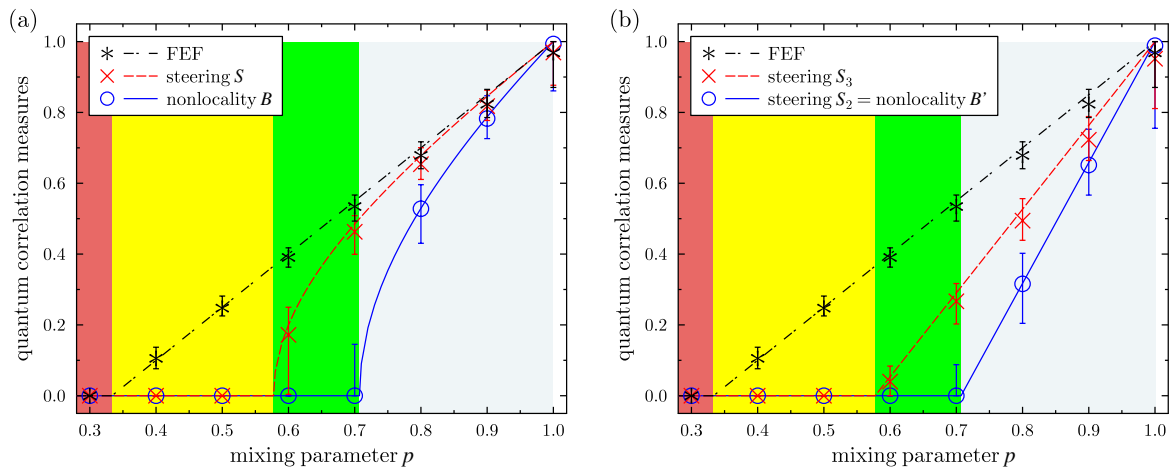


Figure 3. Experimental demonstration of the hierarchy of quantum correlations of the Werner states without full QST: the Bell nonlocality measures (a) B and (b) $B' = S_2$ (solid blue lines and curves), the 3MS steering measures (a) S and (b) S_3 (dashed red), and (a,b) the FEF (dot-dashed black lines) shown versus the mixing parameter p . Symbols depict experimental results and curves represent theoretical predictions.

p	B		S		FEF	
	Theory	Experiment	Theory	Experiment	Theory	Experiment
0.3	0.000	0.000	0.000	0.000	0.000	0.000
0.4	0.000	0.000	0.000	0.000	0.100	0.106[-0.030, +0.031]
0.5	0.000	0.000	0.000	0.000	0.250	0.248[-0.022, +0.034]
0.6	0.000	0.000	0.200	0.172[-0.168, +0.078]	0.400	0.391[-0.028, +0.027]
0.7	0.000	0.000[-0.000, +0.145]	0.485	0.463[-0.064, +0.046]	0.550	0.534[-0.041, +0.032]
0.8	0.529	0.528[-0.098, +0.068]	0.678	0.654[-0.043, +0.047]	0.700	0.679[-0.038, +0.038]
0.9	0.787	0.783[-0.057, +0.064]	0.846	0.818[-0.041, +0.045]	0.850	0.824[-0.038, +0.042]
1.0	1.000	0.993[-0.133, +0.007]	1.000	0.969[-0.092, +0.030]	1.000	0.969[-0.098, +0.031]

Table 1. Quantum correlation measures for the experimental and theoretical Werner states plotted in Fig. 3a, including measures of Bell nonlocality (B) and steering (S) in the 3MS, and the FEF. Experimental values are listed together with their asymmetric errors in square brackets.

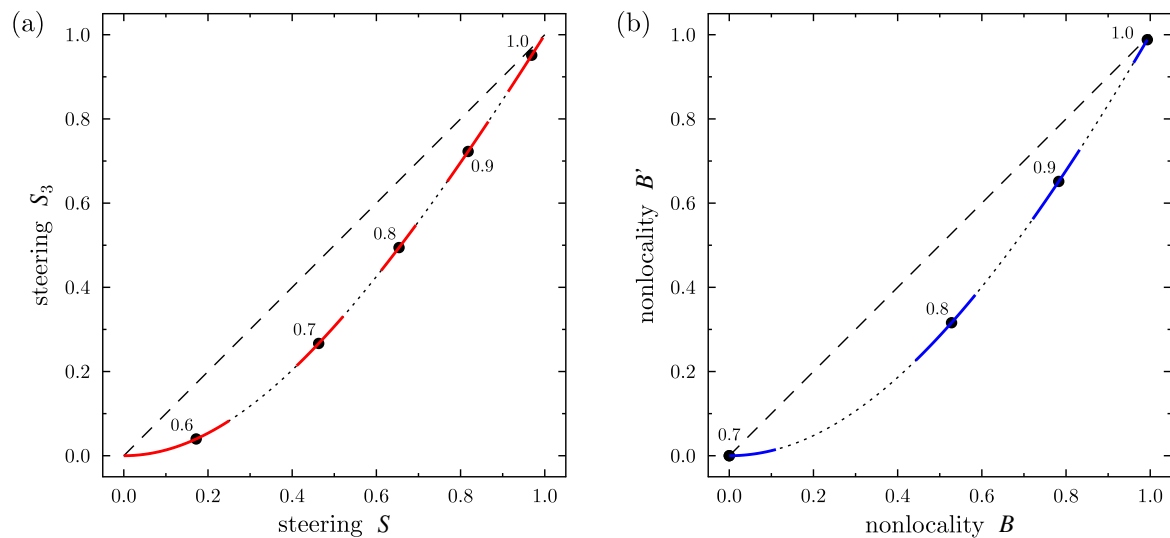


Figure 4. Experimental and theoretical predictions of different measures: (a) S_3 vs S quantifying steering in the 3MS and (b) $S_2 = B'$ vs B describing Bell nonlocality and, equivalently, steering in the 2MS. Symbols depict the measures calculated for the experimental Werner states for the indicated values of the mixing parameter p . The error bars are marked by solid red curves that follow the dotted curves. Arbitrary two-qubit states lie on the dotted curves. The dashed diagonal lines are added just to show the curvature of the solid curves more clearly.

p	S_2		S_3	
	Theory	Experiment	Theory	Experiment
0.3	0.000	0.000	0.000	0.000
0.4	0.000	0.000	0.000	0.000
0.5	0.000	0.000	0.000	0.000
0.6	0.000	0.000	0.054	0.040[−0.040, +0.044]
0.7	0.000	0.000	0.290	0.267[−0.064, +0.050]
0.8	0.317	0.316[−0.112, +0.086]	0.527	0.494[−0.055, +0.062]
0.9	0.659	0.652[−0.085, +0.101]	0.763	0.723[−0.058, +0.066]
1.0	1.000	0.989[−0.233, +0.011]	1.000	0.952[−0.141, +0.048]

Table 2. The Costa–Angelo measures S_3 and $S_2 = B'$ of steering in the 3MS and 2MS, respectively, for the experimental and theoretical Werner states plotted in Fig. 3b.

the requirement on the physicality of the R matrices. Figure 3 shows also the theoretically predicted correlation measures plotted with solid curves, which were calculated for the ideal Werner states.

In the theoretical section we considered the Costa–Angelo steering measures S_2 and S_3 that can be calculated also from the R matrix. We evaluated these steering measures using Eqs. (12) and (13). The results are plotted in Fig. 3b. It is clear that these measures linearly depend on the mixing parameter p . The nonzero regions of the correlation measures, shown in both panels of Fig. 3, are the same. Experimental results shown in Fig. 3b are also summarized in Table 2.

The original correlation matrices R were derived from measured coincidences using two methods of maximum likelihood estimation of Ref.⁶⁹. Both methods lead to the R matrices that are essentially the same. Our experimental results shown in Fig. 3 demonstrate a very good agreement with our theoretical predictions. It is clear that S_2 , S_3 , and FEF are the most stable measures at least for the Werner states and GWSs by exhibiting the smallest errors because of their linear dependence on the mixing parameter p . By contrast to those quantifiers, the measures of steering S in the 3MS and of Bell nonlocality (B) are much steeper functions and that is why they are much more sensitive to unavoidable fluctuations of measured coincidence counts, as reflected in all the derived quantities. A comparison of the steering measures S_3 and S and the Bell nonlocality measures S_2 and B for arbitrary theoretical states and the experimental Werner states are shown in Fig. 4.

In the experiment all imperfections of individual components decrease the resulting correlation measures. Together with the instability and a natural Poisson randomness of the measured coincidences, these effects result in measurement uncertainties. Also our experimentally generated singlet Bell state is not perfect. We tried to simulate all these mentioned imperfections by degrading the input Bell-like state assuming the rest of the measurement to be nearly perfect. These expected imperfections result in a class of generalized states in the form of

$$\rho(p, q) = p|\psi_q^-\rangle\langle\psi_q^-| + (1 - p)|\psi_q^+\rangle\langle\psi_q^+|, \quad (38)$$

where $|\psi_q^\pm\rangle = \sqrt{q}|HV\rangle \pm \sqrt{1-q}|VH\rangle$. The correlation measures for our most entangled experimental Bell-like state read: $B = 0.9933$, $S = 0.9691$, and $\text{FEF} = 0.9685$. We found that these results are the most consistent with $\rho(p, q)$ for the parameters $q \approx 0.474$ and $p \approx 0.994$. This implies the purity of this Bell-like state of about 98.9%.

Conclusions

We reported the detection of quantum correlation measures of two optical polarization qubits without QST. Specifically, we have measured all the elements of the correlation matrix R (which is symmetric by definition) for the Werner states with different amount of white noise. These elements correspond to linear combinations of two-qubit Stokes parameters. With the matrix R , we were able to determine various measures of quantum entanglement, steerability, and Bell nonlocality of the Werner and Werner-like states.

Most notably, our experiment allows us to show the hierarchy of the tested quantum correlation measures. This means that a given Werner state is separable iff its mixing parameter is $p \leq 1/3$. A Werner state for $p \in (1/3, 1/\sqrt{3}]$ is entangled (as revealed by a nonzero FEF), but it is unsteerable and Bell local. Subsequently, a Werner state for $p \in (1/\sqrt{3}, 1/\sqrt{2}]$ is entangled and steerable in the 3MS, but unsteerable in the 2MS, which means that it does not exhibit Bell nonlocality. Finally, a Werner state for $p > 1/\sqrt{2}$ is also Bell nonlocal, so steerable even in the 2MS. It is clear that a specific threshold for steerability depends on the number of measurement settings which in our case equal 2 and 3. Different thresholds have been found for different number of measurement settings, see e.g. Refs.^{6,9,70}. These regions, separated by the three values of $p = \{1/3, 1/\sqrt{3}, 1/\sqrt{2}\} \approx \{0.333, 0.577, 0.707\}$, are depicted with different background colors in Fig. 3. We have also analyzed theoretically a hierarchy (shown in Fig. 1) of some measures of quantum correlations for generalized Werner states, which are defined as arbitrary superpositions of a two-qubit partially-entangled pure state and white noise.

The problem of detecting measures of quantum correlations is essential to assess their suitability for quantum-information protocols especially for quantum communication and cryptography when considering not only trusted but also untrusted devices. We believe that experimental determination of various measures of entanglement, steering, and Bell nonlocality without full QST, as reported in this work, clearly shows its advantage compared to standard methods based on a complete QST. Specifically, our method relies on measuring only 6 real elements instead of 15 (or even 16) elements in a complete two-qubit QST.

Moreover, experimental studies of a hierarchy of quantum-correlation measures might be useful for, e.g.: (i) testing complementarity relations between various measures, (ii) effective estimations of one measure for a specific value of another measure without full QST, or even (iii) quantifying nonclassicality of single-qubit systems via potentials of quantum correlations.

Data availability

All the data necessary to reproduce the results are included in this published article and its digital supplement. We note that all the raw experimental data used in this work were obtained in our experiment reported in Ref.⁴⁸. Of course, their usage and interpretation are very different here compared to the previous work.

Received: 22 February 2023; Accepted: 11 May 2023

Published online: 26 May 2023

References

- Hidary, J. D. *Quantum Computing: An Applied Approach* (Springer, 2019).
- Horodecki, R., Horodecki, P., Horodecki, M. & Horodecki, K. Quantum entanglement. *Rev. Mod. Phys.* **81**, 865–942. <https://doi.org/10.1103/RevModPhys.81.865> (2009).
- Cavalcanti, D. & Skrzypczyk, P. Quantum steering: A review with focus on semidefinite programming. *Rep. Prog. Phys.* **80**, 024001. <https://doi.org/10.1088/1361-6633/80/2/024001> (2017).
- Uola, R., Costa, A. C. S., Nguyen, H. C. & Gühne, O. Quantum steering. *Rev. Mod. Phys.* **92**, 015001. <https://doi.org/10.1103/revmodphys.92.015001> (2020).
- Brunner, N., Cavalcanti, D., Pironio, S., Scarani, V. & Wehner, S. Bell nonlocality. *Rev. Mod. Phys.* **86**, 419–478. <https://doi.org/10.1103/RevModPhys.86.419> (2014).
- Wiseman, H. M., Jones, S. J. & Doherty, A. C. Steering, entanglement, nonlocality, and the Einstein–Podolsky–Rosen paradox. *Phys. Rev. Lett.* **98**, 140402. <https://doi.org/10.1103/physrevlett.98.140402> (2007).
- Jones, S. J., Wiseman, H. M. & Doherty, A. C. Entanglement, Einstein–Podolsky–Rosen correlations, Bell nonlocality, and steering. *Phys. Rev. A* **76**, 052116. <https://doi.org/10.1103/PhysRevA.76.052116> (2007).
- Werner, R. F. Quantum states with Einstein–Podolsky–Rosen correlations admitting a hidden-variable model. *Phys. Rev. A* **40**, 4277. <https://doi.org/10.1103/physreva.40.4277> (1989).
- Jiráková, K., Černoch, A., Lemr, K., Bartkiewicz, K. & Miranowicz, A. Experimental hierarchy and optimal robustness of quantum correlations of two-qubit states with controllable white noise. *Phys. Rev. A* **104**, 062436. <https://doi.org/10.1103/physreva.104.062436> (2021).
- Richter, T. & Vogel, W. Nonclassicality of quantum states: A hierarchy of observable conditions. *Phys. Rev. Lett.* **89**, 283601. <https://doi.org/10.1103/PhysRevLett.89.283601> (2002).
- Vogel, W. Nonclassical correlation properties of radiation fields. *Phys. Rev. Lett.* **100**, 013605. <https://doi.org/10.1103/physrevlett.100.013605> (2008).
- Miranowicz, A., Bartkowiak, M., Wang, X., Xi Liu, Y. & Nori, F. Testing nonclassicality in multimode fields: A unified derivation of classical inequalities. *Phys. Rev. A* **82**, 013824. <https://doi.org/10.1103/physreva.82.013824> (2010).
- Shchukin, E. & Vogel, W. Inseparability criteria for continuous bipartite quantum states. *Phys. Rev. Lett.* **95**, 230502. <https://doi.org/10.1103/physrevlett.95.230502> (2005).

14. Miranowicz, A. & Piani, M. Comment on Inseparability criteria for continuous bipartite quantum states. *Phys. Rev. Lett.* **97**, 058901. <https://doi.org/10.1103/physrevlett.97.058901> (2006).
15. Miranowicz, A., Piani, M., Horodecki, P. & Horodecki, R. Inseparability criteria based on matrices of moments. *Phys. Rev. A* **80**, 052303. <https://doi.org/10.1103/physreva.80.052303> (2009).
16. Navascués, M., Pironio, S. & Acín, A. Bounding the set of quantum correlations. *Phys. Rev. Lett.* **98**, 010401. <https://doi.org/10.1103/physrevlett.98.010401> (2007).
17. Navascués, M., Pironio, S. & Acín, A. A convergent hierarchy of semidefinite programs characterizing the set of quantum correlations. *New J. Phys.* **10**, 073013. <https://doi.org/10.1088/1367-2630/10/7/073013> (2008).
18. Kogias, I., Skrzypczyk, P., Cavalcanti, D., Acín, A. & Adesso, G. Hierarchy of steering criteria based on moments for all bipartite quantum systems. *Phys. Rev. Lett.* **115**, 210401. <https://doi.org/10.1103/physrevlett.115.210401> (2015).
19. Doherty, A. C., Parrilo, P. A. & Spedalieri, F. M. Complete family of separability criteria. *Phys. Rev. A* **69**, 022308. <https://doi.org/10.1103/physreva.69.022308> (2004).
20. Eisert, J., Hyllus, P., Gühne, O. & Curty, M. Complete hierarchies of efficient approximations to problems in entanglement theory. *Phys. Rev. A* **70**, 062317. <https://doi.org/10.1103/PhysRevA.70.062317> (2004).
21. Skrzypczyk, P., Navascués, M. & Cavalcanti, D. Quantifying Einstein–Podolsky–Rosen steering. *Phys. Rev. Lett.* **112**, 180404. <https://doi.org/10.1103/PhysRevLett.112.180404> (2014).
22. Piani, M. & Watrous, J. Necessary and sufficient quantum information characterization of Einstein–Podolsky–Rosen steering. *Phys. Rev. Lett.* **114**, 060404. <https://doi.org/10.1103/physrevlett.114.060404> (2015).
23. Ku, H.-Y., Chen, S.-L., Lambert, N., Chen, Y.-N. & Nori, F. Hierarchy in temporal quantum correlations. *Phys. Rev. A* **98**, 022104. <https://doi.org/10.1103/physreva.98.022104> (2018).
24. Ku, H.-Y. *et al.* Quantifying quantumness of channels without entanglement. *PRX Quantum* **3**, 020338. <https://doi.org/10.1103/PRXQuantum.3.020338> (2022).
25. Chen, S.-L. *et al.* Quantifying non-Markovianity with temporal steering. *Phys. Rev. Lett.* **116**, 020503. <https://doi.org/10.1103/PhysRevLett.116.020503> (2016).
26. Chen, S.-L. *et al.* Spatio-temporal steering for testing nonclassical correlations in quantum networks. *Sci. Rep.* **7**, 3728. <https://doi.org/10.1038/s41598-017-03789-4> (2017).
27. Hill, S. A. & Wootters, W. K. Entanglement of a pair of quantum bits. *Phys. Rev. Lett.* **78**, 5022–5025. <https://doi.org/10.1103/PhysRevLett.78.5022> (1997).
28. Życzkowski, K., Horodecki, P., Sanpera, A. & Lewenstein, M. Volume of the set of separable states. *Phys. Rev. A* **58**, 883–892. <https://doi.org/10.1103/physreva.58.883> (1998).
29. Vedral, V. & Plenio, M. B. Entanglement measures and purification procedures. *Phys. Rev. A* **57**, 1619–1633. <https://doi.org/10.1103/PhysRevA.57.1619> (1998).
30. Verstraete, F. & Wolf, M. M. Entanglement versus Bell violations and their behavior under local filtering operations. *Phys. Rev. Lett.* **89**, 170401. <https://doi.org/10.1103/PhysRevLett.89.170401> (2002).
31. Bartkiewicz, K., Horst, B., Lemr, K. & Miranowicz, A. Entanglement estimation from Bell inequality violation. *Phys. Rev. A* **88**, 052105. <https://doi.org/10.1103/PhysRevA.88.052105> (2013).
32. Horst, B., Bartkiewicz, K. & Miranowicz, A. Two-qubit mixed states more entangled than pure states: Comparison of the relative entropy of entanglement for a given nonlocality. *Phys. Rev. A* **87**, 042108. <https://doi.org/10.1103/PhysRevA.87.042108> (2013).
33. Su, Z., Tan, H. & Li, X. Entanglement as upper bound for the nonlocality of a general two-qubit system. *Phys. Rev. A* **101**, 042112. <https://doi.org/10.1103/PhysRevA.101.042112> (2020).
34. Quan, Q., Zhu, H., Fan, H. & Yang, W.-L. Einstein–Podolsky–Rosen correlations and Bell correlations in the simplest scenario. *Phys. Rev. A* **95**, 062111. <https://doi.org/10.1103/PhysRevA.95.062111> (2017).
35. Fan, X.-G., Yang, H., Ming, F., Wang, D. & Ye, L. Constraint relation between steerability and concurrence for two-qubit states. *Ann. Phys.* **533**, 2100098. <https://doi.org/10.1002/andp.202100098> (2021).
36. Miranowicz, A. & Grudka, A. Ordering two-qubit states with concurrence and negativity. *Phys. Rev. A* **70**, 032326. <https://doi.org/10.1103/PhysRevA.70.032326> (2004).
37. Miranowicz, A. & Grudka, A. A comparative study of relative entropy of entanglement, concurrence and negativity. *J. Opt. B Quantum Semiclass. Opt.* **6**, 542. <https://doi.org/10.1088/1464-4266/6/12/009> (2004).
38. Miranowicz, A. *et al.* Statistical mixtures of states can be more quantum than their superpositions: Comparison of nonclassicality measures for single-qubit states. *Phys. Rev. A* **91**, 042309. <https://doi.org/10.1103/PhysRevA.91.042309> (2015).
39. Sun, W.-Y., Wang, D., Shi, J.-D. & Ye, L. Exploration quantum steering, nonlocality and entanglement of two-qubit x-state in structured reservoirs. *Sci. Rep.* **7**, 1. <https://doi.org/10.1038/srep39651> (2017).
40. Qureshi, H. S., Ullah, S. & Ghafoor, F. Hierarchy of quantum correlations using a linear beam splitter. *Sci. Rep.* **8**, 16288. <https://doi.org/10.1038/s41598-018-34463-y> (2018).
41. Yang, H. *et al.* Estimating quantum steering and Bell nonlocality through quantum entanglement in two-photon systems. *Opt. Express* **29**, 26822. <https://doi.org/10.1364/oe.430964> (2021).
42. Bartkiewicz, K., Horodecki, P., Lemr, K., Miranowicz, A. & Życzkowski, K. Method for universal detection of two-photon polarization entanglement. *Phys. Rev. A* **91**, 032315. <https://doi.org/10.1103/PhysRevA.91.032315> (2015).
43. Augusiak, R., Demianowicz, M. & Horodecki, P. Universal observable detecting all two-qubit entanglement and determinant-based separability tests. *Phys. Rev. A* **77**, 030301. <https://doi.org/10.1103/physreva.77.030301> (2008).
44. Terhal, B. M. & Horodecki, P. Schmidt number for density matrices. *Phys. Rev. A* **61**, 040301. <https://doi.org/10.1103/PhysRevA.61.040301> (2000).
45. Sanpera, A., Bruß, D. & Lewenstein, M. Schmidt-number witnesses and bound entanglement. *Phys. Rev. A* **63**, 050301. <https://doi.org/10.1103/PhysRevA.63.050301> (2001).
46. Sperling, J. & Vogel, W. Determination of the Schmidt number. *Phys. Rev. A* **83**, 042315. <https://doi.org/10.1103/PhysRevA.83.042315> (2011).
47. Fan, X.-G. *et al.* Experimental detection of quantum steerability based on the critical radius in an all-optical system. *Phys. Rev. A* **107**, 012419. <https://doi.org/10.1103/PhysRevA.107.012419> (2023).
48. Bartkiewicz, K., Lemr, K., Černoč, A. & Miranowicz, A. Bell nonlocality and fully entangled fraction measured in an entanglement-swapping device without quantum state tomography. *Phys. Rev. A* **95**, 030102. <https://doi.org/10.1103/physreva.95.030102> (2017).
49. Lemr, K., Bartkiewicz, K. & Černoč, A. Experimental measurement of collective nonlinear entanglement witness for two qubits. *Phys. Rev. A* **94**, 052334. <https://doi.org/10.1103/PhysRevA.94.052334> (2016).
50. Trávníček, V., Bartkiewicz, K., Černoč, A. & Lemr, K. Experimental diagnostics of entanglement swapping by a collective entanglement test. *Phys. Rev. Appl.* **14**, 064071. <https://doi.org/10.1103/PhysRevApplied.14.064071> (2020).
51. Roik, J., Bartkiewicz, K., Černoč, A. & Lemr, K. Entanglement quantification from collective measurements processed by machine learning. *Phys. Lett. A* **446**, 128270. <https://doi.org/10.1016/j.physleta.2022.128270> (2022).
52. Rudnicki, L., Horodecki, P. & Życzkowski, K. Collective uncertainty entanglement test. *Phys. Rev. Lett.* **107**, 150502. <https://doi.org/10.1103/PhysRevLett.107.150502> (2011).
53. Rudnicki, L., Puchała, Z., Horodecki, P. & Życzkowski, K. Collectibility for mixed quantum states. *Phys. Rev. A* **86**, 062329. <https://doi.org/10.1103/PhysRevA.86.062329> (2012).

54. Bartkiewicz, K. & Chiriac, G. Two methods for measuring Bell nonlocality via local unitary invariants of two-qubit systems in Hong–Ou–Mandel interferometers. *Phys. Rev. A* **97**, 012107. <https://doi.org/10.1103/PhysRevA.97.012107> (2018).
55. Horodecki, P. From limits of quantum operations to multicopy entanglement witnesses and state-spectrum estimation. *Phys. Rev. A* **68**, 052101. <https://doi.org/10.1103/PhysRevA.68.052101> (2003).
56. Bovino, F. A. *et al.* Direct measurement of nonlinear properties of bipartite quantum states. *Phys. Rev. Lett.* **95**, 240407. <https://doi.org/10.1103/PhysRevLett.95.240407> (2005).
57. Bennett, C. H., DiVincenzo, D. P., Smolin, J. A. & Wootters, W. K. Mixed-state entanglement and quantum error correction. *Phys. Rev. A* **54**, 3824. <https://doi.org/10.1103/physreva.54.3824> (1996).
58. Horodecki, R., Horodecki, P. & Horodecki, M. Violating Bell inequality by mixed states: Necessary and sufficient condition. *Phys. Lett. A* **200**, 340–344. [https://doi.org/10.1016/0375-9601\(95\)00214-n](https://doi.org/10.1016/0375-9601(95)00214-n) (1995).
59. Luo, S. Quantum discord for two-qubit systems. *Phys. Rev. A* **77**, 042303. <https://doi.org/10.1103/PhysRevA.77.042303> (2008).
60. Cavalcanti, E. G., Jones, S. J., Wiseman, H. M. & Reid, M. D. Experimental criteria for steering and the Einstein–Podolsky–Rosen paradox. *Phys. Rev. A* **80**, 032112. <https://doi.org/10.1103/physreva.80.032112> (2009).
61. Costa, A. C. S. & Angelo, R. M. Quantification of Einstein–Podolsky–Rosen steering for two-qubit states. *Phys. Rev. A* **93**, 020103. <https://doi.org/10.1103/physreva.93.020103> (2016).
62. Wagner, K. *et al.* Entangling the spatial properties of laser beams. *Science* **321**, 541–543. <https://doi.org/10.1126/science.1159663> (2008).
63. Handchen, V. *et al.* Observation of one-way Einstein–Podolsky–Rosen steering. *Nat. Photonics* **6**, 596–599. <https://doi.org/10.1038/nphoton.2012.202> (2012).
64. Zhen, Y.-Z. *et al.* Certifying Einstein–Podolsky–Rosen steering via the local uncertainty principle. *Phys. Rev. A* **93**, 012108. <https://doi.org/10.1103/PhysRevA.93.012108> (2016).
65. Clauser, J. F., Horne, M. A., Shimony, A. & Holt, R. A. Proposed experiment to test local hidden-variable theories. *Phys. Rev. Lett.* **23**, 880–884. <https://doi.org/10.1103/PhysRevLett.23.880> (1969).
66. Miranowicz, A. Violation of Bell inequality and entanglement of decaying Werner states. *Phys. Lett. A* **327**, 272–283. <https://doi.org/10.1016/j.physleta.2004.05.001> (2004).
67. Kwiat, P. G. *et al.* New high-intensity source of polarization-entangled photon pairs. *Phys. Rev. Lett.* **75**, 4337–4341. <https://doi.org/10.1103/PhysRevLett.75.4337> (1995).
68. Nambu, Y., Usami, K., Tsuda, Y., Matsumoto, K. & Nakamura, K. Generation of polarization-entangled photon pairs in a cascade of two type-I crystals pumped by femtosecond pulses. *Phys. Rev. A* **66**, 033816. <https://doi.org/10.1103/physreva.66.033816> (2002).
69. Hradil, Z., Řeháček, J., Fiurášek, J. & Ježek, M. Maximum-likelihood methods in quantum mechanics, chap. 3. In *Quantum State Estimation* Vol. 649 (eds Paris, M. & Řeháček, J.) 266–290 (Springer, Berlin, 2004). https://doi.org/10.1007/978-3-540-44481-7_3.
70. Saunders, D. J., Jones, S. J., Wiseman, H. M. & Pryde, G. J. Experimental epr-steering using bell-local states. *Nat. Phys.* **6**, 845. <https://doi.org/10.1038/nphys1766> (2010).

Acknowledgements

S.A., K.B., and A.M. are supported by the Polish National Science Centre (NCN) under the Maestro Grant No. DEC-2019/34/A/ST2/00081.

Author contributions

The main idea of the manuscript was conceived by A.M.; S.A. and J.S. performed numerical and analytical calculations; the concept of linear-optical implementation was devised by K.B.; the experiment was designed, performed, and raw-data processed by A.Č. and K.L. All the authors were involved in writing and discussing the manuscript.

Competing interests

The authors declare no competing interests.

Additional information

Supplementary Information The online version contains supplementary material available at <https://doi.org/10.1038/s41598-023-35015-9>.

Correspondence and requests for materials should be addressed to J.S. or A.M.

Reprints and permissions information is available at www.nature.com/reprints.

Publisher's note Springer Nature remains neutral with regard to jurisdictional claims in published maps and institutional affiliations.



Open Access This article is licensed under a Creative Commons Attribution 4.0 International License, which permits use, sharing, adaptation, distribution and reproduction in any medium or format, as long as you give appropriate credit to the original author(s) and the source, provide a link to the Creative Commons licence, and indicate if changes were made. The images or other third party material in this article are included in the article's Creative Commons licence, unless indicated otherwise in a credit line to the material. If material is not included in the article's Creative Commons licence and your intended use is not permitted by statutory regulation or exceeds the permitted use, you will need to obtain permission directly from the copyright holder. To view a copy of this licence, visit <http://creativecommons.org/licenses/by/4.0/>.

© The Author(s) 2023

Chapter 2

Hybrid Photon-Phonon Blockade

2.1 Chapter outline

In this chapter, I provide a concise yet comprehensive overview of article [P2] of this thesis. I provide a general introduction to photon and phonon blockade phenomena and provide a short summary of the main results of the article.

2.1.1 Popular introduction

Quantum technologies, such as quantum cryptography, quantum computing, and quantum sensing, form the backbone of the so-called second quantum revolution, where precise control of the quantum properties of individual particles allow the performance of information processing tasks beyond the capabilities of more conventional technologies. In the context of light-based quantum systems, the control of the precise number of photons is often required for various such tasks.

One promising method to generate a precise number of photons is via photon blockade (PB), which was first predicted in [1,17,18]¹ (for reviews see [2-4]). PB, the optical equivalent of Coulomb blockade, is a non-classical phenomenon in which the presence of one photon in a driven nonlinear system prevents the generation of additional photons. This effect can be achieved, in particular, in cavity setups such as cavity quantum electrodynamics (QED) with strong non-linearity introduced by atom-cavity coupling or via a Kerr medium [17-19].

The quantum Rabi model (QRM) is the prototypical model describing the interaction of a two-level atom (which in general can be identified as a qubit) and a single-cavity mode, and is a natural basis to study PB phenomena. However, in

¹These and other references in this chapter correspond to those cited in [P2].

many experiments [5,11], the light-matter coupling g is much smaller than the cavity resonance frequency ω_c and qubit frequency (or level splitting) ω_q . Under these conditions, for a small detuning of the qubit from the cavity frequency ($\omega_c \approx \omega_q$), it is justified to employ the so-called rotating wave approximation (RWA). The QRM atom-cavity interaction contains terms that correspond to the process of exciting the atom with simultaneous de-excitation of the cavity field, and the process of simultaneously exciting or de-exciting both the qubit and cavity field. The latter, so-called energy non-conserving terms lead to fast oscillations at frequency $\sim 2\omega$ under near resonant conditions (where $\omega = \omega_q \sim \omega_c$) and can be essentially neglected when the coupling $g \ll \omega$. This is the essence of the RWA that simplifies the QRM to the famous Jaynes-Cummings (JC) model, which is also a conceptually simpler and exactly solvable model of atom-cavity interactions.

The JC spectrum is characterized by a non-linear energy spacing – the so-called JC ladder – for any nonzero interaction g . PB is easily understood in a JC system as originating from this anharmonic nature of the spectrum. Indeed, in the driven JC system, when an incoming photon resonantly excites the atom-cavity system from the ground state to a specific excited state, subsequent photons at the same frequency are detuned from the next energy levels in the ladder. This type of PB, which is induced by the anharmonicity of the energy ladder, is called *conventional* PB [1,19]. In order to observe such conventional PB as described by the mechanism above, in practice, the decay rates of the atom (γ) and cavity (κ) should be small enough to allow for prolonged atom-cavity interaction, which in combination with the RWA conditions yields the conditions $\kappa, \gamma \leq g \ll \omega_c, \omega_q$, which corresponds to the strong coupling regime of light-matter interactions [64]. Under these conditions, once a single photon is present in the system, the next photon is detuned from the next available excited state even when including the linewidth of that state. As a result, the possibility of observing two photons in the system simultaneously becomes rare. This blockade phenomena can be witnessed in the transmitted field of the cavity, wherein photons emerge from the cavity one at a time [52].

The second-order delay-time correlation function, $g^{(2)}(\tau)$, is an important quantity frequently used to identify PB. It captures the statistical properties of the cavity field and provides information on the effective interactions between the photons in the system. Experimental measurements of $g^{(2)}(\tau)$ usually involve detecting emitted photons using single-photon detectors in the Hanbury Brown and Twiss (HBT) configuration. A necessary signature of PB is sub-Poissonian photon-number statistics, which is tested by $g^{(2)}(\tau = 0) < 1$. This condition is associated with non-

classical photon statistics and indicates that two photons are less likely to be detected together compared to a classical photon system.

Importantly, a true PB effect is associated with photon antibunching, indicated by a dip of the correlation function, at $\tau = 0$, i.e., $g^{(2)}(0) < g^{(2)}(\tau)$. The depth of the dip indicates the strength of the PB phenomenon. While the joint criteria of sub-Poissonian statistics and antibunching are usually used to identify PB (also in our work), it is perhaps worth adding that generally higher-order sub-Poissonian photon-number statistics should also be verified to unambiguously determine PB, but this is rarely studied for practical reasons associated with gathering statistics with low photon numbers.

Conventional PB described above stems from strong nonlinear effects, which are challenging to achieve especially when dealing with a small mean number of photons in the system. In recent years, a new kind of PB has been predicted – so-called unconventional photon blockade (UPB) [46] – that allows the relaxation of the strong conditions on nonlinear interactions required for conventional PB and remarkably allows the observation of PB for very low photon numbers. UPB is induced by introducing an additional degree of freedom, e.g., an additional cavity coupled to the original system, which allows the destructive interference between different excitation paths leading specifically to the inhibition of the process of the simultaneous excitation of two photons. It is important to note, however, that UPB does not necessarily preclude the possibility of observing a higher number of photons, although a small mean number of photons usually reduces the probability of generating multiphoton states or higher-order coherences [12,13]. This unconventional PB method opens up exciting opportunities for manipulating and controlling the behavior of light in quantum systems, offering new avenues for quantum information processing and quantum communication.

While we have summarized photon blockade, fundamentally, conventional and unconventional blockade phenomena can be similarly induced in other systems with discrete field excitations, such as phonons. Indeed formally, the description of vibrational excitations of a quantum nanomechanical resonator are identical to that of field excitations in an optical cavity [47]. Indeed, the description of the vibrational excitations of a quantum nanomechanical resonator is identical to that of the field excitations in an optical cavity. In the following, we shall generally denote by PB various kinds of particle blockade, including the photon, phonon, and hybrid photon-phonon blockade effects, which are the phenomena we consider in the article summarized in this chapter.

The phenomenon opposite to PB is another notable non-classical photon-number correlation effect that can be observed in nonlinear systems, called photon-induced tunneling (PIT) [6]. In PIT, the probability of detecting additional photons in a higher manifold of the system increases when the first photon is generated near the resonance frequency. There are different sets of criteria based again on the characteristics of second- and higher-order delay-time correlation functions that can be used to identify this regime and are explicitly introduced in the article. The common criterion is that the photon number statistics in PIT is super-Poissonian photon-number statistics indicated by $g^{(2)}(0) > 1$. However, the nonclassicality of this effect can be identified by supplemental conditions on the statistics of higher photon-number events and are described in the article.

Finally, we note here that the system under consideration in our study is a open (i.e., amplified and dissipative) quantum system, which exhibits stochastic behavior by definition. In such systems, the state is described by a density matrix ρ , which represents an ensemble-averaged state as $\rho = \sum_n P_n |\psi_n\rangle \langle \psi_n|$ with P_n denoting the probability of the system being in the state $|\psi_n\rangle$. The standard Gorini-Kossakowski-Sudarshan-Lindblad master equation is employed normally to capture the time evolution of such a system. We used two methods in this article to calculate the dynamics of the system. We used the standard master equation to calculate the reduced density matrix of our dissipative system. We calculate $g^{(2)}(0)$ and $g^{(2)}(\tau)$ in the steady state solution of the density matrix. Moreover, to explain analytically the destructive interference of two-particle excitations, leading to UPB, we used a semiclassical description based on a non-Hermitian Hamiltonian, which ignores the quantum-jump terms in the master equation [45].

2.1.2 Motivation

Optomechanical systems offer a promising platform to explore the interaction and correlations between electromagnetic and vibrational modes, i.e., photons and phonons, making it an important area of study in the field of quantum information processing. Intriguingly, these systems can be used to study the number correlation effects not only in both the phonon and photon subsystems individually, but also in hybrid modes consisting of mixed photon and phonon modes (also called polaritons) [65].

Studying such coupled systems enables us to gain valuable insights into the interplay of quantum properties of light and mechanical motion. We perform a thorough theoretical study and classification of the PB and PIT effects that can

occur in coupled systems, focusing on a particular optomechanical superconducting system. Previous research has explored PB and PIT in optomechanical systems (see [56] and references therein). Despite this, there remains a paucity of experimental investigations that specifically focus on hybrid systems composed of both mechanical and optical resonators with similar frequencies. Nevertheless, these systems show promise for experimental realizations, and, thus, are the primary focus of our study [P2]. The driving motivation for our study came from the quest to understand whether PB or PIT can occur under unexpected conditions in such coupled systems. In particular, we wanted to answer the question whether pure hybrid blockade can exist, i.e., hybrid photon-phonon or polariton blockade [65] without blockade in the individual photon and phonon modes.

2.1.3 Main results

To demonstrate the effects of PB and PIT, we analyzed a specific setup involving two linearly coupled resonators: a superconducting microwave resonator (SMR), which can function as a transmission line resonator, and a micromechanical resonator known as a quantum drum (QD), which is capacitively coupled to the SMR. As mentioned earlier, nonlinearity is essential for nonclassical phenomena, such as PB, including conventional and unconventional PB in addition to PIT. In our proposed setup, this nonlinearity was achieved by coupling the SMR to a qubit [17,60,61]. The system can be driven either at the QD or SMR; however, the main focus of our study is on the driven QD. We aimed to propose this system for real-world experimentation, and therefore we carefully selected the parameters for each component based on existing experimental setups in this field. It is important to note that our system is considered an open quantum system because of its interaction with the environment causing dissipation and amplification.

In our research, we focused on investigating the individual photon and phonon modes and the hybrid photon-phonon mode achieved through the coupling of photons from an optical or microwave mode with phonons from a mechanical mode using a balanced linear coupler. Thus, the hybrid modes are two orthogonal modes consisting of equal superpositions of the individual photon and phonon modes.

We begin by introducing the Hamiltonian of the system and transform it into a rotating frame that rotates at the frequency of the optical pump field. Thus, the analysis of the system is simplified and allows us to focus on the relevant dynamics of the system and obtain its steady-state solution. To study the time evolution of the system, we utilized the density matrix formalism and numerically solved the

standard Lindblad master equation. We numerically calculated the second-order correlation functions $g^{(2)}(0)$ and $g^{(2)}(\tau)$ for three sets of parameters to discover different coupling regimes. In particular, the central result is that we discovered a novel type of PB in one of the hybrid (photon-phonon) modes, which occurs even though the photonic and phononic modes individually do not exhibit PB (but exhibit PIT instead).

In the case of the driven SMR, we showed that by adjusting the pump frequency with respect to the hybrid system's energy levels, it is possible to observe conventional PB and PIT that are induced by the energy-level anharmonicity in the regime of strong coupling (or high nonlinearity). However, the outcomes demonstrate that $g^{(2)}(\tau)$ oscillates as a result of the coupling (g) between the SMR and qubit as well as the hopping (f) between the SMR and QD. We showed that a PB can be created in hybrid mode, which is the symmetric superposition of the photon and phonon modes, that last for longer time interval by driving the QD instead of the SMR. Additionally, we used the resonance distance measure D_{nPR} in a specific detuning frequency to show how far our photon/phonon is from the n -photon/phonon resonance (nPR) and is used to identify PB and PIT in our studies through the anharmonicity of energy levels. We further predicted UPB in the mechanical and hybrid modes in the regime with weak coupling (or low nonlinearity) using a method that ignores quantum jumps based on a non-Hermitian Hamiltonian. It is shown that the analytical approximate predictions that we used in this method are in a relatively good agreement with our precise master-equation approach (including quantum jumps).

Moreover, we showed the importance of studying the behavior of $g^{(2)}(\tau)$ in addition to $g^{(2)}(0)$ to accurately characterize the true PB effect via the conditions: $g^{(2)}(0) < 1$ and $g^{(2)}(0) < g^{(2)}(\tau)$. As a result we found such parameter regimes of the system, for which four different types of blockade and tunnelling effects are possible. Moreover, by analyzing only the value of $g^{(2)}(0)$ in each mode (optical, mechanical, and hybrid) in different coupling regimes of the system, we predicted eight different combinations of either PB or PIT in these three modes.

Additionally, we calculated $g^{(n)}(0)$ for $n = 2, 3, 4$ to show the different PB and PIT possibilities, which demonstrates the importance of studying higher-order correlation functions to accurately identify PB and PIT.

The possibility of experimental demonstration of PB and PIT in the hybrid mode are also a focus of this paper. We proposed two different measurement setups to explain how to access this type of PB in the hybrid mode by using existing experimental configurations.

2.1.4 My contribution and importance of the work

The proposal and exploration of the novel hybrid blockade provide new insights into the interaction between photons and phonons, expanding our understanding of the quantum behavior of optomechanical systems. This opens up possibilities for further research and development in the field of quantum information processing.

I performed all numerical and analytical calculations of this study. I utilized Python, specifically with the QuTiP package, for my numerical calculations; while analytical calculations were performed using Mathematica. I have made significant contributions to the interpretation of the obtained results. I drafted the initial version of the article and collaborated with my supervisors to refine and polish the content.

2.2 Reprint of article [P2]

On the subsequent pages, we append a reprint with permission:

[P2] Shilan Abo, Grzegorz Chimczak, Anna Kowalewska-Kudłaszyk,
Jan Peřina Jr., Ravindra Chhajlany, and Adam Miranowicz:

Hybrid photon-phonon blockade,

Scientific Reports 12, 17655 (2022).

<http://dx.doi.org/10.1038/s41598-022-21267-4>

Copyright (2022) is retained by the authors.²

²“Copyright on any research article in open access (OA) journals published by Springer Nature is retained by the author(s). Authors grant Springer Nature a license to publish the article and identify itself as the original publisher. Authors also grant any third party the right to use the article freely as long as its integrity is maintained and its original authors, citation details and publisher are identified. OA articles in Springer Nature journals are predominantly published under Creative Commons Attribution v4.0 International licence (CC BY).” according to Global Open Research Support.

**OPEN** Hybrid photon–phonon blockadeShilan Abo¹, Grzegorz Chimczak¹, Anna Kowalewska-Kudłaszyk¹, Jan Peřina Jr.², Ravindra Chhajlany¹ & Adam Miranowicz¹✉

We describe a novel type of blockade in a hybrid mode generated by linear coupling of photonic and phononic modes. We refer to this effect as hybrid photon–phonon blockade and show how it can be generated and detected in a driven nonlinear optomechanical superconducting system. Thus, we study boson-number correlations in the photon, phonon, and hybrid modes in linearly coupled microwave and mechanical resonators with a superconducting qubit inserted in one of them. We find such system parameters for which we observe eight types of different combinations of either blockade or tunnelling effects (defined via the sub- and super-Poissonian statistics, respectively) for photons, phonons, and hybrid bosons. In particular, we find that the hybrid photon–phonon blockade can be generated by mixing the photonic and phononic modes which do not exhibit blockade.

Photon blockade (PB)¹, also referred to as optical state truncation (see reviews in Refs.^{2,3}), or nonlinear quantum scissors (for a review see Ref.⁴) is an optical analogue of Coulomb's blockade. Specifically, it refers to the effect in which a single photon, generated in a driven nonlinear system, can block the generation of more photons. The light generated by an ideal (or 'true') PB exhibits both sub-Poissonian photon-number statistics and photon antibunching. But even if one of these properties is satisfied, the term PB is often used.

PB has been demonstrated experimentally in various driven nonlinear systems with single^{5–11} and two^{12,13} resonators, in a bimodal cavity¹⁴, or even in cavity-free systems¹⁵. Experimental platforms where PB was observed include: cavity quantum electrodynamics (QED) with Fabry–Perot cavities⁵, photonic crystals⁶, and whispering-gallery-mode cavities¹⁶, as well as circuit QED^{7,8}. Note that the possibility of producing a single-photon state in a driven cavity with a nonlinear Kerr medium was predicted already in Refs.^{17–19}, but only the publication of Ref.¹, where the term 'photon blockade' was coined, has triggered much interest in studying this effect both theoretically and experimentally. Arguably, many studies reported already in the 1970s and 1980s on photon antibunching and sub-Poissonian light (see, e.g., reviews in Refs.^{20–22} and references therein) are actually about PB-related effects, although such a relation (to the optical analogue of Coulomb's blockade) was not mentioned explicitly there.

In addition to the original idea of using PB as a single-photon turnstile device with single^{1,16,23} or multiple²⁴ outputs, PB can have much wider applications in quantum nonlinear optics at the single-photon level, including single-photon induced nonlinear effects, quantum noise reduction via antibunching of photons, simulations of nonreciprocal nonlinear processes, or studying chirality at exceptional points for quantum metrology, etc.

A number of generalisations of the standard single-PB effect were proposed, which include: (1) two- and multi-photon versions of PB, as first predicted in Refs.^{25,26} and demonstrated experimentally in Refs.^{11,27}; (2) unconventional PB as predicted in Ref.²⁸ and experimentally demonstrated in Refs.^{12,13}; (3) conventional and unconventional nonreciprocal PB effects as predicted in Refs.^{29,30} and (at least partially) confirmed experimentally in Ref.³¹; (4) state-dependent PB³², (5) exceptional PB³³, and (6) linear quantum scissors based on conditional measurements for: single-PB^{34–36}, which was experimentally demonstrated in Ref.³⁷, as well as two-PB³⁸, and multi-PB^{39,40} using multiport Mach–Zehnder interferometers⁴¹. This probabilistic approach to PB enables also nondeterministic quantum teleportation and more selective optical-state truncations, e.g. hole burning in the Hilbert space⁴². Concerning example (2), note that PB in two driven Kerr resonators was first studied in Refs.^{43,44}, but only for relatively strong Kerr nonlinearities. Surprisingly, PB remains in such two-resonator systems even for extremely weak Kerr nonlinearities, as first predicted in Ref.²⁸ and explained via destructive quantum interference in Ref.⁴⁵. This effect is now referred to as unconventional PB⁴⁶.

Here we study phonon blockade⁴⁷, which is a mechanical analogue of the mentioned blockade effects, i.e., the blockade of quantum vibrational excitations of a mechanical resonator. This effect has not been demonstrated experimentally yet. However, a number of experimentally feasible methods have been proposed for measuring it, including a magnetomotive technique⁴⁷, an indirect measurement of phonon correlations via optical interferometry⁴⁸, or by coupling a mechanical resonator to a qubit, which is used not only for inducing the resonator nonlinearity, but also to detect the blockade effect itself, i.e., by measuring qubit's states⁴⁹. Among possible applications of phonon blockade, we mention: testing nonclassicality of meso- or macroscopic

¹Institute of Spintronics and Quantum Information, Faculty of Physics, Adam Mickiewicz University, 61-614 Poznan, Poland. ²Joint Laboratory of Optics of Palacký University and Institute of Physics of CAS, Faculty of Science, Palacký University, 17. listopadu 12, 771 46 Olomouc, Czech Republic. ✉email: miran@amu.edu.pl

mechanical systems⁴⁷ and studying single-phonon optomechanics, in addition to offering a source of single- or multiple phonons^{50,51}.

PB can be changed into light transmission⁵², e.g., by photon-induced tunnelling (PIT)⁶. This is another nonclassical photon-number correlation phenomenon, in which the probability of observing more photons in a higher manifold of the system increases with the generation of the first photon near the resonance frequency of the system. Multi-PIT effects were also predicted²⁹, including those generated by squeezing⁵³.

For simplicity, we use here the abbreviation PB, when referring to the blockade of not only photons, but also of phonons or hybrid photon–phonon bosons. The precise meaning can be found from its context, e.g., when we refer to a specific mode, including the optical (*a*), mechanical (*b*), or hybrid (*c*) modes. Analogously, PIT denotes a given particle-induced tunnelling among the three types of excitations.

Nanomechanical resonators can coherently interact with electromagnetic radiation⁵⁴, and quantum correlations between single photons and single phonons were studied for a single entangled photon–phonon pair⁵⁵ or via photon and phonon blockade effects in optomechanical systems⁵⁶. A mechanical switch between PB and PIT has been studied recently⁵⁷. PB and PIT effects in systems comprising mechanical and optical resonators, which are characterised by the same or similar bare frequencies, to our knowledge, have not been studied experimentally yet, although they seem to be experimentally feasible and, thus, they are at focus of this paper.

Crucial signatures of PB and PIT can be observed by measuring the second-order correlation function, $g^{(2)}(0)$. Specifically for photons, (1) the condition of $g^{(2)}(0) < 1$ defines the sub-Poissonian photon-number statistics (also referred to as zero-delay-time photon antibunching), which indicates the possibility of observing PB, while (2) the condition $g^{(2)}(0) > 1$, defines the super-Poissonian statistics (also referred to as zero-delay-time photon bunching), which is a signature of PIT in a given system. To observe the ‘true’ effects of PB and PIT, also other criteria should be satisfied, such as nonzero-delay-time photon antibunching and higher-order sub-Poissonian photon-number statistics. Indeed, an ideal conventional PB, which can be served as a single-photon source, usually should also be verified by studying higher-order correlation functions, $g^{(n)}(0)$ for $n > 2$. For example, in case of single-PB (1PB) conditions $g^{(2)}(0) < 1$ and $g^{(n)}(0) < 1$ for $n > 2$ should be fulfilled.

PB can be verified also in other ways via demonstrating, e.g., a staircase-like dependence of the mean photon number (or measured power transmitted through a nonlinear resonator) on the energy spectrum of the photons incident on the resonator^{8,52}. Such a dependence is the photon analogue of the Coulomb staircase. All of the above criteria are just necessary but not sufficient conditions for demonstrating PB. A sufficient condition could be, e.g., showing a high fidelity of a given generated light (with a nonzero mean photon number) to an ideally truncated two-dimensional state, which is the closest to the generated one. This approach was applied in, e.g.,^{26,35,36}. The latter two types of PB tests are, however, are not applied in this paper.

Conventional single-PB prevents the absorption of a second photon with a specific frequency due to the nonlinearity of a given system. Such a nonlinearity can be described by a Kerr-type interaction and/or can be induced by an atom (real or artificial) coupled to a resonator. An artificial atom can be realised by, e.g., a quantum dot^{23,58,59} in cavity QED¹⁰ or a superconducting qubit or qudit in circuit QED⁵².

Unconventional PB, which is induced by destructive interference, operates better for very low (or even extremely low) mean photon numbers^{12,13}. This can be disadvantageous by considerably decreasing the probability of generating a single photon. But, at the same time, it can be an advantage, because a very small mean photon number usually reduces the chance of generating multi-photon states and inducing higher-order coherence. This is not always the case, and even if the probability of observing two photons is suppressed, higher-order coherence might be enhanced, leading to the generation of multi-photon states⁴⁶.

In this paper, we consider an optomechanical system, which generates photonic and phononic modes. Then we apply a balanced linear coupling transformation to these modes to create hybrid modes (also referred to as supermodes). We study the interplay between photons and phonons resulting in their nonclassical number correlation effects. Thus, we find such system parameters to observe either PB or PIT in the four modes. In particular, we predict PB in one of the hybrid modes, but not in the individual (photon and phonon) modes, i.e., this PB is created from the two modes, which do not exhibit PB. We refer to this effect as hybrid photon–phonon blockade, which is the main result reported here.

Specifically, we define hybrid photon–phonon blockade as the blockade of hybrid-mode bosons (polaritons) obtained by coupling photons of an optical or microwave mode with phonons of a mechanical mode by a balanced linear coupler. The idea and criteria for testing this type of blockade are analogous to those for other known blockade effects (e.g., of photons, phonons, or magnons), but it is predicted for another type of bosons. We show that this hybrid photon blockade can occur by coupling the modes, which exhibit neither photon blockade nor phonon blockade.

To show this effect we analyse the system of two linearly-coupled resonators: a superconducting microwave resonator (SMR), which might be a transmission line resonator, and a micromechanical resonator, referred to as a quantum drum (QD), which is capacitively coupled to the SMR. To generate any kind of PB (including unconventional PB), one needs to incorporate a nonlinearity into a given system^{17,60,61}. This can be done by coupling one of the resonators (e.g., the SMR) to a qubit (e.g., an artificial superconducting two-level atom). We also assume that the system is driven either at the QD or the SMR as described in detail in the next section.

The paper is organised as follows: first, the hybrid optomechanical system and its Hamiltonians are introduced. We also define the hybrid photon–phonon modes, which can be generated by the balanced linear coupling of photonic and phononic modes. Then, we study the correlation effects in the photonic, phononic, and one of the hybrid modes in the system driven at either the optical or mechanical resonator, respectively, for experimentally feasible parameters specified in “Methods”. We then predict and analytically explain the generation of unconventional hybrid-mode blockade via a non-Hermitian Hamiltonian method. We systematically study different weaker and stronger criteria for observing blockade and tunnelling effects in our system. We also find all the eight combinations of the conventional blockade and tunnelling effects in the three modes. In particular,

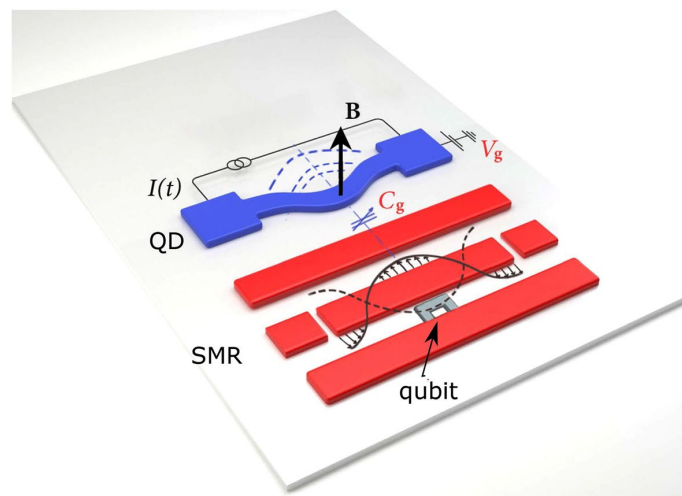


Figure 1. Schematics of the discussed circuit-QED-based realisation of the considered hybrid optomechanical system. It consists of a superconducting qubit embedded in a superconducting microwave resonator (SMR), e.g., a transmission-line resonator, to induce its nonlinearity. A quantum micromechanical resonator, which is referred to as a quantum drum (QD), is coupled to the SMR with a tunable capacitor C_g . We assume that the system is driven either at the SMR or QD. Dashed semicircular curves visualise that the QD is oscillating. The driving and motion detection of the QD can be realised by controlling the static magnetic field B , potential V_g , and alternating current $I(t)$, as described in Ref.⁴⁷ for detecting phonon blockade.

we find a surprising effect that the hybrid-mode photon–phonon blockade can be generated by mixing the photonic and phononic modes exhibiting tunnelling effects. In addition to this study of the second-order correlation effects, we discuss also higher-order effects and their classification in “Methods”. Moreover, we discuss two types of schemes for measuring photon–phonon correlations in hybrid modes. Finally, we summarise our results and indicate their potential applications.

The system and Hamiltonians

Figure 1 shows the schematics of the studied hybrid system, which consists of a superconducting two-level artificial atom (a qubit) embedded in a waveguide and coupled to an SMR, which might be a transmission-line resonator. This qubit induces anharmonicity in the SMR, which is crucial for observing PB. Our setup includes also a microwave-frequency mechanical resonator (a QD), which is capacitively coupled to the SMR. The nonlinearity of the QD is induced indirectly by the linear coupling of the QD to the effectively nonlinear SMR.

The free Hamiltonian of the SMR is $H_a = \hbar\omega_{\text{SMR}} a^\dagger a$, where ω_{SMR} is its resonance frequency (assumed here of the order of tens of GHz) and a (a^\dagger) is the photon annihilation (creation) operator. We can reasonably assume the SMR quality factor as $Q_{\text{SMR}} \approx 10^4$. The free Hamiltonian of the QD is $H_b = \hbar\omega_m b^\dagger b$, where ω_m is its resonance frequency and b (b^\dagger) is the phonon annihilation (creation) operator. In our numerical simulations, we set $\omega_m/2\pi = 7.8$ GHz and the QD quality factor as $Q_m \approx 260$. Moreover a two-level quantum system has the ground state $|g\rangle$ and the excited state $|e\rangle$ with transition frequency ω_q (set here of the order of ω_m and ω_{SMR}). The free qubit Hamiltonian is described as $H_q = \hbar\omega_q \sigma_+ \sigma_-$, where $\sigma_+ = |e\rangle\langle g|$ ($\sigma_- = |g\rangle\langle e|$) is the atomic raising (lowering) operator. Thus, the total free Hamiltonian of the system is $H_0 = H_a + H_b + H_q$. The complete Hamiltonian (without driving) of our coupled system can be given by ($\hbar = 1$)

$$H'_\pm = H_0 + g(a^\dagger \sigma_- + a \sigma_+) + g_r(b + b^\dagger)a^\dagger a + g_l(a \pm a^\dagger)(b + b^\dagger), \quad (1)$$

which includes the three coupling terms: (1) the Jaynes–Cummings term describing the interaction between the SMR and qubit under the rotating-wave approximation (RWA); (2) the radiation-pressure term with coupling strength g_r ; and (3) the Hopfield-type nonlinear coupling term with strength g_l . The g_l coupling can be realized via a capacitor, as shown in Fig. 1 and explained in a more detail in Ref.⁴⁸ for a similar system. Note that the g_l term describes canonical position–position (momentum–position) interactions, where g_l is real (imaginary) for H'_+ (H'_-). These interactions can be interchanged by adding the $\pi/2$ phase to a , a^\dagger , i.e., $a \rightarrow ia$ and $a^\dagger \rightarrow -ia^\dagger$. This extra phase does not change number correlations in the modes a and b . In typical ranges of parameters of analogous superconducting circuits⁶², the g_l term is dominant, so the radiation-pressure term can be neglected⁶³. Moreover, although the counter-rotating terms $ab \pm b^\dagger a^\dagger$, which appear in the g_l -interaction, play an important role in the ultrastrong and deep-strong coupling regimes⁶⁴, but they can be safely omitted under the RWA, which is valid in the weak and strong coupling regimes. Indeed, the latter regimes are solely studied in this paper, as discussed below. Then the Hopfield nonlinear g_l -interaction becomes effectively linearised. Thus, Hamiltonian (1) reduces to

$$H_{\pm} = H_0 + g(a^{\dagger}\sigma_{-} + a\sigma_{+}) + f(ab^{\dagger} \pm a^{\dagger}b), \quad (2)$$

where the linear-coupling strength is denoted by f , which replaces the symbol g_i . Analogously to g_i , f is real (imaginary) for H_{+} (H_{-}). In the following, for simplicity, we focus on studying the canonical position–position interactions between the modes a and b , as described by H_{+} . The eigenstates of Hamiltonian H_{\pm} can be referred to as atomic-optomechanical polaritons or atom-cavity-mechanics polaritons⁶⁵. It is clear that Hamiltonians H_{\pm} conserve the polariton number,

$$N_{\text{polariton}} = a^{\dagger}a + b^{\dagger}b + \sigma_{+}\sigma_{-}, \quad (3)$$

which is the total number of excitations. Thus, H_{\pm} can be diagonalised in each subspace (or manifold) $\mathcal{H}^{(n)}$ with exactly n polaritons.

The RWA is fully justified assuming both (1) the weak- or strong-couplings and (2) small detunings between the SMR and QD, and the SMR and qubit (see, e.g., Ref.⁶⁶). We stress that these conditions are fully satisfied for the parameters applied in all our numerical calculations in this paper. Thus, the Jaynes–Cummings and frequency-converter (or linear-coupler) models can be applied. However, the RWA cannot be applied in the ultrastrong and deep-strong coupling regimes, as defined by $g > 0.1\omega_i$ and $g > \omega_i$, respectively⁶⁴, where $i = \text{SMR}, m, q$. In these regimes, the quantum Rabi and Hopfield models cannot be reduced to the Jaynes–Cummings and frequency-converter models, respectively. However, we study the system for the parameters specified in Eqs. (28)–(30), for which the ratios of the coupling strengths and frequencies, f/ω_i and g/ω_i , are < 0.002 . So, the system is in the strong-coupling regime, and far away from the border line with the USC regime. Moreover, the chosen detunings are $|\omega_{\text{SMR}} - \omega_m|/\omega_{\text{SMR}} \leq 2.6 \times 10^{-3}$ and $|\omega_{\text{SMR}} - \omega_q|/\omega_{\text{SMR}} < 8 \times 10^{-4}$. Thus, it is clearly seen that we can safely apply the RWA. Anyway, as a double test, we have calculated time-dependent second-order correlation functions for the Hamiltonian H_{\pm} and H_{\pm} for the parameters set in Eqs. (28)–(30) for various evolution times assuming classical drives (as specified below) and no dissipation. And we have found that the differences between the correlation functions calculated for the models with and without the RWA are negligible on the scale of figures. The inclusion of dissipation in the system makes such differences even smaller.

We assume that an optical pump field of frequency ω_p is applied either to the SMR mode a , as described by

$$H_{\text{drv}}^{(a)}(t) = \eta_a(e^{i\omega_p t}a + e^{-i\omega_p t}a^{\dagger}), \quad (4)$$

or to the QD mode b , as given by

$$H_{\text{drv}}^{(b)}(t) = \eta_b(e^{i\omega_p t}b + e^{-i\omega_p t}b^{\dagger}), \quad (5)$$

to drive (excite) the system (with coupling strength η_a or η_b) from its ground state and to induce the emission of photons and phonons. Thus, the total Hamiltonian becomes

$$H^{(n)}(t) = H_{+} + H_{\text{drv}}^{(n)}(t) \quad (n = a, b). \quad (6)$$

Direct driving of the QD can be implemented by a weak-oscillating current, as considered in Refs.^{47,48}, where the drive strength η_b is proportional to the current amplitude $I(t)$ and the magnetic field B shown in Fig. 1. The SMR can be driven in circuit-QED systems in various ways⁶².

Note that by driving directly the SMR (or alternatively the QD), one also indirectly drives the QD (SMR) through the capacitive coupling C_g , as shown in the scheme in Fig. 1. So, by referring to the SMR- or QD-driven systems, we indicate only the resonator, which is directly pumped, although finally both resonators are driven.

The inclusion of an additional nonlinearity in the QD and/or applying drives to the qubit(s) and both resonators is not essential for the prediction of hybrid blockade, but this could enable achieving stronger photon–phonon antibunching and more sub-Poissonian statistics.

Considering the case, where the pump field drives only the SMR, to remove the time dependence of the Hamiltonian $H^{(n)}(t)$ and to obtain its steady-state solution, we transform the system Hamiltonian into a reference frame rotating at frequency ω_p .

We apply the unitary transformation $U_R(t) = \exp(-iN_{\text{polariton}}\omega_p t)$ to $H^{(n)}$ according to the general formula

$$H_{\text{rot}}^{(n)} = U_R^{\dagger}H^{(n)}U_R - iU_R^{\dagger}\frac{\partial}{\partial t}U_R. \quad (7)$$

Thus, $H^{(a)}(t)$ reduces the time-independent SMR-driven Hamiltonian:

$$H' \equiv H_{\text{rot}}^{(a)} = \Delta_{\text{SMR}}a^{\dagger}a + \Delta_m b^{\dagger}b + \Delta_q \sigma_{+}\sigma_{-} + g(a^{\dagger}\sigma_{-} + a\sigma_{+}) + f(a^{\dagger}b + ab^{\dagger}) + \eta_a(a + a^{\dagger}), \quad (8)$$

where $\Delta_i = \omega_i - \omega_p$ for $i = a, b, q$. So, in particular, $\Delta_b \equiv \Delta_m$ ($\Delta_a \equiv \Delta_{\text{SMR}}$) is the mechanical (microwave) resonator frequency detuning with respect to the pump frequency. Analogously, in the same rotating frame, $H^{(b)}(t)$ reduces to the QD-driven Hamiltonian:

$$H'' \equiv H_{\text{rot}}^{(b)} = \Delta_{\text{SMR}}a^{\dagger}a + \Delta_m b^{\dagger}b + \Delta_q \sigma_{+}\sigma_{-} + g(a^{\dagger}\sigma_{-} + a\sigma_{+}) + f(a^{\dagger}b + ab^{\dagger}) + \eta_b(b + b^{\dagger}). \quad (9)$$

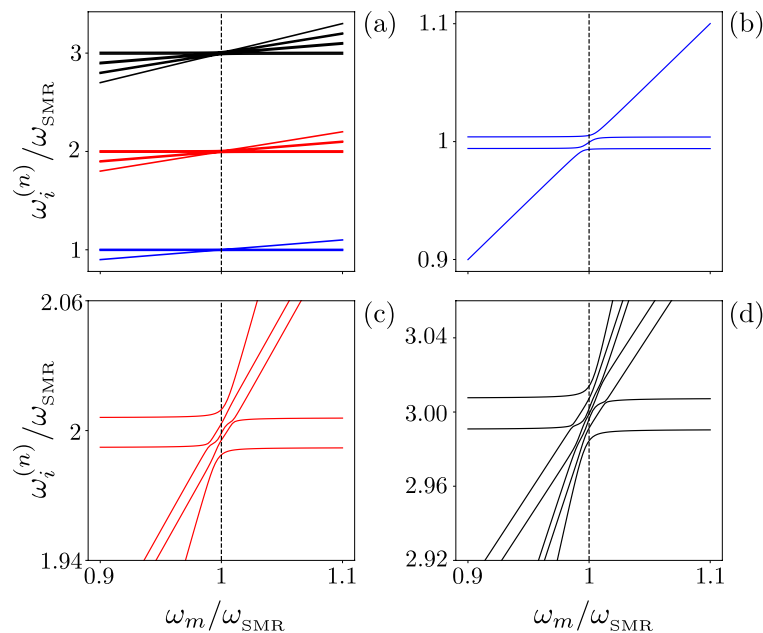


Figure 2. Energy levels ω_n versus the QD frequency ω_m in units of the SMR frequency ω_{SMR} for the Hamiltonian Eq. (2) with the parameters given in Eq. (28) and $g = 7.5\gamma$. The three manifolds of the lowest energy levels in panel (a) are zoomed in panels (b–d) near the resonance $\omega_m = \omega_{\text{SMR}}$ to reveal the anti-crossing of energy levels. Here, $\omega_i^{(n)}$ (with $n = 1, 2, 3$) denotes the frequencies of the n th manifold.

We recall that Eqs. (8) and (9) are directly derived from Eq. (6) for H_+ given in Eq. (2). Moreover, H_+ is derived from Eq. (1) assuming the RWA, which is justified for small detunings in the weak- and strong-coupling regimes, which are the only numerically studied regimes in this paper, as emphasised above. Indeed, the studied ranges of parameters guarantee the system evolution is far from the USC regime. Note that the Hamiltonian H_+ in (1) for $g_r = 0$ with an additional drive term $H_{\text{drv}}^{(n)}(t)$ can be transformed, according to Eq. (7), to $H_{\text{rot}}^{(n)}$ given in Eqs. (8) and (9) but with the additional term $f[ab \exp(2i\omega_p t) + \text{h.c.}]$. In all our numerical calculations we set ω_p of the order of GHz. Thus, the effect of this rapidly oscillating term is negligible compared to all the other terms in the Hamiltonians. Moreover, we have also assumed that the optomechanical term g_r is negligible. In general, this assumption is not necessary, because the g_r term can be reduced (in the red-detuned regime) to an interaction term describing a linear coupler (or a beam splitter), which can be combined with the f term. Anyway, for simplicity concerning both theory and potential experiments, we set $g_r = 0$. We have also assumed that the system is driven at either the mechanical or optical mode to obtain effectively time-independent Hamiltonians in a rotating frame. This simplification would not be directly possible by considering the system driven simultaneously at both modes with different frequencies.

Figure 2 shows the structure of the energy spectrum for the hybrid system Hamiltonian (2). To study the sub-Poissonian light generation in hybrid modes, we apply to the SMR and QD modes a balanced linear coupling transformation, which is formally equivalent to a balanced (50/50) beam splitter (BS). This transformation creates the hybrid (or cross) photon–phonon modes:

$$c = \frac{a+b}{\sqrt{2}}, \quad d = \frac{a-b}{\sqrt{2}}, \quad (10)$$

for the system described by H_+ and related Hamiltonians. Note that if this BS transformation is modified as $a \rightarrow -ia$ and $a^\dagger \rightarrow ia^\dagger$ [which compensates the extra $\pi/2$ phase introduced below Eq. (1)] then all our predictions of number correlations shown in various figures for the hybrid mode c (in addition to those for the modes a , b , and d) are the same as those for the model described by H_- .

Thus, the Hamiltonian H' after the BS transformation reads

$$H'_{\text{BS}} = \Delta_c c^\dagger c + \Delta_d d^\dagger d + \Delta_q \sigma_+ \sigma_- + \delta (c^\dagger d + d^\dagger c) + \frac{1}{\sqrt{2}} [\eta_a (c + c^\dagger) + \eta_a (d + d^\dagger) + g (c^\dagger \sigma_- + c \sigma_+) + g (d^\dagger \sigma_- + d \sigma_+)], \quad (11)$$

which describes the qubit interacting with two hybrid modes c and d , where $\Delta_{c,d} = (\omega_{\text{SMR}} + \omega_m)/2 - \omega_p \pm f$ and $\delta = (\omega_{\text{SMR}} - \omega_m)/2$. It is seen that the two modes c and d have no direct coupling if $\omega_m = \omega_{\text{SMR}}$.

The dynamics of an open system in the presence of losses under the Markov approximation can be described within the Lindblad approach for a system reduced density matrix ρ satisfying the standard master equation,

$$\frac{\partial \rho}{\partial t} = -i[H, \rho] + \kappa_a \mathcal{D}[a]\rho + \kappa_b \mathcal{D}[b]\rho + \gamma \mathcal{D}[\sigma]\rho, \quad (12)$$

which is given in terms of the Lindblad superoperator $\mathcal{D}[O]\rho = \frac{1}{2}(2O\rho O^\dagger - \rho O^\dagger O - O^\dagger O\rho)$, where κ_a , κ_b , and γ are the decay rates for the SMR, QD, and qubit, respectively.

All our numerical calculations and their analyses are given for the system parameters, which satisfy the conditions for the weak or strong-coupling regimes and for small detunings between the SMR, QD, and qubit. Thus, we can safely apply the standard master equation given in Eq. (12). Of course, if one considers Eq. (1) for the system in the USC or deep-coupling regimes, then the master equation in Eq. (12), should be replaced by a generalised one, e.g., of Refs.^{64,67–69}.

We also note that the application even of a single classical drive to the Jaynes–Cummings model in the strong-coupling regime effectively creates counter-rotating terms, which can induce a variety of USC effects, as shown explicitly in Ref.⁷⁰. Thus, to confirm the validity of our results, we have applied the generalised formalism described in Ref.⁶⁷, which is valid for arbitrary light-matter coupling regimes, including the weak-, strong-, and USC regimes. In particular, we calculated the correlation functions $g^{(n)}(0)$ defined in terms of the positive- (X_n^+) and negative- ($X_n^- = (X_n^+)^\dagger$) frequency components of the canonical position operators: $X_a = a + a^\dagger$ for photons, $X_b = b + b^\dagger$ for phonons, and $X_c = c + c^\dagger$ for hybrid-mode bosons in the qubit-SMR-QD dressed basis. We calculated the steady states of the system by solving numerically the generalised master equation of Ref.⁶⁷ for the Hamiltonians H' and H'' . As expected from general considerations, our numerical calculations for the parameters set in Eqs. (28)–(30) using the standard and generalised formalisms based on H' (as well as H'') give effectively the same results.

In our simulations, we assume that the system is prepared in the ground state $|n = 0, g\rangle|m = 0\rangle$ (i.e., with no photons in the SMR, no phonons in the QD, and the qubit is in the ground state), such that a given pump laser can drive the SMR photons in the microwave frequency range. Note that the choice of initial states affects the short-time evolution of our system, but has no effect on the steady-state solutions in the time limit, assuming the single-photon and single-phonon damping channels, as described in Eq. (12). However, as shown in Ref.³², initial states of a system can indeed affect steady states of the system, thus can also change PB, in case of quantum engineered dissipation channels allowing for, e.g., two-photon dissipation only.

In the following sections, we show that it is possible to observe both PB and PIT in the hybrid mode in the weak, mediate, and strong coupling regimes compared to the decay rates of the SMR, QD, and qubit. In particular, we show that the system can generate the hybrid photon–phonon modes with strongly sub-Poissonian (or super-Poissonian) statistics by mixing the SMR and QD modes with strongly super-Poissonian (or sub-Poissonian) statistics.

Hybrid-mode blockade in the SMR-driven system

Here we analyse in detail various blockade and PIT effects in the SMR-driven dissipative system described by the Hamiltonian H' and the master equation (12) for the parameters specified in Eq. (28).

Photon/phonon-number statistics of the modes generated by our hybrid system can be described quantitatively by calculating the zero-delay-time k th-order correlation function (k th-order intensity autocorrelation function),

$$g_z^{(k)}(0) = \lim_{t \rightarrow \infty} \frac{\langle z^{\dagger k}(t) z^k(t) \rangle}{\langle z^\dagger(t) z(t) \rangle^k}, \quad (13)$$

where $z = a, b, c, d$ and $k = 2, 3, \dots$ In the special case of $k = 2$, which is of particular interest in testing single-PB and single-PIT, the three different types of the boson-number statistics can be considered: the Poissonian [if $g^{(2)}(0) = 1$], super-Poissonian [if $g^{(2)}(0) > 1$], and sub-Poissonian (otherwise). Analogously, one can define higher-order Poissonian, sub-Poissonian, and super-Poissonian statistics for $k > 2$. Such higher-order criteria are not only crucial in analysing multi-PB and multi-PIT effects^{11,29,53}, but they are also important in testing whether a specific PB effect is a ‘true’ PB, which can be used for generating single photons or phonons. These higher-order statistics are studied in “Methods”.

Figure 3(a) shows $g^{(2)}(0)$ as a function of the qubit-SMR coupling for the SMR-driven system with the parameters specified in Eq. (28). The regions, when the sub-Poissonian statistics in the hybrid mode c is accompanied by the super-Poissonian statistics in the modes a and b , are indicated by the yellow background in this and other figures. This area in yellow colour is referred to as Case 7 in Table 1, in which we observe strongly super-Poissonian photons (phonons) in the SMR (QD); whereas a single excitation is observed in the hybrid mode. The system parameters, which lead to Case 7, are found by numerical simulations and are discussed below.

Note that Fig. 3a shows these effects in the strong coupling regime⁶⁴, i.e., when the qubit-SMR coupling constant g is larger than the system damping rates: $g/\kappa_{\max} > 1$, where $\kappa_{\max} = \max\{\kappa_a, \kappa_b, \gamma\}$. On the other hand, Fig. 3b shows the same yellow region in the weak-coupling regime, i.e., when $g/\kappa_{\max} < 1$, but this figure was calculated for the QD-driven system, which is discussed in the next section.

By considering the values of Eq. (28), the SMR decay rate is $\kappa_a = 1.5\gamma$, given that the mode a is always in the strong qubit-SMR coupling regime in the region of our interest. This results in Rabi-type oscillations of $g^{(2)}(0)$ that occur in the SMR mode a and the hybrid mode c . In Fig. 3a, both weak and strong coupling regimes are shown corresponding to g smaller or larger than the maximum decay rate of the whole system.

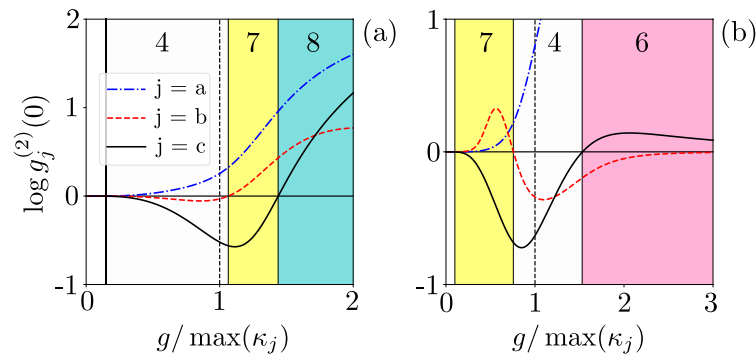


Figure 3. Second-order correlation functions $g_j^{(2)}(0)$ (in the common logarithmic scale) versus the ratio of qubit-SMR coupling strength and the largest decay rate. Different predictions of the sub- and super-Poissonian boson number statistics, which can be interpreted, respectively, as the PB and PIT effects, of the photonic (a), phononic (b), and hybrid (c) modes assuming: (a) the SMR-driven system with parameters specified in Eq. (28) and (b) the QD-driven system with Eq. (29). All the shown Cases (i.e., 4, 6, 7, and 8) correspond to those listed in Table 1. The broken line at $g = \max \kappa_j$ is the border line between the strong- and weak-coupling regimes.

Case	f_{abc}	PNS in mode a	PNS in mode b	PNS in mode c	colour
1	(-, -, -)	Sub-Poissonian	Sub-Poissonian	Sub-Poissonian	Aquamarine
2	(-, -, +)	Sub-Poissonian	Sub-Poissonian	Super-Poissonian	Lime
3	(-, +, -)	Sub-Poissonian	Super-Poissonian	Sub-Poissonian	Light cyan
4	(+, -, -)	Super-Poissonian	Sub-Poissonian	Sub-Poissonian	Mint cream
5	(-, +, +)	Sub-Poissonian	Super-Poissonian	Super-Poissonian	Plum
6	(+, -, +)	Super-Poissonian	Sub-Poissonian	Super-Poissonian	Pink
7	(+, +, -)	Super-Poissonian	Super-Poissonian	Sub-Poissonian	Yellow
8	(+, +, +)	Super-Poissonian	Super-Poissonian	Super-Poissonian	Cyan

Table 1. Different predictions of the super- and sub-Poissonian particle (i.e., photon, phonon or hybrid photon-phonon)-number statistics (PNS) corresponding, respectively, to PIT and PB, for the photon mode a , phonon mode b , and hybrid photon-phonon mode c , where $f_{abc} = (\text{sgn}[g_a^{(2)}(0) - 1], \text{sgn}[g_b^{(2)}(0) - 1], \text{sgn}[g_c^{(2)}(0) - 1])$ and the last column indicates each prediction of the mode a , b , and c in the specific colour that is used in our plots. All these cases can be seen in Fig. 10.

Given the set of parameters in Eq. (28), we are in the good-cavity regime⁷¹, because $\kappa_a < \{\kappa_b, g, f\}$. In the range $g/2\pi \in (4.5, 42)$ MHz, the hybrid mode c has the sub-Poissonian statistics, while the SMR mode has the super-Poissonian statistics in all the shown cases and a very weak sub-Poissonian statistics occur for phonons in the QD mode b , but still corresponding to Case 4 in Table 1. This behaviour changes to the super-Poissonian statistics in the mode b , which corresponds to Case 7, as shown in Fig. 3a. There is a transition for the mode c from the sub-Poissonian to super-Poissonian statistics, which corresponds to switching from Case 7 to Case 8 in the strong-coupling regime, where the other two modes are both super-Poissonian. Observing $g^{(2)}(0) > 1$ witnesses PIT and the quantum nature of this effect is explored further below.

In order to better probe and understand the dynamics of the system in specific parameter regimes, we analyse also the delay-time second-order photon correlation function, defined as

$$g_z^{(2)}(\tau) = \lim_{t \rightarrow \infty} \frac{\langle \mathcal{F} : n_z(t + \tau)n_z(t) : \rangle}{\langle n_z(t) \rangle^2} = \lim_{t \rightarrow \infty} \frac{\langle z^\dagger(t)z^\dagger(t + \tau)z(t + \tau)z(t) \rangle}{\langle z^\dagger(t)z(t) \rangle^2}, \quad (14)$$

where $n_z(t) = z^\dagger(t)z(t)$ is the boson number in the modes $z = a, b, c, d$, and the operator products are written in normal order ($::$) and in time order \mathcal{F} . With $g_z^{(2)}(\tau)$ another quantum optical number-correlation phenomenon can be investigated. Specifically, in case of photons, it is referred to as photon antibunching if $g^{(2)}(0) < g^{(2)}(\tau)$, photon unbunching if $g^{(2)}(0) \approx g^{(2)}(\tau)$, and photon bunching if $g^{(2)}(0) > g^{(2)}(\tau)$, which is usually defined for short or very short delay times τ ⁷². It is worth noting that photon antibunching was first experimentally observed in the 1970s by Kimble, Dagenais, and Mandel⁷³. This was historically the first experimental demonstration of the quantum nature of an electromagnetic field, which cannot be explained classically, unlike photoelectric bunching.

Analogously, one can also investigate the antibunching and bunching of phonons and/or hybrid-mode bosons. Note that the term photon antibunching is often interchangeably used with the sub-Poissonian photon-number

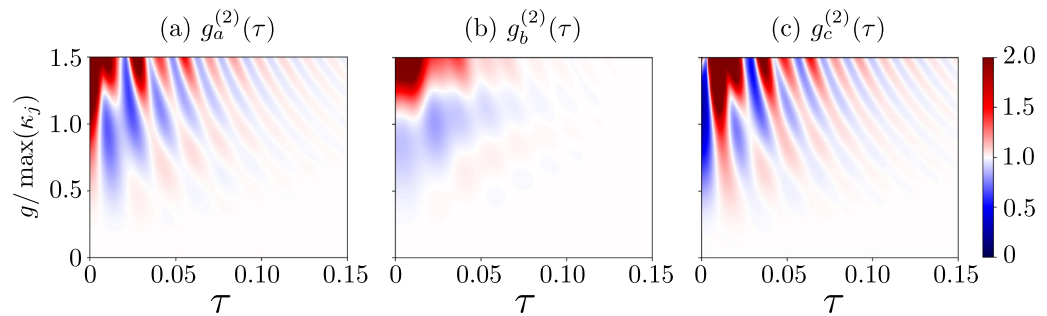


Figure 4. Delay-time second-order correlation functions: (a) $g_a^{(2)}(\tau)$ for the photonic mode, (b) $g_b^{(2)}(\tau)$ for the phononic mode, and (c) $g_c^{(2)}(\tau)$ for the hybrid mode versus the coupling strength g and the delay time τ . We consider here the SMR-driven system with parameters specified in Eq. (28), which enable us to observe the single-photon resonances in the mode c . For clarity, all the values of the correlation functions ≥ 2 are truncated at 2.

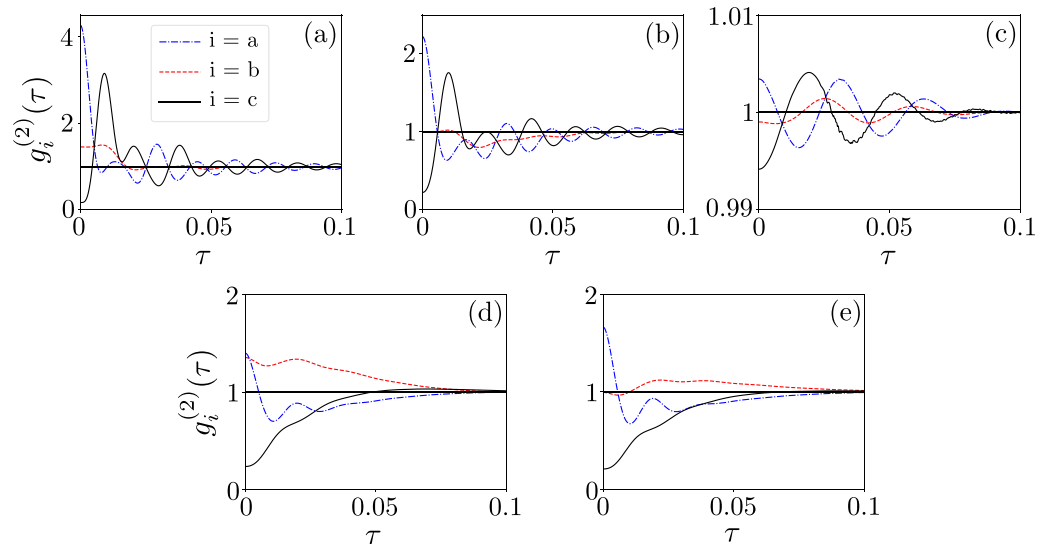


Figure 5. Delay-time second-order correlation functions $g_i^{(2)}(\tau)$ for the SMR mode a , the QD mode b , and the hybrid mode c modes assuming: (a–c) the SMR-driven system specified in Eq. (28) with $f = 5.5\gamma$ and $\kappa_{\max} = \kappa_b = 6\gamma$, and (d,e) the QD-driven system in Eq. (29) with $\kappa_{\max} = 7.5\gamma$, where we additionally set: (a) $g = 1.3\kappa_{\max} = 7.8\gamma$, (b) $g = 1.1\kappa_{\max} = 6.6\gamma$, (c) $g = 0.2\kappa_{\max} = 1.2\gamma$, (d) $g = 0.7\kappa_{\max} = 5.25\gamma$, and (e) $g = 0.758\kappa_{\max} = 5.685\gamma$.

statistics²¹. However, to avoid confusion, one can refer to single-time (or zero-delay-time) photon antibunching if defined by $g^{(2)}(0)$ and two-time (or delay-time) photon antibunching if defined via $g^{(2)}(\tau)$.

In Fig. 4, we plotted $g^{(2)}(\tau)$ for the range $[0, 1.5]$ of g/κ_{\max} . This range is also shown in Fig. 3a, where the examples of Cases 4 and 7 can be identified. As expected, one can see oscillations in the SMR and hybrid modes in Figs. 4a,c, respectively. These oscillations are induced by the competition between the qubit-SMR coupling g and the SMR-QD hopping f in our system. Apparently, by analysing $g^{(2)}(\tau)$ in the weak-coupling regime, the frequency of the oscillations is smaller than that in the strong-coupling regime, in which the oscillations are caused by both couplings g and f . Moreover in a very weak coupling regime, where $g \ll 1$ oscillations occur due to the hopping strength f , with the period $2\pi/f$ ⁷⁴. This means that, in the weak-coupling regime, also the coupling between the SMR and QD can generate oscillations in our system, where in this case the period of oscillations, which are induced by $f = 5.5\gamma$, is approximately equal to $\tau \approx 0.036$, which coincides with the period deduced from the graph, as seen in Fig. 5c. These detrimental oscillations should be suppressed on a time scale longer than the SMR lifetime $\tau = 1/\kappa_a$ to enable boson antibunching to survive in the area of our interest.

Various combinations of correlations effects are shown in Fig. 5. All panels in Fig. 5 show that the photon mode a is super-Poissonian and bunched, while the hybrid mode c is sub-Poissonian and antibunched. However, the properties of the phonon mode b are different in every panel. Specifically, the mode b is in panel:

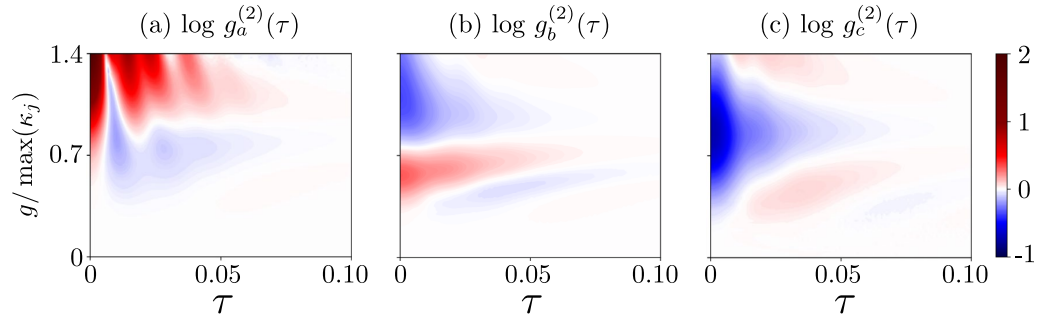


Figure 6. Same as in Fig. 4, but for the QD-driven system with parameters given in Eq. (29). We observe here single-PRs and the corresponding single-PB effects.

(a) super-Poissonian and unbunched [defined as $g_b^{(2)}(0) \approx g_b^{(2)}(\tau)$ for non-zero but short delay times τ], (b) Poissonian and unbunched, (c) sub-Poissonian and unbunched, (d) super-Poissonian and bunched, and (e) Poissonian and bunched, as usually considered for very short delay times τ . Note that panels (a, b, c) are for the SMR-driven system, while the remaining panels (d, e) are for the QD-driven system, which are discussed in detail in the next section.

In particular, it is seen that by decreasing the coupling at $g/\kappa_b = 1.1$ in Fig. 5b, the QD mode b is unbunched with the Poissonian statistics, while the hybrid mode c exhibits antibunching $g^{(2)}(0) < g^{(2)}(\tau)$ and the sub-Poissonian statistics $g^{(2)}(0) < 1$, in both cases. The role of the auxiliary mode b is, in a sense, to convert the super-Poissonian into sub-Poissonian statistics in the mode c .

The destructive interference of both modes a and b , at the balanced linear coupler, can result in the sub-Poissonian statistics of the hybrid modes. We observe this effect even in the weak-nonlinearity (or weak-coupling) regime, which witnesses unconventional PB, as discussed in detail in “Methods”. It is worth noting that in this study we are aiming at observing $g^{(2)}(\tau) < 1$ not only at $\tau = 0$, but also for non-zero delay times (e.g., $\tau \in [0, 0.1]$), as in standard experimental demonstrations of the boson antibunching statistics reported in, e.g., Refs^{7,75}. Thus, the cases shown in Fig. 4a,c can hardly be considered as convincing demonstrations of the sub-Poissonian statistics, because of the oscillations, which occur in $g_{a,c}^{(2)}(\tau)$ with increasing τ . More convincing demonstrations of these effects without such oscillations (or by considerably suppressing them) are presented in Figs. 6 and 7, as analysed in detail in the next section.

To explain the super-Poissonian photon-number statistics and photon bunching in the mode a for the system pumped in the SMR mode, let us analyse Fig. 5a with $g \approx \kappa_m$ concerning the anharmonicity of the energy levels in these cases.

The g term in Eq. (2) corresponds to the standard Jaynes–Cummings model with the familiar eigenvalues⁶²:

$$E_n^\pm \equiv E(|n, \pm\rangle) = n\omega_{\text{SMR}} \pm \frac{1}{2}\sqrt{\Delta_1^2 + \Omega_n^2} \quad (15)$$

with the corresponding eigenstates:

$$\begin{aligned} |n, +\rangle &\equiv \cos\left(\frac{\theta_n}{2}\right)|n\rangle|e\rangle + \sin\left(\frac{\theta_n}{2}\right)|n+1\rangle|g\rangle, \\ |n, -\rangle &\equiv -\sin\left(\frac{\theta_n}{2}\right)|n\rangle|e\rangle + \cos\left(\frac{\theta_n}{2}\right)|n+1\rangle|g\rangle, \end{aligned} \quad (16)$$

which are often referred to as dressed states or dressed-state doublets, where $\theta_n = \Omega_n/\Delta_1$ is the mixing angle, $\Delta_1 = \omega_q - \omega_{\text{SMR}}$ is the detuning between the SMR and qubit. Moreover, $\Omega_n = 2g\sqrt{n+1}$ can be interpreted as the n -photon Rabi frequency on resonance, so, in particular, $\Omega_0 = 2g$ is the vacuum Rabi frequency. Thus, the energy spectrum is clearly anharmonic, which is a necessary condition to observe PB. Note that the Jaynes–Cummings interaction can be effectively described in the dispersive limit (i.e., far off resonance) as a Kerr nonlinearity (for a detailed derivation see, e.g.,⁵⁰), which is the standard nonlinearity assumed in many predictions of PB effects.

To demonstrate the anharmonic energy levels of the complete Hamiltonian H_+ on resonance (see Fig. 2), we assume a weak drive coupling strength η_a . Given that, the system Hilbert space can be truncated. We assume that the polariton number is at most equal to two in this weak-drive regime. The ground state is $|\psi_0\rangle = |0, 0, g\rangle$ with the corresponding eigenvalue $E_0 = 0$. The three eigenvalues of the first manifold (with eigenstates containing a single polariton), as shown in Fig. 2b, are:

$$E_{1,3}^{(1)} = \Delta \mp \sqrt{g^2 + f^2}, \quad E_2^{(1)} = \Delta, \quad (17)$$

while the five eigenvalues of the second manifold (with eigenstates containing two polaritons), which are shown in Fig. 2c, read:

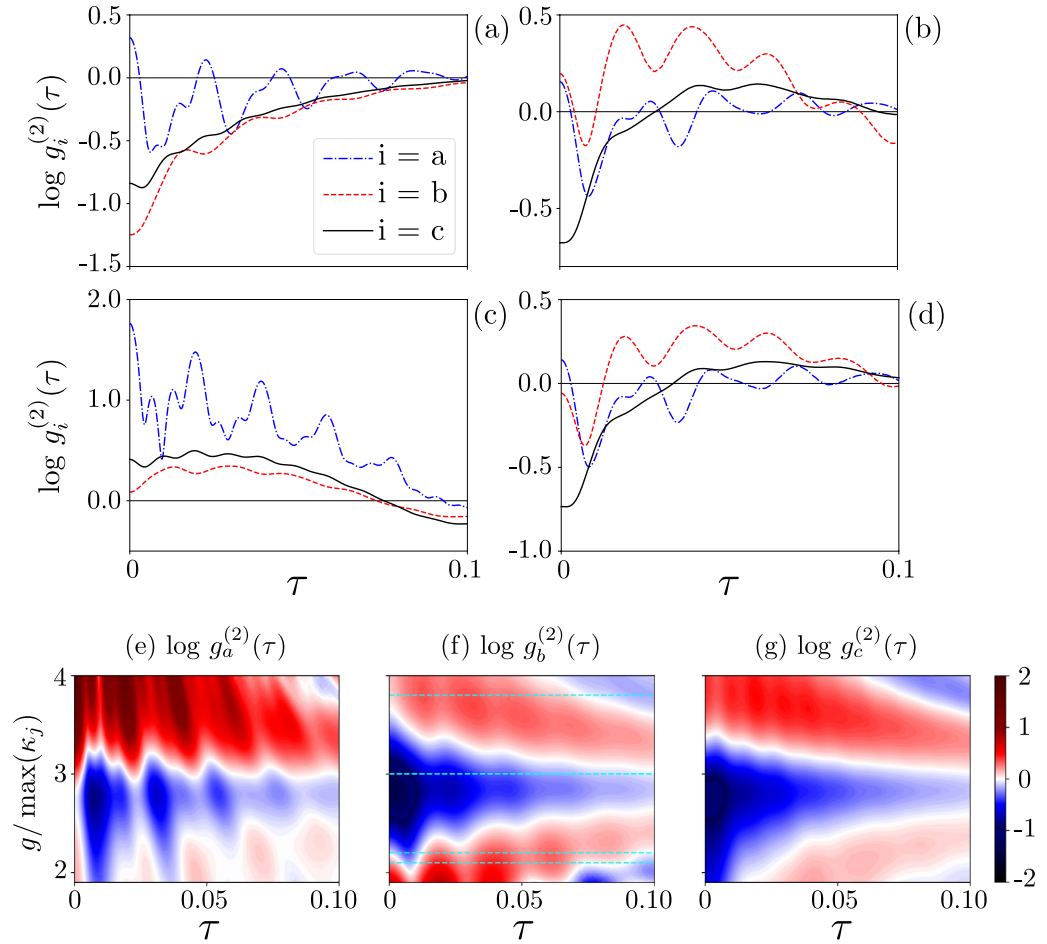


Figure 7. (a–d) Delay-time second-order correlation functions $g_i^{(2)}(\tau)$ (in the logarithmic scale) for the SMR mode a , the QD mode b , and the hybrid mode c modes in the QD-driven system assuming that g/κ_{\max} is equal to: (a) 3, (b) 2.1, (c) 3.8, and (d) 2.2. The four different predictions of correlations for the QD mode b correspond to all the cases listed in Table 2. (e,f) Same as in Fig. 4, but for the parameters given in Eq. (30). Note that panels (a–d) show the cross-sections of the 3D plot in (f) at the values of g/κ_{\max} marked by broken lines.

$$\begin{aligned}
 E_{1,2}^{(2)} &= \frac{1}{2} \left[4\Delta - \sqrt{2(3g^2 + 5f^2 \pm f_1)} \right], \\
 E_3^{(2)} &= 2\Delta, \\
 E_{4,5}^{(2)} &= \frac{1}{2} \left[4\Delta + \sqrt{2(3g^2 + 5f^2 \mp f_1)} \right],
 \end{aligned} \tag{18}$$

where $f_1 = \sqrt{3f^2(10g^2 + 3f^2) + g^4}$. In particular, by assuming $f = 5\gamma$ and $g = 7.5\gamma$, the eigenenergies of the first and second manifolds are, respectively: (1) Δ , $\Delta \pm 9.01388\gamma \approx \Delta \pm 9\gamma$, and (2) 2Δ , $2\Delta \pm 5.82965\gamma \approx 2\Delta \pm 6\gamma$, and $2\Delta \pm 16.11725\gamma \approx 2\Delta \pm 16\gamma$.

A simple way to probe the pumped mode is to record the second-order correlation $g^{(2)}(0)$ as a function of Δ_{SMR} , where the pump frequency ω_p is changing (see Fig. 8). To do so, we first consider the resonance case as $\omega_{\text{SMR}} = \omega_m = \omega_q = \omega$ in Eq. (8) and $\omega - \omega_p = \Delta$. As depicted in Fig. 8a, one can see local minima with negative values in $\log g^{(2)}(0)$ for the three modes, which indicate Case 1 in Table 1, at $\Delta_{\text{SMR}}/\gamma = \pm 9$, which correspond to $\Delta = \pm \sqrt{g^2 + f^2} \approx \pm 9\gamma$, given Eq. (17). This means that the pump frequency is located at the two dressed state doublets with energies $E_1^{(1)}$ and $E_3^{(1)}$. And we are off-resonance from the second energy manifold, which implies the possibility of observing PB at these frequencies.

Furthermore, our simulations predict a maximum of $\log g^{(2)}(0) \approx 3$ showing a strong super-Poissonian statistics in the three modes (corresponding to Case 8 in Table 1) as $\Delta_{\text{SMR}} \rightarrow 0$. In particular, at $\Delta_{\text{SMR}}/\gamma \approx \pm 6$, the pump frequency is near $E_1^{(2)} \approx 6$ and $E_4^{(2)} \approx -6$, respectively, of the second manifold, in which the probability of the two-photon resonance is maximised, as a signature of PIT. It signifies that the pump is in resonance with one

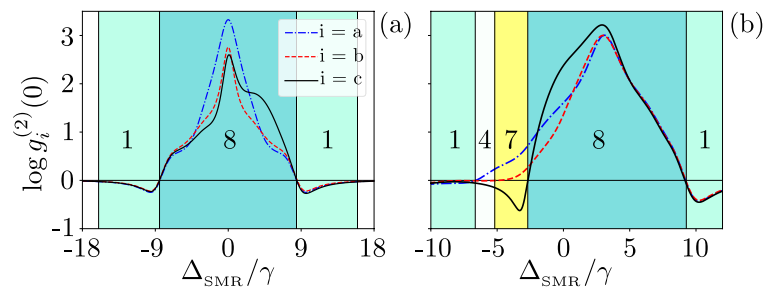


Figure 8. Correlation functions $\log g_i^{(2)}(0)$ versus the frequency detuning Δ_{SMR} (in units of the qubit decay rate γ) between the drive and SMR for: (a) the resonance case $\omega_{\text{SMR}} = \omega_m = \omega_q$ (so also $\Delta_{\text{SMR}} = \Delta_m = \Delta_q$) and (b) the nonresonance case $\omega_{\text{SMR}} \neq \omega_m \neq \omega_q$, where $\omega_b/\gamma = 1560$ MHz. Note that by changing the pump frequency, different detunings appear with respect to the modes a and b , and qubit. We set $g = 7.5\gamma$ and other parameters are given in Eq. (28). The numbering of the coloured regions correspond to the cases listed in Table 1.

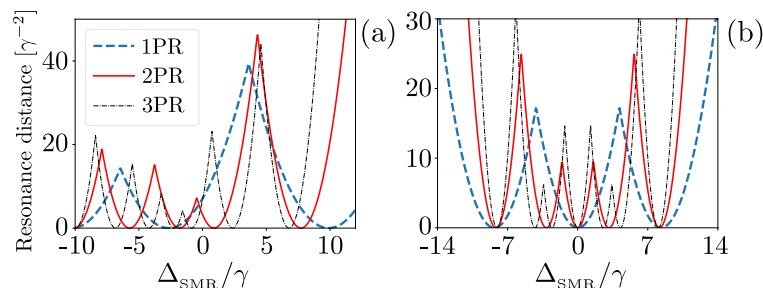


Figure 9. Resonance distances, as defined in Eq. (19), versus the frequency detuning Δ_{SMR} (in units of the qubit decay rate γ) between the drive and SMR for: (a) the SMR-driven system with parameters specified in Eq. (28) with $g = 7.58\gamma$ and (b) the QD-driven system with Eq. (29) with $g = 4.5\gamma$.

of the levels in the second manifold of the hybrid system energy levels, here specifically $E_1^{(2)}$ and $E_4^{(2)}$. One can see in Fig. 8, peaks (global maxima in the analysed range) of $\log g_n^{(2)}(0) > 0$ for $n = a, b, c$ at $\Delta_{\text{SMR}} = 0$. In particular, the probability of absorbing a single photon decreases here. However, if a photon is absorbed, it enhances the probability of capturing subsequent photons, this effect produces the super-Poissonian statistics, which is due to the fact that the probability of observing a single photon is also very small ($P_{10g} \ll 1$) and smaller than the probability of observing two photons^{6,76}.

It is seen that, by tuning the drive frequency to the transition $E_2 - E_0$ in the energy spectrum of the total non-linear system, the probability of admitting two photons increases. This results in the super-Poissonian statistics, which is opposite to the case, when the drive frequency is tuned to the transition $E_1 - E_0$, when the probability of admitting subsequent photons decreases resulting in PB.

By assuming the off-resonance condition, $\omega_{\text{SMR}} \neq \omega_m \neq \omega_q$, we show in Fig. 8b the correlation functions for the three modes (a, b, c) as a function of Δ_{SMR} in the case, when the drive is tuned in-between the dressed state eigenenergies of the hybrid system.

The PB and PIT effects observed in Fig. 8 can be explained by considering some measures of the distances from resonances, as shown in Fig. 9a. The distances of the single-, two-, and three-photon resonances (PRs) are defined here, respectively, as:

$$D_{1\text{PR}} = \min_i |\omega_p - \omega_i^{(1)}|^2, \quad D_{2\text{PR}} = \min_i |2\omega_p - \omega_i^{(2)}|^2, \quad D_{3\text{PR}} = \min_i |3\omega_p - \omega_i^{(3)}|^2, \quad (19)$$

where ω_p is the frequency of the pump that is tuned with respect to the energy of the hybrid system. Here $\omega_i^{(n)}$ are the frequencies (labelled with subscript i) in the n th manifold, so the minimalization is performed over $\omega_i^{(n)}$ for a given manifold n . Figure 9 shows the resonance distances versus Δ_{SMR} , where ω_p is tuned with respect to the energy of the whole system. The dip in $g^{(2)}(0)$ at $\Delta_{\text{SMR}}/\gamma = 10$ (see Fig. 8b), which is characteristic for PB, corresponds to the resonance for a single excitation, as seen from $D_{1\text{PR}}$, and is off-resonance for higher excitations at that frequency (see Fig. 9a). The second-order correlation function $g_c^{(2)}(0)$ for the hybrid mode has a signature of PB around $\Delta_{\text{SMR}}/\gamma = -3.4$, while the modes a and b exhibit the super-Poissonian statistics (indicating PIT), as shown in Fig. 8b. This effect is witnessed as a dip in $D_{1\text{PR}}$ and it is off-resonance for $D_{2\text{PR}}$ and

D_{3PR} , as illustrated in Fig. 9a, while the modes a and b exhibit PIT. This type of unconventional PB is discussed further in sections below.

By decreasing Δ_{SMR}/γ from 0 to -2 , the correlation function $g_a^{(2)}(0)$ for the SMR mode in Fig. 8a resembles a shoulder in shape. We observe PIT at this point or region, as expected from our findings in the resonance-distant diagram in Fig. 9a. Indeed, there is a dip in D_{2PR} for higher resonances at this point, which explains the occurrence of PIT.

Let us consider now $\Delta_{SMR}/\gamma \rightarrow 3$ in Fig. 8b for the pump frequency in resonance with the qubit, $\Delta_q = 0$, which is close to the resonance frequency of the hybrid mode. In this case multi-photon transitions are induced, which result in PIT at $\Delta_{SMR}/\gamma = 3$, and we observe a peak in $\log g^{(2)}(0) > 0$ at this frequency in Fig. 8b. Clearly, we are here in resonance with higher-energy levels, while the drive strength is very small, $\eta_a/\gamma = 0.7$. The probability of observing a single photon is also small as the peak for $\Delta_c = 0$, but if a single photon is absorbed, then the probability of capturing subsequent photons increases, as for PIT.

The analysed system parameters are found by optimising our system to observe the super-Poissonian statistics in the SMR and QD modes. At the sub-Poissonian statistics area of $g^{(2)}(0)$, it is possible to observe in Fig. 14 (in “Methods”) that $g^{(3)}(0) > 1$ and/or $g^{(4)}(0) > 1$, which are signatures of higher-order photon/phonon resonances and multi-PIT (see “Methods”). Actually, by calculating the second-order correlation function to witness the PB and PIT phenomena, higher-order correlation functions can be used to test whether a given effect is indeed: (1) single-PB or single-PIT, (2) multi-PB or multi-PIT, or (3) nonstandard versions of these effects, as discussed in “Methods” and, e.g., in Refs.^{29,53}. As mentioned above, these parameters allow us to achieve the sub-Poissonian statistics for a relatively long delay times.

Hybrid-mode blockade in the QD-driven system

In this section, we analyse steady-state boson-correlation effects, including the hybrid-mode blockade and PIT, in the QD-driven dissipative system, as described by the Hamiltonian H' and the master equation (12) for the parameters specified mostly in Eqs. (29) and (30).

To eliminate or at least to suppress the undesired oscillations in $g^{(2)}(\tau)$, we assume in this section that our system is driven classically at the QD. Moreover, we assume that the SMR is in the bad-cavity regime, as $\kappa_{SMR} \gg g^2/\kappa_{SMR} \gg \gamma^2$. So, we apply the effective system Hamiltonian in the rotating frame, as given by Eq. (9). Even if the lifetime $\tau_{SMR} = 1/\kappa_{SMR}$ of the SMR is much shorter than that assumed in the SMR-driven system, which was discussed in the former section, the hybrid mode, as we show below, reveals no oscillations for quite long delay times, which is due to driving the QD.

To study boson-number statistics of our system, we compute the second-order correlation function $g^{(2)}(0)$ for the optimised parameters, which enables us to demonstrate Cases 4, 6, and 7 of Table 1 in Fig. 3b. In Case 7, which is of our special interest, the modes a and b are super-Poissonian, as $\log g^{(2)}(0) > 0$, while the hybrid mode c is sub-Poissonian, as $\log g_c^{(2)}(0) < 0$. By increasing the coupling g between the SMR and qubit, the mode b becomes sub-Poissonian, as being affected by the nonlinearity of the mode a .

To check the second criterion for PB, the second-order correlation function $g^{(2)}(\tau)$ is considered below. Figure 6 shows $g^{(2)}(\tau)$ corresponding to $g^{(2)}(0)$ plotted in Fig. 3b showing Cases 4, 6, and 7. As expected, boson antibunching is observed for the hybrid mode, as shown in Fig. 6c, while the SMR mode reveals bunching, as illustrated in Fig. 6a. Moreover both phonon antibunching and bunching, in addition to unbunching [i.e., $g_b^{(2)}(0) \approx g_b^{(2)}(\tau)$ for $\tau \gtrsim 0$], have been observed in the studied region of the QD mode, as shown in Fig. 6b. It is clear from Fig. 6 that the antibunching of bosons in the three modes survives in some specific coupling regime (around $g = 0.7\kappa_m$) for a relatively long delay time $\tau > 1/\kappa$ and oscillations in $g_c^{(2)}(\tau)$ are absent in the hybrid mode c . Moreover, boson bunching is observed, when $g_a^{(2)}(\tau)$ drops rapidly for delay times greater than the cavity photon lifetime, as considered in Fig. 5d,e.

To understand the delay-time dependence of the hybrid mode c , we consider Eq. (9), when the SMR, QD, and qubit have the same resonance frequency, $\omega_{SMR} = \omega_m = \omega_q = \omega$ and $g = 4.5\gamma$. As illustrated in Fig. 10a, there are three dips (local minima) in $g_b^{(2)}(0) < 0$ for the mode b of the QD, where we assumed $g < \min\{\kappa_a, \kappa_b\}$ and $f > g$. For these parameters, only a weak nonlinearity is induced in the mode b . Thus, the anharmonicity of energy levels cannot explain the PB effect observed as a dip at these three dips (see Fig. 9b). Actually, these dips in $\log g_b^{(2)}(0)$ are due to single-photon resonant transitions, which correspond to unconventional PB, as explained by the non-Hermitian effective Hamiltonian method in the next section and in “Methods”.

Figure 10c shows $\log g_i^{(2)}(0)$ for the three modes as a function of Δ_{SMR} . In this case, we assume that the resonance frequencies of the SMR, QD, and qubit are not the same, and the detuning of each mode with respect to ω_p is different. It is shown that, when $\Delta_{SMR}/\gamma \rightarrow 2$, multiphoton transitions (and so PIT or multi-PB) can be induced in the mode a , where the pump frequency is in the resonance with the qubit, $\omega_p = \omega_q$. This effect is seen in Fig. 14 (in “Methods”) corresponding to a local maximum in higher-order moments $g_i^{(3)}(0)$ and $g_i^{(4)}(0)$. Likewise the resonance case, unconventional PB in the modes b and c can be explained by the method applied in the next section.

In Fig. 11, we study how the second-order correlation functions reveal the PIT regime, which corresponds to Case 8 in Table 1, as a function of the SMR-pump strength η_a [in panels (a) and (c)] and the QD-pump strength η_b [in panels (b) and (d)]. The hybrid mode c is super-Poissonian for all the shown cases and pump strengths. The modes a and b are super-Poissonian [except the mode a in panel (b)] for small pump strengths $\eta_{a,b}$. By increasing the driving power at least to some values, which can be identified in the figures for specific modes, we observe that the correlation functions $g^{(2)}(0)$ also decrease for all the modes (except the mentioned case). This property confirms the nonclassicality of the predicted PIT in the hybrid system according to an additional criterion of ‘true’ PIT of Ref.¹⁴.

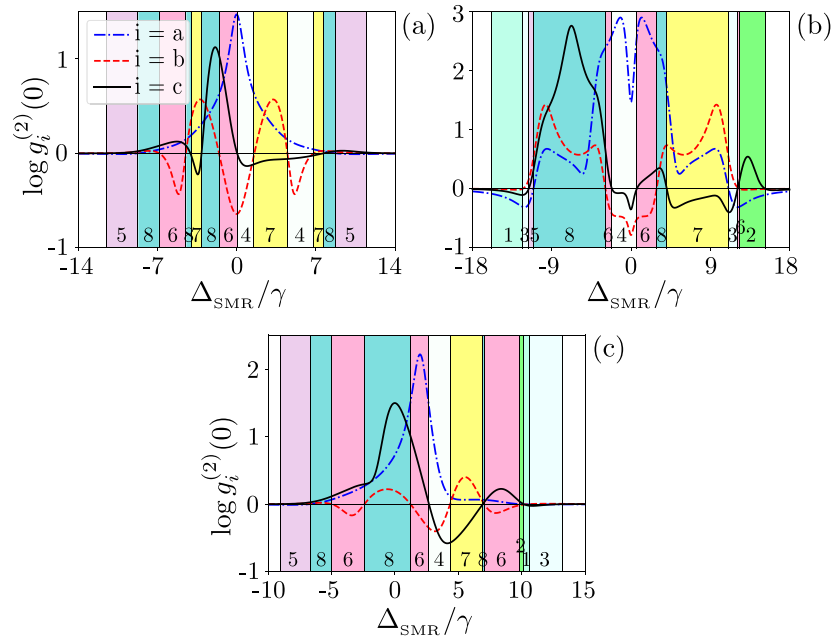


Figure 10. Correlation functions $\log g_i^{(2)}(0)$ versus the frequency detuning Δ_{SMR} (in units of the qubit decay rate γ) between the drive and SMR for the QD-driven system for: **(a,b)** the resonant case with $\omega_{\text{SMR}} = \omega_m = \omega_q$ (so also $\Delta_{\text{SMR}} = \Delta_m = \Delta_q$), and **(c)** the nonresonant case with $\omega_{\text{SMR}} \neq \omega_m \neq \omega_q$. Parameters are set in: Eq. (29) with $g = 4.5\gamma$ for **(a,c)**, and Eq. (30) with $g = 9.5\gamma$ for **(b)**. Eight different predictions, which correspond to all the cases listed in Table 1, are marked for the sub- and super-Poissonian number statistics in the photonic **(a)**, phononic **(b)**, and hybrid photon–phonon **(c)** modes.

Unconventional blockade explanation via non-Hermitian Hamiltonian approach

In this section, we apply the analytical mathematical formalism of Ref.⁴⁵, based on a non-Hermitian Hamiltonian, to identify the quantum interference effect that is responsible for inducing unconventional PB, i.e., strongly sub-Poissonian statistics in the weak-coupling regime or the weak-nonlinearity regime. We stress that this is an approximate approach, where the effect of quantum jumps is ignored^{77,78}.

By considering the system studied in the former section under the weak-pump condition, we can truncate the Hilbert spaces for the modes a and b and the qubit at their two excitations in total. This allows us to consider the total-system Hilbert space of dimension $3 \times 3 \times 2 = 18$. Moreover, the weak-pump condition implies that $C_{00g} \gg C_{10g}, C_{01g}, C_{00e} \gg C_{11g}, C_{10e}, C_{01e}, C_{20g}, C_{02g}$. Thus, the steady-state of the coupled system can be expressed as

$$|\Psi_{abq}(t)\rangle = C_{00g}|00g\rangle + e^{-i\omega_d t}(C_{00e}|00e\rangle + C_{10g}|10g\rangle + C_{01g}|01g\rangle) + e^{-2i\omega_d t}(C_{10e}|10e\rangle + C_{01e}|01e\rangle + C_{11g}|11g\rangle + C_{20g}|20g\rangle + C_{02g}|02g\rangle), \tag{20}$$

where $|n_a, n_b, g/e\rangle$ is the Fock state with n_a photons in the SMR, n_b phonons in the QD, and the lower ($|g\rangle$) or upper ($|e\rangle$) state of the qubit. The effective non-Hermitian Hamiltonian of the system can be written as

$$H_{\text{eff}} = H'' - i\frac{\kappa_a}{2}a^\dagger a - i\frac{\kappa_b}{2}b^\dagger b - i\frac{\gamma}{2}\sigma_+\sigma_-, \tag{21}$$

where H'' is given by Eq. (9). Analogously, one can consider the non-Hermitian Hamiltonian with H' , given by Eq. (8).

In the weak-pump regime, the mean number of photons and phonons in the SMR and QD can be approximated as $\langle n_a \rangle \approx |C_{10g}|^2$ and $\langle n_b \rangle \approx |C_{01g}|^2$, respectively. As derived in detail in “Methods”, the second-order correlation functions for generated photons and phonons, under the same weak-pump conditions, can be given by:

$$g_a^{(2)}(0) = \frac{\langle a^\dagger a^\dagger aa \rangle}{\langle a^\dagger a \rangle^2} \approx \frac{2|C_{20g}|^2}{|C_{10g}|^4}, \tag{22}$$

$$g_b^{(2)}(0) = \frac{\langle b^\dagger b^\dagger bb \rangle}{\langle b^\dagger b \rangle^2} \approx \frac{2|C_{02g}|^2}{|C_{01g}|^4},$$

where the superposition coefficients $C_{n,m,g}$ are given in Eqs. (39) and (41).

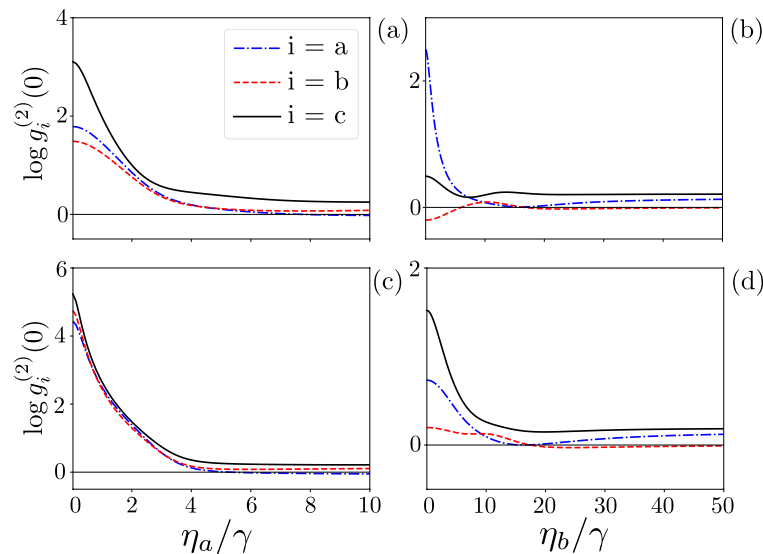


Figure 11. Second-order correlation functions $\log g_i^{(2)}(0)$ versus the drive strengths: **(a,c)** η_a for the SMR-driven system and **(b,d)** η_b for the QD-driven system. Parameters are given in: **(a)** Eq. (28) with $g = 7.5\gamma$ and $\omega_p = 1554\gamma$, which implies $\Delta_q = -3\gamma$, $\Delta_b = 6\gamma$, $\Delta_a = 0$; **(b)** Eq. (29) with $\omega_p = 1568\gamma$, which implies $\Delta_q = 0$, $\Delta_b = -8\gamma$, and $\Delta_a = 2\gamma$; **(c)** Eq. (28) with $g = 7.5\gamma$ and $\omega_p = 1551\gamma$, which implies $\Delta_q = 0$, $\Delta_b = 9\gamma$, and $\Delta_a = 3\gamma$; and **(d)** Eq. (29) with $\omega_p = 1570\gamma$, which implies $\Delta_q = -2\gamma$, $\Delta_b = -10\gamma$, and $\Delta_a = 0$.

The hybrid photon–phonon modes, which are defined in Eq. (10), are the output modes of the balanced linear coupler with the SMR and QD modes at its inputs. As shown in “Methods”, we find, analogously to Eq. (22), the second-order correlation function for the hybrid mode c reads:

$$g_c^{(2)}(0) = \frac{\langle c^\dagger c^\dagger c c \rangle}{\langle c^\dagger c \rangle^2} \approx \frac{2|C'_{20g}|^2}{|C'_{10g}|^4}, \quad (23)$$

where the superposition coefficients $C'_{n,m,g}$ are given in Eqs. (40) and (41), and the sixth formula in Eq. (34).

This approach enables us to explain unconventional PB generated in the hybrid system, which is the result of a destructive quantum interference effect that assures, together with other conditions, that the probability amplitude of having two photons in the SMR and QD is negligible. This method can also be used to find some optimal parameters to observe PB in the system.

Figure 12 presents a comparison of our predictions based on the precise numerical solutions of the master equation in Eq. (12), as shown by thin curves, with those calculated from Eqs. (22) and (23) using the non-Hermitian Hamiltonian approach, as shown by thick curves. The locations of the maxima and minima of the correlation functions are found similar according to both formalisms. However, these extremal values can differ more distinctly, especially for the two global minima in the sub-Poissonian statistics of the mode b and the super-Poissonian maximum of the mode a . The differences result from the effect of quantum jumps, which are properly included in the master-equation approach and totally ignored in the non-Hermitian Hamiltonian approach (Fig. 12).

Different types of blockade and tunnelling effects

The sub-Poissonian statistics of a bosonic field, as described by $g^{(2)}(0) \ll 1$, is not a sufficient criterion for observing a ‘true’ PB, which can be a good single-photon or single-phonon source. In fact, other criteria, such as boson antibunching, $g^{(2)}(0) < g^{(2)}(\tau)$, and the sub-Poissonian statistics of higher-order correlation functions, $g^{(n)}(0) \ll 1$, should also be satisfied (see “Methods”). Anyway, most of the studies of PB, and especially those on unconventional PB, are limited to testing the second-order sub-Poissonian statistics described by $g^{(2)}(0) < 1$.

As explicitly discussed in Refs.^{21,72,79,80}, photon antibunching and sub-Poissonian statistics are different photon-number correlation effects. So, the four cases listed in Table 2, can be considered as different types of PB and PIT. We show that all these effects can be observed in the studied system. For brevity, Table 2 is limited to phononic effects. PB, as defined in Case I and often referred to as a ‘true’ PB, can be a good single-photon source; but, as mentioned above, other higher-order criteria should also be satisfied.

To show these four different effects, we use the parameters set in Eq. (30), where $\kappa_b \ll \kappa_a$ at the $\kappa_b = 0.002\gamma$, which indicates that the quality factor is $Q \approx 200$, and so $\eta_b/\kappa_b \approx 100$ in the case of a strong pump driving the QD mode with $\eta_b = 0.22\gamma$. Apart from the previously mentioned phenomena, such as observing the super-Poissonian statistics and bunching in the SMR and QD modes, while a hybrid mode exhibiting the sub-Poissonian

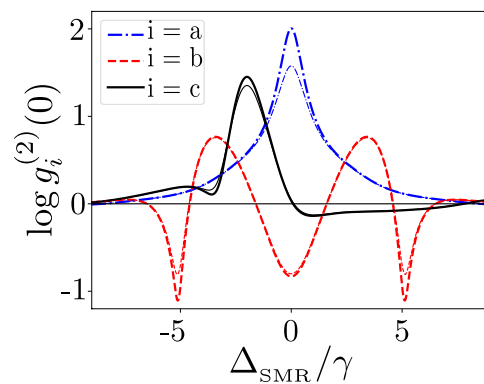


Figure 12. Correlation functions $\log g_i^{(2)}(0)$ versus the frequency detuning Δ_{SMR} in units of γ for the QD-driven system for the resonant case with $\omega_{\text{SMR}} = \omega_m = \omega_q = \gamma \times 1560$ MHz (so also $\Delta_a = \Delta_b = \Delta_q$). The thin curves in each mode are obtained using the master equation in Eq. (12) and the thick curves are obtained from the non-Hermitian Hamiltonian method using Eqs. (22) and (23). Parameters are set in Eq. (29) except $g = 4.5\gamma$ and $\kappa_a = \kappa_b = 6\gamma$.

Case	Effect	Single-time correlations	Two-time correlations	Example of g/κ_a	Figure
I	Stronger form of PB ('true' PB)	Sub-Poissonian PNS $g_b^{(2)}(0) < 1$	Phonon antibunching $g_b^{(2)}(\tau) > g_b^{(2)}(0)$	3.0	7(a)
II	Stronger form of PIT ('true' PIT)	Super-Poissonian PNS $g_b^{(2)}(0) > 1$	Phonon bunching $g_b^{(2)}(\tau) < g_b^{(2)}(0)$	2.1	7(b)
III	Weaker form of PIT or PB	Super-Poissonian PNS $g_b^{(2)}(0) > 1$	Phonon antibunching $g_b^{(2)}(\tau) > g_b^{(2)}(0)$	3.8	7(c)
IV	Weaker form of PB or PIT	Sub-Poissonian PNS $g_b^{(2)}(0) < 1$	Phonon bunching $g_b^{(2)}(\tau) < g_b^{(2)}(0)$	2.2	7(d)

Table 2. Different single- and two-time phonon-number correlation effects induced in the QD mode, which can be observed for different values of the qubit-SMR coupling strength g with respect to the SMR decay rate κ_a , e.g., by setting the other parameters to be the same as in Eq. (30). Here, PNS stands specifically for the phonon-number statistics of the mode b . Note that we also found examples of Cases I, II, and IV for the modes a and c using the same system parameters as for the mode b .

statistics and boson antibunching, we find the four types of PB/PIT in the mode b in different coupling regimes, as shown in Table 2, which includes the examples of specific experimentally feasible values of g/κ_a .

Case I corresponds to a stronger form of PB, which we refer to as a 'true' PB, when the nonclassical nature of bosons is revealed by both their antibunching and sub-Poissonian statistics. Case II corresponds to a stronger form of PIT, which can be called a 'true' PIT, when bosons exhibit both classical effects: the super-Poissonian statistics and bunching. In Case III, one can talk about a weaker form of PIT or, equivalently, another weaker type of PB, as such bosons are characterised by the classical super-Poissonian statistics and their nonclassical nature is revealed by antibunching. Case IV represents another weaker form of PB or, equivalently, of PIT, which is characterised by the nonclassical sub-Poissonian statistics of classically bunched bosons. These results imply that one cannot say in general that the antibunching of bosons leads to their sub-Poissonian statistics and vice versa^{21,79}.

Therefore, $g^{(2)}(\tau) > g^{(2)}(0)$ does not necessarily imply $g^{(2)}(0) < 1$, as in Case III, which can be seen in Fig. 7c,f. In addition, as another example related to Case IV, let us consider a Fock state $|n\rangle$ with $n \geq 2$, for which $g^{(2)}(0) = 1 - 1/n$, such that if $n = 2$ then $g^{(2)}(0) = 0.5$, so $g^{(2)}(0) < 1$ and it is not accompanied by boson antibunching, but bunching in this case.

Our focus in this paper is on the generation of PB in the hybrid mode, while the other two modes exhibit PIT. Note that this is a very special case of Table 1, which shows that eight combinations of boson number correlation phenomena in the modes a , b , and c can be generated in our system, as specified by the numbered coloured regions in various figures corresponding to the cases in Table 1. Thus, we found all the eight possible combinations of the PIT and PB effects in the hybrid system for the parameters specified in Eqs. (28), (29), and (30).

Detection of the hybrid-mode correlation functions

Here, we describe two detection schemes for measuring the intensity autocorrelation functions for the hybrid photon–phonon modes c and d , as shown in Fig. 13.

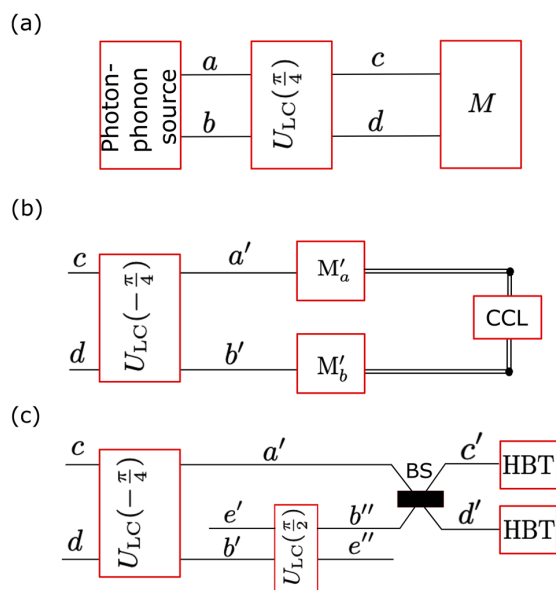


Figure 13. Schematics of the proposed detection schemes: (a) General scheme for the generation of the photonic mode a , phononic mode b , and hybrid modes c, d , and their detection in the measurement unit M , which is shown in specific implementations using: (b) detection method 1 and (c) detection method 2. Key: $U_{LC}(\theta)$ stands for the linear-coupler transformation, which in special cases corresponds to multi-level SWAP (for $\theta = \pi/2$) and Hadamard-like (for $\theta = \pm\pi/4$) gates; BS is the balanced beam splitter, which corresponds to $U_{LC}(\pi/4)$, M'_a (M'_b) is a measurement unit for detecting photons (phonons), CCL is a coincidence and count logic unit, HBT stands for the standard Hanbury–Brown and Twiss optical interferometer. Mode e' (e'') is in the photonic (phononic) vacuum state.

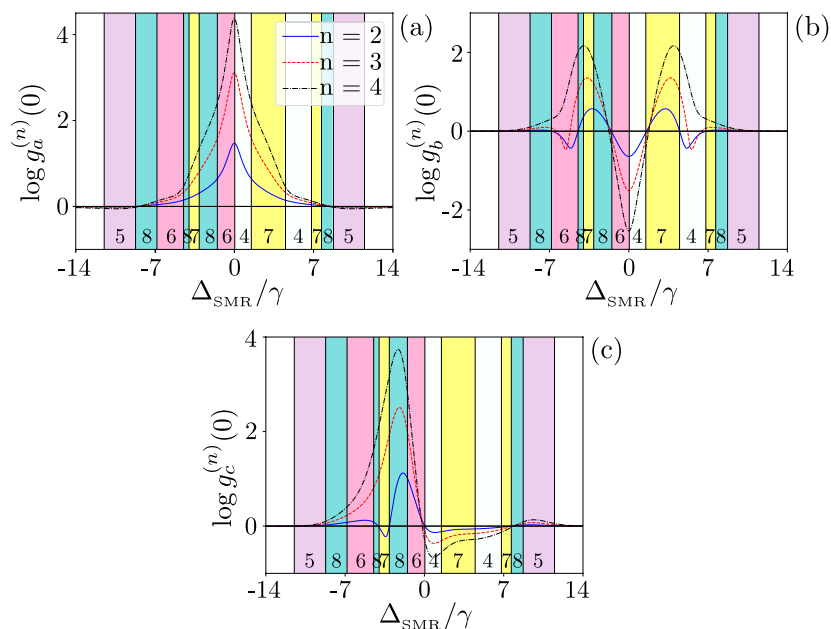


Figure 14. Correlation functions $\log g_i^{(n)}(0)$ of various orders [second (solid curves), third (dashed), and fourth (dot-dashed)] versus the detuning between the drive and SMR (in units of the qubit decay rate γ) for the QD-driven system for: (a) the photonic mode a , (b) the phononic mode b , and (c) the hybrid mode c . All parameters and colourful regions are the same as in Fig. 10a.

The measurements of $g^2(\tau)$ for the photonic mode a and the phononic mode b are quite standard and are usually based on the Hanbury-Brown and Twiss (HBT) optical interferometry and its generalised version for phonons⁸¹, respectively. However, the measurement M (as schematically shown in Fig. 13a) of $g^{(2)}(\tau)$, or even $g^{(2)}(0)$, for the hybrid photonic-phononic modes c and d is quite challenging if applied directly. Here we propose two detection methods, as shown in Fig. 13b,c, for indirect measuring of $g_{c,d}^{(2)}(0)$.

The first operation of the measurement unit M in both schemes is a linear-coupler transformation of the hybrid modes (c, d) into (a', b'), which, assuming that the process is perfect, should be equal to the original purely photonic (a) and phononic (b) modes.

We consider a linear coupler (formally equivalent to a beam splitter) described by a unitary operation $U_{LC}(\theta)$, which transforms the input operators a and b into:

$$\begin{aligned} c(\theta) &= U_{LC}^\dagger(\theta)aU_{LC}(\theta) = a \sin \theta + b \cos \theta, \\ d(\theta) &= U_{LC}^\dagger(\theta)bU_{LC}(\theta) = a \cos \theta - b \sin \theta, \end{aligned} \quad (24)$$

for a real parameter θ , where $T = \cos^2 \theta$ and $R = 1 - T = \sin^2 \theta$ are the transmission and reflection coefficients of the linear coupler, respectively. The studied hybrid modes are the special cases of Eq. (24) for $c \equiv c(\theta = \pi/4)$ and $d \equiv d(\theta = \pi/4)$. Clearly, the first transformation $U_{LC}(-\pi/4)$ in Fig. 13b,c, is the transformation inverse to that in Fig. 13a.

Detection method 1 based on measuring photons and phonons. The correlation functions $g_{c,d}^{(2)}(0)$ in the hybrid photon-phonon modes can be measured indirectly, as indicated in Fig. 13b, by measuring the observables:

$$f_{kl} = (a^\dagger)^k a^l, \quad g_{mn} = (b^\dagger)^m b^n, \quad (25)$$

where $k, l, m, n = 0, 1, 2$, by using the relations:

$$\langle c^\dagger c \rangle = \frac{1}{2} (\langle f_{11} \rangle + \langle g_{11} \rangle + \langle f_{01}g_{10} \rangle + \langle f_{10}g_{01} \rangle), \quad (26)$$

$$\langle c^{\dagger 2} c^2 \rangle = \frac{1}{4} (\langle f_{22} \rangle + 4\langle f_{11}g_{11} \rangle + \langle g_{22} \rangle + 2\langle f_{01}g_{21} \rangle + 2\langle f_{10}g_{12} \rangle + \langle f_{20}g_{02} \rangle + \langle f_{02}g_{20} \rangle + 2\langle f_{21}g_{01} \rangle + 2\langle f_{12}g_{10} \rangle), \quad (27)$$

and analogous relations for the hybrid mode d . The measurement units M'_a and M'_b in this method, as shown in Fig. 13b, describe the measurements of photons and phonons, respectively. It is seen that, in this approach, to determine $g_{c,d}^{(2)}(0)$, one has to measure the following observables: $f_{01}, f_{10}, f_{11}, f_{02}, f_{20}, f_{12}, f_{21}$, and f_{22} . Almost each observable f_{kl} should be measured simultaneously with a specific observable g_{mn} , which can be realised by a coincidence and count logic (CCL) unit in Fig. 13b.

The measurements of all the required photonic observables f_{kl} can be performed by using, e.g., the Shchukin-Vogel method, which is based on balanced homodyne correlation measurements⁸². According to that method, a photonic signal is superimposed on a balanced beam splitter with a local oscillator, which is in a coherent state $|\alpha\rangle = |\alpha\rangle \exp(i\phi)$ with a tunable phase ϕ . A desired mean value of the observable f_{kl} can be obtained by linear combinations of the coincidence counts registered by specific detectors for different local-oscillator phases ϕ . This part of the method corresponds to a Fourier transform. The simplest nontrivial configuration, which enables the measurement of the observables f_{10}, f_{01}, f_{20} , and f_{02} , requires four detectors and three balanced BSs, where additional input ports are left empty, i.e., allowing only for the quantum vacuum noise. By replacing the four detectors with four balanced BSs with altogether eight detectors at their outputs, one can measure any observable f_{kl} for $k + l \leq 4$. These include the desired observables f_{21}, f_{12} , and f_{22} . Of course, the observable f_{22} can be measured in a simpler way via the HBT interferometry. The measurement of phononic observable g_{mn} can be performed analogously just by replacing the balanced BSs by balanced phonon-mode linear couplers and using phonon detectors as, e.g., in Ref.⁸¹. The measurement of two-mode moments $\langle f_{kl}g_{mn} \rangle$ is, at least conceptually, a simple generalisation of the single-mode methods relying on proper coincidences in photonic and phononic detectors. Note that a multimode optical version of the original single-mode method was described in Ref.⁸³.

Detection method 2 based on measuring only photons. Figure 13c shows another realisation of the measurement unit M , to determine $g_{c,d}^{(2)}(0)$, and even $g_{c,d}^{(2)}(\tau)$. This method is, arguably, simpler and more effective than detection method 1, because it is based on measuring only photons and using standard HBT interferometry. Our approach was inspired by Ref.⁴⁸, where the measurement of single-mode phonon blockade was described via an optical method instead of a magnetomotive technique, which was described in Ref.⁴⁷, where phonon blockade was first predicted.

Our measurement setup realises the following three transformations: (1) converting the phononic mode b' into a photonic mode b'' , (2) mixing the optical modes a' and b'' on a balanced BS to generate the modes c' and d' , which, in an ideal case, have the same boson-number statistics as the original hybrid photon-phonon modes c and d ; and finally, (3) applying the conventional optical HBT interferometry for these two optical modes. In unit (1), this conversion corresponds to a multi-level SWAP gate, which can be implemented by a photonic-phononic linear coupler for $\theta = \pi/2$, assuming that the auxiliary input mode e' is in the photonic vacuum state, while the output mode e'' is in the phononic vacuum state. In unit (3), the balanced BS action on the optical modes a' and

b' in Fig. 13c corresponds to the transformation of the balanced linear coupler on the photonic (a) and phononic (b) modes, as shown in Fig. 13a.

Clearly, the linear-coupler transformation $U_{LC}(\theta)$ is applied not only to the modes (a, b), but also to other modes. Thus, Eq. (24) should be adequately modified by replacing (a, b) by (c, d), (e', b'), and (a', b''). For brevity, we omit their explicit obvious definitions here. Note that $U_{LC}(\pi/2)$ and $U_{LC}(\pi/4)$ correspond to a multi-level SWAP and Hadamard-like gates, respectively; while the balanced BS in Fig. 13c corresponds to $U_{LC}(\pi/4)$.

Discussion

We proposed a novel type of boson blockade, as referred to as hybrid photon–phonon blockade, which is a generalisation of the standard photon and phonon blockade effects. We predicted the new effect in a hybrid mode obtained by linear coupling of photonic and phononic modes. We described how hybrid photon–phonon blockade can be generated and detected in a driven nonlinear optomechanical superconducting system. Specifically, we considered the system composed of linearly coupled microwave and mechanical resonators with a superconducting qubit inserted in one of them.

We studied boson-number correlations in the photon, phonon, and hybrid modes in the system. By analysing steady-state second-order correlation functions, we found such parameter regimes of the system for which four different types of boson blockade and/or boson-induced tunnelling can be observed. Thus, we showed that bosons generated in the studied system can exhibit the sub-Poissonian (or super-Poissonian) boson-number statistics accompanied by boson antibunching in some cases or bunching in others. These results can be interpreted as four different types of blockade or tunnelling effects, as summarised in Table 2.

By tuning the pump frequency with respect to the energy levels of the hybrid system, which is driven via the SMR, we showed that it is possible to observe PB and PIT that can be explained by a large energy-level anharmonicity in the strong-coupling (or large-nonlinearity) regime. However, the time evolution of the second-order correlation function $g^{(2)}(\tau)$ oscillates due to the coupling g between the SMR and qubit as well as the hopping f between the SMR and QD. We showed that it is possible to induce PB in the hybrid mode c that survives for much longer delay times by driving the QD instead of the SMR.

We also predicted unconventional PB in the three modes in the weak-coupling (or weak-nonlinearity) regime using a non-Hermitian Hamiltonian approach based on neglecting quantum jumps. Our analytical approximate predictions are in a relatively good agreement with our precise master-equation solutions (including quantum jumps).

Moreover, as summarised in Table 1, we showed the possibility to observe eight different combinations of either PB or PIT in the three modes (a, b , and c) in different coupling regimes of this system. Thus, in particular, we found that the tunnelling effects in the photonic and phononic modes can lead, by their simple linear mixing, to the hybrid photon–phonon blockade effect.

Finally, we discussed two methods of detecting hybrid-mode correlations. One of them is based on measuring various moments of photons and phonons via balanced homodyne correlation measurements. While the other method is based on converting phonons of the hybrid mode into photons, by using a linear coupler acting as a multi-level SWAP gate, and then applying the standard optical HBT interferometry.

We believe that our study of the interplay between photons and phonons can lead to developing new experimental methods for controlling and testing the quantum states of mechanical systems with atom-cavity-mechanics polaritons. We hope that our work can also stimulate research on quantum engineering with hybrid photon–phonon modes.

Methods

Parameters used in our simulations. Our figures, as indicated in their captions, are plotted for the SMR-driven dissipative system described by the Hamiltonian H' , given in Eq. (8), assuming:

$$A_1 = \{\Delta_a = -3\gamma, \Delta_b = 3\gamma, \Delta_q = -6\gamma, f = 5\gamma, \eta_a = 0.7\gamma, \eta_b = 0, \kappa_a = 1.5\gamma, \kappa_b = 6\gamma\}, \quad (28)$$

and for the QD-driven dissipative system for the Hamiltonian H'' , given in Eq. (9), assuming either

$$A_2 = \{\Delta_a = 5\gamma, \Delta_b = -5\gamma, \Delta_q = 3\gamma, f = 7\gamma, \eta_a = 0, \eta_b = 0.5\gamma, \kappa_a = 7.5\gamma, \kappa_b = 6\gamma\}, \quad (29)$$

or

$$A_3 = \{\Delta_a = 4\gamma, \Delta_b = -4\gamma, \Delta_q = 7\gamma, f = 6.4\gamma, \eta_a = 0, \eta_b = 0.22\gamma, \kappa_a = 3.5\gamma, \kappa_b = 0.002\gamma\}, \quad (30)$$

where $\gamma = 10\pi$ MHz. Minor modifications of these parameters are specified in figure captions.

Higher-order correlation effects. Here we briefly study the k th-order boson-number correlation functions $g_z^{(k)}(0)$, as defined in Eq. (13) for $k = 3, 4$, in comparison to the standard second-order function $g_z^{(2)}(0)$ for the photon ($z = a$), phonon (b), and hybrid photon–phonon (c) modes.

Figure 14 shows our results for $g_z^{(3)}(0)$ (dashed curves) and $g_z^{(4)}(0)$ (dot-dashed curves) in comparison to $g_z^{(2)}(0)$ (solid curves) for $z = a, b, c$ in corresponding panels. Note that the same curves for $g_z^{(2)}(0)$ are also shown in Fig. 10a, but we repeat them for a better comparison with $g_z^{(3,4)}(0)$. It is seen that the eight cases of Table 1 can be divided into a number of subcases depending on $g_z^{(3)}(0)$ and $g_z^{(4)}(0)$. Such a classification is quite complex as includes, in principle, $8^3 = 512$ cases. So, instead of that, we present another much-simplified classification of eight cases only, as shown in Table 3 using the auxiliary function g_{234} defined as:

Case	g_{234}	Mode a	Mode b	Mode c
1	(-, -, -)	✓	✓	✓
2	(-, -, +)	×	✓	✓*
3	(-, +, -)	×	×	×
4	(+, -, -)	✓	✓	✓
5	(-, +, +)	×	✓	✓
6	(+, -, +)	×	×	×
7	(+, +, -)	✓	✓	✓
8	(+, +, +)	✓	✓	✓

Table 3. Different predictions of the n th-order super- and sub-Poissonian statistics with $n = 2, 3, 4$ for the photon ($z = a$), phonon (b), and hybrid photon–phonon (c) modes, where g_{234} is defined in Eq. (31). The cases marked with ✓ can be identified under both (1) nonresonance conditions, as shown in Fig. 14b, and (2) resonance conditions, as shown in Fig. 14a, except the case marked with *.

$$g_{234} = \left[\text{sgn} \log g_z^{(2)}(0), \text{sgn} \log g_z^{(3)}(0), \text{sgn} \log g_z^{(4)}(0) \right]. \quad (31)$$

In particular [−, −, −] means that the second-, third- and fourth-order sub-Poissonian photon number-statistics are observed in a given mode, which are the necessary conditions for observing a ‘true’ single-PB. This case can be easily identified in both panels of Fig. 14. One can also find the case when [+ , + , +], which corresponds to the super-Poissonian statistics of orders $k = 2, 3$, and 4, which might be interpreted, as the induced tunnelling by one, two, and three photons. However, we can also find intermediate four out of six cases, which can be interpreted as non-standard types single-PB and/or single-PIT, and in some cases can be identified as multi-PB^{11,26,29,30,53}. However, a detailed classification of such multi-PB and their interpretation is not at the focus of this paper. The presented results show only the possibility of generating in our system a plethora of various photon–phonon correlation effects, which can be revealed by higher-order correlation functions for the experimentally feasible parameters.

Analytical approach via non-Hermitian Hamiltonian in Eq. (21). Here, we follow the method of Ref.⁴⁵ to derive the coefficients $C_{n,m,k}$ and $C'_{n,m,k}$ for $n, m \in 0, 1, 2$ and $k = e, g$, which appear in Eqs. (22) and (23).

First we recall that the balanced linear coupler (or a balanced beam splitter) transformation, which leads to Eq. (24), if applied to the input Fock states $|n_a, n_b\rangle$ for $n_a + n_b \leq 2$ yields:

$$\begin{aligned} |10\rangle &\rightarrow \frac{1}{\sqrt{2}}(|10\rangle - |01\rangle), & |01\rangle &\rightarrow \frac{1}{\sqrt{2}}(|10\rangle + |01\rangle), & |11\rangle &\rightarrow \frac{1}{\sqrt{2}}(|20\rangle - |02\rangle), \\ |02\rangle &\rightarrow \frac{1}{2}(|20\rangle + \sqrt{2}|11\rangle + |02\rangle), & |20\rangle &\rightarrow \frac{1}{2}(|20\rangle - \sqrt{2}|11\rangle + |02\rangle). \end{aligned} \quad (32)$$

So, for the input state $|\Psi_{abq}(t)\rangle$, given in Eq. (20), the output state of the balanced linear coupler can be represented as follows:

$$\begin{aligned} |\Psi_{cdq}(t)\rangle &= C_{00g}|00g\rangle + e^{-i\omega_d t} \left(C_{00e}|00e\rangle + C'_{10g}|10g\rangle + C'_{01g}|01g\rangle \right) \\ &+ e^{-2i\omega_d t} \left(C'_{10e}|10e\rangle + C'_{01e}|01e\rangle + C'_{11g}|11g\rangle + C'_{20g}|20g\rangle + C'_{02g}|02g\rangle \right), \end{aligned} \quad (33)$$

where the superposition coefficients are:

$$\begin{aligned} C'_{10g} &= \frac{1}{\sqrt{2}}(C_{10g} + C_{01g}), \\ C'_{01g} &= \frac{1}{\sqrt{2}}(C_{10g} - C_{01g}), \\ C'_{10e} &= \frac{1}{\sqrt{2}}(C_{10e} + C_{01e}), \\ C'_{01e} &= \frac{1}{\sqrt{2}}(C_{10e} - C_{01e}), \\ C'_{11g} &= \frac{1}{\sqrt{2}}(C_{20g} - C_{02g}), \\ C'_{20g} &= \frac{1}{2}(C_{20g} + \sqrt{2}C_{11g} + C_{02g}), \\ C'_{02g} &= \frac{1}{2}(C_{20g} - \sqrt{2}C_{11g} + C_{02g}). \end{aligned} \quad (34)$$

We can calculate the coefficients $C_{n_a, n_b, g/e}$ iteratively⁴⁵. For a single excitation and assuming the resonance case $\Delta_{\text{SMR}} = \Delta_m = \Delta_q = \Delta$ and $\kappa_a = \kappa_b = \kappa$, the steady-state superposition coefficients can be calculated from:

$$\begin{aligned} 0 &= \left(\Delta - \frac{i\kappa}{2} \right) C_{01g} + fC_{10g} + \eta C_{00g}, \\ 0 &= \left(\Delta - \frac{i\kappa}{2} \right) C_{10g} + fC_{01g} + gC_{00e}, \\ 0 &= \left(\Delta - \frac{i\gamma}{2} \right) C_{00e} + gC_{10g}, \end{aligned} \quad (35)$$

where $\eta = \eta_b$, $\Delta = \omega_i - \omega_p$ and $\omega_{\text{SMR}} = \omega_m = \omega_q = \omega$. Moreover, we assume the weak-driving regime. So, in the first iteration, the contributions from the states with more than a single excitation, such as C_{01e} , C_{11g} , ..., are negligible. From Eq. (35), by comparing the coefficients with a single excitation, we can see that C_{10g} and C_{00e} are much larger than C_{01g} , because of a weak-pump amplitude η , and they can be written as

$$\begin{aligned} C_{10g} &= \frac{f(24\Delta - 2i\kappa)C_{01g}}{(24g^2 - 24\Delta^2 + 14i\kappa\Delta + \kappa^2)}, \\ C_{00e} &= -\frac{24fgC_{01g}}{(24g^2 - 24\Delta^2 + 14i\kappa\Delta + \kappa^2)}. \end{aligned} \quad (36)$$

In the second iteration, to include states with two excitations in total, the steady-state coefficients can be calculated from:

$$\begin{aligned} 0 &= 2\Delta_\kappa C_{11g} + \sqrt{2}fC_{20g} + \sqrt{2}fC_{02g} + gC_{01e} + \eta C_{10g}, \\ 0 &= \Delta_\kappa C_{10e} + \Delta_\gamma C_{10e} + fC_{01e} + \sqrt{2}gC_{20g}, \\ 0 &= \Delta_\kappa C_{01e} + \Delta_\gamma C_{01e} + fC_{10e} + gC_{11g} + \eta C_{00e}, \\ 0 &= 2\Delta_\kappa C_{20g} + \sqrt{2}fC_{11g} + \sqrt{2}gC_{10e}, \\ 0 &= 2\Delta_\kappa C_{02g} + \sqrt{2}fC_{11g} + \sqrt{2}\eta C_{01g}, \end{aligned} \quad (37)$$

where $\Delta_\kappa = \Delta - i\kappa/2$ and $\Delta_\gamma = \Delta - i\gamma/2$. As can be seen from Eq. (37), we have

$$C_{02g} = -(\sqrt{2}fC_{11g} + \sqrt{2}\eta C_{01g})/(2\Delta_\kappa). \quad (38)$$

So, to minimise C_{02g} , the minimalization of C_{11g} and C_{01g} is also required. Destructive interference between the direct and indirect excitation paths in the energy ladders of the total system can enable us minimising C_{02g} . This explains the occurrence of the dip in $g_b^{(2)}(0)$ in the mode b , as a signature of PB. As clearly seen in Fig. 12a, the optimal PB in this mode occurs at $\Delta_{\text{SMR}}/g = \pm 1.2$. The above equations lead us to analytical optimal conditions for the system parameters to maximise the sub-Poissonian character of the QD mode and, thus, to optimise the parameters for observing PB in the mode b . Given Eq. (39) for a single excitation and Eq. (41) for two excitations, which are calculated from Eq. (37), we show that the second-order correlation function calculated by this method and the master equation method both give very similar predictions, as shown in Fig. 12, where the thick curves are calculated based on the non-Hermitian Hamiltonian approach and the thin curves correspond to the master-equation approach for the modes a , b , and c .

Thus we find

$$\begin{aligned} C_{01g} &= (\Delta_\kappa \Delta_\gamma - g^2)\eta X_5^{-1}, \\ C_{10g} &= -\Delta_\gamma f \eta X_5^{-1}, \end{aligned} \quad (39)$$

which yields

$$C'_{10g} = \frac{(\Delta_\kappa \Delta_\gamma - \Delta_\gamma f - g^2)\eta}{\sqrt{2}X_5}, \quad (40)$$

Analogously, we find

$$\begin{aligned} C_{02g} &= \frac{\eta^2[-2\Delta_\kappa^3 \Delta_\gamma X_1 + \Delta_\kappa^2 X_2 g^2 - X_6 g^4 + g^6]}{\sqrt{2}X_5(X_3 - X_4)}, \\ C_{20g} &= -\frac{\eta^2 f^2 [2\Delta_\kappa \Delta_\gamma X_1 + (2\Delta_\kappa - \Delta_\gamma)\Delta_\kappa \gamma g^2 - g^4]}{\sqrt{2}X_5(X_3 - X_4)}, \\ C_{11g} &= \frac{\eta^2 f (2\Delta_\kappa^2 \Delta_\gamma X_1 + X_7 g^2 + \Delta_\gamma g^4)}{X_5(X_3 - X_4)}, \end{aligned} \quad (41)$$

where $\Delta_\kappa \gamma = \Delta_\kappa + \Delta_\gamma$ and the auxiliary functions X_n read: $X_1 = \Delta_\kappa^2 \gamma - f^2$, $X_2 = \Delta_\kappa \gamma (2\Delta_\kappa + 5\Delta_\gamma) - 4f^2$, $X_3 = 2\Delta_\kappa (\Delta_\kappa^2 - f^2) X_1$, $X_4 = [3\Delta_\kappa^2 \Delta_\kappa \gamma + (\Delta_\kappa - \Delta_\gamma) f^2] g^2 - \Delta_\kappa g^4$, $X_5 = \Delta_\kappa^2 \Delta_\gamma - \Delta_\gamma f^2 - \Delta_\kappa g^2$,

$X_6 = 3\Delta_\kappa^2 + 4\Delta_\kappa\Delta_\gamma + f^2$, and $X_7 = \Delta_\kappa(2f^2 - 3\Delta_\gamma\Delta_\kappa\gamma)$. These formulas, together with C'_{20g} in Eq. (34), enable us to calculate analytically the correlation functions in Eqs. (22) and (23).

Data availability

All the data necessary to reproduce the results are included in this published article.

Received: 20 July 2022; Accepted: 26 September 2022

Published online: 21 October 2022

References

1. Imamoglu, A., Schmidt, H., Woods, G. & Deutsch, M. Strongly interacting photons in a nonlinear cavity. *Phys. Rev. Lett.* **79**, 1467–1470 (1997).
2. Miranowicz, A., Leoński, W. & Imoto, N. Quantum-optical states in finite-dimensional Hilbert space. I. General formalism. *Adv. Chem. Phys.* **119**(1), 155–193 (2001).
3. Leoński, W. & Miranowicz, A. Quantum-optical states in finite-dimensional Hilbert space. II. State generation. *Adv. Chem. Phys.* **119**(1), 195–213 (2001).
4. Leoński, W. & Kowalewska-Kudłaszyk, A. Quantum scissors: Finite-dimensional states engineering. *Prog. Opt.* **56**, 131–185 (2011).
5. Birnbaum, K. M. *et al.* Photon blockade in an optical cavity with one trapped atom. *Nature (London)* **436**, 87–90 (2005).
6. Faraon, A. *et al.* Coherent generation of non-classical light on a chip via photon-induced tunnelling and blockade. *Nat. Phys.* **4**, 859–863 (2008).
7. Lang, C. *et al.* Observation of resonant photon blockade at microwave frequencies using correlation function measurements. *Phys. Rev. Lett.* **106**, 243601 (2011).
8. Hoffman, A. J. *et al.* Dispersive photon blockade in a superconducting circuit. *Phys. Rev. Lett.* **107**, 053602 (2011).
9. Reinhard, A. *et al.* Strongly correlated photons on a chip. *Nat. Photon.* **6**, 93 (2011).
10. Müller, K. *et al.* Coherent generation of nonclassical light on chip via detuned photon blockade. *Phys. Rev. Lett.* **114**, 233601 (2015).
11. Hamsen, C., Tolazzi, K. N., Wilk, T. & Rempe, G. Two-photon blockade in an atom-driven cavity QED system. *Phys. Rev. Lett.* **118**, 133604 (2017).
12. Snijders, H. *et al.* Observation of the unconventional photon blockade. *Phys. Rev. Lett.* **121**, 043601 (2018).
13. Vaneph, C. *et al.* Observation of the unconventional photon blockade in the microwave domain. *Phys. Rev. Lett.* **121**, 043602 (2018).
14. Majumdar, A., Bajcsy, M. & Vučković, J. Probing the ladder of dressed states and nonclassical light generation in quantum-dot-cavity QED. *Phys. Rev. A* **85**, 041801 (2012).
15. Peyronel, T. *et al.* Quantum nonlinear optics with single photons enabled by strongly interacting atoms. *Nature (London)* **488**, 57–60 (2012).
16. Dayan, B. *et al.* A photon turnstile dynamically regulated by one atom. *Science* **319**, 1062–1065 (2008).
17. Tian, L. & Carmichael, H. J. Quantum trajectory simulations of two-state behavior in an optical cavity containing one atom. *Phys. Rev. A* **46**, R6801 (1992).
18. Leoński, W. & Tanaš, R. Possibility of producing the one-photon state in a kicked cavity with a nonlinear Kerr medium. *Phys. Rev. A* **49**, R20–R23 (1994).
19. Miranowicz, A., Leoński, W., Dyrting, S. & Tanaš, R. Quantum state engineering in finite-dimensional Hilbert space. *Acta Phys. Slov.* **46**, 451 (1996).
20. Paul, H. Photon antibunching. *Rev. Mod. Phys.* **54**, 1061–1102 (1982).
21. Teich, M. C. & Saleh, B. E. A. Photon bunching and antibunching. *Prog. Opt.* **26**, 1–104 (1988).
22. Kozierowski, M. Photon antibunching in nonlinear optical phenomena. *Kvantovaya Elektron.* **6**, 695 (1980).
23. Michler, P. A quantum dot single-photon turnstile device. *Science* **290**, 2282–2285 (2000).
24. Wang, X., Miranowicz, A., Li, H.-R. & Nori, F. Multiple-output microwave single-photon source using superconducting circuits with longitudinal and transverse couplings. *Phys. Rev. A* **94**, 053858 (2016).
25. Shamilov, S., Parkins, A., Collett, M. & Carmichael, H. Multi-photon blockade and dressing of the dressed states. *Opt. Commun.* **283**, 766–772 (2010).
26. Miranowicz, A., Paprzycka, M., Liu, Y.-X., Bajer, J. & Nori, F. Two-photon and three-photon blockades in driven nonlinear systems. *Phys. Rev. A* **87**, 023809 (2013).
27. Chakram, S. *et al.* Multimode photon blockade. arXiv preprint (2020). [arXiv:2010.15292](https://arxiv.org/abs/2010.15292).
28. Liew, T. C. H. & Savona, V. Single photons from coupled quantum modes. *Phys. Rev. Lett.* **104**, 183601 (2010).
29. Huang, R., Miranowicz, A., Liao, J.-Q., Nori, F. & Jing, H. Nonreciprocal photon blockade. *Phys. Rev. Lett.* **121**, 153601 (2018).
30. Li, B., Huang, R., Xu, X., Miranowicz, A. & Jing, H. Nonreciprocal unconventional photon blockade in a spinning optomechanical system. *Photon. Res.* **7**, 630 (2019).
31. Yang, P. *et al.* Realization of Nonlinear Optical Nonreciprocity on a Few-Photon Level Based on Atoms Strongly Coupled to an Asymmetric Cavity. *Phys. Rev. Lett.* **123**, 233604 (2019).
32. Miranowicz, A. *et al.* State-dependent photon blockade via quantum-reservoir engineering. *Phys. Rev. A* **90**, 033831 (2014).
33. Huang, R. *et al.* Exceptional photon blockade: Engineering photon blockade with chiral exceptional points. *Laser Photonics Rev.* **16**, 2100430 (2022).
34. Pegg, D. T., Phillips, L. S. & Barnett, S. M. Optical State Truncation by Projection Synthesis. *Phys. Rev. Lett.* **81**, 1604–1606 (1998).
35. Özdemir, S. K., Miranowicz, A., Koashi, M. & Imoto, N. Quantum-scissors device for optical state truncation: A proposal for practical realization. *Phys. Rev. A* **64**, 063818 (2001).
36. Özdemir, S. K., Miranowicz, A., Koashi, M. & Imoto, N. Pulse-mode quantum projection synthesis: Effects of mode mismatch on optical state truncation and preparation. *Phys. Rev. A* **66**, 053809 (2002).
37. Babichev, S. A., Ries, J. & Lvovsky, A. I. Quantum scissors: Teleportation of single-mode optical states by means of a nonlocal single photon. *EPL (Europhys. Lett.)* **64**, 1–7 (2003).
38. Koniorczyk, M., Kurucz, Z., Gábris, A. & Janszky, J. General optical state truncation and its teleportation. *Phys. Rev. A* **62**, 013802 (2000).
39. Miranowicz, A. Optical-state truncation and teleportation of qudits by conditional eight-port interferometry. *J. Opt. B: Quant. Semicl. Opt.* **7**, 142 (2005).
40. Miranowicz, A., Paprzycka, M., Pathak, A. & Nori, F. Phase-space interference of states optically truncated by quantum scissors. *Phys. Rev. A* **89**, 033812 (2014).
41. Reck, M., Zeilinger, A., Bernstein, H. J. & Bertani, P. Experimental realization of any discrete unitary operator. *Phys. Rev. Lett.* **73**, 58–61 (1994).
42. Miranowicz, A., Özdemir, S. K., Bajer, J., Koashi, M. & Imoto, N. Selective truncations of an optical state using projection synthesis. *J. Opt. Soc. Am. B* **24**, 379–383 (2007).

43. Leoński, W. & Miranowicz, A. Kerr nonlinear coupler and entanglement. *J. Opt. B* **6**, S37–S42 (2004).
44. Miranowicz, A. & Leoński, W. Two-mode optical state truncation and generation of maximally entangled states in pumped nonlinear couplers. *J. Phys. B* **39**, 1683–1700 (2006).
45. Bamba, M., Imamoğlu, A., Carusotto, I. & Ciuti, C. Origin of strong photon antibunching in weakly nonlinear photonic molecules. *Phys. Rev. A* **83**, 021802 (2011).
46. Flayac, H. & Savona, V. Unconventional photon blockade. *Phys. Rev. A* **96**, 053810 (2017).
47. Liu, Y.-X. *et al.* Qubit-induced phonon blockade as a signature of quantum behavior in nanomechanical resonators. *Phys. Rev. A* **82**, 032101 (2010).
48. Didier, N., Pugnetti, S., Blanter, Y. M. & Fazio, R. Detecting phonon blockade with photons. *Phys. Rev. B* **84**, 054503 (2011).
49. Wang, X., Miranowicz, A., Li, H.-R. & Nori, F. Method for observing robust and tunable phonon blockade in a nanomechanical resonator coupled to a charge qubit. *Phys. Rev. A* **93**, 063861 (2016).
50. Miranowicz, A., Bajer, J., Lambert, N., Liu, Y.-X. & Nori, F. Tunable multiphonon blockade in coupled nanomechanical resonators. *Phys. Rev. A* **93**, 013808 (2016).
51. Shi, H.-Q., Zhou, X.-T., Xu, X.-W. & Liu, N.-H. Tunable phonon blockade in quadratically coupled optomechanical systems. *Sci. Rep.* **8**, 2212 (2018).
52. Liu, Y. X., Xu, X. W., Miranowicz, A. & Nori, F. From blockade to transparency: Controllable photon transmission through a circuit-QED system. *Phys. Rev. A* **89**, 043818 (2014).
53. Kowalewska-Kudłaszyk, A. *et al.* Two-photon blockade and photon-induced tunneling generated by squeezing. *Phys. Rev. A* **100**, 053857 (2019).
54. Aspelmeyer, M., Kippenberg, T. J. & Marquardt, F. Cavity optomechanics. *Rev. Mod. Phys.* **86**, 1391 (2014).
55. Xu, X.-W., Shi, H.-Q., Liao, J.-Q. & Chen, A.-X. Generation of single entangled photon-phonon pairs via an atom-photon-phonon interaction. *Phys. Rev. A* **100**, 053802 (2019).
56. Xu, X.-W., Shi, H.-Q., Chen, A.-X. & Liu, X.Y. Cross-correlation between photons and phonons in quadratically coupled optomechanical systems. *Phys. Rev. A* **98**, 013821 (2018).
57. Zhai, C., Huang, R., Jing, H. & Kuang, L.-M. Mechanical switch of photon blockade and photon-induced tunneling. *Opt. Express* **27**, 27649 (2019).
58. Santori, C., Pelton, M., Solomon, G., Dale, Y. & Yamamoto, Y. Triggered single photons from a quantum dot. *Phys. Rev. Lett.* **86**, 1502 (2001).
59. Ding, X. *et al.* On-demand single photons with high extraction efficiency and near-unity indistinguishability from a resonantly driven quantum dot in a micropillar. *Phys. Rev. Lett.* **116**, 020401 (2016).
60. Grangier, P., Walls, D. F. & Gheri, K. M. Comment on strongly interacting photons in a nonlinear cavity. *Phys. Rev. Lett.* **81**, 2833 (1998).
61. Kimble, H. J. Strong interactions of single atoms and photons in cavity QED. *Phys. Scripta* **T76**, 127 (1998).
62. Gu, X., Kockum, A. F., Miranowicz, A., Liu, Y.-X. & Nori, F. Microwave photonics with superconducting quantum circuits. *Phys. Rep.* **718–719**, 1–102 (2017).
63. Tian, L. Ground state cooling of a nanomechanical resonator via parametric linear coupling. *Phys. Rev. B* **79**, 193407 (2009).
64. Kockum, A. F., Miranowicz, A., Liberato, S. D., Savasta, S. & Nori, F. Ultrastrong coupling between light and matter. *Nat. Rev. Phys.* **1**, 19–40 (2019).
65. Restrepo, J., Ciuti, C. & Favero, I. Single-polariton optomechanics. *Phys. Rev. Lett.* **112**, 013601 (2014).
66. Larson, J. & Mavrogordatos, T. *The Jaynes–Cummings Model and Its Descendants* (IOP Publishing, 2021).
67. Ridolfo, A., Leib, M., Savasta, S. & Hartmann, M. J. Photon blockade in the ultrastrong coupling regime. *Phys. Rev. Lett.* **109**, 193602 (2012).
68. Garziano, L. *et al.* Multiphoton quantum rabi oscillations in ultrastrong cavity QED. *Phys. Rev. A* **92**, 063830 (2015).
69. Mercurio, A., Abo, S., Mauceri, F., Russo, E., Macri, V., Miranowicz, A., Savasta, S. & Di Stefano, O. Pure dephasing of light-matter systems in the ultrastrong and deep-strong coupling regimes (2022). [arXiv:2205.05352](https://arxiv.org/abs/2205.05352).
70. Sánchez Muñoz, C., Frisk Kockum, A., Miranowicz, A. & Nori, F. Simulating ultrastrong-coupling processes breaking parity conservation in Jaynes-Cummings systems. *Phys. Rev. A* **102**, 033716 (2020).
71. Kuhn, A. *Cavity Induced Interfacing of Atoms and Light* (Springer, 2015).
72. Mandel, L. & Wolf, E. *Optical Coherence and Quantum Optics* (Cambridge University Press, 1995).
73. Kimble, H. J., Dagenais, M. & Mandel, L. Photon antibunching in resonance fluorescence. *Phys. Rev. Lett.* **39**, 691 (1977).
74. Verhagen, E., Deléglise, S., Weis, S., Schliesser, A. & Kippenberg, T. J. Quantum-coherent coupling of a mechanical oscillator to an optical cavity mode. *Nature (London)* **482**, 63–67 (2012).
75. Walls, D. F. & Milburn, G. J. *Quantum Optics* (Springer, 1994).
76. Kubanek, A. *et al.* Two-photon gateway in one-atom cavity quantum electrodynamics. *Phys. Rev. Lett.* **101**, 203602 (2008).
77. Minganti, F., Miranowicz, A., Chhajlany, R. W. & Nori, F. Quantum exceptional points of non-Hermitian Hamiltonians and Liouvillians: The effects of quantum jumps. *Phys. Rev. A* **100**, 062131 (2019).
78. Minganti, F., Miranowicz, A., Chhajlany, R. W., Arkhipov, I. I. & Nori, F. Hybrid-Liouvillian formalism connecting exceptional points of non-Hermitian Hamiltonians and Liouvillians via postselection of quantum trajectories. *Phys. Rev. A* **101**, 062112 (2020).
79. Zou, X. T. & Mandel, L. Photon-antibunching and sub-Poissonian photon statistics. *Phys. Rev. A* **41**, 475 (1990).
80. Miranowicz, A., Bartkowiak, M., Wang, X., Liu, Y.-X. & Nori, F. Testing nonclassicality in multimode fields: A unified derivation of classical inequalities. *Phys. Rev. A* **82**, 013824 (2010).
81. Hong, S. *et al.* Hanbury Brown and Twiss interferometry of single phonons from an optomechanical resonator. *Science* **358**, 203–206 (2017).
82. Shchukin, E. V. & Vogel, W. Nonclassical moments and their measurement. *Phys. Rev. A* **72**, 043808 (2005).
83. Shchukin, E. & Vogel, W. Universal measurement of quantum correlations of radiation. *Phys. Rev. Lett.* **96**, 200403 (2006).

Acknowledgements

This work was supported by the Polish National Science Centre (NCN) under the Maestro Grant No. DEC-2019/34/A/ST2/00081. J.P. acknowledges the support from MŚMT ČR projects No. CZ.02.2.69/0.0/0.0/18_05_3/0016919.

Author contributions

A.M. conceived the original idea and supervised the work. S.A. performed numerical and analytical calculations, which were double checked by G.C. and A.K.-K. S.A. and A.M. wrote the paper with input from all the authors. All the authors were involved in the revision and discussion of the manuscript.

Competing interests

The authors declare no competing interests.

www.nature.com/scientificreports/

Additional information

Correspondence and requests for materials should be addressed to A.M.

Reprints and permissions information is available at www.nature.com/reprints.

Publisher's note Springer Nature remains neutral with regard to jurisdictional claims in published maps and institutional affiliations.



Open Access This article is licensed under a Creative Commons Attribution 4.0 International License, which permits use, sharing, adaptation, distribution and reproduction in any medium or format, as long as you give appropriate credit to the original author(s) and the source, provide a link to the Creative Commons licence, and indicate if changes were made. The images or other third party material in this article are included in the article's Creative Commons licence, unless indicated otherwise in a credit line to the material. If material is not included in the article's Creative Commons licence and your intended use is not permitted by statutory regulation or exceeds the permitted use, you will need to obtain permission directly from the copyright holder. To view a copy of this licence, visit <http://creativecommons.org/licenses/by/4.0/>.

© The Author(s) 2022

Chapter 3

Two-photon blockade via squeezing

3.1 Chapter outline

This chapter provides an overview of article [P3]. In contrast to results presented in Chapter 2, where photon-number-correlation phenomena emerged due to system nonlinearities, we discuss in article [P3] instead how coupling of a linear system (a harmonic cavity) to a nonlinear (in this case, squeezed) bath can result in various photon correlation effects. In particular, we show that various kinds of single-photon blockade (PB), as well as two-PB, and photon-induced tunneling (PIT) can be observed under appropriate conditions in such a setup.

3.1.1 Popular introduction to multi photon blockade (multi-PB)

PB is a quantum phenomenon that, as also described in previous chapter, conventionally requires strong light-matter interactions at the single-particle level, where a single photon can block the transmission of subsequent photons through a cavity, as first predicted in Refs. [29,31,32].¹ In contrast PIT refers to the quantum phenomena in which the presence of the first photon in a driven cavity enhances the probability of generating subsequent photons, as first described under this term in Ref. [38]. The measurement of the zero-delay-time second-order correlation function, $g^{(2)}(0)$, and the delay-time second-order correlation function, $g^{(2)}(\tau)$, provides the information required to verify the criterion for one-PB. The antibunching of photons, as tested by $g^{(2)}(0) < g^{(2)}(\tau)$, in a sub-Poissonian light beam, as characterized $g^{(2)}(0) < 1$, is a critical feature of PB, which occurs in strongly nonlinear systems and significantly

¹These and other references in this chapter correspond to those cited in [P3].

reduces the probability of detecting two photons simultaneously. However, achieving such strong nonlinearity is difficult. As demonstrated in previous works, the desired nonlinearity can be achieved by coupling a qubit to the cavity, to form the Jaynes-Cummings (JC) system, or by incorporating a Kerr nonlinear material into the system. Note that a Kerr-type Hamiltonian can be obtained from the JC model in the dispersive limit, i.e., when the atom-light detuning is much larger than the coupling and decay rates.

In article [P3], we mainly focused on observing two-PB in addition to different types of nonstandard PB which we introduced in detail with their criteria. Two-PB occurs when the presence of two photons with the same frequency in the system suppresses the probability of observing more photons, as first predicted in Refs. [52,53]. In other words, the generation of single- and two-photon Fock states inhibits the generation of higher photon numbers. The first experimental demonstration of two-PB, using an optical cavity where a single atom was strongly coupled to a cavity, was performed in 2017 by the group of Prof. Gerhard Rempe at the Max Planck Institute in Garching and reported in Ref. [11]. This particular configuration revealed that driving the atom results in significantly greater optical nonlinearity compared to driving the cavity alone. This increased nonlinearity enhances the occurrence of a single-PB and enables a successful observation of the two-PB effect. To observe PB, one needs a system with strong nonlinear interactions that overcome its dissipation rates. This is hard to achieve. Most PB studies assumed that a nonlinear system (i.e., a nonlinear cavity) interacts with a thermal bath, so the PB system loses energy linearly to a harmonic reservoir. Only a very few studies looked at PB in systems with quantum nonlinear reservoirs such as those studied in Refs. [74,75]. Indeed PB can be induced by a system nonlinearity, a reservoir nonlinearity, or both. The mentioned study by the Ash Clerk group [75] demonstrated that the one-PB criteria could be fulfilled by optimized amplitude-squeezed Gaussian states, which can be realized by effectively coupling the cavity to a squeezed reservoir. So, quantum reservoir engineering can be used to produce a high-quality intracavity squeezing. This is when a cavity interacts with an engineered reservoir through dissipative squeezing interactions.

3.1.2 Motivation

The above-mentioned recent observation of two-photon blockade (2PB) by Hamsen et al. [11] in a strongly driven non-linear system motivated our study presented in article [P3]. Successfully demonstrating conventional PB phenomena experimen-

tally generally entails meeting stringent requirements on strength of nonlinearities (including the atom-photon coupling or the photon-photon Kerr-type interaction). In article [P3], we studied an alternative approach, where the driven system itself has no nonlinearities of any kind. Instead we considered whether a linear system coupled to an engineered nonlinear (squeezed) reservoir can specifically induce multi-photon correlation effects. This, in particular, allows also the consideration of PB beyond the conventional (based on strong nonlinear interactions) and unconventional (based on multi-path interference) scenarios that have been previously summarized in Chapter 2.

Most previous studies of single PB phenomena (both conventional and unconventional) focused on the setting of nonlinear systems coupled to harmonic (linear, i.e., thermal) baths. To our knowledge only a few works have dealt with engineered reservoirs in the context of blockade phenomena [74,75]. In particular, single and multi-PB was studied in systems with Kerr nonlinear interactions coupled to a squeezed bath [74], and single-PB was studied in a linear system coupled to a squeezed bath [75]. Thus, it was a pertinent question to address whether a squeezed bath itself can generate multiphoton correlation effects in a linear system. In considering this problem, we also characterized in detail various kinds of single-PB effects that can occur using the studied reservoir engineering.

3.1.3 Main results

We showed in [P3] the possibility of observing two-PB, three-PT, and different kinds of nonstandard one-PB in linear system that is dissipatively coupled to the nonlinear reservoir. In this study, we investigated a system configuration consisting of a linear optical cavity with resonance frequency ω_c that is externally stimulated by a laser field of amplitude ϵ and frequency ω_d . First, we wrote the effective Hamiltonian of our system in a rotating frame. To study the time evolution of our system interacting with the squeezed reservoir, we applied a squeezed-reservoir master equation (see, e.g., [82]). This equation incorporates additional terms that account for the two-photon loss mechanism, in addition to one-photon dissipation described by the standard master equation. In this way, the steady-state solution was obtained by solving this generalized master equation.

Based on higher-order correlation functions, one can introduce criteria for two-PB [44]. In article [P3] we applied two types of criteria (i.e., *simplified* and *refined*) to investigate the possibility of n -PB and n -PIT in our proposed system. The simplified criteria are obtained from refined criteria under the assumption that the mean

photon number is very small as $\langle \hat{n} \rangle \ll 1$. We calculated the delay-time second-order correlation function, $g^{(2)}(\tau)$, for the steady-state solution of the master equation in addition to the zero-delay-time n -order correlation functions, $g^{(n)}(0)$ for $n = 2, 3, 4$, to check the possibility of true PB and other different kinds of nonstandard PB.

In this work, we have shown that the squeezing of the field in the reservoir leads to the generation of one-PB in the linear-cavity field, resulting in the sub-Poissonian photon-number statistics, described by $g^{(2)}(0) < 1$. On the other hand, the interaction of the linear system with the thermal field of the environment leads to the super-Poissonian photon-number statistics, with $g^{(2)}(0) > 1$, known as PIT. The lower values of $g^{(2)}(0)$ can be achieved by detuning $\Delta = 0$ between the cavity and driving frequencies and using weaker driving strength. In addition, by taking into account $g^{(2)}(\tau)$, we showed the possibility to find nonstandard PB indicated by the conditions: $g^{(2)}(0) < 1$ and $g^{(2)}(0) > g^{(2)}(\tau)$, which is in contrast to the standard PB effect defined by: $g^{(2)}(0) < 1$ and $g^{(2)}(0) < g^{(2)}(\tau)$. Our numerical calculations showed that two-PB in the harmonic cavity coupled to the squeezed reservoir is only possible if we consider the refined criteria for this case and it is not possible to observe two-PB according to simplified criteria. I should note that for two-PB we need to measure $g^{(3)}(0)$ in addition to $g^{(2)}(0)$. These outcomes emphasize the significance of the two-photon dissipation process in a linear optical system for the generation of the one- and two-PB, as well as the other three nonstandard types of one-PB observed for our system. Instead of analyzing the cavity that is coupled to the squeezed reservoir, we also showed that by preparing the cavity field in a squeezed coherent state (SCS) and a displaced squeezed thermal state (DSTS), it is possible to obtain analogous results, as described above.

We analytically calculated $g^{(n)}(0)$ for $n = 2, 3, 4$ and found the parameters in which the criteria for specific multi-PB effects are fulfilled. We explicitly explained the relationship between the squeezed-state simulations of these effects and their generation via the squeezed reservoir.

The results of our simulation are clearly demonstrated through our plots showing the regions of the displacement (α) and squeezing (r) parameters for SCSs and DSTSs in which different single- and two-PB effects might be observed. Moreover, our findings for both SCSs and DSTSs confirmed that it is possible to observe two-PB only according to refined criteria within a specific range of parameters as in our proposed model. Additionally, the findings highlight the detrimental influence of thermal photons in the observation of two-PB.

We also addressed the question of the nonclassicality of the studied effects and states. We show that all our numerical predictions for different single- and multiphoton types of PB are nonclassical effects. For this we used two measures of nonclassicality: an entanglement potential (EP) and a squeezing variance (SV). We also identified parameter regimes, which enable the observation of PIT and other photon-number correlation effects predicted in our studies.

Our findings highlight that the presence of a squeezed reservoir can lead to different forms of PB and PIT, including the emergence of two-photon effects in a driven harmonic resonator.

3.1.4 My contribution and importance of the work

In this article, we have proposed a new method of quantum reservoir engineering that can create novel effects in linear systems coupled to nonlinear reservoirs, such as multi-PB and PIT. It highlighted the potential applications and implications of our method for the fields of optical and microwave photonics, and we hoped to encourage further research in this direction.







Anna Kowalewska-Kudłaszyk and I have performed all the numerical and analytical calculations, as well as we wrote the paper with input from all the authors. Moreover, I have made significant contributions to the interpretation of the obtained results, as confirmed by the signed declaration of the all co-authors.

3.2 Reprint of article [P3]

On the subsequent pages, we append a reprint with permission from the American Physical Society:

[P3] Anna Kowalewska-Kudłaszyk, Shilan I. Abo, Grzegorz Chimczak, Jan Peřina Jr., Franco Nori, and Adam Miranowicz, *Two-photon blockade and photon-induced tunneling generated by squeezing*, Phys. Rev. A **100**, 053857 (2019).
<http://dx.doi.org/10.1103/PhysRevA.100.053857>
Copyright (2019) by the American Physical Society.

Two-photon blockade and photon-induced tunneling generated by squeezing

Anna Kowalewska-Kudłaszuk ¹, Shilan Ismael Abo ^{1,2}, Grzegorz Chimczak ¹, Jan Peřina Jr. ³,
Franco Nori ^{4,5} and Adam Miranowicz ^{1,4}

¹*Faculty of Physics, Adam Mickiewicz University, 61-614 Poznań, Poland*

²*Department of Physics, University of Duhok, 1006 AJ Duhok, Kurdistan Region, Iraq*

³*Joint Laboratory of Optics, Faculty of Science, Palacký University, 17. listopadu 12, 771 46 Olomouc, Czech Republic*

⁴*RIKEN Center for Emergent Matter Science, Wako, Saitama 351-0198, Japan*

⁵*Department of Physics, University of Michigan, Ann Arbor, Michigan 48109-1040, USA*



(Received 22 August 2019; published 27 November 2019)

Inspired by the recent experiment of Hamsen *et al.* [*Phys. Rev. Lett.* **118**, 133604 (2017)], which demonstrated two-photon blockade in a driven nonlinear system (composed of a harmonic cavity with a driven atom), we show that two-photon blockade and other nonstandard types of photon blockade and photon-induced tunneling can be generated in a driven harmonic cavity without an atom or any other kind of nonlinearity, but instead coupled to a nonlinear (i.e., squeezed) reservoir. We also simulate these single- and two-photon effects with squeezed coherent states and displaced squeezed thermal states.

DOI: [10.1103/PhysRevA.100.053857](https://doi.org/10.1103/PhysRevA.100.053857)

I. INTRODUCTION**A. Squeezed states of light**

Squeezed states of light [1], which have less quantum noise in one quadrature than a coherent state, are a powerful resource for quantum technologies. These include quantum communication, improving the precision of optical measurements, and fundamental spectroscopic tests of general relativity and quantum mechanics [2–6]. Although squeezed states were already studied in 1927 by Kennard [7] and the squeezing operator was introduced in 1955 [8,9], these states had not been attracting much attention for 50 years. A real practical interest in squeezed states has been triggered only 40 years ago by finding their first applications for detecting gravitational waves via supersensitive interferometry [10–13]. Since the pioneering experimental generation of squeezed states via four-wave mixing in 1985 by Slusher *et al.* [14], shortly followed by two other experiments [15,16], various methods of squeezed-light generation have been implemented experimentally not only for optical fields [6], but also for microwave fields using superconducting quantum circuits [17]. The first long-term practical applications of squeezed-vacuum states were demonstrated in 2013 for increasing the astrophysical limits of gravitational-wave detectors including the laser interferometer gravitational-wave observatory (LIGO) [18] and the gravitational-wave observatory (GEO 600) detectors [19]. Among many applications of squeezing, we mention also recent proposals of an exponential enhancement of light-matter interactions via squeezing [20–25] (for a review see Ref. [26]). Such increased interactions at the single-photon level can fundamentally change nonlinear optical effects, including photon blockade (PB) [27,28]. (This and other abbreviations used in this paper are also defined in Table I.) Here we study multiphoton correlations in squeezed coherent states (SCS), displaced squeezed thermal states (DSTS), and light generated

by a driven harmonic cavity coupled to a squeezed reservoir for generating (or simulating) various kinds of PB.

B. Single-photon blockade

The phenomenon of Coulomb's blockade has its optical analog, known as PB [29] (also referred to as nonlinear quantum scissors [30]). PB (or more precisely single-photon blockade, 1PB) refers to the effect in which a single photon generated in a driven nonlinear system (as those schematically shown in Fig. 1) can block the generation of more photons in the system. This effect was first predicted by Tian and Carmichael [31], Leoński and Tanaś [32], and later by Imamoğlu *et al.* [29], who coined the term *photon blockade* and studied the effect in the steady-state limit. Indeed, Ref. [31] predicted PB by demonstrating a two-state behavior in a driven optical cavity containing one atom, as shown in Fig. 1(b) and discussed in Appendix A, applying the quantum trajectory method to the Jaynes-Cummings model, while Ref. [32] predicted the PB effect in a driven Kerr nonlinear cavity and showed its application for the generation of the single-photon Fock state. Note that the Jaynes-Cummings model in the dispersive limit (i.e., far off resonance) becomes equivalent to the Kerr Hamiltonian, which shows the correspondence of the PB predictions of Refs. [31,32]. We also mention that PB has a mechanical analog referred to as phonon blockade, i.e., blockade of quantum excitations of mechanical oscillators [33–36].

PB has been experimentally generated in a number of driven systems of single [37–44] and two [45,46] resonators with a nonlinearity, as shown schematically in Figs. 1(b) and 1(c), respectively. Such a nonlinearity can be induced by a two-level atom (or atoms) coupled to one or both cavities. In the dispersive regime, such atom-cavity interaction can effectively lead to a Kerr-type nonlinearity as mentioned above. Note that PB can be generated not only in a

TABLE I. Abbreviations used in this paper.

Full Name	Abbreviation
Photon blockade	PB
Nonstandard photon blockade	NPB
Single-photon (two-photon) blockade	1PB (2PB)
Photon-induced tunneling	PIT
Two-photon (three-photon) tunneling	2PT (3PT)
Squeezed coherent states	SCS
Displaced squeezed thermal states	DSTS
Photon antibunching	PAB

Kerr-nonlinear driven cavity, but also other types of nonlinearities enable the generation of PB. The occurrence of PB is usually experimentally characterized by the second-order correlation function $g^{(2)}(0) < 1$, which means that the PB generated state exhibits the sub-Poissonian photon-number statistics, also referred to as (single-time) photon antibunching (PAB). PB and the generation of Bell states in two-cavity driven nonlinear systems, as shown in Fig. 1(c) and discussed in Appendix A, were first demonstrated in Refs. [47,48]. It was later shown in Refs. [49,50] that the nonlinear system of Fig. 1(c) can exhibit surprisingly strong single-time PAB for weak nonlinearities or, equivalently, weak atom–cavity-field couplings. This effect is now usually referred to as unconventional PB [51].

Note that this single-time PAB should not be confused with standard two-time PAB, defined by $g^{(2)}(\tau) > g^{(2)}(0)$ for small delay times τ , which is another important feature of PB. Indeed, if one considers single-PB as a true source of single photons, one would be required to satisfy not only single-time PAB, but also two-time PAB, characterized by a local minimum of the second-order correlation function,

$$g^{(2)}(\tau) = \lim_{t \rightarrow \infty} \frac{\langle \hat{a}^\dagger(t) \hat{a}^\dagger(t+\tau) \hat{a}(t+\tau) \hat{a}(t) \rangle}{\langle \hat{a}^\dagger(t) \hat{a}(t) \rangle \langle \hat{a}^\dagger(t+\tau) \hat{a}(t+\tau) \rangle}, \quad (1)$$

as a function of the delay time $\tau \approx 0$, where \hat{a} (\hat{a}^\dagger) is the annihilation (creation) operator of an optical mode. Thus, at least the following conditions should be satisfied for “true” single-PB:

$$g^{(2)}(0) < 1 \quad \text{and} \quad g^{(2)}(0) < g^{(2)}(\tau), \quad (2)$$

for small τ . For brevity, we analyze two-time PAB only in Sec. III and Fig. 2. Otherwise we limit our characterization of PB to single-time correlation functions.

C. Multiphoton blockade

Single-PB has been generalized to include two-PB and multi-PB effects [52–61]. Two-PB was first experimentally demonstrated by Hamsen *et al.* in 2017 [44]. We also note earlier theoretical works on multi-PB in dissipation-free driven Kerr systems [62,63] (for reviews see Refs. [30,64]). *Multi-photon* blockade, which is a mechanical analog of multi-PB, was studied in Ref. [35]. Multi-PB in dissipation-free

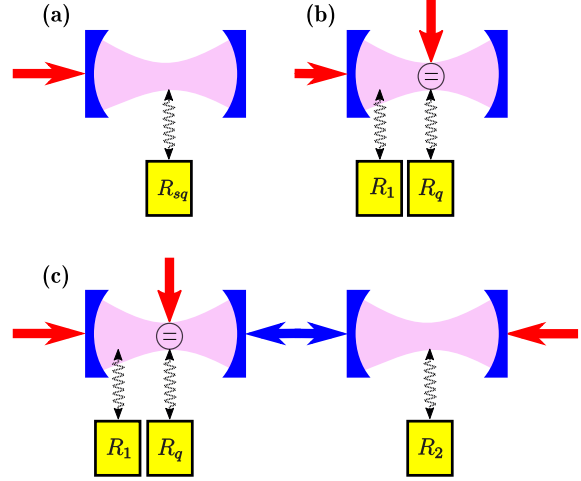


FIG. 1. Schematics of three prototype systems for observing photon blockade and photon-induced tunneling. (a) An unusual photon blockade device, described in Sec. III A, which is composed of a driven harmonic cavity coupled to a quantum (squeezed) reservoir R_{sq} . Panel (a) is shown in contrast to the common photon blockade devices (see Appendix A for more details). (b) A driven anharmonic cavity (due to the atom) coupled to a harmonic reservoir R_1 . (c) A two-cavity system, which is the anharmonic resonator shown in panel (b) coupled to a harmonic (or anharmonic) resonator linked to a harmonic reservoir R_2 . The anharmonicity can be induced in a harmonic resonator by its coupling to a two-level atom (qubit) as shown in panels (b) and (c). This qubit is coupled to a reservoir R_q . Red arrows denote classical coherent drives applied to a cavity or a qubit. Note that in setup (a) the cavity anharmonicity is replaced by the reservoir anharmonicity.

systems enables generation of quantum optical states in a finite-dimensional Hilbert space including finite-dimensional analogs of coherent and squeezed states of light [62,64–67].

Intuitively, two-PB (and analogously multi-PB) occurs if the single- and two-photon Fock states, which are generated in a driven nonlinear system, block the generation of more photons in the system. This paper is focused on the *study of two-PB and other kinds of single- and two-photon correlations*.

For any classical states, the second-order equal-time correlation function satisfies $g^{(2)}(0) \geq 1$, which is a property of classical intensity fluctuations. The states for which $g^{(2)}(0) < 1$ have the sub-Poissonian photon-number statistics and, thus, are *nonclassical* (see Appendix C). This condition is also used for identifying the presence of single-photon blockade (1PB). The analysis of higher-order correlations is necessary to characterize multi-PB or other types of nonstandard PB (NPB).

Thus, in our study of multi-PB, we apply the k th-order equal-time correlation functions, $g^{(k)}(0) = \langle (\hat{a}^\dagger)^k \hat{a}^k \rangle / \langle \hat{a}^\dagger \hat{a} \rangle^k$, describing the probability of measuring simultaneously k photons. In PB experiments, the second-order correlation functions $g^{(2)}(0)$ and $g^{(2)}(\tau)$ are usually measured, except the experiment of Hamsen *et al.* [44], where also the third-order correlation functions $g^{(3)}(0)$ and $g^{(3)}(\tau)$ were measured to confirm two-PB.

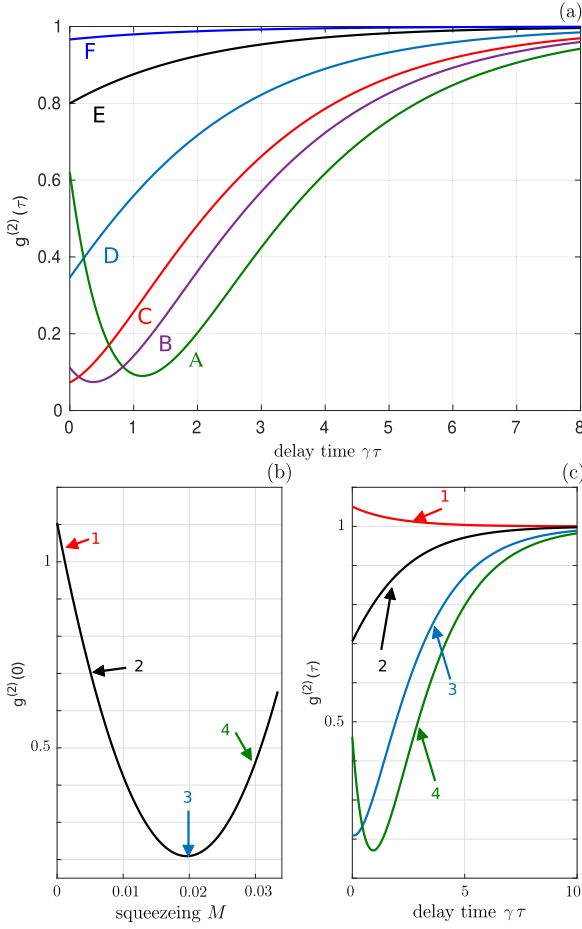


FIG. 2. Squeezed-reservoir model: steady-state second-order correlation function $g^{(2)}(\tau)$ vs (a), (c) the (rescaled) delay time $\gamma\tau$ between the measurements of subsequent photons and (b) the reservoir squeezing parameter M for various values of the external field strength ε at the resonance, $\Delta = 0$, between the cavity and driving fields, with the damping rate $\gamma = 1$. Moreover, in panel (a) we set $\varepsilon/\gamma = 0.05$ (curve A), 0.06 (B), 0.07 (C), 0.1 (D), 0.2 (E), and 0.5 (F), and assume that the reservoir is maximally squeezed with the reservoir mean photon number $n = 0.003$, which corresponds to $M = 0.017$. The τ dependences for the four specific points in panel (b) are shown in panel (c). In panels (b) and (c) we set $\varepsilon/\gamma = 0.07$ and $n = 0.001$. It is evident that the curves 2 and 3 (1 and 4) show two-time photon antibunching (bunching) in panel (c). This implies that only the points 2 and 3 in panel (b) can correspond to “true” single-photon blockade states.

We note that experimental tests of PB are not limited to measuring $g^{(k)}(0)$ and $g^{(k)}(\tau)$. Indeed, the occurrence of PB can also be revealed by showing, e.g., a staircase dependence of the total transmitted power through a driven nonlinear system for different incident photon bandwidths, which was experimentally demonstrated by Hoffman *et al.* [40] or a staircase dependence of the mean photon number in the ground state of a given Kerr nonlinear system on a rescaled detuning [68]. Such dependences are photonic

TABLE II. Different types of photon blockade and photon tunneling classified via $g^{(2)}(0)$ and $g^{(3)}(0)$. Four of these types of photon-number correlations can be exhibited by the steady-state light generated by the squeezed-reservoir system, as well as squeezed coherent states and displaced squeezed thermal states, which are shown in Figs. 3–5, respectively.

Case	Permutation	Inequalities	Effect
a	(1 2 3)	$1 < g^{(2)}(0) < g^{(3)}(0)$	3PT
b	(1 3 2)	$1 < g^{(3)}(0) < g^{(2)}(0)$	2PT
c	(2 1 3)	$g^{(2)}(0) < 1 < g^{(3)}(0)$	1PB (type 2)
d	(2 3 1)	$g^{(2)}(0) < g^{(3)}(0) < 1$	1PB (type 3)
e	(3 1 2)	$g^{(3)}(0) < 1 < g^{(2)}(0)$	2PB and 2PT
f	(3 2 1)	$g^{(3)}(0) < g^{(2)}(0) < 1$	1PB (type 1)

analog of a Coulomb-blockade staircase. This paper is focused on characterizing multi-PB via $g^{(k)}(0)$ and $g^{(2)}(\tau)$ only.

D. Photon-induced tunneling

Photon-induced tunneling (PIT) refers to a photon-number correlation effect, which *enhances* the probability of subsequent photons (from a coherent drive) to enter the driven cavity [38,60,61,69–73]. Evidently, this process is inverse to PB, in which the probability that the subsequent photons of a drive enter the driven cavity is *decreased* (or even essentially vanishing). PIT has been observed experimentally in Refs. [38,69,72].

Standard two-photon tunneling (two-PT), where the simultaneous arrival of two photons is enhanced compared to single-photon arrivals, is usually characterized by the super-Poissonian photon-number statistics (i.e., single-time photon bunching), when $1 < g^{(2)}(0)$ [69–71]. Analogously, standard three-photon tunneling (three-PT) is a photon-number correlation effect, in which the simultaneous arrival of three photons is enhanced compared to the two-photon and single-photon arrivals. Thus, three-PT can be characterized by the conditions [60,71]

$$1 < g^{(2)}(0) < g^{(3)}(0). \quad (3)$$

Note that other definitions of PIT are used in the literature (see Ref. [60] for a comparison), e.g., those based on a local maximum of $g^{(2)}(\tau)$ at $\tau = 0$ (i.e., corresponding to two-time photon bunching) [38] or the requirement that $g^{(3)}(0) > g^{(2)}(0)$, i.e., the simultaneous arrival of three photons is enhanced compared to the simultaneous two-photon arrivals [72] without specifying whether $g^{(2)}(0)$ exhibits the super- or sub-Poissonian statistics. Various types of PIT in comparison to PB are listed in Table II.

E. Photon blockade and photon-induced tunneling via squeezing

It is known that SCS can exhibit the (second-order) sub-Poissonian photon-number statistics (also referred to as single-time PAB). This effect is also an important feature of light generated via photon blockade.

The vast majority of previous works on PB assumed that dissipation of a PB system can be modeled via its linear

coupling to a harmonic reservoir (a thermal bath). Only a few works, including Refs. [74,75], were analyzing PB in systems coupled to nonlinear reservoirs. In such dissipative systems, PB can result from (i) a system nonlinearity, (ii) a reservoir nonlinearity, or (iii) both of them. Single- and multi-PB effects in a Kerr-nonlinear system coupled to a nonlinear (squeezed) reservoir were analyzed in Ref. [74]. Shortly after that publication, a single-PB effect generated solely by a nonlinear (squeezed) reservoir was studied in a linear system in Ref. [75]. Here we analyze various PB effects and PIT in a harmonic cavity coupled to squeezed systems, as shown in Fig. 1(a). The other two common systems, which enable the generation of conventional and unconventional PB, are schematically shown in Figs. 1(b) and 1(c), respectively. Note that some other schemes for PB can be obtained by combining the three schemes shown in this figure.

The main objective of this paper is to analyze whether squeezing plays an important role in generating various types of PB (especially multiphoton effects). In other words, we address the question whether PB can be observed in a driven harmonic resonator without a strongly nonlinear medium [like in the standard PB setup shown in Fig. 1(b)] and without relying on multipath interference, as in the PB setup shown in Fig. 1(c).

The paper is organized as follows. In Sec. II, we specify the criteria of multi-PB and PIT. In Sec. III, we numerically show that a two-photon decay process of light generated in an optically linear system (a harmonic resonator) can induce two-PB. Then, in Sec. IV, we analytically study the relations between $g^{(2)}(0)$ and the higher-order correlation functions $g^{(k)}(0)$ for the squeezed coherent states and the displaced squeezed thermal states, to demonstrate more explicitly the possibility of generating two-PB, three-PT, and various types of nonstandard single-PB via squeezing. The question of nonclassicality of the studied effects and states is addressed in Sec. V and Appendices C–E. We also compare the proposed method for generating multi-PB with the standard PB setups in Appendix A. Moreover, for pedagogical reasons, we present more details about the master equation for a squeezed reservoir and recall its relation to the standard master equation in Appendix B. We conclude in Sec. VI.

In the main paper, we use several abbreviations. We concisely list them in Table I to facilitate the following exposition.

II. CRITERIA FOR VARIOUS TYPES OF PHOTON BLOCKADE

A. Refined criteria for multiphoton blockade

The mechanisms of both conventional and unconventional single-PB under proper resonance conditions can be generalized to generate also two- and multi-PB, i.e., the generation of two or a larger number of photons at the same instance of time.

Intuitively, k -PB can be understood as the generation of a state $\hat{\rho}$ satisfying the conditions for the photon-number probabilities $P_k = \langle k|\hat{\rho}|k\rangle$ as follows [44,53]:

$$P_{k+1} \approx 0 \quad \text{and} \quad P_k \gg P_{k+1}. \quad (4)$$

However, in more realistic scenarios, the conditions in Eq. (4) are replaced by weaker criteria, where the photon-number

distribution P_k of $\hat{\rho}$ is compared with the Poissonian distribution P_k^{CS} , describing the photon-number statistics of a coherent state. Specifically,

$$P_{k+1} < P_{k+1}^{\text{CS}} \quad \text{and} \quad P_k \geq P_k^{\text{CS}}, \quad (5)$$

where the probability $P_k^{\text{CS}} = |\langle \alpha|k\rangle|^2$ is for a coherent state α with the same mean photon number as that for $\hat{\rho}$, i.e., $\langle \alpha|\hat{n}|\alpha\rangle = |\alpha|^2 = \text{Tr}(\hat{\rho}\hat{n})$, where $\hat{n} = \hat{a}^\dagger\hat{a}$ is the photon-number operator. The conditions for the probabilities P_k can be replaced by those based on the experimentally accessible k th-order correlation function,

$$g^{(k)}(0) = \frac{\langle (\hat{a}^\dagger)^k \hat{a}^k \rangle}{\langle \hat{n} \rangle^k} = \frac{\langle \hat{n}^{[k]} \rangle}{\langle \hat{n} \rangle^k} = \frac{\sum_{n=0}^{\infty} P_n n^{[k]}}{\langle \hat{n} \rangle^k}, \quad (6)$$

where, as usual, \hat{a} (\hat{a}^\dagger) is the annihilation (creation) operator, $\langle \hat{n}^{[k]} \rangle = \langle (\hat{a}^\dagger)^k \hat{a}^k \rangle$, and $n^{[k]} = n(n-1)\cdots(n-k+1)$ is the factorial power (also called the falling power). Thus, the criteria for PB given in Eq. (4) can be replaced by

$$g^{(k+1)}(0) \approx 0 \quad \text{and} \quad g^{(k)}(0) \gg g^{(k+1)}(0). \quad (7)$$

In this paper, we assume that k -PB is defined by the following two criteria derived by Hamsen *et al.* [44]:

$$\begin{aligned} \text{Criterion 1:} \quad & g^{(k+1)}(0) < A \equiv \exp(-\langle \hat{n} \rangle); \\ \text{Criterion 2:} \quad & g^{(k)}(0) \geq B^{(k)} \equiv A + \langle \hat{n} \rangle g^{(k+1)}(0), \end{aligned} \quad (8)$$

which replace the criteria in Eq. (5).

We note that the definition of multi-PB in Eq. (8) has some drawbacks and limitations. Strictly speaking, the criteria in Eq. (8) can only be considered a PB witness, i.e., necessary but not sufficient conditions of PB. Note that second-order single-time photon antibunching [$g^{(2)}(0) < 1$] is the most common test of single-PB, but it is also only a necessary but not sufficient condition for PB. An intuitive ‘‘orthodox’’ interpretation of single- and multi-PB effects can be given as follows: k -PB ($k = 1, 2, \dots$) corresponds to the effect, in which the photon occupation of the first k energy levels of a driven nonlinear system blocks the generation of more photons in the system. In other words, k -PB corresponds to an effective truncation of the Hilbert space spanning a given state at the k -photon Fock state $|k\rangle$ so the contributions of the Fock states $|k+l\rangle$ for $l > 0$ can be effectively ignored, which means that $\langle k|\hat{\rho}|k\rangle \gg \langle k+l|\hat{\rho}|k+l\rangle$ or, alternatively, $g^{(k)}(0) \gg g^{(k+l)}(0)$, for any $l > 0$. However, the above conditions are usually only checked for $l = 1$, ignoring the analysis of the cases for $l > 1$. Such objection also applies to many studies of single-PB based on requiring $g^{(2)}(0) < 1$ and ignoring the values of $g^{(3)}(0)$ and higher-order correlation functions.

B. Simplified criteria for multiphoton blockade

Note that if $\langle \hat{n} \rangle \ll 1$ then the refined conditions for multi-PB, given in Eq. (8), simplify to the following familiar criteria for $\hat{\rho}$:

$$g^{(k+1)}(0) < 1 \quad \text{and} \quad g^{(k)}(0) \geq 1, \quad (9)$$

which mean that, in this small photon-number limit, the state generated via k -PB exhibits (single-time) $(k+1)$ -PAB, and

k -photon bunching if $g^{(k)}(0) > 1$ or the so-called unbunching if $g^{(k)}(0) = 1$.

Thus, two-photon and three-PB effects can be given by the following relations for the correlation functions:

$$g^{(2)}(0) \geq 1 \quad \text{and} \quad g^{(3)}(0) < 1; \quad (10)$$

$$g^{(2)}(0), g^{(3)}(0) \geq 1 \quad \text{and} \quad g^{(4)}(0) < 1, \quad (11)$$

respectively. Note that we have added an extra condition for $g^{(2)}(0)$ in Eq. (11), which is not required in the criteria specified in Eqs. (8) and (9). Moreover, in this simplified characterization of PB we ignore the requirements on two-time correlation functions $g^{(k)}(\tau)$, including $g^{(2)}(\tau)$.

Thus, in the case of two-PB, the three-photon probability has to be suppressed and simultaneously the probability of observing two photons should be enhanced. Analogously, the suppression of the four-photon probability and the increase in the probabilities of a lower number of photons would lead to three-PB.

Both types of PB, which are characterized by the simplified and refined criteria, correspond to nonclassical effects, because they require the sub-Poissonian photon-number statistics (of any given order k), as described in greater detail in Appendix C.

As mentioned above, the refined criteria in Eq. (8) reduce to the conditions in Eq. (10) for small photon numbers $\langle \hat{n} \rangle \ll 1$. But, in principle, these simplified criteria can be applied even if $\langle \hat{n} \rangle > 1$, but then the predicted PB can differ from that based on the refined criteria in Eq. (8). It might also be the case that a given state exhibits, e.g., two-PB according to the refined criteria, but not according to the simplified criteria. Actually, we will show such cases in the following sections.

Now, we consider a simple example of such different predictions of two-PB according to Eqs. (8) and (9). Specifically, the two-photon Fock state $|2\rangle$, for which $g^{(2)}(0) = 1/2$ and $g^{(3)}(0) = 0$, can be considered a two-PB state according to the refined criteria in Eq. (8), because $g^{(2)}(0) > \exp(-2) \approx 0.135$ and $g^{(3)}(0) < \exp(-2)$. Note that the simplified criteria in Eq. (9) can, in principle, be applied to the two-photon Fock state $|2\rangle$. However, since $A \equiv \exp(-\langle \hat{n} \rangle)$ is not negligible, the predictions of PB for $|2\rangle$ according to the refined and simplified criteria are different. Indeed, the Fock state $|2\rangle$ is not considered a two-PB state according to the simplified criteria (9).

C. Nonstandard types of photon blockade

As described in previous subsections, the simplified condition for observing single PB corresponds to the requirement of single-time PAB. If the following additional condition $g^{(3)}(0) < g^{(2)}(0)$ is satisfied, as desirable for good single-photon sources, then we refer to this effect as single-PB of type 1, which is characterized by

$$g^{(3)}(0) < g^{(2)}(0) < 1. \quad (12)$$

Apart from this single-PB, there are other possibilities of obtaining quantum photon-number statistics by specifying the relations between higher-order single-time correlations $g^{(k)}(0)$ and/or the second-order two-time correlations $g^{(2)}(\tau)$. These include the following types of PB.

(1) We recall that, in order to consider single-PB as a true source of single photons, the generated light via PB should also exhibit two-time PAB as given in Eq. (2). Indeed, it is known that the sub-Poissonian photon-number statistics (i.e., single-time PAB) of a field can be accompanied with both two-time PAB and two-time photon bunching, and vice versa (see, e.g., Ref. [76] and references therein). Thus, if light exhibits single-time PAB and two-time photon bunching [i.e., a local maximum of $g^{(2)}(\tau)$ for small τ], one can refer to it as nonstandard single-PB, because it is *not* characterized by Eq. (2). Examples of this nonstandard PB are analyzed in Sec. III and shown in Fig. 2. In the following we mainly analyze other types of nonstandard PB based solely on single-time correlation functions.

(2) In greater detail we analyze a special kind of nonstandard PB characterized by the single-time correlation functions satisfying the conditions

$$g^{(2)}(0) < 1 < g^{(3)}(0), \quad (13)$$

which was first studied in greater detail in Ref. [77] under the name *unconventional PB*. However, in order to avoid confusion of this type of PB and unconventional PB studied in Refs. [45,46,51], we refer to the effect characterized by Eq. (13) as nonstandard PB of type 2.

It is seen that this nonstandard PB occurs when the probability of measuring two photons at the same time is suppressed and, simultaneously, the probability of obtaining three photons is enhanced. Note that this effect can be generated by different physical mechanisms in different systems: (i) by using large nonlinearities in conventional PB systems, as shown in Fig. 1(b); (ii) by small nonlinearities and multipath interference in unconventional PB systems, as shown in Fig. 1(c); or (iii) by exploiting squeezing in, e.g., linear systems coupled to a squeezed reservoir, as shown in Fig. 1(a) and studied here.

(3) One can modify the condition for $g^{(3)}(0)$ in Eq. (13) to consider another type (say type 3) of single-PB, as characterized by

$$g^{(2)}(0) < g^{(3)}(0) < 1. \quad (14)$$

The latter two types of nonstandard single-PB are listed in Table II and a few examples of such effects generated via squeezing are discussed in the following sections and shown in Figs. 3–6.

Note that we found examples of nonstandard PB concerning unusual properties of both single- and two-time correlation functions. But, for brevity, we do not present such examples here.

We also note that nonclassical states often satisfy the conditions $g^{(2)} < g^{(3)} < \dots < g^{(k)} < 1$, as those studied in Refs. [78,79], where the sub-Poissonian statistics was resulting from postselection. Such states can also be used for simulating nonstandard single-PB effects.

III. VARIOUS TYPES OF PHOTON BLOCKADE AND TUNNELING GENERATED BY A SQUEEZED RESERVOIR

A. Model

Here we will show that a squeezed reservoir can induce various types of PB and PIT, including two-photon effects in a driven *harmonic* resonator.

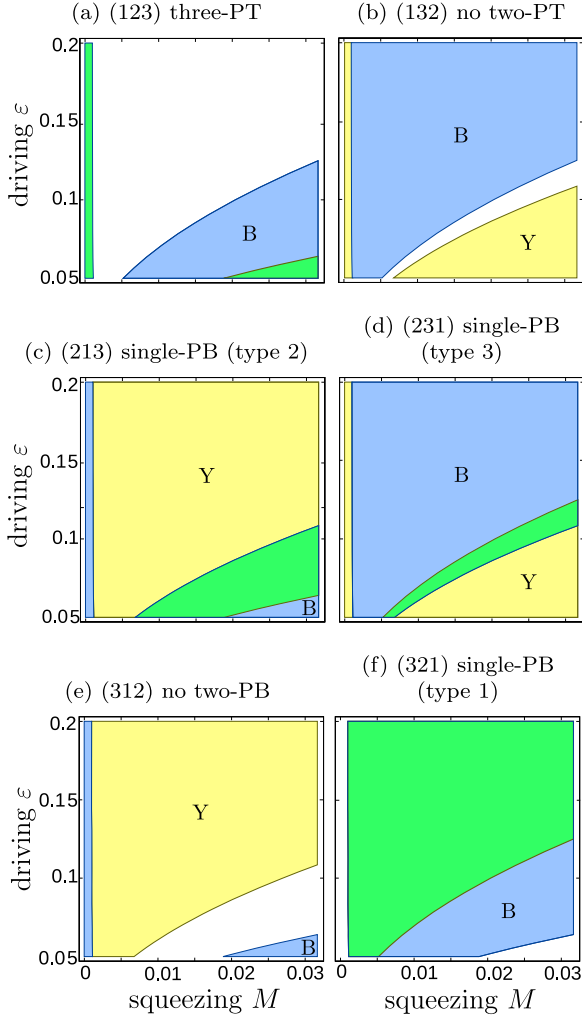


FIG. 3. Squeezed-reservoir model: photon-number correlations of light generated in a driven harmonic cavity coupled to a squeezed reservoir, assuming $n = 0.01$ and $\Delta = 0$. The regions of the driving strength ε and the reservoir squeezing parameter M satisfying the six conditions, which are listed in Table II for the correlation functions $g^{(2)}(0)$ and $g^{(3)}(0)$, are shown here in yellow (Y) and blue (B), respectively. The regions in green show the ranges of the parameters M and ε for which given criteria are satisfied simultaneously by $g^{(2)}(0)$ and $g^{(3)}(0)$ indicating a specific type of photon blockade or photon-induced tunneling. In grayscale, yellow is the brightest, and green looks slightly darker than blue. Yellow is also indicated by “Y,” and blue is indicated by “B.”

Specifically, as an example of a physical system, in which squeezing interactions induce PB, we use a single optical cavity of a frequency ω_c , which is externally driven by a laser field of an amplitude ε with a frequency ω_d . The cavity decays into a squeezed reservoir characterized by the reservoir squeezing parameter M . The model is presented in Fig. 1(a). We will show that for such a linear optical system the two-photon dissipation process plays a crucial role in obtaining

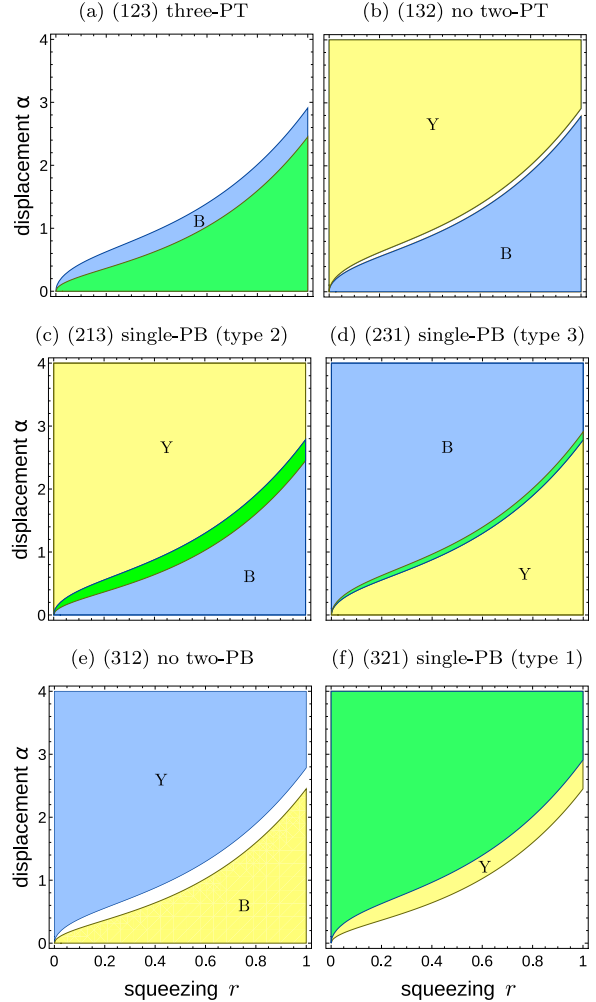


FIG. 4. Photon-number correlations in the squeezed coherent states showing the regions of the displacement (α) and squeezing (r) parameters for which the conditions in Table II are satisfied. This figure uses the same notation and coloring, and carries a similar message as in Fig. 3. For example, the green region in figure (c) (213) shows the ranges of parameters for which the conditions $g^{(2)}(0) < 1 < g^{(3)}(0)$ are satisfied, as in Table II (c). The yellow (blue) region shows the parameter ranges satisfying solely the condition $g^{(2)}(0) < 1$ [$g^{(3)}(0) > 1$]. Yellow (blue) is also indicated by “Y” (“B”).

single- and two-PB, as well as other nonstandard types of nonclassical photon correlations.

The Hamiltonian of the system has the following form (hereafter we set $\hbar = 1$):

$$\hat{H}' = \omega_c \hat{a}^\dagger \hat{a} + \varepsilon (\hat{a} e^{i\omega_d t} + \hat{a}^\dagger e^{-i\omega_d t}). \quad (15)$$

After its transformation to the interaction picture to the frame rotating with the driving frequency ω_d , one obtains the following effective Hamiltonian of the system:

$$\hat{H} = \Delta \hat{a}^\dagger \hat{a} + \varepsilon (\hat{a}^\dagger + \hat{a}), \quad (16)$$

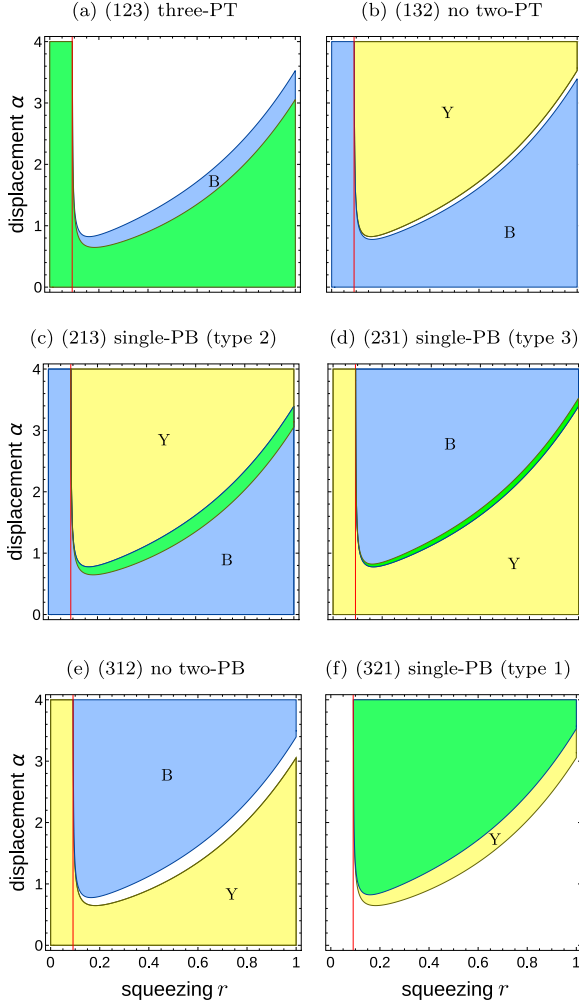


FIG. 5. Photon-number correlations in the displaced squeezed thermal states satisfying the inequalities in Table II, the same as in Fig. 4 but for the states defined in Eq. (23) with $n_{\text{th}} = 0.1$. The parameter region on the left-hand (right-hand) side of the red vertical line in all the plots corresponds to the classical (nonclassical) regimes of the states. This red line is plotted at the critical squeezing parameter $r_0 = 0.0912$, which is shown later in Fig. 12 by the solid curve for $n_{\text{th}} = 0.1$ for the vanishing entanglement potential, EP = 0.

where $\Delta = \omega_c - \omega_d$ is the detuning between the cavity and driving frequencies.

The evolution of the driven cavity interacting with a squeezed reservoir is governed by the following master equation [80–82]:

$$\begin{aligned} \frac{d\hat{\rho}}{dt} = & -i[\hat{H}, \hat{\rho}] + \frac{1}{2}\gamma(n+1)(2\hat{a}\hat{\rho}\hat{a}^\dagger - \hat{a}^\dagger\hat{a}\hat{\rho} - \hat{\rho}\hat{a}^\dagger\hat{a}) \\ & + \frac{1}{2}\gamma n(2\hat{a}^\dagger\hat{\rho}\hat{a} - \hat{a}\hat{a}^\dagger\hat{\rho} - \hat{\rho}\hat{a}\hat{a}^\dagger) \\ & - \frac{1}{2}\gamma M(2\hat{a}\hat{\rho}\hat{a} - \hat{a}\hat{a}\hat{\rho} - \hat{\rho}\hat{a}\hat{a}) \\ & - \frac{1}{2}\gamma M^*(2\hat{a}^\dagger\hat{\rho}\hat{a}^\dagger - \hat{a}^\dagger\hat{a}^\dagger\hat{\rho} - \hat{\rho}\hat{a}^\dagger\hat{a}^\dagger). \end{aligned} \quad (17)$$

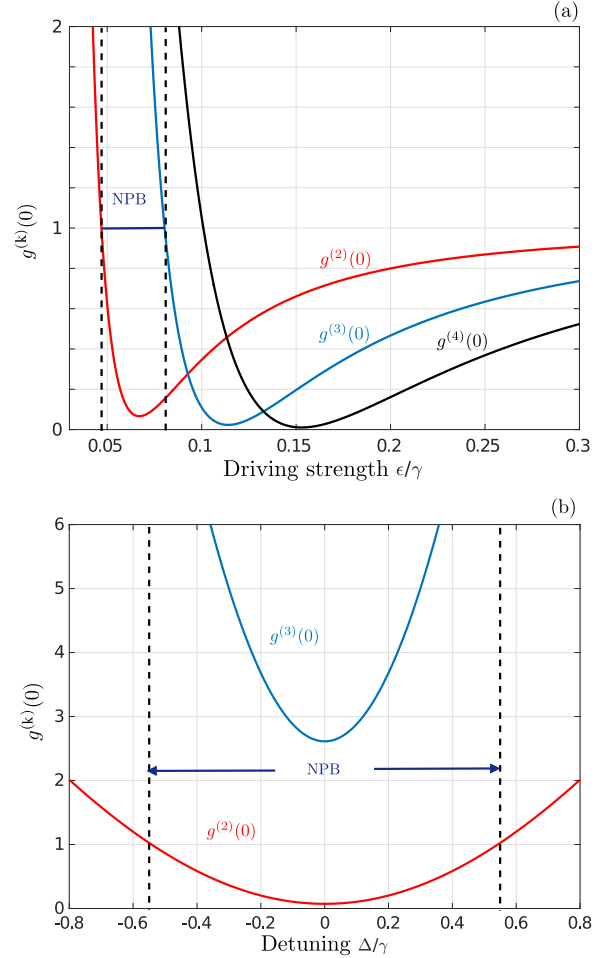


FIG. 6. Squeezed-reservoir model: correlation functions $g^{(k)}(0)$ vs (a) the driving strength ϵ for fixed $\Delta = 0$ and (b) the detuning Δ for the maximally squeezed reservoir for $n = 3 \times 10^{-4}$, which corresponds to $M = 0.017$, for fixed $\epsilon = 0.07\gamma$. All the parameters are scaled in γ units. The regions between the broken lines correspond to nonstandard single-photon blockade (type 2).

We refer to M as a reservoir squeezing parameter and to n as the mean number of reservoir photons. These parameters satisfy the inequality $|M| \leq \sqrt{n(n+1)}$. For the squeezed-vacuum reservoir, these parameters are given by $n = \sinh^2(r)$ and $M = \cosh(r) \sinh(r) \exp(-i\theta)$, implying the equality $|M| = \sqrt{n(n+1)}$, where r and θ correspond, respectively, to the amplitude and phase of the squeezing parameter $\xi = r \exp(i\theta)$ (see Appendix B for more details). Apart from the standard parts in Eq. (17), which describe a thermal-like Markovian reservoir with the mean photon number n allowing for single-photon dissipation, this master equation includes also two-photon decay processes. Indeed, Eq. (17) reduces to the standard master equation for the thermal reservoir by setting $M \rightarrow 0$ and $n \rightarrow n_{\text{th}} = \{\exp[\hbar\omega/(k_B T)] - 1\}^{-1}$, which becomes the mean number of thermal photons at the frequency ω and temperature T , where k_B is the Boltzmann constant.

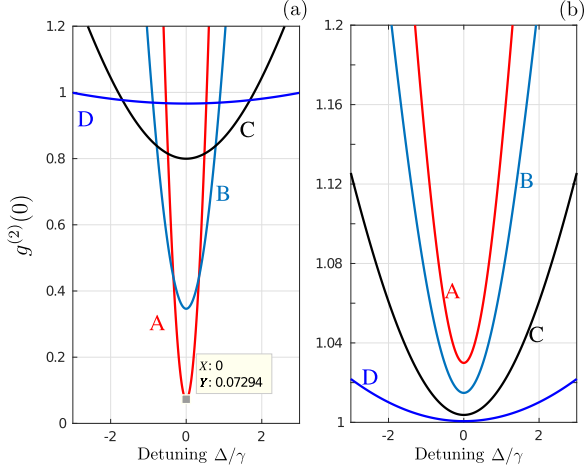


FIG. 7. Squeezed-reservoir model: single-photon blockade in a driven harmonic resonator coupled to a squeezed reservoir. Specifically, the steady-state second-order correlation function $g^{(2)}(0)$ vs the detuning Δ between the cavity and driving frequencies for various values of the external field strength ε , assuming (a) the squeezed-vacuum reservoir (see Appendix B) with $M = \sqrt{n(n+1)}$ and (b) no squeezing ($M = 0$) of the reservoir. We set the reservoir mean photon number as $n = 3 \times 10^{-4}$, and $\varepsilon/\gamma = 0.07$ (curve A), 0.1 (B), 0.2 (C), and 0.5 (D). All the parameters are scaled in $\gamma = 1$ units. Panel (a) shows strong single-time photon antibunching, especially for $\varepsilon = 0.07\gamma$ and $\Delta = 0$, which characterizes single-photon blockade. Panel (b) shows single-time photon bunching, which confirms that the single-photon blockade in panel (a) results from the squeezed reservoir.

B. Standard single-photon blockade

As mentioned above, the standard indicator of single-PB is the condition $g^{(2)}(0) < 1$ showing the decreased probability of measuring simultaneously two photons during the process of the cavity-field dissipation.

In Figs. 7(a) and 7(b), we have shown the dependence of single-time steady-state second-order correlation function $g^{(2)}(0)$ versus the detuning Δ for the harmonic cavity field decaying, respectively, into (a) the squeezed-vacuum reservoir [i.e., the maximally squeezed reservoir with $M = \sqrt{n(n+1)}$] and (b) the standard thermal reservoir ($M = 0$) with the same mean number $n = 0.003$ of reservoir photons. Various external-driving-field strengths are considered. Our first conclusion is that the squeezing of the field in the reservoir is responsible for generating single-PB of the linear-cavity field, as described by the sub-Poissonian photon-number statistics shown in Fig. 7(a), while the interaction with the thermal field of the environment inevitably leads to the super-Poissonian photon-number statistics of the cavity field shown in Fig. 7(b). This effect can be interpreted as PIT. In all of these cases, by tuning the frequency of the external excitation with the cavity frequency, one can assure the lowest possible value of $g^{(2)}(0)$. Additionally, a weaker external driving is preferable to obtain lower values of $g^{(2)}(0)$. For the parameters presented in Fig. 7(a), the lowest value of $g^{(2)}(0)$ is 0.0729. By decreasing the mean photon number inside the squeezed reservoir, or by applying a weaker external field, one can

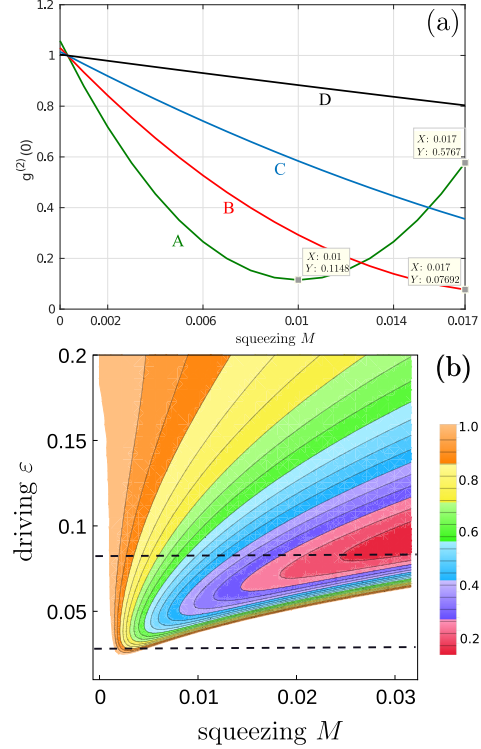


FIG. 8. Squeezed-reservoir model: steady-state correlation function $g^{(2)}(0)$ vs the reservoir squeezing parameter M and the driving strength ε in a driven harmonic resonator coupled to a squeezed reservoir. We set $\varepsilon/\gamma = 0.05$ (curve A), 0.07 (B), 0.1 (C), and 0.2 (D). Moreover, we assume resonance between the cavity and external fields, $\Delta = 0$, and the mean photon number of the squeezed reservoir is $n = 3 \times 10^{-4}$. All the parameters are scaled in γ units. It is seen that, usually, a larger reservoir squeezing parameter M implies stronger single-time PAB, reaching the smallest value of $g^{(2)}(0)$ for the squeezed-vacuum reservoir with $M = \sqrt{n(n+1)}$ (see Appendix B). However, this is not the case for, e.g., $\varepsilon = 0.05\gamma$ in panel (a), when there is an optimal value of $M \ll \sqrt{n(n+1)}$, which results in the strongest single-time PAB. The same surprising result is shown in panel (b) in the area between the dashed lines indicating the range of the external field strength ε for which $g^{(2)}(0)$ has a minimum for $M < \sqrt{n(n+1)}$.

obtain even smaller values of $g^{(2)}(0)$ under the exact resonance condition $\Delta = 0$.

Figures 8(a) and 8(b) show the dependence of the steady-state single-time second-order correlation $g^{(2)}(0)$ on the reservoir squeezing parameter M and the driving strength ε . Usually, the minimal possible values of $g^{(2)}(0)$ are obtained when the field inside the reservoir is maximally squeezed, i.e., for the squeezed-vacuum reservoir satisfying $M = \sqrt{n(n+1)}$. However, for very weak excitations, the dependence $g^{(2)}(0)$ versus M has a minimum for $M < \sqrt{n(n+1)}$. Thus, it is worth stressing that it is possible to use a nonmaximally squeezed reservoir, which still enables strong single-time PAB for very weak excitations, as shown in Fig. 8(a).

C. Nonstandard single-photon blockade with two-time photon bunching

Here we discuss whether a squeezed reservoir can generate nonstandard PB exhibiting two-time photon bunching, and single-time PAB. Three examples of this type of PB are shown in Figs. 2(a) and 2(c) by the curves marked as A, B, and 4. These examples should be compared with the examples of true single-PB indicated there by arrows 2 and 3.

More specifically, in Fig. 2(a), the steady-state two-time second-order correlation function $g^{(2)}(\tau)$ is shown versus the rescaled delay time $\gamma\tau$ for the same values of the parameters as those in Fig. 8(a). We assumed here the maximal squeezing of the field in the reservoir, i.e., $M = \sqrt{n(n+1)}$. For each of the considered cases, having the minimum of $g^{(2)}(0) < 1$, the cavity field clearly exhibits two-time PAB, $g^{(2)}(\tau) > g^{(2)}(0)$. When ε takes such a value, which results in the minimal value of $g^{(2)}(0)$ for a nonmaximally squeezed reservoir field, the cavity field exhibits two-time bunching of photons for short delay time. PAB appears for longer delay time. In Figs. 2(b) and 2(c), this behavior is studied in more detail. It appears that, depending on the reservoir squeezing degree M of the reservoir, both two-time photon bunching and antibunching are possible. But bunching for short delay times is possible only for such values of M , which result in decreasing $g^{(2)}(0)$ for increasing M .

D. Nonstandard single-photon blockade of types 2 and 3

We will show now the possibility of generating nonstandard single-PB of the second and third types in the system considered here.

In Fig. 6(a), the correlation functions of $g^{(2)}(0)$, $g^{(3)}(0)$, and $g^{(4)}(0)$ are shown in their dependence on the external excitation strength ε for a specified mean number of photons in the squeezed reservoir, while Fig. 6(b) shows $g^{(2)}(0)$ and $g^{(3)}(0)$ as a function of the detuning Δ . As one can see, there are ranges of the excitation strengths ε and the detuning Δ for which $g^{(2)}(0) < 1$ is accompanied by the additional condition for $g^{(3)}(0) > 1$, which implies the occurrence of NPB of type 2. For these regions, the condition $g^{(2)}(0) < 1$ is not sufficient for identifying “true” single-PB, because there still exists a nonzero probability of measuring more than two photons at the same time. Only the two-photon statistics is suppressed and that can be also achieved when the external driving field is off resonance with the cavity frequency. Larger values of ε are related to the simultaneous suppression of the higher-order correlations. Although the values of $g^{(2)}(0)$ are increasing, still we can decrease the higher-order correlations below the value of $g^{(2)}(0)$, as shown in Fig. 6(a).

Moreover, in Fig. 4(d), we show the ranges of the squeezing r and displacement α parameters, for which another type of nonstandard single-PB (i.e., type 3) can be observed. This NPB in Fig. 4(d) is shown in addition to the NPB of type 2 presented in Fig. 4(c).

E. Two-photon blockade

As shown in Fig. 3, various types of single-PB can be generated via dissipation of a linearly driven optical cavity field into a squeezed environment. However, two-PB,

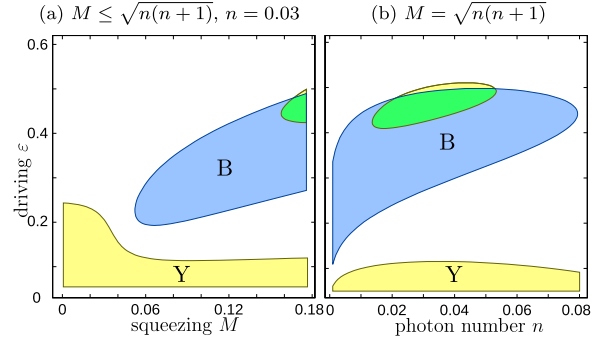


FIG. 9. Squeezed-reservoir model: two-photon blockade generated in a driven harmonic cavity coupled to a squeezed reservoir according to the refined criteria in Eq. (8) for $n = 0.03$ and (a) $M \leq \sqrt{n(n+1)}$ and (b) $M = \sqrt{n(n+1)}$ corresponding to the squeezed-vacuum reservoir (see Appendix B), assuming $\Delta = 0$. Specifically, by changing the driving strength ε vs (a) the reservoir squeezing parameter M and (b) the reservoir mean photon number n , we show the regions in which the criteria 1 and 2 are satisfied, as indicated in yellow and blue, respectively. Two-photon blockade occurs when both criteria 1 and 2 are satisfied, which corresponds to the green regions.

according to the *simplified* criteria in Eq. (10), is not observed in this model, which is demonstrated in Fig. 3(e) for a specific choice of n . Also our numerical calculations show that it is very unlikely to generate three-PB according to the *simplified* criteria Eq. (11) for an arbitrary value of n .

However, two-PB, according to the *refined* criteria in Eq. (8), can be observed in this model. Indeed, the green regions in Fig. 9 show the ranges of the parameters M , ε , and n for which two-PB can be observed.

IV. SIMULATING VARIOUS TYPES OF PHOTON BLOCKADE AND TUNNELING WITH SQUEEZED COHERENT STATES

A. Squeezed coherent states

Ideal SCS, or more precisely the displaced squeezed vacuum, can be obtained by applying the squeezing and displacement operators to the vacuum state as follows:

$$|\alpha, \xi\rangle = \hat{D}(\alpha)\hat{S}(\xi)|0\rangle, \quad (18)$$

where

$$\hat{S}(\xi) = \exp\left[\frac{1}{2}(\xi^* \hat{a}^2 - \xi \hat{a}^{\dagger 2})\right] \quad (19)$$

is the squeezing operator with a complex squeezing parameter $\xi = r \exp(i\theta)$ and $D(\alpha) = \exp(\alpha \hat{a}^\dagger - \alpha^* \hat{a})$ is the displacement operator with $\alpha = \bar{\alpha} \exp(i\phi)$, for arbitrary phases $\theta, \phi \in [0, 2\pi]$ and amplitudes $\bar{\alpha}, r \geq 0$.

The second-order correlation function $g^{(2)}(0)$ for the SCS with arbitrary values of θ and ϕ is given by

$$g^{(2)}(0) = 3 + 2(1 - 2\bar{\alpha}^2)\bar{N}^{-1} - \bar{\alpha}^2[1 + C]\bar{N}^{-2}, \quad (20)$$

where the mean photon number is

$$\bar{N} \equiv \langle \hat{a}^\dagger \hat{a} \rangle = \frac{1}{2}[2\bar{\alpha}^2 + \cosh(2r) - 1], \quad (21)$$

and $C = \cos(2\phi - \theta) \sinh(2r)$. For a special case with the optimally squeezed amplitude quadrature ($\theta = 2\phi$), Eq. (20) simplifies to the formula given in Ref. [75]. Note that such phase optimization corresponds to the so-called principal squeezing [76,83,84].

Our main objective is to determine whether two-PB (2PB) and three-PB (3PB), as well as various types of nonstandard single-PB (NPB) and other phenomena such as PIT, can be generated or simulated with squeezed states. Thus, we have to examine higher-order correlation functions, namely, $g^{(3)}(0)$ and $g^{(4)}(0)$. We find that the third-order correlation function for the SCS with arbitrary angles θ and ϕ is

$$g^{(3)}(0) = 15 + 9(1 - 3\bar{\alpha}^2)\bar{N}^{-1} - 9\bar{\alpha}^2(1 + B)\bar{N}^{-2} + 2\bar{\alpha}^2(2\bar{\alpha}^2 + 3C)\bar{N}^{-3}, \quad (22)$$

which considerably simplifies for the optimally squeezed amplitude quadratures ($\theta = 2\phi$).

The analytical solution of the simplified criteria in Eq. (10) can be obtained for the optimally squeezed state holding the relation of $\theta = 2\phi$. Additionally, analytical solutions can also be found whenever one of the phases is fixed and the other takes any value from the range $[0, 2\pi]$. Our numerical and analytical results show that it is very unlikely to obtain the simplified conditions in Eq. (10) for two- and three-PB for the SCS having the optimally squeezed amplitude quadratures. The same conclusion holds for the SCS with one of the phases fixed and for any values of the other phase, α , and r . This conclusion has been confirmed numerically for 10^6 randomly generated SCS without fixing any parameters.

Thus, we have shown that multi-PB, according to the simplified criteria in Eq. (10), are very unlikely for any choice of the parameters of the SCS. This suggests that, by having a physical system evolving into a squeezed state, one can expect the possibility of generating single-PB but standard squeezing does *not* lead to the generation of this type of multi-PB.

In contrast to this, we find that two-PB is still possible, but according to the refined criteria in Eq. (8). Indeed, for properly chosen parameters M and ε of the SCS, two-PB can be observed as shown by the green regions in Fig. 9.

Nonstandard single-PB (of type 2) can occur for the SCS. Indeed, we have found analytical solutions satisfying both criteria in Eq. (13). Such solutions exist only for some relations between the phases of the displacement and squeezing operators. The ranges of these phases are collected in Table III. The nonstandard PB effect cannot be observed for other phase relations.

B. Displaced squeezed thermal states

In addition to the SCS, we also analyze the displaced squeezed thermal states (DSTS), which can be obtained by applying the displacement $\hat{D}(\alpha)$ and squeezing $\hat{S}(\xi)$ operators to a thermal state $\hat{\rho}_{\text{th}}(n_{\text{th}})$, i.e.,

$$\hat{\rho}(\alpha, \xi, n_{\text{th}}) = \hat{D}(\alpha)\hat{S}(\xi)\hat{\rho}_{\text{th}}(n_{\text{th}})\hat{S}^\dagger(\xi)\hat{D}^\dagger(\alpha). \quad (23)$$

The thermal state is characterized by the density matrix $\hat{\rho}_{\text{th}}(n_{\text{th}}) = \sum_n P_n |n\rangle\langle n|$, where $P_n = n_{\text{th}}^n / (1 + n_{\text{th}})^{n+1}$ is the probability of finding n thermal photons in a thermally excited mode having a geometric probability distribution, and n_{th} is the mean number of thermal photons.

TABLE III. Squeezed coherent states simulating nonstandard photon blockade (of type 2), for which $g^{(2)}(0) < 1$ and $g^{(3)}(0) > 1$ hold, vs the phase $\phi = \arg \alpha$ of the displacement operator and the phase $\theta = \arg \xi$ of the squeezing parameter.

θ	ϕ	NPB
0	$(-\pi/4; \pi/4)$ and $(3\pi/4; 5\pi/4)$	Yes
	$[\pi/4; 3\pi/4]$ and $[5\pi/4; 7\pi/4]$	No
π	$(\pi/4; 3\pi/4)$ and $(5\pi/4; 7\pi/4)$	Yes
	$[-\pi/4; \pi/4]$ and $[3\pi/4; 5\pi/4]$	No
$(-\pi/2; \pi/2)$	$0, \pi$	Yes
$[\pi/2; 3\pi/2]$		No
$[-\pi/2; \pi/2]$	$\pi/2$	No
$(\pi/2; 3\pi/2)$		Yes

In Appendix E we show explicitly that the DSTS $\hat{\rho}(\alpha, \xi, n_{\text{th}})$ are nonclassical if and only if the squeezing parameter $r \equiv |\xi|$ is greater than the critical value r_0 :

$$r > r_0 \equiv \frac{1}{2} \ln(1 + 2n_{\text{th}}). \quad (24)$$

These states are nonclassical, independent of the displacement parameter α , because they are described by a non-positive-semidefinite Glauber-Sudarshan P function. This is demonstrated in Appendix E without recalling the explicit form of the P function for the DSTS. Further discussion of the nonclassical ($r > r_0$) and classical ($r \leq r_0$) regimes of the DSTS in relation to their simulation of PIT is presented in Sec. V.

Applying the definition of the k th-order correlation functions $g^{(k)}(0)$, we can easily obtain the following relations describing the second- and third-order equal-time correlation functions:

$$g^{(2)}(0) = 3 + (1 - 2\bar{\alpha}^2)\bar{N}^{-1} - h^-, \quad (25)$$

$$g^{(3)}(0) = 15 + 9(1 - 3\bar{\alpha}^2)\bar{N}^{-1} - 9h^+ + 2\bar{\alpha}^2[2\bar{\alpha}^2 + 3(2n_{\text{th}} + 1)B]\bar{N}^{-3}, \quad (26)$$

where the mean photon number is

$$\bar{N} \equiv \langle \hat{a}^\dagger \hat{a} \rangle = \frac{1}{2}[2\bar{\alpha}^2 + (1 + 2n_{\text{th}}) \cosh(2r) - 1], \quad (27)$$

and the auxiliary functions are

$$h^\pm = \{n_{\text{th}}(1 + n_{\text{th}}) + \bar{\alpha}^2[1 \pm (2n_{\text{th}} + 1)C]\}\bar{N}^{-2}, \quad (28)$$

where C is defined below Eq. (21). For $\theta = 2\phi$, Eqs. (25) and (26) considerably simplify. In this special case, Eq. (25) reduces to the corresponding formula given in Ref. [75].

C. Photon correlations in squeezed coherent states

Here we analyze different kinds of PB and PIT effects as listed in Table II and shown in Figs. 3–12.

(i) Three-PT occurs when $1 < g^{(2)}(0) < g^{(3)}(0)$. We find that these conditions are satisfied for the SCS if $r > 0$ and α is smaller than a critical parameter α_0 , i.e.,

$$0 < \alpha < \alpha_0 \equiv \frac{1}{\sqrt{2}} \sqrt{1 + c^4 + c(2c + s)(cs - 1)}, \quad (29)$$

where hereafter $c = \cosh(r)$ and $s = \sinh(r)$.

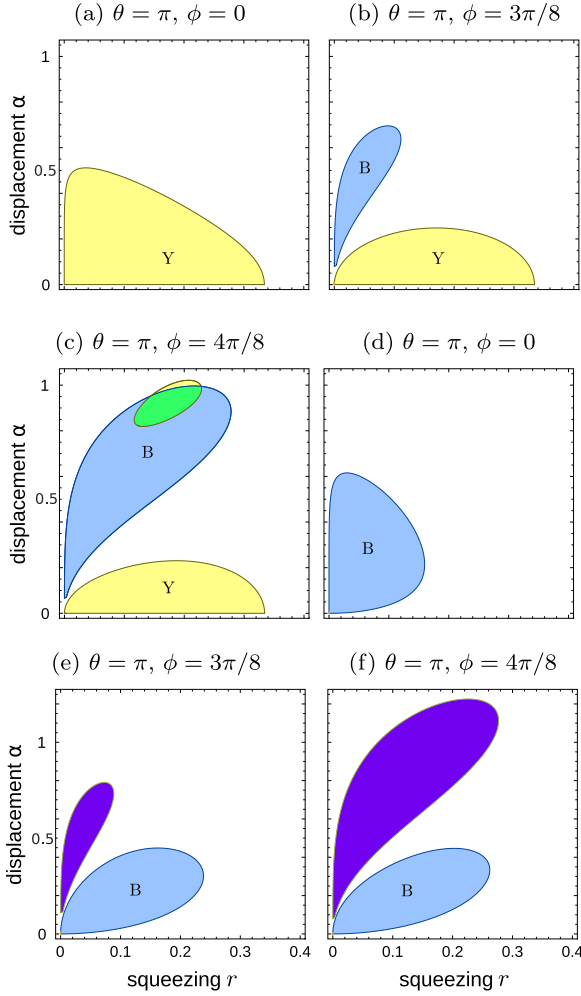


FIG. 10. Squeezed coherent states: regions of the displacement (α) and squeezing (r) parameters for which the *refined* photon blockade criteria in Eq. (8) are satisfied for two-photon (a)–(c) and three-photon (d)–(f) blockades. Specifically, the regions of the SCS parameters, where the criteria 1 and 2, are satisfied for $g^{(2)}(0)$, $g^{(3)}(0)$, and $g^{(4)}(0)$, are shown in yellow, blue, and violet (or navy blue), respectively. In grayscale, yellow (indicated by “Y”) is the brightest, and violet is the darkest color. Blue is marked by “B.” Two-photon blockade occurs if the criteria for $g^{(2)}(0)$ and $g^{(3)}(0)$ are both satisfied, which corresponds to the green region in (c). Three-photon blockade does not occur as the regions for $g^{(3)}(0)$ and $g^{(4)}(0)$ do not overlap.

(ii) Nonstandard single-PB of type 2, which is also referred to as unconventional PB in Ref. [77], occurs if $g^{(2)}(0) < 1 < g^{(3)}(0)$, which can be observed for the SCS if $\alpha \in (\alpha_0, \alpha_1)$ for $r > 0$, where the critical parameter α_0 is defined in Eq. (29) and another critical value of α is

$$\alpha_1 = \frac{1}{4\sqrt{6s}} \sqrt{3f_7 - 4(3c - 21s) + 8\sqrt{3\beta_1}(c + s)s^2}, \quad (30)$$

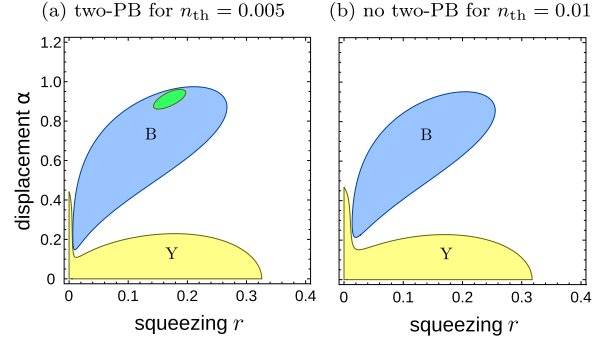


FIG. 11. Simulation of two-photon blockade with the displaced squeezed thermal states according to the refined criteria 1 and 2. Same as in Fig. 10 but for the DSTS with (a) $n_{\text{th}} = 0.005$ and (b) $n_{\text{th}} = 0.01$. We set here $\theta \equiv \arg \xi = \pi$ and $\phi \equiv \arg \alpha = 4\pi/8$. Two-photon blockade occurs only in panel (a) (in the green region). This green region is much larger for $n_{\text{th}} = 0$ as shown in Fig. 10(c). It is seen that even a very small number of thermal photons severely shrinks the range of the parameters allowing for the observation of two-photon blockade.

given in terms of the auxiliary functions:

$$f_x = x \exp(-3r) - 4 \exp(3r) + \exp(5r),$$

$$\beta_1 = 35 + 94c^4 + 2cs(70 + 47cs) - 2c^2(51 + 88cs). \quad (31)$$

(iii) Nonstandard three-PT occurs when $g^{(2)}(0) < g^{(3)}(0) < 1$. This effect can be observed for the SCS if $\alpha \in (\alpha_1, \alpha_2)$ for $r > 0$, where α_1 is defined in Eq. (30) and

$$\alpha_2 = \frac{1}{4\sqrt{2r}} \sqrt{f_9 - 2(3c - 17s) + 8\sqrt{2\beta_2}(c + s)s^2},$$

$$\beta_2 = 10 + 29c^4 + cs(40 + 29cs) - c^2(31 + 56cs). \quad (32)$$

(iv) Single-PB is usually verified by the simplified condition $g^{(2)}(0) < 1$. Stricter conditions for single-PB can be given as $g^{(3)}(0) < g^{(2)}(0) < 1$. These conditions are satisfied for the SCS if $\alpha > \alpha_2$ and $r > 0$.

(v) Our numerical and analytical calculations show that there are no solutions for α satisfying the conditions $1 < g^{(3)}(0) < g^{(2)}(0)$ for two-PT.

(vi) Two-PB can indeed be observed according to the refined conditions given in Eq. (8) for both SCS and DSTS, as shown by the green regions in Figs. 10(c) and 11(a), respectively, for specific choices of the squeezing phase $\theta = \pi$ and the displacement phase $\phi = 4\pi/8$. It is seen in Figs. 10(a) and 10(b) that two-PB cannot be observed for the phases $\phi = 0, 3\pi/8$. Figures 10(c) and 11 show the destructive role of thermal photons n_{th} for the generation of two-PB. Indeed, the green region in Figs. 10(c) and 11 decreases with increasing n_{th} , and it is not seen any more for $n_{\text{th}} = 0.01$ in Fig. 11(b).

In contrast to this refined two-PB, our analytical and numerical calculations show that the simplified criteria in Eq. (10) for two-PB are very unlikely to be satisfied as graphically explained in Fig. 4(e) for the SCS and Fig. 5(e) for the DSTS.

Moreover, our both numerical and analytical results show that three-PB can be simulated by neither SCS nor DSTS

according to the refined and simplified criteria of PB, given in Eqs. (8) and (9), respectively. Indeed, the criteria 1 and 2 can be satisfied separately, as shown by the violet and blue regions in Figs. 10(d) and 10(e), but they cannot be satisfied simultaneously for the same values of the squeezing parameter r and the displacement parameter α . This result implies that the colored regions in these figures do not overlap.

V. NONCLASSICAL AND CLASSICAL EFFECTS AND STATES

Now we address the question whether the analyzed effects and states are nonclassical or not.

We apply here the standard quantum-optical definition (or criterion) of the nonclassicality of a single-mode bosonic state $\hat{\rho}$ in terms of the Glauber-Sudarshan P function [85]:

$$\hat{\rho} = \int d^2\beta P(\beta, \beta^*) |\beta\rangle\langle\beta|, \quad (33)$$

where $|\beta\rangle$ is a coherent state with a complex amplitude β . According to this common definition (see, e.g., Refs. [76,85]), a given state $\hat{\rho}$ is referred to as classical, if it is described by a classical-like (i.e., non-negative) P function. Otherwise, a state $\hat{\rho}$ is considered nonclassical (or quantum), i.e., when it is described by a negative (or more precisely nonpositive or non-positive-semidefinite) P function. Thus, according to this definition, *only* coherent states and their mixtures (including thermal states) can be considered classical, while all other mixed and pure states (including squeezed states) are nonclassical.

Single- and multi-PB effects are indeed purely nonclassical as shown explicitly in Appendix C.

PIT is usually also considered a quantum effect (as emphasized in, e.g., Refs. [38,60]), even if it is characterized by a classical-like property of the photon-number distributions, i.e., the second-order or higher-order super-Poissonian photon-number statistics (i.e., single-time photon bunching). We note that $g^{(2)}(0) \geq 1$ is usually regarded as “a general property of all kinds of classical light” [86]. Indeed, thermal states, which are classical as given by the mixtures of coherent states, can simulate PIT as shown in Appendix D.

A number of nonclassicality measures of bosonic fields have been proposed, which include nonclassical depth [87], nonclassical distance [88], and the nonclassicality volume [89], which corresponds to the volume of the negative part of the Wigner function (see, e.g., Ref. [90] and references therein). Here, we apply an entanglement potential (EP) introduced by Asbóth *et al.* [91]. Entanglement potentials are, in general, numerically and experimentally simpler than other formally defined nonclassicality measures, including the nonclassical depth and distance. Moreover, entanglement potentials are much more sensitive in detecting nonclassicality compared to the nonclassicality volume. Indeed, the nonclassicality volume of the SCS studied here is exactly zero, although the states are nonclassical according to entanglement potentials.

The basic idea of entanglement potentials is physically quite simple: By combining a classical single-mode light with the vacuum on a beam splitter (BS), then the output state is separable. In contrast to this, if the input light is nonclassical

then the output light from a lossless beam splitter is entangled. Moreover, the degree of nonclassicality is not changed by lossless linear-optical transformations (including beam splitters). Thus, the degree of nonclassicality of the input state can be measured by the output-state entanglement by applying standard entanglement measures [92], e.g., the negativity, the concurrence, or the relative entropy of entanglement [91,93].

To be more specific, the nonclassicality of a single-mode state $\hat{\rho} \equiv \hat{\rho}_{\text{in}}$ can be quantified, according to Ref. [91], by the entanglement of the output state ρ_{out} of an auxiliary lossless balanced BS with the state $\hat{\rho}$ and the vacuum $|0\rangle$ at the inputs, i.e.,

$$\hat{\rho}_{\text{out}} = \hat{U}_{\text{BS}}(\hat{\rho}_{\text{in}} \otimes |0\rangle\langle 0|)\hat{U}_{\text{BS}}^\dagger, \quad (34)$$

where \hat{U}_{BS} is the unitary transformation of a balanced (50:50) lossless beam splitter,

$$\hat{U}_{\text{BS}} = \exp\left[-i\frac{\pi}{2}(\hat{a}_1^\dagger\hat{a}_2 + \hat{a}_1\hat{a}_2^\dagger)\right], \quad (35)$$

and $\hat{a}_{1,2}$ ($\hat{a}_{1,2}^\dagger$) are the annihilation (creation) operators of the input modes. We apply here the EP based on the negativity (N) [91,92]:

$$\begin{aligned} \text{EP}(\hat{\rho}_{\text{in}}) &\equiv E_N(\hat{\rho}_{\text{out}}) = \log_2[N(\hat{\rho}_{\text{out}}) + 1] \\ &= \log_2\|\hat{\rho}_{\text{out}}^\Gamma\|_1, \end{aligned} \quad (36)$$

which is given in terms of the trace norm $\|\hat{\rho}^\Gamma\|_1$ of the partially transposed statistical operator $\hat{\rho}^\Gamma$, and the logarithmic negativity E_N . We note that the negativity and, thus, the corresponding entanglement potential determine, e.g., (i) the entanglement cost $E_{\text{cost}} \equiv E_N$ under operations preserving the positivity of the partial transpose (at least for single-PB entangled states) [92] and (ii) the dimensionality of entanglement, which is the number of the degrees of freedom of entangled beams [35,94].

The entanglement potential, defined in Eq. (36), for the DSTS is given by the following simple formula [91]:

$$\text{EP}[\hat{\rho}(\alpha, \xi, n_{\text{th}})] = \frac{r - r_0}{\ln 2}, \quad (37)$$

where the critical parameter r_0 is given in Eq. (24). This entanglement potential is plotted in Fig. 12(a) together with the squeezing variance, which is another nonclassicality measure of the DSTS. Indeed, in Fig. 12(b), we plotted the truncated squeezing variance defined as [95]

$$\tilde{V} \equiv \min[0, -\langle(\Delta\hat{X}_{\varphi_0})^2\rangle], \quad (38)$$

where the squeezing variance for the DSTS is (see Appendix E)

$$\langle(\Delta\hat{X}_{\varphi_0})^2\rangle = \frac{1}{2}\left(\frac{1}{2} + n_{\text{th}}\right)\exp(-2r) = \frac{1}{4}\exp[-2(r - r_0)], \quad (39)$$

and $\langle(\Delta\hat{X}_{\varphi_0})^2\rangle = \langle(\Delta\hat{X}_{\varphi_0})^2\rangle - 1/4$. We note that, in general, squeezing for an optimal phase φ_0 is referred to as principal squeezing [76,83] and its geometrical interpretation can be provided by Booth's elliptical lemniscates [84]. Figure 12(b) clearly shows the same nonclassical and classical regimes of the DSTS, as those in Fig. 12(a) for the entanglement potential, as explained in greater detail in Appendix E.

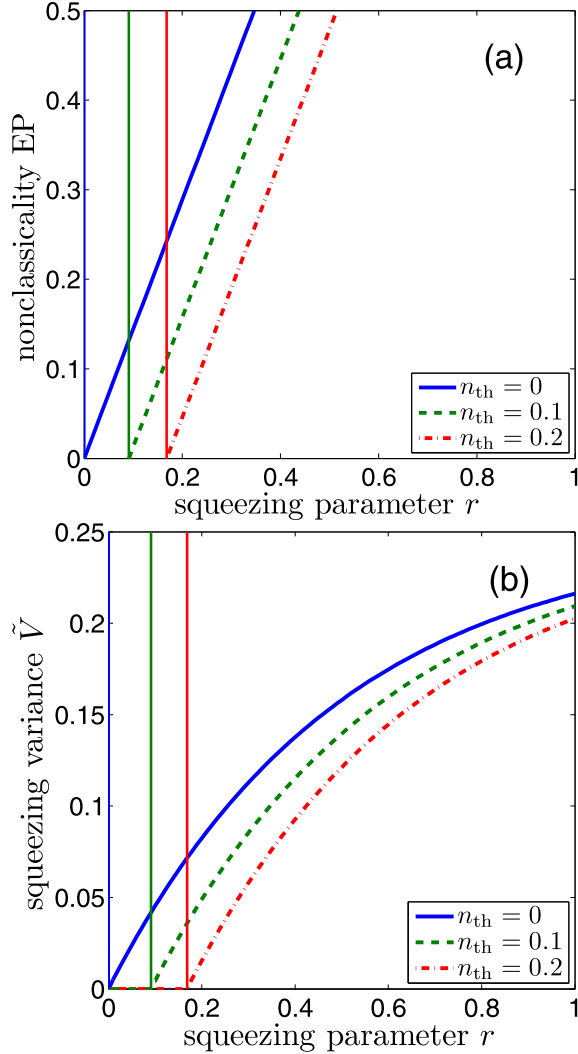


FIG. 12. Nonclassicality measures of the displaced squeezed thermal states: (a) entanglement potential, EP, of $\hat{\rho}(\alpha, \xi, n_{\text{th}})$ and (b) the truncated squeezing variance \tilde{V} , defined in Eq. (38), vs the squeezing parameter $r = |\xi|$ for different values of the mean numbers of thermal photons n_{th} . The EP and squeezing variance are independent of the displacement parameter α and the squeezing phase θ . It is seen that the critical values r_0 (specifically, $r_0 = 0, 0.0912, 0.1682$) of the squeezing parameter r increase with increasing n_{th} (i.e., $n_{\text{th}} = 0, 0.1, 0.2$), according to Eq. (24) as indicated by the vertical thin solid lines.

By comparing Eqs. (37) and (39), it is seen that the EP is a monotonic function of the squeezing variance for the DSTS, i.e.,

$$\text{EP} = -\frac{1}{2} \log_2 \langle (\Delta \hat{X}_{\varphi_0})^2 \rangle - 1. \quad (40)$$

Note that these quantities are also monotonically related to the nonclassical depth for the DSTS [87].

The nonclassicality of an arbitrary two-mode Gaussian state $\hat{\rho}_{\text{out}}$ (which includes an arbitrary single-mode state $\hat{\rho}_{\text{in}}$

studied in this paper) can also be analyzed by applying a numerically efficient nonclassicality invariant proposed in Ref. [96]. That quantifier is invariant under any global unitary photon-number-preserving transformations of the covariance matrix of a Gaussian state.

Thus, we have shown that not all our numerical predictions of PIT and other photon-number correlations correspond to quantum states, but only those for $r > r_0$ are nonclassical for the DSTS. To make this distinction clearer, we plotted in Figs. 5 and 12 the borderline at $r = r_0$ between the classical and nonclassical regimes of the DSTS. We emphasize that all SCS with nonzero squeezing parameter r are nonclassical, which is a special case of the DSTS for $n_{\text{th}} = 0$. Thus, all our numerical predictions shown in Figs. 4 and 10 correspond to nonclassical states.

VI. CONCLUSIONS

Single- and two-photon blockades have been usually studied in a driven nonlinear cavity [see Fig. 1(b)] or cavities [see Fig. 1(c)] coupled to a harmonic reservoir (a thermal bath). Only a few works (including Refs. [74,75]) were devoted to the analysis of single-photon blockade via quantum nonlinear reservoir engineering.

In this paper we showed that a driven harmonic cavity coupled to a squeezed reservoir, as schematically shown in Fig. 1(a), can generate light exhibiting various types of photon blockade and related phenomena. These include two-photon blockade (as defined in Sec. II A), three-photon tunneling (defined in Sec. I D), and three nonstandard types of single-photon blockade (defined in Sec. II C), in addition to standard single-photon blockade. Our theoretical interest in studying two-photon blockade [53] has been stimulated by a recent experiment of the Rempe group [44].

As shown in Refs. [97,98], the roles of the Kerr nonlinear interaction and two-photon dissipation can be interchanged in the steady states of the systems undergoing these processes. This might explain why the linear system shown in Fig. 1(a), being coupled to a squeezed reservoir, enables the generation of photon blockade analogously to the standard Kerr nonlinear systems shown in Figs. 1(b) and 1(c) in the dispersive limit. Indeed, a squeezed reservoir allows for two-photon dissipation.

We considered various types of nonstandard photon-number-correlation effects by analyzing different properties of second- and third-order single-time correlation functions (as listed in Table II), and two-time correlations described by $g^{(2)}(\tau)$.

We also simulated these multiphoton effects with squeezed coherent states and displaced squeezed thermal states, inspired by the prediction [75] of single-photon blockade in a linear system with nonlinear damping. The relation between the squeezed-state simulations of these effects and their generation via squeezed reservoir is explained in Appendix B.

Photon blockade in nonlinear systems coupled to thermal reservoirs has already attracted considerable interest, as confirmed by a number of experimental demonstrations [37–46]. Thus, we hope that the described method of quantum reservoir engineering, which enables the generation of multiphoton blockade, photon-induced tunneling, and related phenomena,

can also stimulate further theoretical and experimental research in optical and microwave photonics [17].

ACKNOWLEDGMENTS

The authors kindly acknowledge insightful discussions with Fabrizio Minganti and Wei Qin. J.P. is supported by GA ĆR Project No. 18-22102S. F.N. is supported in part by the Multidisciplinary University Research Initiative Center for Dynamic Magneto-Optics via the Air Force Office of Scientific Research (Grant No. FA9550-14-1-0040), Asian Office of Aerospace Research and Development (Grant No. FA2386-18-1-4045), Japan Science and Technology Agency (via the Q-LEAP program and CREST Grant No. JPMJCR1676), Japan Society for the Promotion of Science (JSPS) (JSPS-RFBR Grant No. 17-52-50023 and JSPS-FWO Grant No. VS.059.18N), the FQXi, the NTT PHi Lab, and the RIKEN-AIST Challenge Research Fund. Finally, F.N. and A.M. are supported by the Army Research Office (Grant No. W911NF-18-1-0358).

APPENDIX A: STANDARD SYSTEMS FOR STUDYING CONVENTIONAL AND UNCONVENTIONAL PHOTON BLOCKADE

For a better comparison of the proposed PB system shown in Fig. 1(a), we briefly recall here the prototype systems for generating conventional [see Fig. 1(b)] and unconventional [see Fig. 1(c)] PB effects.

(1) Conventional PB is usually studied in a driven Kerr nonlinear system described by the Hamiltonian

$$\hat{H}_a = \omega_c \hat{a}^\dagger \hat{a} + \varepsilon (\hat{a} e^{i\omega_a t} + \hat{a}^\dagger e^{-i\omega_a t}) + \chi \hat{a}^\dagger \hat{a}^\dagger \hat{a} \hat{a}, \quad (\text{A1})$$

where χ is a Kerr nonlinearity proportional to the third-order susceptibility $\chi^{(3)}$, and the other terms of this Hamiltonian are the same as in Eq. (15). The Hamiltonian (A1) can be effectively derived (see, e.g., Ref. [53] and references therein) from the Jaynes-Cummings model in the dispersive limit (i.e., far off resonance) describing a driven cavity interacting with a two-level system (qubit) under the rotating wave approximation. Thus, the system shown schematically in Fig. 1(b) can be given by the Hamiltonian

$$\begin{aligned} \hat{H}_a^q &= \frac{1}{2} \omega \hat{\sigma}_z + \omega_c \hat{a}^\dagger \hat{a} + g (\hat{\sigma}^+ \hat{a} + \hat{a}^\dagger \hat{\sigma}^-) \\ &+ \varepsilon (\hat{a} e^{i\omega_a t} + \hat{a}^\dagger e^{-i\omega_a t}), \end{aligned} \quad (\text{A2})$$

where $\hat{\sigma}^-$ ($\hat{\sigma}^+$) is the qubit lowering (raising) operator; $\sigma_z = |e\rangle\langle e| - |g\rangle\langle g|$ is a Pauli operator; and $|g\rangle$ ($|e\rangle$) is the ground (excited) state of the two-level system.

(2) The prototype Hamiltonian for generating unconventional PB is given by [47–50]

$$\hat{H}_{ab} = \hat{H}_a + \hat{H}_b + J \hat{a}^\dagger \hat{b} + J^* \hat{a} \hat{b}^\dagger, \quad (\text{A3})$$

where

$$\hat{H}_b = \omega'_c \hat{b}^\dagger \hat{b} + \varepsilon' (\hat{b} e^{i\omega'_a t} + \hat{b}^\dagger e^{-i\omega'_a t}) + \chi' \hat{b}^\dagger \hat{b}^\dagger \hat{b} \hat{b}, \quad (\text{A4})$$

where \hat{b} (\hat{b}^\dagger) is the annihilation (creation) operator of the optical mode in the second cavity, χ' is the Kerr nonlinearity of the second cavity, and the quantities ω'_c , ω'_a , and ε' correspond, respectively, to ω_c , ω_a , and ε in Eq. (15), but for the second cavity.

In analogy to the derivation of the conventional Kerr-nonlinear Hamiltonian in Eq. (A1) from Eq. (A2), also Eq. (A3) can be derived from the two linearly coupled driven Jaynes-Cummings systems in the dispersive limit. Such a two-cavity system can be described by

$$\hat{H}_{ab}^q = \hat{H}_a^q + \hat{H}_b^q + J \hat{a}^\dagger \hat{b} + J^* \hat{a} \hat{b}^\dagger, \quad (\text{A5})$$

where \hat{H}_b^q is defined analogously to \hat{H}_a^q in Eq. (A2), but for the mode \hat{b} of the second cavity. This two-atom system can be simplified to include only one atom, which is the case shown in Fig. 1(c).

The dissipative evolution of such PB systems has been usually studied assuming their coupling to a thermal reservoir within the Lindblad master equation,

$$\frac{d\hat{\rho}}{dt} = -i[\hat{H}, \hat{\rho}] + \frac{1}{2}\gamma\{(n_{\text{th}} + 1)\Gamma_1[\hat{a}]\hat{\rho} + n_{\text{th}}\Gamma_1[\hat{a}^\dagger]\hat{\rho}\}, \quad (\text{A6})$$

for the reduced density matrix $\hat{\rho}$, where the Lindblad superoperator $\Gamma_1[\hat{x}]\hat{\rho}$ is defined in Eq. (B2) in Appendix B, γ is the damping rate, and $n_{\text{th}} = \{\exp[\hbar\omega/(k_B T)] - 1\}^{-1}$ is the mean thermal photon number.

APPENDIX B: MASTER EQUATION FOR THE SQUEEZED-VACUUM RESERVOIR

Here, we show more explicitly the relation between squeezed states and a squeezed reservoir by studying the master equation for the squeezed-vacuum reservoir, given in Eq. (17) in its special case for $|M| = \sqrt{n(n+1)}$. Our presentation is based on Refs. [80–82] (see also, e.g., Ref. [99]).

The master equation in Eq. (17), with the system Hamiltonian \hat{H} in Eq. (16), can be rewritten more compactly as

$$\begin{aligned} \frac{d\hat{\rho}}{dt} &= -i[\hat{H}, \hat{\rho}] + \frac{1}{2}\gamma\{(n+1)\Gamma_1[\hat{a}]\hat{\rho} + n\Gamma_1[\hat{a}^\dagger]\hat{\rho} \\ &- M\Gamma_2[\hat{a}]\hat{\rho} - M^*\Gamma_2[\hat{a}^\dagger]\hat{\rho}\}, \end{aligned} \quad (\text{B1})$$

using the superoperators defined as

$$\Gamma_1[\hat{x}]\hat{\rho} = 2\hat{x}\hat{\rho}\hat{x}^\dagger - \hat{x}^\dagger\hat{x}\hat{\rho} - \hat{\rho}\hat{x}^\dagger\hat{x}, \quad (\text{B2})$$

$$\Gamma_2[\hat{x}]\hat{\rho} = 2\hat{x}\hat{\rho}\hat{x} - \hat{x}\hat{x}\hat{\rho} - \hat{\rho}\hat{x}\hat{x}. \quad (\text{B3})$$

This master equation can be derived by considering a system described by \hat{H}' in Eq. (15) or, equivalently, \hat{H} in Eq. (16), with its cavity mode \hat{a} being linearly coupled to an infinite set of reservoir modes \hat{b}_k [99]. We assume that the reservoir modes \hat{b}_k are initially in the squeezed vacuum states,

$$|\vec{\xi}\rangle = \prod_k |\xi_k\rangle = \prod_k \hat{S}_k(\xi)|0_k\rangle, \quad (\text{B4})$$

where the k th-mode squeezing operator is given by

$$\hat{S}_k = \exp(\xi^* \hat{b}_{k_0+k} \hat{b}_{k_0-k} - \text{H.c.}), \quad (\text{B5})$$

where $k_0 = \omega_c/c$, $\xi = r \exp(i\theta)$ is the usual complex squeezing parameter, and H.c. denotes the corresponding Hermitian-conjugate term. Thus, \hat{S}_k in Eq. (B5) is a two-mode squeezing operator for each k . Note that the master equation in Eq. (B1) can also be derived for a single-mode squeezing operator acting on each reservoir mode k [81]. The total initial state

is assumed to be $\hat{\rho}_T = \hat{\rho}(0) \otimes |\bar{\xi}\rangle\langle\bar{\xi}|$, and the total system-reservoir Hamiltonian reads

$$\hat{H}_T = \hat{H}' + \sum_k \omega_k \hat{b}_k^\dagger \hat{b}_k + \sum_k g_k (\hat{a} \hat{b}_k^\dagger + \hat{a}^\dagger \hat{b}_k), \quad (\text{B6})$$

where g_k is the coupling strength between the system mode \hat{a} and the reservoir mode \hat{b}_k . The standard procedure of deriving the equation of motion for the reduced density matrix $\hat{\rho}$ under the Markov approximation results in the master equation, given in Eq. (B1) in the interaction picture, where

$$\begin{aligned} \langle \hat{b}_k^\dagger \hat{b}_{k'} \rangle &= n \delta_{kk'} = \sinh^2(r) \delta_{kk'}, \\ \langle \hat{b}_k \hat{b}_{k'} \rangle &= -M^* \delta_{kk'} = -\cosh(r) \sinh(r) e^{i\theta} \delta_{kk'}, \end{aligned} \quad (\text{B7})$$

with $k' = 2k_0 - k$. By applying the Bogoliubov transformation,

$$\begin{aligned} \hat{a}_s &= \hat{S}^\dagger \hat{a} \hat{S} = \cosh(r) \hat{a} - \sinh(r) e^{i\theta} \hat{a}^\dagger, \\ \hat{a}_s^\dagger &= \hat{S}^\dagger \hat{a}^\dagger \hat{S} = \cosh(r) \hat{a}^\dagger - \sinh(r) e^{-i\theta} \hat{a}, \end{aligned} \quad (\text{B8})$$

where $\hat{S}(\xi)$ is the squeezing operator defined in Eq. (19), the master equation in Eq. (B1) for $\Delta = 0$ reduces, in the squeezed-vacuum frame, to the standard-form master equation without Γ_2 terms, i.e.,

$$\frac{d\hat{\rho}}{dt} = -i[\hat{H}_s, \hat{\rho}] + \frac{\gamma}{2} \Gamma_1[\hat{a}_s] \hat{\rho}, \quad (\text{B9})$$

or, equivalently,

$$\frac{d\hat{\rho}_s}{dt} = -i[\hat{H}, \hat{\rho}_s] + \frac{\gamma}{2} \Gamma_1[\hat{a}] \hat{\rho}_s, \quad (\text{B10})$$

where $\hat{\rho}_s = \hat{S} \hat{\rho} \hat{S}^\dagger$ and

$$\hat{H}_s = \hat{S}^\dagger \hat{H} \hat{S} = \varepsilon (\hat{a}_s^\dagger + \hat{a}_s). \quad (\text{B11})$$

As mentioned above, the resonant case $\Delta = 0$ is assumed here. Note that for $\Delta \neq 0$ terms proportional to \hat{a}^2 and $(\hat{a}^\dagger)^2$ should be added to the master equations in (B9) and (B10).

APPENDIX C: NONCLASSICALITY OF PHOTON BLOCKADE

Here we recall that PB is a nonclassical effect. First we show this for single-PB using the P -function approach. And then we apply another approach for any multi-PB.

We first recall that $(\hat{a}^\dagger)^2 \hat{a}^2 = \hat{n}(\hat{n}-1) =: \hat{n}^2$, where $:$ means the normal ordering of the creation and annihilation operators. The photon-number variance $(:\Delta\hat{n}^2:)$ is simply related to $g^{(2)}(0)$ as follows:

$$(:\Delta\hat{n}^2:) = (:\hat{n}^2:) - \langle\hat{n}\rangle^2 = [g^{(2)}(0) - 1] \langle\hat{n}\rangle^2, \quad (\text{C1})$$

where $\Delta\hat{n} = \hat{n} - \langle\hat{n}\rangle$. So, $g^{(2)}(0) < 1$ if and only if the variance is negative:

$$(:\Delta\hat{n}^2:) = \int d^2\beta P(\beta, \beta^*) (|\beta|^2 - \langle\hat{n}\rangle)^2 < 0. \quad (\text{C2})$$

Because the terms $(|\beta|^2 - \langle\hat{n}\rangle)^2 \geq 0$ and $(:\Delta\hat{n}^2:) < 0$, then $P(\beta, \beta^*)$ must also be negative in some regions of phase space. This means that the state $\hat{\rho}$, which exhibits single-PB, is described by a non-positive-semidefinite $P(\beta, \beta^*)$, and, thus, has to be nonclassical.

The nonclassicality of single- and multi-PB can be shown even faster by recalling the following facts: (1) classical states of light are either coherent states or their mixtures; (2) coherent states are characterized by $g^{(k)}(0) = 1$, for any $k \geq 1$; (3) k -PB requires $g^{(k+1)}(0) < 1$, or even the sharper condition $g^{(k+1)}(0) < A \equiv \exp(-\langle\hat{n}\rangle) \leq 1$, according to the refined PB criterion 1 in Eq. (8). So, single- and multi-PB can occur only for photon-number distributions which are sharper [79] than that of a coherent state and, therefore, also sharper than any mixtures of coherent states. This completes our proofs.

APPENDIX D: CLASSICAL SIMULATION OF PHOTON-INDUCED TUNNELING WITH THERMAL STATES

Here we show that usual thermal states can simulate the PIT of an arbitrary number of photons.

The thermal-state probability P_n of measuring n photons can be compactly written as $P_n = yx^n$, where $x = \langle\hat{n}\rangle y$, $y = 1/(1 + \langle\hat{n}\rangle)$, and $\langle\hat{n}\rangle \equiv \bar{n}_{\text{th}} = \{\exp[\hbar\omega/(k_B T)] - 1\}^{-1}$. Then the geometric series for the second- and higher-order correlation functions $g^{(k)}(0)$ can be easily calculated as

$$\begin{aligned} g^{(2)}(0) &= \frac{y}{\langle\hat{n}\rangle^2} \sum_n x^n n(n-1) = 2, \\ g^{(3)}(0) &= \frac{y}{\langle\hat{n}\rangle^3} \sum_n x^n n(n-1)(n-2) = 6. \end{aligned} \quad (\text{D1})$$

These values can also be obtained from Eqs. (25) and (26) in their special cases for $\alpha = r = 0$.

By induction, we conclude that for any order $k > 1$ the correlation function $g^{(k)}(0)$ for the thermal state with the mean photon number $\langle\hat{n}\rangle$ becomes

$$g^{(k)}(0) = \langle\hat{n}\rangle^{-k} \sum_n P_n n^{[k]} = k!, \quad (\text{D2})$$

where $n^{[k]} = n(n-1)\cdots(n-k+1)$. This implies that for any $k > 1$ and $\langle\hat{n}\rangle > 0$ the following holds:

$$1 < g^{(k)}(0) < g^{(k+1)}(0). \quad (\text{D3})$$

Thus, thermal states can simulate the PIT of any number of (thermal) photons. In particular, this includes two- and three-PB, which are characterized by the conditions $1 < g^{(2)}(0)$ and Eq. (3), respectively.

APPENDIX E: NONCLASSICAL AND CLASSICAL REGIMES OF DISPLACED SQUEEZED THERMAL STATES

For completeness of our presentation, we show explicitly that the DSTS, given by $\hat{\rho}(\alpha, \xi, n_{\text{th}})$, are nonclassical if the inequality $|\xi| > r_0$, given in Eq. (24), is satisfied.

By defining a phase-dependent quadrature operator

$$\hat{X}_\varphi = \frac{1}{2}[\hat{a} \exp(i\varphi) + \hat{a}^\dagger \exp(-i\varphi)], \quad (\text{E1})$$

the minimum value of the normally ordered variance $\langle : (\Delta \hat{X}_\varphi)^2 : \rangle$ for the DSTS is given by

$$\min_{\varphi} \langle : (\Delta \hat{X}_\varphi)^2 : \rangle \equiv \langle : (\Delta \hat{X}_{\varphi_0})^2 : \rangle = \frac{1}{4} \exp[-2(r - r_0)] - \frac{1}{4}, \quad (\text{E2})$$

where φ_0 denotes the optimal value of the quadrature phase φ . In particular, $\varphi_0 = 0$ for the squeezing phase $\theta = 0$. Moreover, $::$ denotes normal ordering and $\Delta \hat{X}_\varphi = \hat{X}_\varphi - \langle \hat{X}_\varphi \rangle$. It is seen that Eq. (E2) is independent of the displacement parameter α and, thus, equivalent to the variance for the squeezed thermal states first derived in Ref. [100].

Squeezing occurs if $\langle : (\Delta X_{\varphi_0})^2 : \rangle < 0$. This normally ordered variance can be directly calculated from the corresponding P function:

$$\langle : (\Delta X_{\varphi_0})^2 : \rangle = \int d^2\beta P(\beta, \beta^*) [X_{\varphi_0}(\beta, \beta^*) - \langle \hat{X}_{\varphi_0} \rangle]^2 < 0, \quad (\text{E3})$$

where

$$X_{\varphi_0} = \frac{1}{2} [\beta \exp(i\varphi_0) + \beta^* \exp(-i\varphi_0)]. \quad (\text{E4})$$

Because the term $[...]^2$ is non-negative and $\langle : (\Delta X_{\varphi_0})^2 : \rangle$ is negative for any squeezed state, then $P(\beta, \beta^*)$ has to be negative in some regions of phase space. This means that the DSTS for $r > r_0$ are nonclassical. This result is confirmed by Eq. (37) for the entanglement potential, and shown in Fig. 12. Thus, the requirement $r > r_0$ is the necessary and sufficient condition of the P -function-based nonclassicality for the DSTS. This implies that any nonclassical DSTS exhibits quadrature squeezing.

In a special case of the SCS, given by $|\alpha, \xi\rangle = \hat{D}(\alpha)\hat{S}(\xi)|0\rangle$, we recover the well-known result that $r_0 = 0$, which means that any SCS with a nonzero squeezing parameter is nonclassical [3].

Thus, to show the nonclassicality of the DSTS, we have plotted the entanglement potential and the squeezing variance in Figs. 12(a) and 12(b), respectively. Moreover, we plotted the red vertical line at $r = r_0$ in Fig. 5 to show more explicitly the borderline between the classical and nonclassical regimes of the DSTS.

-
- [1] V. Dodonov, “Nonclassical” states in quantum optics: A ‘squeezed’ review of the first 75 years, *J. Opt. B: Quant. Semiclass. Opt.* **4**, R1 (2002).
- [2] D. F. Walls, Squeezed states of light, *Nature (London)* **306**, 141 (1983).
- [3] R. Loudon and P. Knight, Squeezed Light, *J. Mod. Opt.* **34**, 709 (1987).
- [4] *Theory of Nonclassical States of Light*, edited by V. Dodonov and V. Man’ko (Taylor & Francis, London, 2002).
- [5] *Quantum Squeezing*, edited by P. D. Drummond and Z. Ficek (Springer-Verlag, Berlin, 2004).
- [6] U. L. Andersen, T. Gehring, C. Marquardt, and G. Leuchs, 30 years of squeezed light generation, *Phys. Scr.* **91**, 053001 (2016).
- [7] E. H. Kennard, Zur Quantenmechanik einfacher Bewegungstypen, *Z. Phys.* **44**, 326 (1927).
- [8] L. Infeld and J. Plebański, On a certain class of unitary transformations, *Acta Phys. Pol.* **14**, 41 (1955).
- [9] J. Plebański, Wave functions of a harmonic oscillator, *Phys. Rev.* **101**, 1825 (1956).
- [10] J. N. Hollenhorst, Quantum limits on resonant-mass gravitational-radiation detectors, *Phys. Rev. D* **19**, 1669 (1979).
- [11] C. M. Caves, K. S. Thorne, R. W. P. Drever, V. D. Sandberg, and M. Zimmermann, On the measurement of a weak classical force coupled to a quantum-mechanical oscillator. I. Issues of principle, *Rev. Mod. Phys.* **52**, 341 (1980).
- [12] V. Dodonov, V. Man’ko, and V. Rudenko, Nondemolition measurements in gravitational-wave experiments, *Sov. Phys. JETP* **51**, 443 (1980).
- [13] C. M. Caves, Quantum-mechanical noise in an interferometer, *Phys. Rev. D* **23**, 1693 (1981).
- [14] R. E. Slusher, L. W. Hollberg, B. Yurke, J. C. Mertz, and J. F. Valley, Observation of Squeezed States Generated by Four-Wave Mixing in an Optical Cavity, *Phys. Rev. Lett.* **55**, 2409 (1985).
- [15] L.-A. Wu, H. J. Kimble, J. L. Hall, and H. Wu, Generation of Squeezed States by Parametric Down Conversion, *Phys. Rev. Lett.* **57**, 2520 (1986).
- [16] R. M. Shelby, M. D. Levenson, S. H. Perlmutter, R. G. DeVoe, and D. F. Walls, Broad-Band Parametric Deamplification of Quantum Noise in an Optical Fiber, *Phys. Rev. Lett.* **57**, 691 (1986).
- [17] X. Gu, A. F. Kockum, A. Miranowicz, Y.-X. Liu, and F. Nori, Microwave photonics with superconducting quantum circuits, *Phys. Rep.* **718–719**, 1 (2017).
- [18] LIGO Scientific Collaboration, Enhanced sensitivity of the LIGO gravitational wave detector by using squeezed states of light, *Nat. Photonics* **7**, 613 (2013).
- [19] H. Grote, K. Danzmann, K. L. Dooley, R. Schnabel, J. Slutsky, and H. Vahlbruch, First Long-Term Application of Squeezed States of Light in a Gravitational-Wave Observatory, *Phys. Rev. Lett.* **110**, 181101 (2013).
- [20] M. Bartkowiak, L.-A. Wu, and A. Miranowicz, Quantum circuits for amplification of Kerr nonlinearity via quadrature squeezing, *J. Phys. B* **47**, 145501 (2014).
- [21] X.-Y. Lü, Y. Wu, J. R. Johansson, H. Jing, J. R. Zhang, and F. Nori, Squeezed Optomechanics with Phase-Matched Amplification and Dissipation, *Phys. Rev. Lett.* **114**, 093602 (2015).
- [22] M.-A. Lemonde, N. Didier, and A. A. Clerk, Enhanced nonlinear interactions in quantum optomechanics via mechanical amplification, *Nat. Commun.* **7**, 11338 (2016).
- [23] W. Qin, A. Miranowicz, P.-B. Li, X.-Y. Lü, J. Q. You, and F. Nori, Exponentially Enhanced Light-Matter Interaction, Cooperativities, and Steady-State Entanglement Using Parametric Amplification, *Phys. Rev. Lett.* **120**, 093601 (2018).
- [24] C. Leroux, L. C. G. Govia, and A. A. Clerk, Enhancing Cavity Quantum Electrodynamics via Antisqueezing: Synthetic Ultrastrong Coupling, *Phys. Rev. Lett.* **120**, 093602 (2018).

- [25] W. Qin, V. Macri, A. Miranowicz, S. Savasta, and F. Nori, Emission of photon pairs by mechanical stimulation of the squeezed vacuum, *Phys. Rev. A* (to be published), [arXiv:1902.04216](https://arxiv.org/abs/1902.04216).
- [26] A. F. Kockum, A. Miranowicz, S. D. Liberato, S. Savasta, and F. Nori, Ultrastrong coupling between light and matter, *Nat. Rev. Phys.* **1**, 19 (2019).
- [27] A. Ridolfo, M. Leib, S. Savasta, and M. J. Hartmann, Photon Blockade in the Ultrastrong Coupling Regime, *Phys. Rev. Lett.* **109**, 193602 (2012).
- [28] A. Le Boité, M.-J. Hwang, H. Nha, and M. B. Plenio, Fate of photon blockade in the deep strong-coupling regime, *Phys. Rev. A* **94**, 033827 (2016).
- [29] A. Imamoğlu, H. Schmidt, G. Woods, and M. Deutsch, Strongly Interacting Photons in a Nonlinear Cavity, *Phys. Rev. Lett.* **79**, 1467 (1997).
- [30] W. Leoński and A. Kowalewska-Kudłaszyk, Quantum Scissors: Finite-Dimensional States Engineering, *Prog. Opt.* **56**, 131 (2011).
- [31] L. Tian and H. J. Carmichael, Quantum trajectory simulations of two-state behavior in an optical cavity containing one atom, *Phys. Rev. A* **46**, R6801(R) (1992).
- [32] W. Leoński and R. Tanaś, Possibility of producing the one-photon state in a kicked cavity with a nonlinear Kerr medium, *Phys. Rev. A* **49**, R20(R) (1994).
- [33] Y.-X. Liu, A. Miranowicz, Y. B. Gao, J. Bajer, C. P. Sun, and F. Nori, Qubit-induced phonon blockade as a signature of quantum behavior in nanomechanical resonators, *Phys. Rev. A* **82**, 032101 (2010).
- [34] N. Didier, S. Pugnetti, Y. M. Blanter, and R. Fazio, Detecting phonon blockade with photons, *Phys. Rev. B* **84**, 054503 (2011).
- [35] A. Miranowicz, J. Bajer, N. Lambert, Y.-X. Liu, and F. Nori, Tunable multiphonon blockade in coupled nanomechanical resonators, *Phys. Rev. A* **93**, 013808 (2016).
- [36] X. Wang, A. Miranowicz, H.-R. Li, and F. Nori, Method for observing robust and tunable phonon blockade in a nanomechanical resonator coupled to a charge qubit, *Phys. Rev. A* **93**, 063861 (2016).
- [37] K. M. Birnbaum, A. Boca, R. Miller, A. D. Boozer, T. E. Northup, and H. J. Kimble, Photon blockade in an optical cavity with one trapped atom, *Nature (London)* **436**, 87 (2005).
- [38] A. Faraon, I. Fushman, D. Englund, N. Stoltz, P. Petroff, and J. Vučković, Coherent generation of non-classical light on a chip via photon-induced tunnelling and blockade, *Nat. Phys.* **4**, 859 (2008).
- [39] C. Lang, D. Bozyigit, C. Eichler, L. Steffen, J. M. Fink, A. A. Abdumalikov, M. Baur, S. Filipp, M. P. da Silva, A. Blais, and A. Wallraff, Observation of Resonant Photon Blockade at Microwave Frequencies Using Correlation Function Measurements, *Phys. Rev. Lett.* **106**, 243601 (2011).
- [40] A. J. Hoffman, S. J. Srinivasan, S. Schmidt, L. Spietz, J. Aumentado, H. E. Türeci, and A. A. Houck, Dispersive Photon Blockade in a Superconducting Circuit, *Phys. Rev. Lett.* **107**, 053602 (2011).
- [41] A. Reinhard, T. Volz, M. Winger, A. Badolato, K. J. Hennessy, E. L. Hu, and A. Imamoğlu, Strongly correlated photons on a chip, *Nat. Photonics* **6**, 93 (2011).
- [42] T. Peyronel, O. Firstenberg, Q.-Y. Liang, S. Hofferberth, A. V. Gorshkov, T. Pohl, M. D. Lukin, and V. Vuletić, Quantum nonlinear optics with single photons enabled by strongly interacting atoms, *Nature (London)* **488**, 57 (2012).
- [43] K. Müller, A. Rundquist, K. A. Fischer, T. Sarmiento, K. G. Lagoudakis, Y. A. Kelaita, C. Sánchez Muñoz, E. del Valle, F. P. Laussy, and J. Vučković, Coherent Generation of Non-classical Light on Chip via Detuned Photon Blockade, *Phys. Rev. Lett.* **114**, 233601 (2015).
- [44] C. Hamsen, K. N. Tolazzi, T. Wilk, and G. Rempe, Two-Photon Blockade in an Atom-Driven Cavity QED System, *Phys. Rev. Lett.* **118**, 133604 (2017).
- [45] H. J. Snijders, J. A. Frey, J. Norman, H. Flayac, V. Savona, A. C. Gossard, J. E. Bowers, M. P. van Exter, D. Bouwmeester, and W. Löffler, Observation of the Unconventional Photon Blockade, *Phys. Rev. Lett.* **121**, 043601 (2018).
- [46] C. Vaneph, A. Morvan, G. Aiello, M. Féliant, M. Aprili, J. Gabelli, and J. Estève, Observation of the Unconventional Photon Blockade in the Microwave Domain, *Phys. Rev. Lett.* **121**, 043602 (2018).
- [47] W. Leoński and A. Miranowicz, Kerr nonlinear coupler and entanglement, *J. Opt. B* **6**, S37 (2004).
- [48] A. Miranowicz and W. Leoński, Two-mode optical state truncation and generation of maximally entangled states in pumped nonlinear couplers, *J. Phys. B* **39**, 1683 (2006).
- [49] T. C. H. Liew and V. Savona, Single Photons from Coupled Quantum Modes, *Phys. Rev. Lett.* **104**, 183601 (2010).
- [50] M. Bamba, A. Imamoğlu, I. Carusotto, and C. Ciuti, Origin of strong photon antibunching in weakly nonlinear photonic molecules, *Phys. Rev. A* **83**, 021802(R) (2011).
- [51] H. Flayac and V. Savona, Unconventional photon blockade, *Phys. Rev. A* **96**, 053810 (2017).
- [52] S. Shamilov, A. Parkins, M. Collett, and H. Carmichael, Multi-photon blockade and dressing of the dressed states, *Opt. Commun.* **283**, 766 (2010).
- [53] A. Miranowicz, M. Paprzycka, Y.-X. Liu, J. Bajer, and F. Nori, Two-photon and three-photon blockades in driven nonlinear systems, *Phys. Rev. A* **87**, 023809 (2013).
- [54] G. H. Hovsepyan, A. R. Shahinyan, and G. Y. Kryuchkyan, Multiphoton blockades in pulsed regimes beyond stationary limits, *Phys. Rev. A* **90**, 013839 (2014).
- [55] H. J. Carmichael, Breakdown of Photon Blockade: A Dissipative Quantum Phase Transition in Zero Dimensions, *Phys. Rev. X* **5**, 031028 (2015).
- [56] W.-W. Deng, G.-X. Li, and H. Qin, Enhancement of the two-photon blockade in a strong-coupling qubit-cavity system, *Phys. Rev. A* **91**, 043831 (2015).
- [57] C. J. Zhu, Y. P. Yang, and G. S. Agarwal, Collective multiphoton blockade in cavity quantum electrodynamics, *Phys. Rev. A* **95**, 063842 (2017).
- [58] S. Felicetti, D. Z. Rossatto, E. Rico, E. Solano, and P. Forn-Díaz, Two-photon quantum Rabi model with superconducting circuits, *Phys. Rev. A* **97**, 013851 (2018).
- [59] S. Felicetti, M.-J. Hwang, and A. Le Boité, Ultrastrong-coupling regime of nondipolar light-matter interactions, *Phys. Rev. A* **98**, 053859 (2018).
- [60] R. Huang, A. Miranowicz, J.-Q. Liao, F. Nori, and H. Jing, Nonreciprocal Photon Blockade, *Phys. Rev. Lett.* **121**, 153601 (2018).
- [61] B. Li, R. Huang, X. Xu, A. Miranowicz, and H. Jing, Non-reciprocal unconventional photon blockade in a spinning optomechanical system, *Photonics Res.* **7**, 630 (2019).

- [62] A. Miranowicz, W. Leoński, S. Dyrting, and R. Tanaś, Quantum state engineering in finite-dimensional Hilbert space, *Acta Phys. Slov.* **46**, 451 (1996).
- [63] W. Leoński, Fock states in a Kerr medium with parametric pumping, *Phys. Rev. A* **54**, 3369 (1996).
- [64] W. Leoński and A. Miranowicz, Quantum-optical states in finite-dimensional Hilbert space. II. State generation, *Adv. Chem. Phys.* **119**, 195 (2001).
- [65] W. Leoński, Finite-dimensional coherent-state generation and quantum-optical nonlinear oscillator models, *Phys. Rev. A* **55**, 3874 (1997).
- [66] A. Miranowicz, K. Piątek, and R. Tanaś, Coherent states in a finite-dimensional Hilbert space, *Phys. Rev. A* **50**, 3423 (1994).
- [67] A. Miranowicz, W. Leoński, and N. Imoto, Quantum-optical states in finite-dimensional Hilbert space. I. General formalism, *Adv. Chem. Phys.* **119**, 155 (2001).
- [68] Y.-X. Liu, X.-W. Xu, A. Miranowicz, and F. Nori, From blockade to transparency: Controllable photon transmission through a circuit-QED system, *Phys. Rev. A* **89**, 043818 (2014).
- [69] A. Majumdar, M. Bajcsy, A. Rundquist, and J. Vučković, Loss-Enabled Sub-Poissonian Light Generation in a Bimodal Nanocavity, *Phys. Rev. Lett.* **108**, 183601 (2012).
- [70] A. Majumdar, M. Bajcsy, and J. Vučković, Probing the ladder of dressed states and nonclassical light generation in quantum-dot-cavity QED, *Phys. Rev. A* **85**, 041801(R) (2012).
- [71] X.-W. Xu, Y.-J. Li, and Y.-X. Liu, Photon-induced tunneling in optomechanical systems, *Phys. Rev. A* **87**, 025803 (2013).
- [72] A. Rundquist, M. Bajcsy, A. Majumdar, T. Sarmiento, K. Fischer, K. G. Lagoudakis, S. Buckley, A. Y. Piggott, and J. Vučković, Nonclassical higher-order photon correlations with a quantum dot strongly coupled to a photonic-crystal nanocavity, *Phys. Rev. A* **90**, 023846 (2014).
- [73] C. Zhai, R. Huang, H. Jing, and L.-M. Kuang, Mechanical switch of photon blockade and photon-induced tunneling, *Opt. Express* **27**, 27649 (2019).
- [74] A. Miranowicz, J. Bajer, M. Paprzycka, Y.-X. Liu, A. M. Zagoskin, and F. Nori, State-dependent photon blockade via quantum-reservoir engineering, *Phys. Rev. A* **90**, 033831 (2014).
- [75] M.-A. Lemonde, N. Didier, and A. A. Clerk, Antibunching and unconventional photon blockade with Gaussian squeezed states, *Phys. Rev. A* **90**, 063824 (2014).
- [76] A. Miranowicz, M. Bartkowiak, X. Wang, Y.-X. Liu, and F. Nori, Testing nonclassicality in multimode fields: A unified derivation of classical inequalities, *Phys. Rev. A* **82**, 013824 (2010).
- [77] M. Radulaski, K. A. Fischer, K. G. Lagoudakis, J. L. Zhang, and J. Vučković, Photon blockade in two-emitter-cavity systems, *Phys. Rev. A* **96**, 011801(R) (2017).
- [78] J. Peřina Jr., V. Michálek, and O. Haderka, Higher-order sub-Poissonian-like nonclassical fields: Theoretical and experimental comparison, *Phys. Rev. A* **96**, 033852 (2017).
- [79] J. Peřina Jr., V. Michálek, and O. Haderka, Simultaneous observation of higher-order non-classicalities based on experimental photocount moments and probabilities, *Sci. Rep.* **9**, 8961 (2019).
- [80] G. S. Agarwal, Master Equation Methods in Quantum Optics, *Prog. Opt.* **11**, 1 (1973).
- [81] J. Peřina, *Quantum Statistics of Linear and Nonlinear Optical Phenomena* (Kluwer, Dordrecht, 1991).
- [82] M. O. Scully and M. S. Zubairy, *Quantum Optics* (Cambridge University, Cambridge, England, 1997).
- [83] A. Lukš, V. Peřinová, and J. Peřina, Principal squeezing of vacuum fluctuations, *Opt. Commun.* **67**, 149 (1988).
- [84] R. Loudon, Graphical representation of squeezed-state variances, *Opt. Commun.* **70**, 109 (1989).
- [85] W. Vogel and D. Welsch, *Quantum Optics* (Wiley, New York, 2006).
- [86] R. Loudon, *The Quantum Theory of Light* (Oxford University, London, 1973).
- [87] C. T. Lee, Measure of the nonclassicality of nonclassical states, *Phys. Rev. A* **44**, R2775(R) (1991).
- [88] M. Hillery, Nonclassical distance in quantum optics, *Phys. Rev. A* **35**, 725 (1987).
- [89] A. Kenfack and K. Życzkowski, Negativity of the Wigner function as an indicator of non-classicality, *J. Opt. B: Quantum Semicl. Opt.* **6**, 396 (2004).
- [90] A. Miranowicz, K. Bartkiewicz, A. Pathak, J. Peřina, Jr., Y.-N. Chen, and F. Nori, Statistical mixtures of states can be more quantum than their superpositions: Comparison of nonclassicality measures for single-qubit states, *Phys. Rev. A* **91**, 042309 (2015).
- [91] J. K. Asbóth, J. Calsamiglia, and H. Ritsch, Computable Measure of Nonclassicality for Light, *Phys. Rev. Lett.* **94**, 173602 (2005).
- [92] R. Horodecki, P. Horodecki, M. Horodecki, and K. Horodecki, Quantum entanglement, *Rev. Mod. Phys.* **81**, 865 (2009).
- [93] A. Miranowicz, K. Bartkiewicz, N. Lambert, Y.-N. Chen, and F. Nori, Increasing relative nonclassicality quantified by standard entanglement potentials by dissipation and unbalanced beam splitting, *Phys. Rev. A* **92**, 062314 (2015).
- [94] C. Eltschka and J. Siewert, Negativity as an Estimator of Entanglement Dimension, *Phys. Rev. Lett.* **111**, 100503 (2013).
- [95] M. Bartkowiak, A. Miranowicz, X. Wang, Y.-X. Liu, W. Leoński, and F. Nori, Sudden vanishing and reappearance of nonclassical effects: General occurrence of finite-time decays and periodic vanishings of nonclassicality and entanglement witnesses, *Phys. Rev. A* **83**, 053814 (2011).
- [96] I. I. Arkhipov, J. Peřina Jr., J. Svozilík, and A. Miranowicz, Nonclassicality invariant of general two-mode Gaussian states, *Sci. Rep.* **6**, 26523 (2016).
- [97] N. Bartolo, F. Minganti, W. Casteels, and C. Ciuti, Exact steady state of a Kerr resonator with one- and two-photon driving and dissipation: Controllable Wigner-function multimodality and dissipative phase transitions, *Phys. Rev. A* **94**, 033841 (2016).
- [98] F. Minganti, N. Bartolo, J. Lolli, W. Casteels, and C. Ciuti, Exact results for Schrödinger cats in driven-dissipative systems and their feedback control, *Sci. Rep.* **6**, 26987 (2016).
- [99] J.-H. An, S.-J. Wang, H.-G. Luo, and C.-L. Jia, Production of squeezed state of single mode cavity field by the coupling of squeezed vacuum field reservoir in nonautonomous case, *Chin. Phys. Lett.* **21**, 1 (2004).
- [100] H. Fearn and M. Collett, Representations of squeezed states with thermal noise, *J. Mod. Opt.* **35**, 553 (1988).

Chapter 4

Pure dephasing in the ultrastrong coupling regime

4.1 Chapter outline

In this chapter, I provide a summary of article [P4] and describe how quantum system behave in the ultrastrong coupling (USC) and deep-strong coupling (DSC) regimes. Furthermore, I introduce the main result of the article. This results explain how to correctly define the perturbation Hamiltonian describing pure dephasing of subsystems in the USC regime based on the adopted gauge.

4.1.1 Popular introduction

The evolution of a closed quantum system is reversible. However, in practice systems are not isolated and undergo some form of decoherence. In particular, control and readout of a quantum system additionally also requires coupling to an external environment.

Understanding how the decoherence of subsystems affects the performance of a hybrid quantum system (here a two-level system (TLS) interacting with a single-mode cavity field) is a fascinating problem with possible implications for enhancing the capabilities of quantum devices [22,23]¹. Hybrid light-matter quantum systems play a central role in cavity- and circuit-quantum electrodynamics (QED) and have already been at the forefront of quantum technology development.

Relaxation and pure dephasing generate decoherence in a quantum system. In particular, pure dephasing affects the off-diagonal elements of the system density

¹This and other references in this chapter correspond to those cited in [P4].

matrix. The description of dephasing in cavity- and circuit-QED systems is the focus of article [P4] and this chapter. In the fields of QED, the interaction between an atom and a cavity field is typically described by the quantum Rabi model (QRM).

The QRM describes the light-matter interaction even in the ultra-strong coupling (USC) and deep-strong coupling (DSC) regimes, where the interaction strength is comparable or even exceeds the bare transition frequencies of the subsystems. This model reduces to the Jaynes-Cummings (JC) model to the strong-coupling (SC) regime, where the rotating-wave approximation (RWA) is applicable. Whether the coupling is strong (weak) is determined by whether the coupling strength g is greater (smaller) than the system losses. However, the standard definition of the USC compares g to the system's bare frequencies ω_i , while dissipation rates should just be much smaller than ω_i , the same as in the SC regime [31,32]. A significant amount of theoretical and experimental research has been conducted in the weak-coupling and SC regimes. Nevertheless, as the demand for quantum technologies relying on light-matter interactions grows, experimental efforts have successfully achieved stronger coupling strengths. In particular, the new regimes of rapidly growing interest are the USC and DSC regimes in which $g > 0.1\omega_i$ and $g > \omega_i$, respectively.

In the QRM, when the coupling rate increases, the counter-rotating terms start to play an important role in the USC regime, where the RWA is no longer applicable. The counter-rotating terms induce processes that do not conserve the number of excitations in an USC light-matter system, leading to its ground state that contains virtual excitations.

Moreover, the description of the light-matter interaction depends on the chosen gauge. For example, in the context of QED one often works in the so-called Coulomb gauge or the dipole gauge. However, the principle of gauge invariance dictates that physical outcomes cannot depend on the choice of gauge. The QRM in the Coulomb gauge seems to break the principle of gauge invariance in the USC regime [40,41]. This issue has been linked to the two level approximation of the matter system in the QRM. In the above cited paper, Salvatore Savasta from Messina University and Franco Nori from RIKEN in Wakoshi with their groups proposed a way to obtain light-matter Hamiltonians in reduced Hilbert spaces, which can give correct gauge-invariant physical results even when the light-matter interaction is very strong as in the USC and DSC regimes.

Moreover, the standard master equation that correctly describes the open quantum system dynamics ranging from the weak to strong coupling regimes also appears to fail in the USC. One notable issue arising from the standard quantum optics

master equation in the USC and DSC regimes involves unrealistic effects in the relaxation and dephasing of both cavity and qubit.

In particular, the dissipation terms tend to bring the qubit-cavity system to the ground state $|g_0\rangle$ of the JC Hamiltonian. However, in the USC regime, this is not correct, because the ground state of the qubit-cavity system is not $|g_0\rangle$ anymore and contains virtual photons and atom excitations. Therefore, if we use the standard master equation in USC regime, one obtains an incorrect result for the steady-state state of qubit-cavity systems.

To tackle this problem, a new master equation has been derived that properly describes the dissipation in terms of the dressed state basis of the atom-cavity system [22,23].

Importantly however, it is not *a priori* clear whether this new master equation is gauge invariant in general. In article [P4], we considered this problem and showed that the standard description of pure dephasing in this master equation is indeed not gauge invariant. We have provided means of correctly solving this problem by studying the case of pure dephasing in systems described by the QRM and the Hopfield model describing collective (bosonic) matter excitations interacting with a single mode light field.

4.1.2 Motivation

The generalized master equation in the dressed picture mentioned above was considered in article [P4] in the context of pure dephasing. A prominent issue of this equation is that the original formulation by A. Blais et al. [22] considers stochastic Hamiltonian for pure dephasing that are not affected by the strength of light-matter interaction. We explicitly demonstrated that this is a severe limitation: the form of the pure dephasing Hamiltonian is gauge dependent and the interaction between light and matter can significantly affect the form of the stochastic perturbation describing the dephasing of one of the components of the hybrid system depending on the adopted gauge. Effects associated with this subtlety are most significant in the USC and DSC regimes.

4.1.3 Main results

We derive the correct pure dephasing rate of subsystems in the QRM and Hopfield model in the USC and DSC regimes. To do this derivation correctly we needed to expand a perturbation Hamiltonian that modeled pure dephasing of subsystems

in the master equation in the dressed-state picture, while we took into account the appropriate form of this noise Hamiltonian according to the adopted gauge.

It has been shown that the QRM in the Coulomb gauge violates gauge invariance [40,41]. The generalized minimal coupling replacement in the form of a unitary transformation, which correctly constrains the light-matter interaction within a truncated subspace, resolves the gauge invariant issue that occurs in the Coulomb gauge [41]. Therefore, the correct Coulomb-gauge Hamiltonian for the QRM can be obtained by applying generalized minimal coupling as an appropriate transformation of the free field and matter Hamiltonians. This study has shown that the dipole and Coulomb gauge Hamiltonians of the QRM are related by a suitable unitary gauge transformation ($\hat{\mathcal{H}}^D = \hat{\mathcal{U}}^\dagger \hat{\mathcal{H}}_C \hat{\mathcal{U}}$) in the USC regime.

Furthermore, light-matter interaction can change the form of quantum operators that describe physical observables, and these changes are usually gauge dependent. It means that different gauges (e.g., the Coulomb gauge and the dipole gauge) have different effects on how the particle's physical momentum and the field momentum are defined concerning the light-matter interaction. For instance, in the Coulomb gauge, in contrast with the field momenta, the matter momenta are modified by the light-matter interaction as

$$\hat{\sigma}_z^C = \hat{\mathcal{U}} \hat{\sigma}_z \hat{\mathcal{U}}^\dagger = \sigma_z \cos[2\eta(\hat{a} + \hat{a}^\dagger)] + \hat{\sigma}_y \sin[2\eta(\hat{a} + \hat{a}^\dagger)],$$

where η is the normalized qubit-cavity coupling strength. On the other hand, in the dipole gauge the electric-field operator transformed and we have the gauge transformation of the cavity operators as

$$\hat{a}^D = \hat{\mathcal{U}}^\dagger \hat{a} \hat{\mathcal{U}} = \hat{a} + i\eta \hat{\sigma}_x,$$

while the matter momenta remain unaffected. So, the light-matter interaction can modify the form of quantum operators describing physical observables, and these changes are usually gauge dependent. Given this explanation, the light-matter interaction affects the form of the perturbation Hamiltonian describing the dephasing of subsystems in the USC and DSC regimes, depending on the adopted gauge.

We show that one must apply the generalized minimal coupling replacements discussed above to pure-dephasing perturbations of subsystems to obtain accurate descriptions of pure dephasing effects and gauge-invariant results in the presence of light-matter interactions in the USC and DSC regimes. Beside, the master equation

in the dressed basis should be used to study the dynamics of quantum systems in the USC regime.

We demonstrated that by solely expanding the perturbation Hamiltonian (e.g., $\hat{\mathcal{H}}_{\text{dep}} = f(t)\hat{\sigma}_z$) in the dressed basis is insufficient to ensure accurate results. We derived the pure dephasing rate of subsystems considering the adopted gauges by applying the minimal coupling replacement to the perturbation Hamiltonian related to each subsystem.

We analyzed pure dephasing effects on the two lowest transitions in the QRM: $\alpha_{\pm} = (\tilde{1}_{\pm}, \tilde{0})$ considering only the qubit pure dephasing and the cavity pure dephasing separately. Our results show that, for example, in the case of qubit pure dephasing, the lowest energy transition becomes dephasing free. However, if we do not consider gauge dependency, the results show a wrong and large pure dephasing rate for the lowest energy transition. Therefore, our results explicitly demonstrate the importance of correctly calculating the pure dephasing rate in the QRM in cavity QED. We also performed an analogous analysis for polaritons in the simplest form of the Hopfield model describing the interaction of a single-mode electromagnetic resonator with a bosonic matter field. Similar to what was explained in the QRM, our studies show that while the two-level approximation can work well in the dipole gauge, but it fails to provide the correct spectra in the Coulomb gauge in this model. We use the generalized minimal coupling replacements on the Hamiltonian of a single-mode electromagnetic resonator with a bosonic matter field to obtain the correct Hamiltonian in each gauge. By diagonalizing the Hamiltonians in the polariton basis we obtained the polariton operators (lower and upper polaritons) which are gauge dependent, because their Hopfield coefficients are gauge dependent.

Similar to what is explained for the QRM here indeed, when using the Coulomb gauge, the matter operator \hat{b} , after applying the unitary transformation $\hat{T} = \exp\left[i\lambda(\hat{a} + \hat{a}^*)(\hat{b} + \hat{b}^*)\right]$, where λ is the normalized coupling strength, becomes $\hat{b}^C = \hat{T}^{\dagger}\hat{b}\hat{T} = \hat{b} - i\lambda(\hat{a} + \hat{a}^*)$, since the minimal coupling is applied to the matter system. On the contrary, when using the dipole gauge, the minimal coupling is applied to the photonic system, and the photonic operator becomes $\hat{a}^D = \hat{T}\hat{a}\hat{T}^{\dagger} = \hat{a} + i\lambda(\hat{b} + \hat{b}^*)$.

Clearly, the perturbation Hamiltonian describing pure dephasing also is gauge dependent. For example, in the article, we analyzed the pure dephasing rates of the lower and upper polaritons, originating from exciton dephasing. Our results demonstrate the importance to use a proper perturbation Hamiltonian, such as $\hat{\mathcal{H}}_{\text{dep}}^D = f_x(t)\hat{b}^{\dagger}\hat{b}$ in the dipole gauge, and $\hat{\mathcal{H}}_{\text{dep}}^C = f_x(t)\hat{b}_C^{\dagger}\hat{b}_C$ in the Coulomb gauge.

Our findings reveal that by using a proper gauge, the pure dephasing effects in the lower polaritons tend to be reduced in the USC and DSC regimes. Instead, the influence of pure dephasing increases for the upper polaritons by increasing coupling strengths. The upper polaritons clearly display a larger line broadening with respect to the lower polaritons, which is in agreement with the number of experiments (see [54] and references therein). This interesting behavior of the lower and upper polaritons in the USC and DSC regimes in the Hopfield model could be of interest to experimentalists in the field.

We compared the behavior of the correct (using the appropriate gauge transformation) and wrong (when not considering the gauge transformation) pure dephasing rates in the USC and DSC regimes of both the QRM and the Hopfield model. We emphasized the importance of using the correct description of the pure dephasing rate in two prototypical models: the QRM and the Hopfield model, and demonstrated that neglecting this issue can lead to wrong and unphysical results in both the USC and DSC regimes.

In brief conclusion, one can say that in the USC and DSC regimes, the generalized minimal coupling replacements have to be also applied to any perturbation affecting the matter or light subsystems.

4.1.4 My contribution and importance of the work

Exploring the interaction between light and matter in the USC and DSC regimes is of paramount importance. These regimes can be achieved in many different systems, such as organic molecules, polaritons in different materials, magnons, Landau polaritons, and superconducting circuits. These systems can cover a wide range of frequencies from microwave to ultraviolet radiation. The effects of pure dephasing are common in spectroscopy and quantum condensed matter physics and have a lot of applications in quantum technologies.

This work broadens the knowledge of dephasing in cavity QED beyond the conventional weak and strong coupling regimes, and the results can be readily tested with state-of-the-art experimental techniques.

Alberto Mercurio and I conducted all numerical and analytical calculations, created plots, and played a significant role in interpreting the results. As affirmed by all coauthors (refer to the enclosed signed coauthors' statements at the end of the thesis), Alberto Mercurio and I have made equal and substantial contributions to this work.

4.2 Reprint of article [P4]

On the subsequent pages, we append a reprint with permission from the American Physical Society:

[P4] Alberto Mercurio, Shilan Abo, Fabio Mauceri, Enrico Russo, Vincenzo Macri, Adam Miranowicz, Salvatore Savasta, Omar Di Stefano, *Pure Dephasing of Light-Matter Systems in the Ultrastrong and Deep-Strong Coupling Regimes*, Phys. Rev. Lett. **130**, 123601 (2023).
<http://dx.doi.org/10.1103/PhysRevLett.130.123601>
Copyright (2023) by the American Physical Society.

Pure Dephasing of Light-Matter Systems in the Ultrastrong and Deep-Strong Coupling Regimes

Alberto Mercurio¹, Shilan Abo^{1,2,*}, Fabio Mauceri^{1,†}, Enrico Russo¹, Vincenzo Macrì³, Adam Miranowicz², Salvatore Savasta¹, and Omar Di Stefano¹

¹Dipartimento di Scienze Matematiche e Informatiche, Scienze Fisiche e Scienze della Terra, Università di Messina, I-98166 Messina, Italy

²Institute of Spintronics and Quantum Information, Adam Mickiewicz University, 61-614, Poznan, Poland

³Theoretical Quantum Physics Laboratory, RIKEN Cluster for Pioneering Research, Wako-shi, Saitama 351-0198, Japan

(Received 19 May 2022; accepted 1 February 2023; published 21 March 2023)

Pure dephasing originates from the nondissipative information exchange between quantum systems and environments, and plays a key role in both spectroscopy and quantum information technology. Often pure dephasing constitutes the main mechanism of decay of quantum correlations. Here we investigate how pure dephasing of one of the components of a hybrid quantum system affects the dephasing rate of the system transitions. We find that, in turn, the interaction, in the case of a light-matter system, can significantly affect the form of the stochastic perturbation describing the dephasing of a subsystem, depending on the adopted gauge. Neglecting this issue can lead to wrong and unphysical results when the interaction becomes comparable to the bare resonance frequencies of subsystems, which correspond to the ultrastrong and deep-strong coupling regimes. We present results for two prototypical models of cavity quantum electrodynamics: the quantum Rabi and the Hopfield model.

DOI: 10.1103/PhysRevLett.130.123601

Introduction.—In reality, there is no perfectly isolated quantum system. For example, the coupling of a radiating atom with the infinitely many modes of a free electromagnetic field results in decoherence and spontaneous emission. Such interaction determines an energy relaxation time T_1 associated to a given optical transition. If the population of an excited state decays, so does the polarization too, which results in decoherence. In the presence of only energy relaxation mechanisms, such transverse relaxation time is $T_2 = 2T_1$ [1,2]. However, quantum systems, displaying optical transitions, do not only interact with an electromagnetic field, but can be affected by additional dephasing mechanisms inducing the decay of the dipole coherence without changing the populations of the systems. These pure dephasing effects can originate from fluctuations in the environmental fields affecting the phases of the emitter wave functions; see, e.g., Refs. [3–8]. In general, the phase (transverse) relaxation time is most often shorter than twice the energy relaxation time: $T_2 \leq 2T_1$. In optical spectroscopy, the full width at half maximum (FWHM) of homogeneous broadening corresponds to $2/T_2$.

It is well known that decoherence tends to destroy quantum coherence and quantum correlations [9,10]. It is known that this mechanism becomes faster with the increase of the *size* of a quantum system [11]. This explains the absence of quantum superpositions in the macroscopic world [12]. Decoherence can, thus, strongly affect and limit quantum information processing (QIP) [13,14]. Depending on the specific environment, mechanisms to protect

qubits from dephasing have been proposed (see, e.g., Refs. [14–18]).

Devices for QIP, secure communication, and high-precision sensing were implemented combining different systems ranging from photons, atoms, and spins to mesoscopic superconducting and nanomechanical structures. Complementary functionalities of these hybrid quantum systems can be essential for the development of new quantum technologies [19–21]. Understanding how decoherence of one or more subsystems can affect the performance of the whole system is an interesting problem, relevant for improving the performance of quantum devices [22,23].

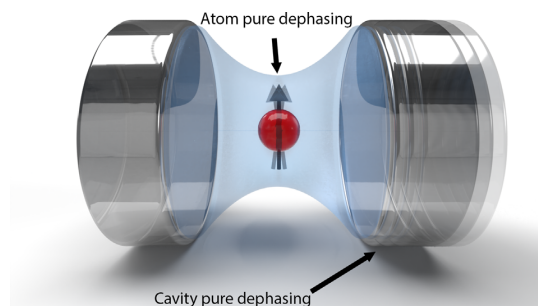


FIG. 1. Pictorial representation of a two-level system interacting with a single-mode cavity field, when both subsystems are affected by pure dephasing.

Cavity [10] and circuit [24,25] quantum electrodynamics (QED) systems are among the most studied hybrid quantum systems. They are playing a key role in quantum optics and in the development of new quantum technologies [26–29]. Pure dephasing can significantly affect the performance of these systems, not necessarily in a negative way. For example, it has been shown that pure dephasing is a promising resource for solid-state emitters, since it can improve the performance of nanophotonic devices, such as single-photon sources and nanolasers [30].

Decoherence effects in hybrid quantum systems are often introduced by using the standard quantum optics master equation, where the coupling of a multicomponent system with the environment is introduced by neglecting the interaction between the subsystems. When such interaction is not negligible compared with the bare transition frequencies of the components, as in the light-matter ultrastrong coupling (USC) or deep-strong coupling (DSC) regimes [31,32], this approximation can give rise to unphysical results. These regimes can give rise to new physical effects and applications (see, e.g., [33–39]), and they also challenge our understanding of fundamental aspects of cavity QED, like a proper definition of subsystems, their quantum measurements, and the structure of the light-matter ground states, leading also to gauge ambiguities [40–46,48].

A master equation method for cavity QED systems, describing both losses and pure dephasing, and taking into account light-matter interaction, has been proposed in Refs. [22,23]. However, these models, as well as previous ones, consider perturbation Hamiltonians for pure dephasing which are not affected by light-matter interaction. Here we show that the interaction between light and matter can significantly affect the form of a stochastic perturbation describing the dephasing of one of the components. We find that neglecting this issue can lead to wrong and unphysical results in both USC and DSC regimes. We present results for two prototypical models of cavity QED: the quantum Rabi model (QRM) and the Hopfield model. However, the approach here considered can also be applied to describe more complex light-matter systems.

Quantum Rabi model.—Pure dephasing effects on both the qubit and electromagnetic field can be described by introducing two zero-mean stochastic functions $f_c(t)$, $f_q(t)$ modulating their resonance frequency (Fig. 1). The perturbation Hamiltonian can be written as

$$\hat{V}_{\text{dep}} = f_c(t)\hat{a}^\dagger\hat{a} + f_q(t)\hat{\sigma}_z. \quad (1)$$

By expanding \hat{V}_{dep} in the basis of the eigenstates of the total system Hamiltonian, a master equation describing the effects of qubit dephasing on the system dynamics can be obtained [22]. For the sake of simplicity, we consider stochastic functions with a low-frequency spectral density (with respect to the relevant transition frequencies of the

system). The resulting master equation can be written as ($\hbar = 1$) [47]

$$\frac{d}{dt}\hat{\rho}(t) = -i[\hat{H}_s, \hat{\rho}] + \frac{\gamma_\phi^{(q)}}{2}\mathcal{D}[\hat{\Phi}]\hat{\rho} + \frac{\gamma_\phi^{(c)}}{2}\mathcal{D}[\hat{\Xi}]\hat{\rho}, \quad (2)$$

where \hat{H}_s is the Hamiltonian of the total system and

$$\mathcal{D}[\hat{O}]\hat{\rho} = \frac{1}{2}(2\hat{O}\hat{\rho}\hat{O}^\dagger - \hat{\rho}\hat{O}^\dagger\hat{O} - \hat{O}^\dagger\hat{O}\hat{\rho}) \quad (3)$$

is the Lindbladian superoperator, while $\hat{\Phi} = \sum_j \sigma_z^{jj}|j\rangle\langle j|$ and $\hat{\Xi} = \sum_j \langle j|\hat{a}^\dagger\hat{a}|j\rangle|j\rangle\langle j|$, with $|j\rangle$ being the eigenstates of \hat{H}_s , and $\sigma_z^{jj} = \langle j|\hat{\sigma}_z|j\rangle$. The bare dephasing rates $\gamma_\phi^x = 2S_f(0)$ are determined by the low-frequency spectral densities $S_f^{(x)}(\omega)$ of $f_x(t)$, with $x = q, c$. Additional dephasing terms can appear, when the spectral density functions $S_f(\omega)$ are not negligible at the transition frequencies of the system (see the Supplemental Material [49]).

We apply the above procedure to the simplest model of cavity QED, i.e., the QRM. Its Hamiltonian in the dipole gauge can be written as $\hat{H}_D = \hat{H}_{\text{ph}} + \hat{H}_q + \hat{V}_D$, where $\hat{H}_q = \omega_q\hat{\sigma}_z/2$, and the free field Hamiltonian is $\hat{H}_{\text{ph}} = \omega_c\hat{a}^\dagger\hat{a}$, where $\hat{\sigma}_j$ ($j = x, y, z$) are the Pauli operators, and \hat{a} and \hat{a}^\dagger are the photon destruction and creation operators. Neglecting the constant term $\eta^2\omega_c$, the interaction term can be written as $\hat{V}_D = -i\eta\omega_c(\hat{a} - \hat{a}^\dagger)\hat{\sigma}_x$, where η is the normalized qubit-cavity coupling strength. It has been shown that the standard quantum Rabi Hamiltonian in the Coulomb gauge violates gauge invariance [40]. The correct Coulomb-gauge quantum Rabi Hamiltonian [41] can be obtained by writing the sum of the free field and matter Hamiltonians and then by applying a suitable unitary transformation (generalized minimal coupling) to the free matter Hamiltonian [41]: $\hat{H}_C = \hat{H}_{\text{ph}} + \hat{U}\hat{H}_q\hat{U}^\dagger$, where $\hat{U} = \exp[i\hat{\lambda}\hat{\sigma}_x]$, with $\hat{\lambda} = \eta(\hat{a} + \hat{a}^\dagger)$. We obtain

$$\hat{H}_C = \hat{H}_{\text{ph}} + \frac{\omega_q}{2}[\hat{\sigma}_z \cos(2\hat{\lambda}) + \hat{\sigma}_y \sin(2\hat{\lambda})]. \quad (4)$$

The dipole and Coulomb gauge Hamiltonians are related by the unitary gauge transformation $\hat{H}_D = \hat{U}^\dagger\hat{H}_C\hat{U}$; thus the dipole gauge Hamiltonian can also be obtained by applying a generalized minimal coupling replacement to the free field Hamiltonian: $\hat{H}_D = \hat{U}^\dagger\hat{H}_{\text{ph}}\hat{U} + \hat{H}_q$.

Following the standard approach, pure dephasing effects can be directly introduced by using Eqs. (1) and (2), which provides gauge invariant expectation values, as can be easily shown [50]. However, this is not sufficient to ensure that the obtained results are physically correct. However, we will show below that this naive approach can provide incorrect and/or gauge dependent results, especially when the light-matter interaction strength is very strong.

Actually, light-matter interaction can modify the form of quantum operators describing physical observables, and these changes are usually gauge dependent [51]. For example, in the Coulomb gauge the form of the physical momentum of the particle is affected by light-matter interaction, while in the dipole gauge it is interaction independent. On the contrary, the dipole gauge affects the definition of the field momentum. As a consequence, in this gauge, the canonical momentum is no more proportional to the electric field operator. We may thus expect that the form of operators describing pure dephasing shall be modified by light-matter interaction too. In order to obtain correct descriptions of pure dephasing effects, as well as gauge-invariant results, in the presence of light-matter interactions one has to apply the generalized minimal coupling replacements considered above to pure dephasing perturbations in Eq. (1) too. In the Coulomb and dipole gauge, respectively, we obtain

$$\hat{V}_\phi^C = f_q(t)\hat{\sigma}_z^C + f_c(t)\hat{a}^\dagger\hat{a}, \quad (5)$$

$$\hat{V}_\phi^D = f_q(t)\hat{\sigma}_z + f_c(t)\hat{a}_D^\dagger\hat{a}_D, \quad (6)$$

where $\hat{\sigma}_z^C = \hat{U}\hat{\sigma}_z\hat{U}^\dagger$ and $\hat{a}_D = \hat{U}^\dagger\hat{a}\hat{U} = \hat{a} + i\eta\hat{\sigma}_x$ are atomic and field operators modified by the light-matter interaction in the Coulomb and dipole gauge, respectively.

In the following, we label the QRM states by generalizing the notation of the Jaynes-Cummings (JC) model. In particular, $|\tilde{0}\rangle$ denotes the ground state, and $|\tilde{n}_\pm\rangle$ the states that tend to the JC states $|n_\pm\rangle$, when the coupling vanishes. Moreover, we use not-primed (primed) states to indicate the Coulomb (dipole) gauge states. As an example we analyze pure dephasing effects on the two lowest transitions in the QRM: $\alpha_\pm \equiv (\tilde{1}_\pm, \tilde{0})$, and considering only qubit pure dephasing [$f_c(t) = 0$]. In the interaction picture, from Eq. (2), we obtain [49]

$$\dot{\tilde{\rho}}_{\alpha_\pm}^{\alpha_\pm}(t) = -(\gamma_\phi^{\alpha_\pm}/2)\tilde{\rho}_{\alpha_\pm}(t), \quad (7)$$

with

$$\gamma_\phi^{\alpha_\pm} = \frac{\gamma_\phi^{(q)}}{2} |\sigma_z^{\tilde{1}_\pm, \tilde{1}_\pm} - \sigma_z^{\tilde{0}, \tilde{0}}|^2. \quad (8)$$

We observe that the obtained dephasing rates are gauge invariant ($\gamma_\phi^{\alpha_\pm} = \gamma_\phi^{\alpha_\pm}$), because the expectation values are unitary invariant, when transforming both operator and states: $\gamma_\phi^{\alpha_\pm} = \gamma_\phi^{(q)} |\sigma_z^{C, \tilde{1}_\pm, \tilde{1}_\pm} - \sigma_z^{C, \tilde{0}, \tilde{0}}|^2/2$. Figure 2(a) displays the normalized pure dephasing rate $\gamma_{\tilde{1}_\pm, \tilde{0}}/\gamma_\phi^0$ for the two lowest energy transitions, considering a small qubit-cavity detuning $\delta = 3 \times 10^{-3}$ and in the case of only qubit pure dephasing. In the limit of negligible coupling strength, where $|\tilde{1}_+^C\rangle \rightarrow |e, 0\rangle$ and $|\tilde{1}_-^C\rangle \rightarrow |g, 1\rangle$, the standard results

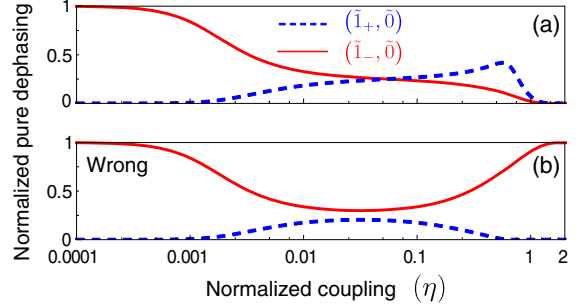


FIG. 2. Quantum Rabi model. Normalized pure dephasing rate for the two lowest energy transitions, for a small qubit-cavity detuning $\delta = 3 \times 10^{-3}$ and considering only the qubit pure dephasing. (a) Correct gauge-invariant versus (b) wrong Coulomb gauge results.

are recovered, and only $(\tilde{1}_-, \tilde{0})$ is affected by the qubit pure dephasing. When the coupling becomes comparable to the detuning, as expected, pure dephasing is shared among the two transitions, since the energy eigenstates $|\tilde{1}_\pm^C\rangle$ tend to become an equally weighted superposition of $|e, 0\rangle$ and $|g, 1\rangle$. For the normalized coupling strengths $\eta > 0.1$ (the USC regime), pure dephasing becomes less effective for the transition $(\tilde{1}_-, \tilde{0})$, until at stronger couplings (the DSC regime), both the transitions tend to become dephasing free. This behavior reflects the fact that, when the coupling rate is larger than the bare qubit frequency, a fluctuation at the qubit resonance frequency can have a very low impact on the dressed-state energies. On the contrary, Fig. 2(b) shows a wrong large pure dephasing rate for the lowest energy transition. Analogous calculations can be carried out for the case of cavity pure dephasing [49].

Hopfield model.—A similar analysis can be carried out for polaritons. We consider the simplest version of the Hopfield model [52], describing the interaction of a single-mode electromagnetic resonator with a bosonic matter field (with the bosonic annihilation \hat{b} and creation \hat{b}^\dagger operators) modeling some kind of collective matter excitations. The system Hamiltonian in the dipole gauge reads as

$$\hat{H}_D = \hat{H}_0 + i\lambda\omega_c(\hat{a}^\dagger - \hat{a})(\hat{b} + \hat{b}^\dagger) + \omega_c\lambda^2(\hat{b} + \hat{b}^\dagger)^2, \quad (9)$$

where $\hat{H}_0 = \omega_c\hat{a}^\dagger\hat{a} + \omega_x\hat{b}^\dagger\hat{b}$, and λ is the normalized coupling strength. An equivalent model can be obtained in the Coulomb gauge [53]:

$$\hat{H}_C = \hat{H}_0 - i\omega_x\lambda(\hat{b}^\dagger - \hat{b})(\hat{a}^\dagger + \hat{a}) + \mathcal{D}(\hat{a}^\dagger + \hat{a})^2, \quad (10)$$

where $\mathcal{D} = \omega_x\lambda^2$. These two Hamiltonians can be directly obtained by generalized minimal coupling replacements: $H_C = \omega_c\hat{a}^\dagger\hat{a} + \omega_x\hat{U}\hat{b}^\dagger\hat{b}\hat{U}^\dagger$ and $H_D = \omega_c\hat{U}^\dagger\hat{a}^\dagger\hat{a}\hat{U} + \omega_x\hat{b}^\dagger\hat{b}$, where $\hat{U} = \exp[i\lambda(\hat{a} + \hat{a}^\dagger)(\hat{b} + \hat{b}^\dagger)]$. As is well known, the interaction gives rise to polaritonic resonances, which

results from the mixing of the two bosonic modes. It is possible to diagonalize the system expressing the photon and exciton operators in terms of polaritonic (bosonic) operators [52]. For $\mu = 1, 2$ (lower and upper polariton, respectively), we have

$$\hat{y} = \sum_{\mu=1}^2 (U_y^\mu \hat{P}_\mu - V_y^\mu \hat{P}_\mu^\dagger), \quad (\hat{y} = \hat{a}, \hat{b}). \quad (11)$$

The diagonalization procedure determines both polariton eigenfrequencies Ω_μ , which are gauge invariant, and the Hopfield coefficients, which are gauge dependent. As a consequence, also the polariton operators are gauge dependent. We use primed operators and coefficients for the dipole gauge.

By neglecting issues related to the light-matter interaction, dephasing effects can be modeled by introducing the perturbation Hamiltonian

$$\hat{V}_{\text{dep}}(t) = f_c(t) \hat{a}^\dagger \hat{a} + f_x(t) \hat{b}^\dagger \hat{b}, \quad (12)$$

describing the stochastic fluctuation of the resonance frequencies of the components. Following the reasoning of the previous section, when including the light-matter interaction, it turns out that Eq. (12) is incorrect, and its corrected form is gauge dependent:

$$\hat{V}_{\text{dep}}^D(t) = f_c(t) \hat{a}_D^\dagger \hat{a}_D + f_x(t) \hat{b}^\dagger \hat{b}, \quad (13)$$

$$\hat{V}_{\text{dep}}^C(t) = f_c(t) \hat{a}^\dagger \hat{a} + f_x(t) \hat{b}_C^\dagger \hat{b}_C, \quad (14)$$

where $\hat{a}_D = \hat{T} \hat{a} \hat{T}^\dagger = \hat{a} + i\lambda(\hat{b} + \hat{b}^\dagger)$ and $\hat{b}_C = \hat{T}^\dagger \hat{b} \hat{T} = \hat{b} - i\lambda(\hat{a} + \hat{a}^\dagger)$. Notice that here \hat{a}_D (\hat{b}_C) is the *physical* photonic (excitonic) annihilation operator in the dipole (Coulomb) gauge. By *physical*, we mean the operators that describe the annihilation of the physical quanta of the fields [53]. The polariton pure dephasing rates can be obtained by expanding Eqs. (13) and (14) in terms of the polariton operators, and then applying the standard master equation method to obtain the Lindbladian terms, in analogy with the results of the previous section [49]. From the obtained master equation, the equations of motion for the mean values of the polariton operators are $\partial_t \langle \hat{P}_\mu \rangle = (-i\Omega_\mu - \gamma_\phi^\mu/2) \langle \hat{P}_\mu \rangle$, where

$$\gamma_\phi^\mu = \gamma_c^0 (|U_a^\mu|^2 + |V_a^\mu|^2) + \gamma_x^0 (|U_b^\mu|^2 + |V_b^\mu|^2). \quad (15)$$

This result can be very different from what could be obtained starting from Eq. (12) and ignoring the modifications in the perturbation Hamiltonian induced by the light-matter interaction. Figure 3(a) shows the normalized pure dephasing rates for the two polariton modes ($\gamma_\phi^\mu/\gamma_x^0$), for the case of the zero photonic noise ($\gamma_c^0 = 0$), and

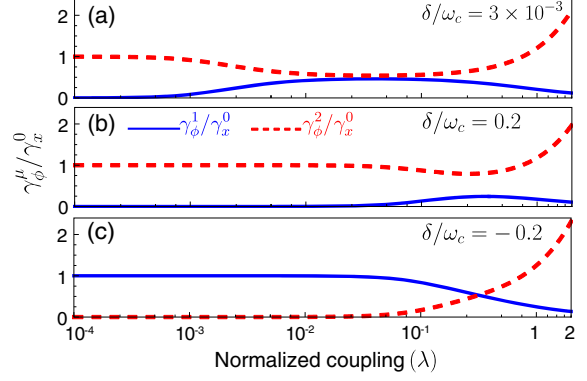


FIG. 3. Hopfield model. Normalized pure dephasing rate of the lower and upper polaritons, originating from exciton dephasing, versus the normalized coupling strength, obtained for different exciton-cavity detunings, and considering only the matter pure dephasing.

considering three different values of the exciton-cavity detuning δ . We observe that, at large coupling rates, independently of the detuning, the lower polariton dephasing rate tends to zero. This effect is a direct consequence of the fact that the lower polariton resonance frequency tends rapidly to zero for $\lambda \rightarrow \infty$ [see Fig. 4(c)], independently of the detuning. This implies that any small fluctuation of the resonance frequencies of the components does not induce fluctuations and, hence, dephasing in the polariton mode. For comparison, Figs. 4(a)–4(b) display the wrong result $\gamma_\phi^\mu/\gamma_x^0 = |U_b^\mu|^2 + |V_b^\mu|^2$, obtained by neglecting the changes

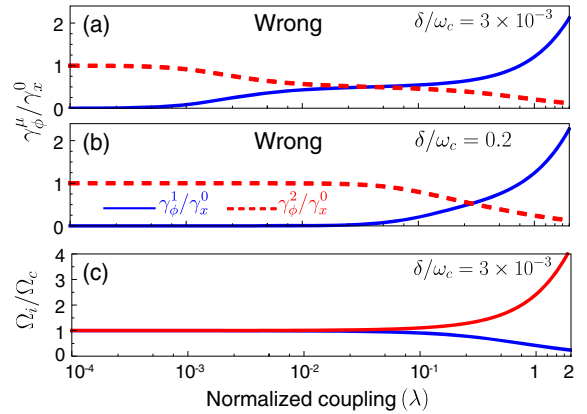


FIG. 4. Hopfield model. Wrong (see text) normalized pure dephasing rates of the lower and upper polaritons, originating from exciton dephasing, versus the normalized coupling strength, obtained for two different exciton-cavity detunings, and considering only the matter pure dephasing (a),(b). (c) Frequencies of the two polariton modes for a qubit-cavity detuning $\delta/\omega_c = 3 \times 10^{-3}$.

of the form of subsystems-observables, which can be induced by the interaction, as calculated for two different detunings. Evident differences emerge when entering the USC regime with $\lambda \sim 0.1$. Moreover, at larger coupling rates, in the DSC regime, the behavior of the lower and upper polaritons is clearly inverted.

Conclusions.—We have shown how to calculate correctly the pure dephasing rate in cavity QED systems, considering two prototypical models: the QRM and the Hopfield model. In the latter model, we found that pure dephasing effects in the lower polariton branch tend to be reduced in the USC regime, and tend to get suppressed increasing further the coupling [see Fig. 3(a)]. On the contrary, the influence of pure dephasing increases at increasing coupling strengths for upper polaritons. We hope that these results will stimulate experimental tests for various polariton systems, where these interaction regimes have been observed [31]. In a number of experiments, it was observed that the upper polariton clearly displays a larger line broadening with respect to the lower one [54–57] in agreement with the results presented here. However, since in these systems different broadening mechanisms enter into play, further investigations are required. The approach shown here can be applied to more complex light-matter systems and/or to full quantum models of pure dephasing [22,58]. The general lesson is that when the light-matter interaction rate becomes comparable to the bare resonance frequencies of the relevant bare transitions of the system components, the generalized minimal coupling replacements introducing the light-matter interaction have to be also applied to any perturbation affecting the matter or light subsystems.

S. S. acknowledges the Army Research Office (ARO) (Grant No. W911NF-19-1-0065). A. M. and S. A. are supported by the Polish National Science Centre (NCN) under the Maestro Grant No. DEC-2019/34/A/ST2/00081. S. A. was also supported by Grant No. POWR.03.05.00-00-Z303/17 within the University of Tomorrow Project of Adam Mickiewicz University.

*shsavan@gmail.com

†fabio.mauceri@unime.it

- [1] L. Allen and J. H. Eberly, *Optical Resonance and Two-Level Atoms* (Wiley-Interscience, New York, 1987), Vol. 28.
- [2] P. Lambropoulos and D. Petrosyan, *Fundamentals of Quantum Optics and Quantum Information* (Springer, New York, 2007), Vol. 23.
- [3] P. Borri, W. Langbein, S. Schneider, U. Woggon, R. L. Sellin, D. Ouyang, and D. Bimberg, *Phys. Rev. Lett.* **87**, 157401 (2001).
- [4] P. Borri, W. Langbein, U. Woggon, M. Schwab, M. Bayer, S. Fafard, Z. Wasilewski, and P. Hawrylak, *Phys. Rev. Lett.* **91**, 267401 (2003).
- [5] E. A. Muljarov, T. Takagahara, and R. Zimmermann, *Phys. Rev. Lett.* **95**, 177405 (2005).
- [6] M. R. Delbecq *et al.*, *Phys. Rev. Lett.* **116**, 046802 (2016).
- [7] I. Kilen, M. Kolesik, J. Hader, J. V. Moloney, U. Huttner, M. K. Hagen, and S. W. Koch, *Phys. Rev. Lett.* **125**, 083901 (2020).
- [8] F. Katsch, M. Selig, and A. Knorr, *Phys. Rev. Lett.* **124**, 257402 (2020).
- [9] T. Yu and J. H. Eberly, *Phys. Rev. B* **68**, 165322 (2003).
- [10] S. Haroche, *Rev. Mod. Phys.* **85**, 1083 (2013).
- [11] W. H. Zurek, *Rev. Mod. Phys.* **75**, 715 (2003).
- [12] S. Habib, K. Shizume, and W. H. Zurek, *Phys. Rev. Lett.* **80**, 4361 (1998).
- [13] D. P. DiVincenzo, *Science* **270**, 255 (1995).
- [14] S. I. Bogdanov, A. Boltasseva, and V. M. Shalaev, *Science* **364**, 532 (2019).
- [15] D. A. Lidar, I. L. Chuang, and K. B. Whaley, *Phys. Rev. Lett.* **81**, 2594 (1998).
- [16] A. Grodecka and P. Machnikowski, *Phys. Rev. B* **73**, 125306 (2006).
- [17] M. Ban, S. Kitajima, and F. Shibata, *Phys. Lett. A* **349**, 415 (2006).
- [18] Q. Guo *et al.*, *Phys. Rev. Lett.* **121**, 130501 (2018).
- [19] Z.-L. Xiang, S. Ashhab, J. Q. You, and F. Nori, *Rev. Mod. Phys.* **85**, 623 (2013).
- [20] G. Kurizki, P. Bertet, Y. Kubo, K. Mølmer, D. Petrosyan, P. Rabl, and J. Schmiedmayer, *Proc. Natl. Acad. Sci. U.S.A.* **112**, 3866 (2015).
- [21] A. Clerk, K. Lehnert, P. Bertet, J. Petta, and Y. Nakamura, *Nat. Phys.* **16**, 257 (2020).
- [22] F. Beaudoin, J. M. Gambetta, and A. Blais, *Phys. Rev. A* **84**, 043832 (2011).
- [23] A. Settineri, V. Macrì, A. Ridolfo, O. Di Stefano, A. F. Kockum, F. Nori, and S. Savasta, *Phys. Rev. A* **98**, 053834 (2018).
- [24] Z.-L. Xiang, S. Ashhab, J. Q. You, and F. Nori, *Rev. Mod. Phys.* **85**, 623 (2013).
- [25] X. Gu, A. F. Kockum, A. Miranowicz, Y.-X. Liu, and F. Nori, *Phys. Rep.* **718–719**, 1 (2017).
- [26] B. Lounis and M. Orrit, *Rep. Prog. Phys.* **68**, 1129 (2005).
- [27] J. M. Gambetta, J. M. Chow, and M. Steffen, *npj Quantum Inf.* **3**, 2 (2017).
- [28] M. Ganzhorn *et al.*, *Phys. Rev. Appl.* **11**, 044092 (2019).
- [29] R. Uppu *et al.*, *Sci. Adv.* **6**, eabc8268 (2020).
- [30] A. Auffèves, D. Gerace, J.-M. Gérard, M. F. Santos, L. C. Andreani, and J.-P. Poizat, *Phys. Rev. B* **81**, 245419 (2010).
- [31] A. F. Kockum, A. Miranowicz, S. D. Liberato, S. Savasta, and F. Nori, *Nat. Rev. Phys.* **1**, 19 (2019).
- [32] P. Forn-Díaz, L. Lamata, E. Rico, J. Kono, and E. Solano, *Rev. Mod. Phys.* **91**, 025005 (2019).
- [33] K. K. W. Ma and C. K. Law, *Phys. Rev. A* **92**, 023842 (2015).
- [34] L. Garziano, R. Stassi, V. Macrì, A. F. Kockum, S. Savasta, and F. Nori, *Phys. Rev. A* **92**, 063830 (2015).
- [35] T. H. Kyaw, S. Felicetti, G. Romero, E. Solano, and L.-C. Kwek, *Sci. Rep.* **5**, 8621 (2015).
- [36] L. Garziano, V. Macrì, R. Stassi, O. Di Stefano, F. Nori, and S. Savasta, *Phys. Rev. Lett.* **117**, 043601 (2016).
- [37] R. Stassi and F. Nori, *Phys. Rev. A* **97**, 033823 (2018).
- [38] R. Stassi, M. Cirio, and F. Nori, *npj Quantum Inf.* **6**, 1 (2020).

- [39] V. Macrì, A. Mercurio, F. Nori, S. Savasta, and C. S. Muñoz, *Phys. Rev. Lett.* **129**, 273602 (2022).
- [40] D. De Bernardis, P. Pilar, T. Jaako, S. De Liberato, and P. Rabl, *Phys. Rev. A* **98**, 053819 (2018).
- [41] O. Di Stefano, A. Settineri, V. Macrì, L. Garziano, R. Stassi, S. Savasta, and F. Nori, *Nat. Phys.* **15**, 803 (2019).
- [42] M. A. D. Taylor, A. Mandal, W. Zhou, and P. Huo, *Phys. Rev. Lett.* **125**, 123602 (2020).
- [43] O. Dmytruk and M. Schiró, *Phys. Rev. B* **103**, 075131 (2021).
- [44] A. Settineri, O. Di Stefano, D. Zueco, S. Hughes, S. Savasta, and F. Nori, *Phys. Rev. Res.* **3**, 023079 (2021).
- [45] A. Stokes and A. Nazir, *Phys. Rev. Res.* **3**, 013116 (2021).
- [46] S. Savasta, O. Di Stefano, A. Settineri, D. Zueco, S. Hughes, and F. Nori, *Phys. Rev. A* **103**, 053703 (2021).
- [47] H.-P. Breuer and F. Petruccione, *The Theory of Open Quantum Systems* (Oxford University Press, New York, 2002).
- [48] C. Gustin, S. Franke, and S. Hughes, *Phys. Rev. A* **107**, 013722 (2023).
- [49] See Supplemental Material at <http://link.aps.org/supplemental/10.1103/PhysRevLett.130.123601> for detailed derivation of pure dephasing terms on both quantum Rabi and Hopfield models. Analytical derivation of dephasing rates transitions.
- [50] A. Mercurio, V. Macrì, C. Gustin, S. Hughes, S. Savasta, and F. Nori, *Phys. Rev. Res.* **4**, 023048 (2022).
- [51] C. Cohen-Tannoudji, J. Dupont-Roc, and G. Grynberg, *Photons and Atoms: Introduction to Quantum Electrodynamics* (Wiley-VCH, New York, 1997).
- [52] J. Hopfield, *Phys. Rev.* **112**, 1555 (1958).
- [53] L. Garziano, A. Settineri, O. Di Stefano, S. Savasta, and F. Nori, *Phys. Rev. A* **102**, 023718 (2020).
- [54] G. Scalari *et al.*, *Science* **335**, 1323 (2012).
- [55] S. Gambino *et al.*, *ACS Photonics* **1**, 1042 (2014).
- [56] A. Bayer, M. Pozimski, S. Schambeck, D. Schuh, R. Huber, D. Bougeard, and C. Lange, *Nano Lett.* **17**, 6340 (2017).
- [57] S. Rajabali, G. Scalari, J. Keller, M. Beck, and J. Faist, in *2019 44th International Conference on Infrared, Millimeter, and Terahertz Waves (IRMMW-THz)* (IEEE, 2019), p. 1, 10.1109/IRMMW-THz.2019.8874524.
- [58] H. Carmichael, *An Open Systems Approach to Quantum Optics* (Springer Berlin, Heidelberg, 2009), Vol. 18.

Supplemental Material to Pure Dephasing of Light-Matter Systems in the Ultrastrong and Deep-Strong Coupling Regimes

CONTENTS

Comparison of the basic formulas in the Coulomb and dipole gauges for the quantum Rabi and Hopfield models.	S1
Pure dephasing in the quantum Rabi model	S1
Analytical derivation of the pure dephasing rates	S2
Pure dephasing in bosonic systems	S3
Non-interacting harmonic oscillator	S3
Hopfield model	S4
Additional Figures	S6
References	S7

COMPARISON OF THE BASIC FORMULAS IN THE COULOMB AND DIPOLE GAUGES FOR THE QUANTUM RABI AND HOPFIELD MODELS.

Hamiltonians & operators	Coulomb gauge	Dipole gauge
Rabi Hamiltonian	$\hat{\mathcal{H}}_C$ in Eq. (M-4)	$\hat{\mathcal{H}}_D = \hat{\mathcal{T}}\hat{\mathcal{H}}_C\hat{\mathcal{T}}^\dagger$ above Eq. (M-4) with $\hat{\mathcal{T}} = \exp[-i\hat{\mathcal{A}}\hat{\sigma}_x]$
Rabi annihilation operators	$\hat{a}_C = \hat{a}$	$\hat{a}_D = \hat{\mathcal{T}}\hat{a}\hat{\mathcal{T}}^\dagger = \hat{a} + i\eta\hat{\sigma}_x$ below Eq. (M-6)
Rabi perturbation Hamiltonian for pure dephasing	$\hat{\mathcal{V}}_\phi^C$ in Eq. (M-5)	$\hat{\mathcal{V}}_\phi^D$ below Eq. (M-4)
Hopfield Hamiltonian	\hat{H}_C in Eq. (M-10)	$\hat{H}_D = \hat{\mathcal{T}}\hat{H}_C\hat{\mathcal{T}}^\dagger$ in Eq. (M-9) with $\hat{\mathcal{T}} = \exp[-i\lambda(\hat{a} + \hat{a}^\dagger)(\hat{b} + \hat{b}^\dagger)]$
Hopfield annihilation operators	$\hat{a}_C = \hat{a}$ $\hat{b}_C = \hat{\mathcal{T}}^\dagger\hat{a}\hat{\mathcal{T}} = \hat{b} - i\lambda(\hat{a} + \hat{a}^\dagger)$ below Eq. (M-14)	$\hat{a}_D = \hat{\mathcal{T}}\hat{a}\hat{\mathcal{T}}^\dagger = \hat{a} + i\lambda(\hat{b} + \hat{b}^\dagger)$ below Eq. (M-14) $\hat{b}_D = \hat{b}$
Hopfield perturbation Hamiltonian for pure dephasing	$\hat{\mathcal{V}}_{\text{dep}}^C$ in Eq. (M-14)	$\hat{\mathcal{V}}_{\text{dep}}^D$ in Eq. (M-13)

TABLE I. Comparison of the basic formulas in the Coulomb and dipole gauges for the quantum Rabi and Hopfield models. Note the label M- is introduced to refer to equations number in the main text.

PURE DEPHASING IN THE QUANTUM RABI MODEL

Here we analyze how to describe the correct and gauge invariant pure dephasing effects in the quantum Rabi model (QRM), following the procedure described in Ref. [S1] and considering both cavity and qubit decoherence. We start by considering the quantum Rabi Hamiltonian with an additional zero-mean stochastic modulation of the qubit resonance frequency $\hat{\mathcal{V}}_{\text{dep}}^q = f_q(t)\hat{\sigma}_z$. Expressing the Hamiltonian in the dressed basis and moving to the interaction picture with respect to $\hat{\mathcal{V}}_{\text{dep}}^q$, we obtain

$$\hat{\mathcal{V}}_{\text{dep}}^q(t) = f(t) \sum_{j,k} \langle j|\hat{\sigma}_z|k\rangle |j\rangle\langle k| e^{i\omega_{jk}t}, \quad (\text{S1})$$

S2

where $|j\rangle$ are the eigenstates of the total Hamiltonian and ω_{jk} are the transition frequencies. Expressing $f(t)$ in terms of its Fourier decomposition, and assuming that the main contribution to dephasing results from a small frequency interval around ω_{jk} [S1], we obtain

$$\hat{V}_{\text{dep}}^q(t) = \sum_{j,k} \sigma_z^{jk} |j\rangle\langle k| f_{-\omega_{jk}}(t), \quad (\text{S2})$$

where

$$f_{\omega_{jk}}(t) = \sqrt{S_f(\omega_{jk})} \xi_{\omega_{jk}}(t), \quad (\text{S3})$$

$S_f(\omega)$ is the spectral density of $f(t)$, and $\xi(\omega)$ such that $\langle \xi(\omega) \rangle = 0$ and $\langle \xi(\omega) \xi(\omega') \rangle = \delta(\omega - \omega')$ (i.e., corresponding to white noise). If the transition frequencies ω_{jk} are well-separated, we can treat each term of the above summation as an independent noise [S1].

We are now able to write down the dressed Lindbladian in case of qubit pure dephasing:

$$\mathcal{L}_{\text{dr}} \cdot = \mathcal{D} \left[\sum_j \Phi^j |j\rangle\langle j| \right] \cdot + \sum_{j,k \neq j} \Gamma_\phi^{jk} \mathcal{D} [|j\rangle\langle k|] \cdot, \quad (\text{S4})$$

where

$$\Phi^j = \sqrt{\frac{\gamma_\phi(0)}{2}} \sigma_z^{jj}, \quad (\text{S5})$$

and

$$\Gamma_\phi^{jk} = \frac{\gamma_\phi(\omega_{kj})}{2} |\sigma_z^{jk}|^2. \quad (\text{S6})$$

The whole procedure described above can also be applied to the case of cavity pure dephasing, by considering the QRM Hamiltonian with an additional zero-mean stochastic modulation of the cavity resonance frequency $\hat{V}_{\text{dep}}^c = f_c(t) \hat{a}^\dagger \hat{a}$. In this case, this stochastic perturbation, expressed in the dressed basis and in the interaction picture, becomes

$$\hat{V}_{\text{dep}}^c(t) = \sum_{j,k} \langle j | \hat{a}^\dagger \hat{a} | k \rangle |j\rangle\langle k| f_{-\omega_{jk}}(t), \quad (\text{S7})$$

while the Lindbladian remains in the same form of Eq. (S4), with the only difference of Φ^j and Γ_ϕ^{jk} , which become respectively,

$$\Phi^j = \sqrt{\frac{\gamma_\phi(0)}{2}} \langle j | \hat{a}^\dagger \hat{a} | j \rangle, \quad (\text{S8})$$

$$\Gamma_\phi^{jk} = \frac{\gamma_\phi(\omega_{kj})}{2} |\langle j | \hat{a}^\dagger \hat{a} | k \rangle|^2. \quad (\text{S9})$$

However, we have seen in the main text that the approach described above does not reproduce the correct results. In particular, we have shown that, if one uses the Coulomb or dipole gauge, significantly different results can be obtained. For example, when using the Coulomb gauge, the bare $\hat{\sigma}_z$ operator becomes $\hat{\sigma}_z^C = \hat{T}^\dagger \hat{\sigma}_z \hat{T}$, since the minimal coupling is applied to the matter system, while the photonic operator $\hat{a}^\dagger \hat{a}$ becomes $\hat{a}_D^\dagger \hat{a}_D = \hat{T} \hat{a}^\dagger \hat{a} \hat{T}^\dagger$ in the dipole gauge. Thus, to correctly describe pure dephasing effects, we need to substitute in the Lindbladian given in Eq. (S4): $\hat{\sigma}_z \rightarrow \hat{\sigma}_z^C$ in the Coulomb gauge, and $\hat{a}^\dagger \hat{a} \rightarrow \hat{a}_D^\dagger \hat{a}_D$ in the dipole gauge.

Analytical derivation of the pure dephasing rates

By adopting the procedure described above, we are able to derive analytically the pure dephasing rates of both cavity and qubit. Starting from the Coulomb gauge and using Eq. (S4), we discard the off-diagonal terms Γ_ϕ^{jk} since

S3

this contribution is significant only if the dephasing bath has a spectral weight at the potentially high frequency ω_{jk} , leading to the following equation:

$$\dot{\hat{\rho}} = -i[\hat{\mathcal{H}}_C, \hat{\rho}] + \frac{\gamma\phi(0)}{2}\mathcal{D}\left[\sum_j \sigma_z^{C,jj} |j\rangle\langle j|\right] \hat{\rho}, \quad (\text{S10})$$

where $\sigma_z^{C,jj} = \langle j|\hat{\sigma}_z|j\rangle$. We now expand the Lindblad dissipator

$$\mathcal{D}\left[\sum_j \sigma_z^{C,jj} |j\rangle\langle j|\right] \hat{\rho} = \frac{1}{2}\left[2\sum_j \sum_{j'} \sigma_z^{C,jj} \sigma_z^{C,j'j'} |j\rangle\langle j| \hat{\rho} |j'\rangle\langle j'| - \sum_j \sum_{j'} \sigma_z^{C,jj} \sigma_z^{C,j'j'} |j'\rangle\langle j'| \hat{\rho} |j\rangle\langle j| \right. \quad (\text{S11})$$

$$\left. - \sum_j \sum_{j'} \sigma_z^{C,jj} \sigma_z^{C,j'j'} \hat{\rho} |j'\rangle\langle j'| |j\rangle\langle j| \right], \quad (\text{S12})$$

and we focus on the matrix element of the density matrix relative to the transition $(\tilde{1}_-, \tilde{0})$, but the same procedure can be applied to all the other transitions. The corresponding equation (in the interaction picture) for that matrix element becomes

$$\begin{aligned} \frac{d}{dt} \hat{\rho}_{\tilde{1}_-, \tilde{0}}^{(I)} &= \frac{\gamma\phi(0)}{4} \langle \tilde{1}_- | \left[2\sum_j \sum_{j'} \sigma_z^{C,jj} \sigma_z^{C,j'j'} |j\rangle\langle j| \hat{\rho}^{(I)} |j'\rangle\langle j'| - \sum_j |\sigma_z^{C,jj}|^2 |j\rangle\langle j| \hat{\rho}^{(I)} - \sum_j |\sigma_z^{C,jj}|^2 \hat{\rho}^{(I)} |j\rangle\langle j| \right] | \tilde{0} \rangle \\ &= \frac{\gamma\phi(0)}{4} \left[2\sum_j \sum_{j'} \sigma_z^{C,jj} \sigma_z^{C,j'j'} \langle \tilde{1}_- | j \rangle \langle j | \hat{\rho}^{(I)} | j' \rangle \langle j' | \tilde{0} \rangle - \sum_j |\sigma_z^{C,jj}|^2 \langle \tilde{1}_- | j \rangle \langle j | \hat{\rho}^{(I)} | \tilde{0} \rangle \right. \\ &\quad \left. - \sum_j |\sigma_z^{C,jj}|^2 \langle \tilde{1}_- | \hat{\rho}^{(I)} | j \rangle \langle j | \tilde{0} \rangle \right] \\ &= \frac{\gamma\phi(0)}{4} \left[2\sigma_z^{C, \tilde{1}_- \tilde{1}_-} \sigma_z^{C, \tilde{0} \tilde{0}} \langle \tilde{1}_- | \hat{\rho}^{(I)} | \tilde{0} \rangle - |\sigma_z^{C, \tilde{1}_- \tilde{1}_-}|^2 \langle \tilde{1}_- | \hat{\rho}^{(I)} | \tilde{0} \rangle - |\sigma_z^{C, \tilde{0} \tilde{0}}|^2 \langle \tilde{1}_- | \hat{\rho}^{(I)} | \tilde{0} \rangle \right] \\ &= -\frac{\gamma\phi(0)}{4} \left| \sigma_z^{C, \tilde{1}_- \tilde{1}_-} - \sigma_z^{C, \tilde{0} \tilde{0}} \right|^2 \hat{\rho}_{\tilde{1}_-, \tilde{0}}^{(I)}. \end{aligned} \quad (\text{S13})$$

By choosing the dipole gauge, one should replace $\sigma_z^{C,jj} \rightarrow \sigma_z^{jj}$. The same procedure is valid also for cavity pre dephasing, where we need to use $\hat{a}^\dagger \hat{a}$ in the Coulomb gauge and $\hat{a}_D^\dagger \hat{a}_D$ in the dipole gauge.

PURE DEPHASING IN BOSONIC SYSTEMS

We now consider pure dephasing effects in bosonic systems. First, we consider a simple non-interacting harmonic oscillator, then we analyze the Hopfield model.

Non-interacting harmonic oscillator

Here we consider a single-mode bosonic field described by the harmonic oscillator Hamiltonian $\hat{H}_0 = \omega_0 \hat{a}^\dagger \hat{a}$ affected by pure dephasing. Analogously to what we described in previous sections, in order to consider the dephasing effects, we introduce an additional zero-mean stochastic modulation of the resonance frequency $\hat{V}_{\text{dep}}^h = f_h(t) \hat{a}^\dagger \hat{a}$. Moving to the interaction picture, we notice that this component does not rotate, since it has a zero-frequency oscillation. Thus, transforming $f_h(t)$ in its Fourier components, and assuming that the main contribution to dephasing comes from a small frequency interval around $\omega = 0$ [S1], we obtain

$$\hat{V}_{\text{dep}}^h(t) = f_0(t) \hat{a}^\dagger \hat{a}, \quad (\text{S14})$$

where $f_0(t) = \sqrt{S_f(0)} \xi_0(t)$. This equation is quite similar to Eq. (S2) with the only difference that here we do not have the expansion in the dressed basis (since we are not considering a hybrid quantum system), and that we have only

S4

the zero-frequency contribution (since $\hat{\mathcal{V}}_{\text{dep}}^h$ rotates at zero frequency in the interaction picture). These considerations allow us to write the Lindbladian describing this pure dephasing effect as

$$\mathcal{L} \cdot = \sqrt{\frac{\gamma_\phi(0)}{2}} \mathcal{D} [\hat{a}^\dagger \hat{a}] \cdot, \quad (\text{S15})$$

with $\gamma_\phi(0) = 2S_f(0)$.

Hopfield model

Here we analyze pure dephasing effects in the Hopfield model, following the procedure described in the previous sections and extending the results of Ref. [S1]. Moreover, we consider both light and matter decoherence. First, it is useful to diagonalize the Hopfield Hamiltonian using the polaritonic operators [S2], where the lower and upper polariton operators ($\mu = 1, 2$) can be defined as

$$\hat{P}^\mu = U_b^\mu \hat{b} + U_a^\mu \hat{a} + V_b^\mu \hat{b}^\dagger + V_a^\mu \hat{a}^\dagger. \quad (\text{S16})$$

Using the property

$$|U_b^\mu|^2 + |U_a^\mu|^2 - |V_b^\mu|^2 - |V_a^\mu|^2 = 1, \quad (\text{S17})$$

which guarantee the correct polariton commutation rules [S2], we can invert Eq. (S16) in order to obtain

$$\hat{a} = \sum_{\mu=1}^2 \left(U_a^\mu \hat{P}_\mu - V_a^\mu \hat{P}_\mu^\dagger \right), \quad (\text{S18a})$$

$$\hat{b} = \sum_{\mu=1}^2 \left(U_b^\mu \hat{P}_\mu - V_b^\mu \hat{P}_\mu^\dagger \right). \quad (\text{S18b})$$

To describe the matter pure dephasing, we consider an additional zero-mean stochastic modulation of the matter resonance frequency $\hat{\mathcal{V}}_{\text{dep}}^x = f_x(t) \hat{b}^\dagger \hat{b}$. In terms of the polaritonic operators we have

$$\hat{b}^\dagger \hat{b} = A_1 \hat{P}_1^\dagger \hat{P}_1 + A_2 \hat{P}_2^\dagger \hat{P}_2 + B_{12} \hat{P}_1^\dagger \hat{P}_2 + B_{21} \hat{P}_2^\dagger \hat{P}_1, \quad (\text{S19})$$

with

$$A_\mu = |U_b^\mu|^2 + |V_b^\mu|^2 \quad (\text{S20})$$

$$B_{12} = B_{21}^* = U_b^{1*} U_b^2 + V_b^1 V_b^{2*}, \quad (\text{S21})$$

where we have included only the terms which do not oscillate in time, or oscillate at low frequency, corresponding to applying the rotating wave approximation (RWA), and we have eliminated the constants derived from commutation rules, which have no dynamical consequences. Moving to the interaction picture, this contribution becomes

$$\hat{\mathcal{V}}_{\text{dep}}^x(t) = f_x(t) \left[A_1 \hat{P}_1^\dagger \hat{P}_1 + A_2 \hat{P}_2^\dagger \hat{P}_2 + e^{-i\omega_{21}t} B_{12} \hat{P}_1^\dagger \hat{P}_2 + e^{i\omega_{21}t} B_{21} \hat{P}_2^\dagger \hat{P}_1 \right], \quad (\text{S22})$$

where $\omega_{21} = \omega_2 - \omega_1$ with the polaritonic eigenfrequencies ω_i . Equation (S22) can be written in a more compact form as

$$\hat{\mathcal{V}}_{\text{dep}}^x = f_x(t) \left[\hat{D}_{12} + e^{-i\omega_{21}t} \hat{M}_{12} + e^{i\omega_{21}t} \hat{M}_{12}^\dagger \right],$$

with

$$\hat{D}_{12} = A_1 \hat{P}_1^\dagger \hat{P}_1 + A_2 \hat{P}_2^\dagger \hat{P}_2, \quad (\text{S23})$$

$$\hat{M}_{12} = B_{12} \hat{P}_1^\dagger \hat{P}_2, \quad (\text{S24})$$

and using the results presented in the previous sections, we obtain

$$\hat{\mathcal{V}}_{\text{dep}}^x(t) = f_0(t) \hat{D}_{12} + f_{\omega_{21}}(t) \hat{M}_{12} + f_{-\omega_{21}}(t) \hat{M}_{12}^\dagger, \quad (\text{S25})$$

with $f_\omega(t)$ expressed in Eq. (S3). Thus, the resulting Lindbladian in the case of matter pure dephasing is

$$\mathcal{L}\cdot = \frac{1}{2}\gamma_\phi(\omega_{21})\mathcal{D}[\hat{M}_{12}]\cdot + \frac{1}{2}\gamma_\phi(-\omega_{21})\mathcal{D}[\hat{M}_{12}^\dagger]\cdot + \frac{1}{2}\gamma_\phi(0)\mathcal{D}[\hat{D}_{12}]\cdot, \quad (\text{S26})$$

with $\gamma_\phi(\omega) = 2S_f(\omega)$.

The same procedure, as described above, can also be applied to the case of cavity pure dephasing, by considering an additional zero-mean stochastic modulation of the cavity resonance frequency $\hat{V}_{\text{dep}}^c = f_c(t)\hat{a}^\dagger\hat{a}$. The procedure remains the same for the matter dephasing case, except that now we consider

$$\hat{a}^\dagger\hat{a} = A_1\hat{P}_1^\dagger\hat{P}_1 + A_2\hat{P}_2^\dagger\hat{P}_2 + B_{12}\hat{P}_1^\dagger\hat{P}_2 + B_{21}\hat{P}_2^\dagger\hat{P}_1, \quad (\text{S27})$$

where

$$A_\mu = |U_a^\mu|^2 + |V_a^\mu|^2, \quad (\text{S28})$$

$$B_{12} = B_{21}^* = U_a^{1*}U_a^2 + V_a^1V_a^{2*}. \quad (\text{S29})$$

This yields a Lindbladian of the same form of Eq. (S26) with the only difference for the polariton coefficients expressed in Eqs. (S28) and (S29).

However, we have seen in the main text that this approach can lead to wrong results, depending on the chosen gauge. Indeed, when using the Coulomb gauge, the matter operator \hat{b} becomes $\hat{b}_C = \hat{T}^\dagger\hat{b}\hat{T}$, since the minimal coupling is applied to the matter system. On the contrary, when using the dipole gauge, the minimal coupling is applied to the photonic system, and the *dressed* photonic operator becomes $\hat{a}_D = \hat{T}\hat{a}\hat{T}^\dagger$. This consideration leads us to note that the polariton diagonalization leads to different Hopfield coefficients if we choose the Coulomb or dipole gauge. In particular, in the dipole gauge, we have

$$\hat{b} = \sum_{\mu=1}^2 \left(U_b^{\mu\mu}\hat{P}'_\mu - V_b^{\mu\mu}\hat{P}^\dagger_\mu \right), \quad (\text{S30})$$

where P'_μ are the polariton operators obtained by diagonalizing the Hopfield Hamiltonian in the dipole gauge. While in the Coulomb gauge we have

$$\begin{aligned} \hat{b}_C &= \hat{T}^\dagger \left[\sum_{\mu=1}^2 \left(U_b^{\mu\mu}\hat{P}'_\mu - V_b^{\mu\mu}\hat{P}^\dagger_\mu \right) \right] \hat{T} \\ &= \sum_{\mu=1}^2 \left(U_b^{\mu\mu}\hat{T}^\dagger\hat{P}'_\mu\hat{T} - V_b^{\mu\mu}\hat{T}^\dagger\hat{P}^\dagger_\mu\hat{T} \right) \\ &= \sum_{\mu=1}^2 \left(U_b^{\mu\mu}\hat{P}_\mu - V_b^{\mu\mu}\hat{P}^\dagger_\mu \right), \end{aligned} \quad (\text{S31})$$

which contains the polariton operators obtained by diagonalizing the Hamiltonian in the Coulomb gauge, but with the same coefficients of the dipole gauge. To obtain Eq. (S31), we have used the relation

$$\hat{P}_\mu = \hat{T}^\dagger\hat{P}'_\mu\hat{T}, \quad (\text{S32})$$

which, although intuitively obvious, can be rigorously demonstrated using the definition of polaritonic operators; in particular, those operators that, each in its specific gauge, enable the diagonalization of the gauge-correspondent Hamiltonian. For example, we have:

$$[\hat{P}_\mu, \hat{\mathcal{H}}_C] = \Omega_\mu\hat{P}_\mu, \quad (\text{S33a})$$

$$[\hat{P}'_\mu, \hat{\mathcal{H}}_D] = \Omega_\mu\hat{P}'_\mu. \quad (\text{S33b})$$

In order to demonstrate Eq. (S32), we can calculate how Eq. (S33a) transforms from the Coulomb to dipole gauge. Gauge invariance implies that the final result has to be equal to Eq. (S33b). We obtain:

$$\hat{T}[\hat{P}_\mu, \hat{\mathcal{H}}_C]\hat{T}^\dagger = \Omega_\mu\hat{T}\hat{P}_\mu\hat{T}^\dagger, \quad (\text{S34a})$$

$$\begin{aligned} \hat{T}[\hat{P}'_\mu, \hat{\mathcal{H}}_C]\hat{T}^\dagger &= \hat{T}(\hat{P}'_\mu\hat{\mathcal{H}}_C - \hat{\mathcal{H}}_C\hat{P}'_\mu)\hat{T}^\dagger \\ &= \hat{T}\hat{P}'_\mu\hat{\mathcal{H}}_C\hat{T}^\dagger - \hat{T}\hat{\mathcal{H}}_C\hat{P}'_\mu\hat{T}^\dagger \\ &= \hat{T}\hat{P}'_\mu\hat{T}^\dagger\hat{T}\hat{\mathcal{H}}_C\hat{T}^\dagger - \hat{T}\hat{\mathcal{H}}_C\hat{T}^\dagger\hat{T}\hat{P}'_\mu\hat{T}^\dagger \\ &= \hat{T}\hat{P}'_\mu\hat{T}^\dagger\hat{\mathcal{H}}_D - \hat{\mathcal{H}}_D\hat{T}\hat{P}'_\mu\hat{T}^\dagger = [\hat{T}\hat{P}'_\mu\hat{T}^\dagger, \hat{\mathcal{H}}_D]. \end{aligned} \quad (\text{S34b})$$

S6

Combining the results of Eqs. (S34a) and (S34b), we obtain:

$$[\hat{T}\hat{P}_\mu\hat{T}^\dagger, \hat{H}_D] = \Omega_\mu\hat{T}\hat{P}_\mu\hat{T}^\dagger, \quad (\text{S35})$$

which is the definition of the polariton operators \hat{P}'_μ in the dipole-gauge (which are the operators that allow the diagonalization of $\hat{\mathcal{H}}_D$) given by Eq. (S33b). Hence, Eq. (S32) is the correct gauge transformation for the polaritonic operators.

The whole analysis described above can be summarized as follows: in the case of matter pure dephasing, the stochastic perturbation is: $\hat{V}_{\text{dep}}^x = f_x(t)\hat{b}^\dagger\hat{b}$ in the dipole gauge, and $\hat{V}_{\text{dep}}^x = f_x(t)\hat{b}_C^\dagger\hat{b}_C$ in the Coulomb gauge, where

$$\hat{b}^\dagger\hat{b} = A'_1\hat{P}'_1\hat{P}'_1 + A'_2\hat{P}'_2\hat{P}'_2 + B'_{12}\hat{P}'_1\hat{P}'_2 + B'_{21}\hat{P}'_2\hat{P}'_1 \quad (\text{S36})$$

and

$$\hat{b}_C^\dagger\hat{b}_C = A'_1\hat{P}'_1\hat{P}'_1 + A'_2\hat{P}'_2\hat{P}'_2 + B'_{12}\hat{P}'_1\hat{P}'_2 + B'_{21}\hat{P}'_2\hat{P}'_1, \quad (\text{S37})$$

with

$$A'_\mu = |U_b^{\mu\mu}|^2 + |V_b^{\mu\mu}|^2, \quad (\text{S38})$$

$$B'_{12} = B'_{21} = U_b^{1'2'}U_b^{2'1'} + V_b^{1'}V_b^{2'}. \quad (\text{S39})$$

As a result, to correctly describe the matter pure dephasing, we need to use the dipole coefficients, given in Eqs. (S38) and (S39), in the Lindbladian expressed in Eq. (S26), even when using the Coulomb gauge. On the contrary, for the photonic pure dephasing, the stochastic perturbation is: $\hat{V}_{\text{dep}}^c = f_c(t)\hat{a}^\dagger\hat{a}$ in the Coulomb gauge, and $\hat{V}_{\text{dep}}^c = f_c(t)\hat{a}_D^\dagger\hat{a}_D$ in the dipole gauge. Thus, we need to use the Coulomb polariton coefficients in the Lindbladian even when using the dipole gauge.

ADDITIONAL FIGURES

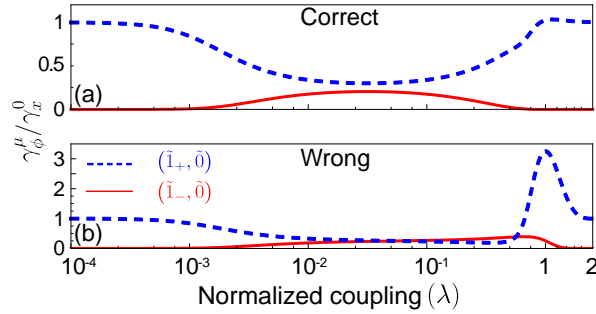


FIG. S1. Quantum Rabi model: Normalized pure dephasing rate for the two lowest energy transitions, for a small qubit-cavity detuning $\delta = 3 \times 10^{-3}$ assuming only the cavity pure dephasing. (a) Correct gauge-invariant results versus (b) wrong Coulomb gauge results.

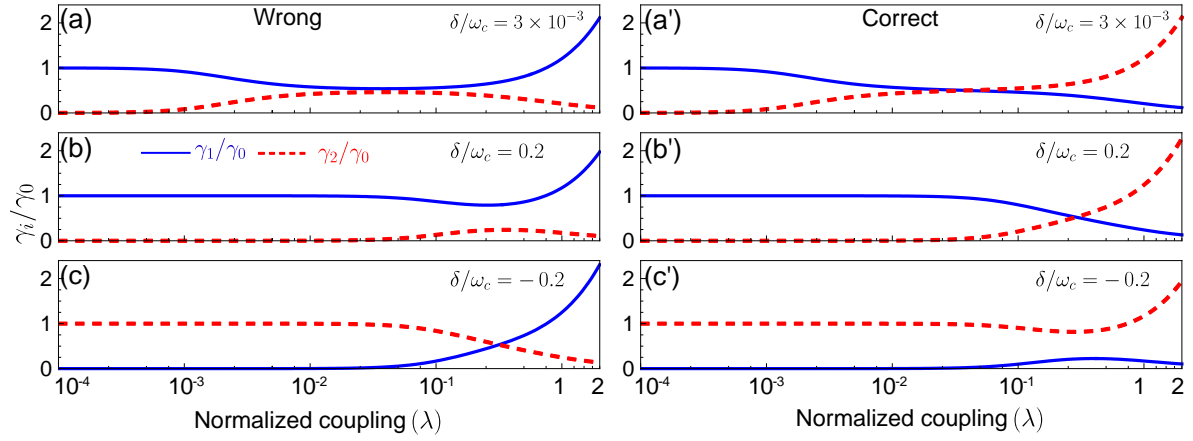


FIG. S2. Hopfield model: Pure dephasing rate of the lower and upper polaritons, originating from exciton dephasing, versus the normalized coupling strength, obtained for different exciton-cavity detunings, and considering only cavity pure dephasing.

[S1] F. Beaudoin, J. M. Gambetta, and A. Blais, *Phys. Rev. A* **84**, 043832 (2011).

[S2] J. Hopfield, *Phys. Rev.* **112**, 1555 (1958).

Chapter 5

Quantum exceptional points of non-Hermitian systems via quantum process tomography

5.1 Chapter outline

This chapter is intended to give a summary of article [P5]. I explain here one of the intriguing features of non-Hermitian systems, which are quantum Liouvillian exceptional points (LEPs), and how quantum process tomography (QPT) can be used to reveal and control them, through the introductory and motivation sections. Moreover, I concentrate below on the main findings of the paper, which show the experimental evidence of observing LEPs in a lossy single-qubit system using QPT.

5.1.1 Popular introduction

Hermitian Hamiltonian systems are isolated, conservative, and exhibit time-reversal symmetry. However, the majority of physical systems interact with their surroundings. To describe them properly, non-Hermitian Hamiltonians (NHHs) can be used. These are mathematical operators that partially capture the dynamics of quantum systems that are not isolated, and they play a pivotal role in describing the dynamics of open systems in non-Hermitian quantum mechanics formulated by Carl Bender et al. [1]¹, as well as in the quantum-trajectory method [115], which is also known

¹This and other references in this chapter correspond to those cited in [P5].

as the quantum-jump method [117], Monte Carlo wave-function method [116], or the wave-function approach to dissipative processes [114].

Non-Hermitian systems that experience energy gain or loss can behave very differently from Hermitian systems that conserve energy. The most noticeable difference is the appearance of exceptional points (EPs), which occur when two or more eigenvalues and their associated eigenvectors coalesce to form degenerate NHH systems [12-14].

A particular family of NHHs are the so-called parity-time (PT) symmetric systems [1,2,3], which have real energy spectra, same as those of Hermitian Hamiltonians. A Hamiltonian H is PT-symmetric if and only if it commutes with the PT operator, that is, $[H, PT] = 0$, where the time operator T denotes complex conjugation and the parity operator P denotes the reflection with respect to the center of symmetry.

One of the interesting effects, associated with PT-symmetry, is their phase transition arising at an EP [105,106]. At these transitions, the eigenvalue spectrum of these systems from real becomes complex, unveiling its non-Hermitian nature. The EP of an NHH called Hamiltonian EP (HEP) refers to the degenerate eigenvalues of the NHH, which correspond to coalescent eigenvectors. The eigenspectra of the effective Hamiltonian, is determined, by $H_{\text{eff}}|E_n\rangle = E_n|E_n\rangle$, where H_{eff} is the Hamiltonian of a given NHH system and $E_n, |E_n\rangle$ are, respectively, the eigenvalues and the corresponding eigenvectors of the system.

A multitude of intriguing properties associated with systems at HEPs have been predicted, including stimulated emission [46-51], spontaneous emission [52], chirality [53-55], unidirectional invisibility [56], control of whispering-gallery microcavities [57, 58], exceptional Kerr effect [59], and related exceptional photon blockade [60], as well as the generation of higher-order HEPs [31, 61-63]. For recent reviews on HEPs, consult the articles in Nature Materials [12] and Science [13].

However, the Hamiltonian-based definition of exceptional points neglects quantum jumps in the evolution of quantum systems. The effects of quantum jumps can be accounted for by considering a master equation and the corresponding Liouvillian and its exceptional points (LEPs), as proposed in 2019 [76-77] (These works are coauthored by the two supervisors of this thesis).

The master equation, given by $\dot{\hat{\rho}} = \mathcal{L}\rho(t)$, using the Liouvillian superoperator \mathcal{L} , describes the evolution of a reduced density matrix $\hat{\rho}$. The quantum trajectory interpretation of the master equation provides an intuitive understanding of the system dynamics, highlighting the role of effective non-Hermitian Hamiltonians in describing energy, coherence, and information losses in the system. In quantum

trajectory method, the standard Gorini-Kossakowski-Sudarshan-Lindblad master equation is written in the form

$$\dot{\hat{\rho}} = \mathcal{L}\hat{\rho}(t) = -i \left[\hat{H}_{\text{eff}}\hat{\rho}(t) - \hat{\rho}(t)\hat{H}_{\text{eff}}^\dagger \right] + \sum_{\mu} \hat{\Gamma}_{\mu}\hat{\rho}(t)\hat{\Gamma}_{\mu}^\dagger. \quad (5.1)$$

where $\hat{\Gamma}_{\mu}$ is a quantum jump operator, and

$$\hat{H}_{\text{eff}} = \hat{H} - \frac{i}{2} \sum_{\mu} \hat{\Gamma}_{\mu}^\dagger \hat{\Gamma}_{\mu}, \quad (5.2)$$

is the effective NHH for a given Hermitian Hamiltonian H . This form of the master equation includes two types of terms: the continuous non-unitary dissipation evolution described by \hat{H}_{eff} and the quantum-jump term that captures the sudden changes in the wave function.

The master equation describes how a system changes over time under the influence of a Liouvillian superoperator, which is a non-Hermitian matrix that can exhibit EPs. These EPs are called quantum EPs (QEPs) or LEPs because they are degeneracies of quantum Liouvillians.

The spectrum of the Liouvillian \mathcal{L} is given by $\mathcal{L}\hat{\rho}_i = \lambda_i\hat{\rho}_i$, where λ_i and $\hat{\rho}_i$ represent the eigenvalues and right eigenmatrices of the Liouvillian superoperator, respectively. The eigenmatrices of the Liouvillian superoperator \mathcal{L} are not necessarily normalized by default. But one can normalized them by using the Hilbert-Schmidt norm as $\langle \hat{\rho}_i, \hat{\rho}_i \rangle = \text{Tr}[\hat{\rho}_i^\dagger \hat{\rho}_i]$. Moreover, since a Liouvillian does not need to be a Hermitian superoperator, in general different $\hat{\rho}_i$ (and $\hat{\rho}_j$) will not be orthogonal.

LEPs are different from HEPs, which are degeneracies of non-Hermitian Hamiltonians. LEPs take into account both the continuous nonunitary dissipation and discrete quantum jumps that can occur in an open quantum system, whereas HEPs only consider the dissipation part. LEPs have attracted growing attention in both theoretical and experimental realms. Notably, recent experiments with a single superconducting qubit (reported in PRL [34, 35]) and a single trapped ion (reported in Nature Communication [78] and PRL [79]) have been conducted.

Quantum process tomography (QPT), also known as a quantum channel tomography, is a powerful technique for experimentally characterizing an unknown quantum process, channel, or quantum device [85–87]. The purpose of QPT is the reconstruction of a unknown Liouvillian superoperator, which fully describes the dynamics of the quantum process under investigation. QPT is considered an ex-

tension of quantum state tomography (QST) [88], where quantum output states are reconstructed for different input states.

QPT can be used for determining how a quantum system changes when it interacts with its surroundings. For example, when qubits pass through a quantum gate or quantum channel, they may be affected by noise and lose their quantum properties. This can cause errors in the quantum information that needs to be stored or processed. QPT allows us to discern the actual behavior of a quantum gate or channel, facilitating a subsequent comparison with the ideal process. This can help us to improve quantum control and reduce decoherence. To perform QPT, we do not need to use all possible input states for the system, but only a limited number. Then, we can see what output states we obtain after the system undergoes the quantum process. By comparing the input and output states, we can determine a given quantum process [89].

To our knowledge, the LEPs of reconstructed Liouvillians via QPT have not yet been studied. Hence, the primary objective of this study is to ascertain the LEPs via QPT for a given simple system, which is a single qubit experiencing dissipation across three channels.

5.1.2 Motivation

Exceptional points are exotic degeneracies of non-Hermitian systems, for which at least eigenvalues and corresponding eigenvectors simultaneously coalesce in the parameter space. They exhibit a special topological structure that leads to various counterintuitive phenomena and novel applications. HEPs and LEPs show their equivalence in the semiclassical regime, but can exhibit fundamental differences in the quantum regime [76]. Studying LEPs can help us to develop novel quantum devices for sensing, communication, and computation. QPT has now been established as an indispensable method for characterizing quantum processes, including quantum information processing. In this article, we reconstructed Liouvillians via QPT and subsequently found LEPs both theoretically using three equivalent methods introduced in this article and experimentally on IBM quantum processors.

5.1.3 Summary of the main results

We demonstrated theoretically and experimentally (on an IBMQ processors) how standard QPT, which reveals the dynamics of a quantum system, can be readily applied to reveal and characterize LEPs of non-Hermitian systems.

It is important to note that QST has been experimentally applied to reveal LEPs in Refs. [34, 35] (see also [33]). However, to our knowledge, QPT has not yet been applied to reveal LEPs and HEPs to date. In particular, a LEP-based quantum heat engine was studied experimentally in [78, 79], but neither QST nor QPT was applied.

We analyzed a prototype model of a single qubit decaying through three competing channels to demonstrate how to tune system parameters for observing LEPs, although the model does not exhibit HEPs. Specifically, we tomographically reconstructed the corresponding experimental Liouvillian and its LEPs by applying single- and two-qubit operations on an IBM quantum processor.

We believe that QPT can become an indispensable tool for precisely monitoring and controlling LEP-based quantum devices, including quantum heat engines [78, 79].

5.1.4 More details on the applied methods

Here I explain our method and some results in a greater detail.

As explained above, QPT is a technique that aims to identify unknown operations. The foundation for QPT is QST, which is a technique that reconstructs an unknown quantum state from a set of measurements. The standard QPT method consists of the following steps:

1. Prepare a complete basis of input states $\rho_{\text{in}}^n = |\psi_{\text{in}}^n\rangle\langle\psi_{\text{in}}^n|$. For example, for a single qubit, one can choose the eigenstates of the three Pauli operators: $|\psi_{\text{in}}^n\rangle \in \{|0\rangle, |1\rangle, \frac{1}{\sqrt{2}}(|0\rangle \pm |1\rangle), \frac{1}{\sqrt{2}}(|0\rangle \pm i|1\rangle)\}$.
2. Apply the unknown process \mathcal{E} to each input state.
3. Apply QST to reconstruct the output states $\mathcal{E}(\rho_{\text{in}}^n)$ for each ρ_{in}^n .

The goal of QPT is to find the process \mathcal{E} that maps the input states to the output states. However, not every process is physically valid. A physically valid process must be a completely positive map (CP-map), which is a linear map that preserves the positivity of operators in any Hilbert space [125,126]. A CP-map also must be trace-preserving, which means that it preserves the total probability of quantum states. However, due to experimental noise and using a limited number of measurements, the reconstructed process \mathcal{E} may not be a CP-map. Therefore, some methods (like maximum likelihood estimation, MLE) are needed to ensure that the QPT results are physically valid. In this study, we aimed to use QPT to identify the LEPs of the Liouvillian, which is a CP-map of the discussed open single qubit.

Studies have shown that LEPs can be calculated via the standard superoperator formalism, but here, we introduced three equivalent experimentally feasible methods of finding LEPs via QPT for a lossy single qubit. We have experimentally implemented one of the methods, which according to our simulations gives the highest fidelity of the reconstruction on an IBMQ processor. Each of these three QPT approaches enables us to reconstruct the Liouvillian of our proposed system, which is a single qubit model which evolves under the influence of the three different decay channels (σ_x, σ_y , and σ_-). In this study, we show that these three approaches are analytically and numerically equivalent. We explained that these approaches theoretically showed the ideal QPT of Liouvillians. However, performing QPT for Liouvillians is experimentally quite challenging because there can be many sources of errors in the experiments, such as imperfect preparation or measurement of the quantum states, or unwanted interactions with other qubits or other systems. We discussed the possible sources of error through the QPT for our system.

In our study, we implemented our CP-map on an extended Hilbert space and designed a quantum circuit using Qiskit for QPT to reconstruct the Liouvillians of a single-qubit model theoretically and experimentally, which was implemented on a quantum processor using the IBMQ platform [103]. We calculated the eigenspectra of both theoretical and experimental Liouvillians, and then demonstrated the LEPs of our system.

It should be noted that we demonstrated the spectral properties of the Liouvillian by calculating the imaginary and real parts of the Liouvillian eigenvalues as a function of γ_x/ω . Moreover, we demonstrated the scalar product of eigenvectors as a function of γ_x/ω , where γ_x is the decaying rate through the channel σ_x .

The QPT quantum circuit, designed using Qiskit, includes three qubits to reconstruct the Liouvillians of a lossy single qubit. In our QPT circuit design, we considered that the two qubits act as a noisy environment for the single qubit that we aimed to reconstruct its Liouvillian.

We performed the experiment first on a noiseless simulator then on a simulator with a chosen noise model for a selected IBM quantum processor and, finally, on real IBM quantum processors consisting of up to seven qubits. I should mention that the results demonstrated in the article were chosen from the results of the experiment done using the Open Quantum Assembly Language (OpenQASM) simulator and `ibmq_nairobi`.

Three sets of experimental results are presented and discussed in the article. The first case, which is the main setup, is the result of the quantum circuit of the three

qubits. In this case, the results were noisy even when we used error mitigation for our experimental results. However, our results showed that it is still possible to observe an LEP, as expected, which is similar to the theoretical result, but very noisy.

To obtain better results, we removed one of the qubits from our designed experimental QPT quantum circuit to reduce the noise. In this case, in the quantum circuit of two quantum registers, only one qubit plays the role of environmental noise. Consequently, the experimental results are in very good agreement with the theory, and the reduction in noise is significant.

Moreover, we performed a QPT experiment with a quantum circuit having only one qubit register as the input, in which we removed two other qubits from the circuit. Then we obtained experimental results with the best agreement with the theory. All the three methods confirmed the theoretical predictions of LEPs for our single lossy qubit by QPT.

5.1.5 My contribution and importance of the work

We anticipate that exploring LEPs may result in the development of more robust readout techniques. This advancement could prove valuable, particularly in mitigating readout errors in quantum computers. We are confident that QPT, as applied in article [P5] for the first time in research related to LEPs, has the potential to become an essential tool in this area of research. Arguably, QPT is superior in many ways to QST for precise monitoring and controlling LEP-based quantum devices, which can find applications for quantum metrology and quantum thermodynamics, to mention quantum heat engines.

I and Patrycja Tulewicz have executed all the experiments for this work on IBMQ using different processors. Ultimately, the paper exclusively incorporates only my experimental data. I have conducted both analytical and numerical calculations, inclusive of data postprocessing, with thorough validation by other co-authors. The first version of the paper was written by me and subsequently refined through collaborative revision by all authors. Moreover, I have made significant contributions to the interpretation of the obtained experimental results.

5.2 Preprint of article [P5]

On the subsequent pages, we append an arXiv preprint:

[P5] Shilan Abo, Patrycja Tulewicz, Karol Bartkiewicz, Sahin K. Özdemir, and Adam Miranowicz,
Liouvillian Exceptional Points of Non-Hermitian Systems via Quantum Process Tomography,
e-print arXiv:2401.14993,
DOI:10.48550/arXiv.2401.14993.

Copyright (2022) is retained by the authors.

Liouvillian Exceptional Points of Non-Hermitian Systems via Quantum Process Tomography

Shilan Abo,^{1,*} Patrycja Tulewicz,¹ Karol Bartkiewicz,^{1,†} Şahin K. Özdemir,² and Adam Miranowicz^{1,‡}

¹*Institute of Spintronics and Quantum Information, Faculty of Physics,
Adam Mickiewicz University, 61-614 Poznań, Poland*

²*Department of Engineering Science and Mechanics, and Materials Research Institute,
Pennsylvania State University, Pennsylvania 16802, USA*

(Dated: January 29, 2024)

Hamiltonian exceptional points (HEPs) are spectral degeneracies of non-Hermitian Hamiltonians describing classical and semiclassical open systems with gain and/or loss. However, this definition overlooks the occurrence of quantum jumps in the evolution of open quantum systems. These quantum effects are properly accounted for by considering Liouvillians and their exceptional points (LEPs) [Minganti *et al.*, Phys. Rev. A **100**, 062131 (2019)]. Here, we explicitly describe how standard quantum process tomography, which reveals the dynamics of a quantum system, can be readily applied to reveal and characterize LEPs of non-Hermitian systems. We conducted experiments on an IBM quantum processor to implement a prototype model simulating the decay of a single qubit through three competing channels. Subsequently, we performed tomographic reconstruction of the corresponding experimental Liouvillians and their LEPs using both single- and two-qubit operations. This example underscores the efficacy of process tomography in tuning and observing LEPs, despite the absence of HEPs in the model.

Introduction.—Systems with dissipation and/or amplification can be described by non-Hermitian Hamiltonians (NHHs) whose eigenvalues are either real or complex conjugate pairs depending on whether the system is operated in the exact or broken parity-time (\mathcal{PT}) symmetric phase, respectively. This result, which was theoretically demonstrated by Bender and Boettcher [1] (see also Refs. [2, 3] for early reviews), has triggered impressive interest in studying non-Hermitian quantum mechanics [4, 5]. Indeed, over the past two decades, \mathcal{PT} -symmetric systems have evolved from a mathematical curiosity to a powerful resource for controlling electromagnetic waves and their interactions with matter by judiciously engineering loss-imbalance in passive (i.e., without amplification) non-Hermitian (NH) systems, and dissipation vs amplification rates in active NH systems, as well as dissipation vs the coupling strength between subsystems. Early demonstrations involved optical [6, 7], electronic [8], plasmonic [9], metamaterial [10], and optomechanical [11] systems.

The exact and broken \mathcal{PT} -symmetric phases are separated by the so-called Hamiltonian exceptional points (HEPs), where two or more of the eigenvalues of the effective non-Hermitian Hamiltonian (NHH) describing a given system, and their associated eigenvectors, become degenerate, leading to dimensionality reduction [12–14]. Numerous studies, focused on \mathcal{PT} -symmetry and/or HEPs, of engineered non-Hermitian systems have been reported in diverse fields, including: optics [6, 7, 14–20], electronics [8], plasmonics [9, 21, 22], acoustics [11, 23–27], cavity optomechanics [11, 28–31], atom optics [32],

circuit quantum electrodynamics (QED) [33–35], and cavity QED [36–38], for various systems, e.g.: photonic [15–18] and atomic [32] lattices, metamaterials [10, 39–42], exciton-polaritons [43], atomic vapours [44], and trapped ions [45].

A plethora of intriguing properties of such systems induced or enhanced at HEPs (or near them) have been predicted, including stimulated emission [46–51], spontaneous emission [52], chirality [53–55], unidirectional invisibility [56], control of whispering-gallery microcavities [57, 58], exceptional Kerr effect [59] and related exceptional photon blockade [60], or the generation of higher-order HEPs [31, 61–63]. The existence of HEPs in the absence of the \mathcal{PT} -symmetry was studied in [64]. Various applications of HEPs in photonics have been proposed aiming at enhanced quantum sensing, i.e., an increased response of non-Hermitian system to external perturbations in the vicinity of its HEPs [61, 65–75].

While effective NHHs and HEPs are sufficient to describe coherent nonunitary evolution of the dynamics of classical and semi-classical systems, they fell short in describing the evolution of quantum systems which involves quantum jumps and associated noise. To address this shortcoming, LEPs, which are the exceptional points of the Liouvillian superoperator describing the evolution of the density operator of the quantum system, were proposed [76]. LEPs are a natural generalization of HEPs by taking into account quantum jumps and, thus, they provide a consistent description of decoherence and noise in quantum systems in which the canonical commutation relations are satisfied.

Quantum Liouvillian exceptional points (LEPs) are defined as degeneracies of quantum Liouvillians associated with their coalescing eigenvalues and eigenvectors [76]. LEPs depend not only on a continuous nonunitary dissipation of a given system (as described by NHHs), but

* shsavan@gmail.com

† bark@amu.edu.pl

‡ adam.miranowicz@amu.edu.pl

also on its quantum jumps. By contrast to LEPs, HEPs are not affected by quantum jumps, so in that sense can be considered classical. The connection between HEPs and LEPs can be explicitly shown both theoretically and experimentally via a proper postselection of quantum trajectories following the hybrid-Liouvillian formalism of Ref. [77]. Recent experiments with a single superconducting qubit [34, 35] and a single trapped ion [78, 79] have indicated the importance of LEPs by revealing, for example, the pivotal significance of quantum jumps in generalizing the applications of classical non-Hermitian systems to open quantum systems for sensing and control [34] and “LEP-enabled control of quantum heat engines and of thermodynamic processes in open quantum systems” [79]. The discussed formalism of finding LEPs is based on the Lindblad master equation, so relies on the standard formalism of quantum mechanics eliminating the need to track the evolution of a system-dependent metric [80, 81]. Without calculating this metric, violations of no-go theorems in quantum mechanics can be wrongly predicted.

Since the introduction of the concept of LEPs in [76], there has been a growing theoretical interest, which is stimulated by experimental progress [33–35, 78, 79], in observing, understanding, and utilizing quantum aspects of Liouvillian singularities. The progress includes also closely related concepts of Liouvillian diabolical points (i.e., spectral degeneracies, where eigenvalues coalesce, but the associated eigenvectors remain orthogonal) [82], hybrid LEPs (which interpolate between HEPs and LEPs) [34, 77], and higher-order eigenspectrum degeneracies exhibiting hybrid properties of both diabolical and exceptional points [83] (see also [84]).

Quantum process tomography (QPT) is a procedure that enables a complete experimental characterization of an unknown quantum device (which can be considered a quantum black box) or, in mathematical terms, the reconstruction of the Liouvillian superoperator, which completely characterizes the dynamics of an unknown quantum process. QPT is often considered a quantum-channel tomography, because any physical operation that describes the dynamics of quantum states can be interpreted as a quantum channel. QPT was introduced in the late 1990s in [85–87] as a generalization of quantum state tomography (QST) [88] for reconstructing quantum channels via reconstructing quantum output states for various input states. Similarities between QPT and QST include even the use of maximum-likelihood estimation to guarantee that an experimentally reconstructed Liouvillian superoperator (or density matrix) really describes a physical process (or state) [89, 90]). First experimental demonstrations of QPT were reported for characterizing two-qubit gates using nuclear-magnetic-resonance (NMR) spectroscopy [91], and single- [92, 93] and two-qubit [94–96] gates using linear optics and conditional measurements. As already mentioned in [93], a multi-qubit (say n qubit) QPT can, in principle, be realized by replicating (n times) a given experimental setup for a

single-qubit QPT. Of course, the dimension of a reconstructed Liouvillian superoperator (and, thus, the complexity of QPT itself) grows exponentially with the number of qubits. QPT has now been established as an indispensable method for characterizing quantum processes, including quantum information processing (for a review see [97]). Recent experimental implementations of QPT include: trapped-ion qubit gates [98], superconducting quantum processors [99, 100], and photon polarization damping channels (see, e.g., [101] and references therein), or a plasmonic metamaterial as the polarization-dependent loss channel in quantum plasmonics [102], among many other experimental quantum platforms and processes. However, to our knowledge, finding LEPs of the Liouvillians reconstructed via QPT has not been demonstrated in detail yet.

Here we analyze and experimentally implement QPT and reveal LEPs on simple single- and two-qubit superconducting systems using an IBM quantum processor [103]. We argue that various experimental methods used for single-qubit QST [33] and QPT (e.g., [99, 104]) can be modified to induce and reveal LEPs along the lines described here. QPT can enable experimental finding not only LEPs but also quantum diabolical points, which are defined via degenerate eigenvalues of Liouvillians for which the corresponding eigenvectors are orthogonal. Such points can reveal dissipative phase transitions and Liouvillian spectral collapses [105, 106].

We note that QST has been applied across LEPs in [34, 35] (see also [33]). But to our knowledge QPT has not been applied to reveal LEPs yet. In particular, a LEP-based quantum heat engine was studied experimentally in [78, 79], but neither QST nor QPT was applied.

Our method can be readily applied for finding LEPs of multi-qubit processes via multi-qubit QPT, which corresponds to taking tensor products of single-qubit projectors. The method of finding LEPs can also be applied to QPT of infinite-dimensional systems (continuous variable) with [87] or without [107] homodyne detection. However, such an infinite-dimensional QPT is not discussed here.

Let us consider the dissipative evolution of a quantum system within the Lindblad master equation. Thus, we make the standard assumption that the system weakly interacts with a Markovian environment. In the case of the QPT of composite systems (e.g., a qubit and a cavity mode), it is usually also assumed that the interaction between the subsystems (e.g., light and matter) is weak. Therefore, each of the subsystems dissipates through its own coupling to the environment (i.e., via a separate dissipative channel) rather than combined channels, which would require applying generalized master equations [108–110]. Moreover, the expected photon output rate in the ultrastrongly coupled light-matter systems is not directly related to the number of photons in a cavity [111]. Thus, a generalized QPT should be applied.

A general-form Lindblad master equation can be expressed via the Liouvillian superoperator \mathcal{L} [112, 113]

($\hbar = 1$):

$$\frac{\partial}{\partial t}\hat{\rho} = \mathcal{L}\hat{\rho}(t) = -i[\hat{H}, \hat{\rho}(t)] + \sum_{\mu} \mathcal{D}[\hat{\Gamma}_{\mu}]\hat{\rho}(t), \quad (1)$$

acting on the density matrix $\hat{\rho}(t)$ of the system described by a Hermitian Hamiltonian \hat{H} at an evolution moment t . The Lindbladian dissipators $\mathcal{D}[\hat{\Gamma}_{\mu}]$ are given by

$$\mathcal{D}[\hat{\Gamma}_{\mu}]\hat{\rho}(t) = \hat{\Gamma}_{\mu}\hat{\rho}(t)\hat{\Gamma}_{\mu}^{\dagger} - \frac{1}{2}[\hat{\Gamma}_{\mu}^{\dagger}\hat{\Gamma}_{\mu}\hat{\rho}(t) + \hat{\rho}(t)\hat{\Gamma}_{\mu}^{\dagger}\hat{\Gamma}_{\mu}], \quad (2)$$

where $\hat{\Gamma}_{\mu}$ can be interpreted as a quantum jump operator within the quantum trajectory approach (also known as the wave-function Monte Carlo method) [114–118]. Following that approach, one can also introduce an effective NHH,

$$\hat{H}_{\text{eff}} = \hat{H} - \frac{i}{2} \sum_{\mu} \hat{\Gamma}_{\mu}^{\dagger} \hat{\Gamma}_{\mu}, \quad (3)$$

and, thus, the Liouvillian in Eq. (1) can be rewritten as

$$\mathcal{L}\hat{\rho}(t) = -i \left[\hat{H}_{\text{eff}}\hat{\rho}(t) - \hat{\rho}(t)\hat{H}_{\text{eff}}^{\dagger} \right] + \sum_{\mu} \hat{\Gamma}_{\mu}\hat{\rho}(t)\hat{\Gamma}_{\mu}^{\dagger}. \quad (4)$$

Thus, the master equation includes two types of terms and corresponding evolutions [113, 119]: the terms, which describe a continuous non-unitary dissipative evolution via \hat{H}_{eff} , and the quantum-jump term, which describes a sudden stochastic change of the wave-function due to the effect of the measurement on the state of the studied system [113, 120, 121]. It is seen that this quantum-trajectory interpretation of the master equation is physically very intuitive and reveals the importance of effective NHHs, which are used in standard quantum mechanics and not limited to \mathcal{PT} -symmetric systems. They describe continuous losses of energy, coherence, and quantum information of the system into the environment. Moreover, this master-equation interpretation also reveals the crucial role of quantum jumps. Their omission can be justified in the semiclassical limit or by applying a proper postselection of quantum trajectories.

The eigenspectra of the effective NHH, \hat{H}_{eff} , and the Liouvillian, \mathcal{L} , in Eq. (4) are determined, respectively, by

$$\hat{H}_{\text{eff}}|E_n\rangle = E_n|E_n\rangle, \quad (5)$$

$$\mathcal{L}\hat{\rho}_n = \lambda_n\hat{\rho}_n, \quad \mathcal{L}^{\dagger}\hat{\sigma}_n = \lambda_n^*\hat{\sigma}_n, \quad (6)$$

where E_n and $|E_n\rangle$ are the eigenvalues and eigenvectors of the NHH operator; while λ_n , $\hat{\rho}_n$, and $\hat{\sigma}_n$ are the eigenvalues and the right and left eigenmatrices of the Liouvillian superoperator, respectively. With these eigenspectra, HEPs and LEPs can be found. Note that $\hat{\rho}_n$ and $\hat{\sigma}_n$ for a given n are mutually orthonormal. However, different $\hat{\rho}_n$ (as well as $\hat{\sigma}_n$) are not, in general, orthogonal. The time evolution of a given density matrix $\hat{\rho}(t)$ can be expressed in the eigenmatrix basis $\{\hat{\rho}_n\}$ or $\{\hat{\sigma}_n\}$. The real part of λ_n for any n is non-positive and describes a

relaxation rate towards the system steady state [112]. By representing (i.e., flattening) the eigenmatrices $\hat{\rho}_n$ and $\hat{\sigma}_n$ as vectors $|\tilde{\rho}_n\rangle$ and $\langle\tilde{\sigma}_n|$, respectively, and treating the Liouvillian superoperator \mathcal{L} as a matrix $\tilde{\mathcal{L}}$, Eq. (6) can be rewritten as

$$\tilde{\mathcal{L}}|\tilde{\rho}_n\rangle = \lambda_n|\tilde{\rho}_n\rangle, \quad \langle\tilde{\sigma}_n|\tilde{\mathcal{L}} = \lambda_n\langle\tilde{\sigma}_n|, \quad (7)$$

where $\tilde{\mathcal{L}}$ can be measured (reconstructed) by a given QPT method. Then, the LEPs of $\tilde{\mathcal{L}}$ can be calculated by applying the standard superoperator formalism as described in Ref. [76]. Such LEPs can be easily found experimentally via the QPT based on 6×6 projectors, i.e., assuming that the input and output states (or projections) are the eigenstates of all the Pauli operators:

$$|\text{in}_i\rangle, |\text{out}_j\rangle \in \{|x_+\rangle, |x_-\rangle, |y_+\rangle, |y_-\rangle, |z_+\rangle, |z_-\rangle\}, \quad (8)$$

where $|x_{\pm}\rangle = \frac{1}{\sqrt{2}}(|0\rangle \pm |1\rangle)$, $|y_{\pm}\rangle = \frac{1}{\sqrt{2}}(|0\rangle \mp i|1\rangle)$, and $|z_+\rangle \equiv |0\rangle$ ($|z_-\rangle \equiv |1\rangle$). These projections can be used for the QPT of a transmon qubit, where $|0\rangle$ ($|1\rangle$) corresponds to its ground (excited) state. Thus, for a dissipative and/or amplified process described by the Lindblad master equation with a Liouvillian \mathcal{L} , one can measure all its elements

$$L_{ij} = \langle\text{out}_j|\mathcal{L}(\hat{\rho} = |\text{in}_i\rangle\langle\text{in}_i|)|\text{out}_j\rangle, \quad (9)$$

and, thus, one can reconstruct the full 6×6 transformation matrix $L = [L_{ij}]$, which represents \mathcal{L} . Other approaches to QPT, as described in the Supplement Material [122], can also be used to reveal the same LEPs.

The dynamics of an open quantum system is governed by the master equation in Eq. (1). For short evolution steps dt this can be expressed as

$$\hat{\rho}(t + dt) = (\mathcal{L}dt + 1)\hat{\rho}(t) \equiv S\hat{\rho}(t). \quad (10)$$

This corresponds to the short-time evolution of a quantum system $\hat{\rho}(t)$ under the non-Hermitian dynamics, where S is the effective quantum operation, which is the subject of quantum tomography. Note that S has the same spectral decomposition as \mathcal{L} up to an affine transformation for all eigenvalues related to scaling by dt and translation by 1. Thus, by performing QPT on S we can study LEPs. Next, we perform the QPT of a process S by choosing a dt which depends on the specific form of \mathcal{L} , and is small enough to realize the dynamics corresponding to the master equation in Eq. (1). If this quantum operation S is applied to a system n times, the evolution of the system is effectively described by the Lindblad master equation with a given Liouvillian \mathcal{L} for the evolution time ndt .

Driven lossy qubit.—In our experimental demonstration on an IBM quantum processor [103], we applied QPT to reveal LEPs in a driven lossy single-qubit (spin-1/2) prototype model, which exhibits LEPs but not HEPs [76, 77]. Specifically, the system is described by the Hamiltonian $\hat{H} = \frac{\omega}{2}\hat{\sigma}_z$, and decays through three

competing channels ($\hat{\sigma}_x$, $\hat{\sigma}_y$, and $\hat{\sigma}_-$), as described by the Liouvillian,

$$\mathcal{L}\hat{\rho}(t) = -i[\hat{H}, \hat{\rho}(t)] + \left(\gamma_- \mathcal{D}[\hat{\sigma}_-] + \gamma_x \mathcal{D}[\hat{\sigma}_x] + \gamma_y \mathcal{D}[\hat{\sigma}_y] \right) \hat{\rho}(t), \quad (11)$$

which includes the effects of three dissipation channels, where $\hat{\sigma}_{x,y,z}$ are the Pauli matrices, and $\hat{\sigma}_\pm = (\hat{\sigma}_x \mp i\hat{\sigma}_y)/2$ are the qubit lowering and raising operators, respectively. The Liouvillian, given by Eq. (11), is invariant under the exchange $\hat{\sigma}_- \rightarrow -\hat{\sigma}_-$, indicating a \mathbb{Z}_2 symmetry [123, 124]. The relaxation rate towards the steady state is influenced by the Hamiltonian oscillations, the dissipation channels along the x and y axes, and the spin flips described by $\hat{\sigma}_-$. We note that some typos in the corresponding equation in [76] have been corrected here to ensure that the numerical results can be accurately reproduced. In addition, the oscillations induced by the Hamiltonian, the dissipation occurring along the x and y axes and the spin flipping that the $\hat{\sigma}_-$ operator describes can compete for how quickly the system reaches a steady state.

The NHH structure is straightforward, as the effective Hamiltonian \hat{H}_{eff} is already in the diagonal form in the standard computational basis. Additionally, the matrix representation of \hat{H}_{eff} can be written as:

$$\hat{H}_{\text{eff}} = \frac{1}{2} \text{diag}([\omega - i\gamma_x - i\gamma_y - i\gamma_-, -\omega - i\gamma_x - i\gamma_y]), \quad (12)$$

which has no HEP as there is no way to adjust the parameters to make the two eigenvalues equal. However, despite this, the Liouvillian still exhibits LEPs. Specifically, one finds [76] the eigenvalues: $\lambda_0 = 0$, $\lambda_3 = \gamma_- - 2(\gamma_y + \gamma_x)$, and

$$\lambda_{1,2} = -\frac{\gamma_-}{2} - \gamma_x - \gamma_y \pm \Omega, \quad (13)$$

together with the corresponding right eigenmatrices:

$$\begin{cases} \hat{\rho}_0 \propto \frac{\text{diag}([\gamma_x + \gamma_y, \gamma_x + \gamma_y + \gamma_-])}{2\gamma_x + 2\gamma_y + \gamma_-}, \\ \hat{\rho}_{1,2} \propto \begin{pmatrix} 0 & -i\omega \pm \Omega \\ \gamma_x - \gamma_y & 0 \end{pmatrix}, \\ \hat{\rho}_3 \propto \text{diag}([-1, 1]), \end{cases} \quad (14)$$

where $\Omega = \sqrt{\gamma_x^2 + \gamma_y^2 - 2\gamma_x\gamma_y - \omega^2}$. For brevity, the left eigenmatrices $\hat{\sigma}_n$ are not shown here. Therefore, in the case $\gamma_y > \omega$, this Liouvillian exhibits two LEPs at $\gamma_x^\pm \equiv \gamma_y \pm \omega$. We study this configuration experimentally by setting $\gamma_- = 0$ and $\gamma_y = 2\omega$. Figure 1 shows the theoretical eigenvalues $\lambda_{1,2}$, given by Eq. (13) (see blue dashed curves), and modified eigenvalues (black solid curves), which are obtained via a more-realistic QPT simulation assuming white noise. Specifically, any experimental pure-like states, which are the input states for QPT, are effectively mixed with white noise. Thus, this undesired effect has been included in our refined simulations, as

discussed in [122]. These simulated eigenvalues are compared with the experimental eigenvalues λ_n^{exp} obtained in our single-qubit [in panels (a,b)] and two-qubit [in panels (c,d)] experiments. The observed bifurcations of the experimental eigenvalues near $\gamma_x^\pm = (2 \pm 1)\omega$ are in a good agreement with our theoretical predictions. In Fig. , we show the scalar products (overlaps) $O_{12}^{\text{exp}} = |\langle \tilde{\sigma}_1^{\text{exp}} | \tilde{\rho}_2^{\text{exp}} \rangle|$ between the experimental right and left eigenmatrices, $\tilde{\sigma}_1^{\text{exp}}$ and $\tilde{\rho}_2^{\text{exp}}$, compared to $O_{12}^{\text{th}} = |\langle \tilde{\sigma}_1^{(0)} | \tilde{\rho}_2^{(0)} \rangle|$ for the ideal theoretical case. It is seen that $\tilde{\sigma}_1^{\text{exp}}$ and $\tilde{\rho}_2^{\text{exp}}$ are practically coalescent (as $O_{12}^{\text{exp}} \approx 1$) near γ_x^\pm confirming the generation of LEPs.

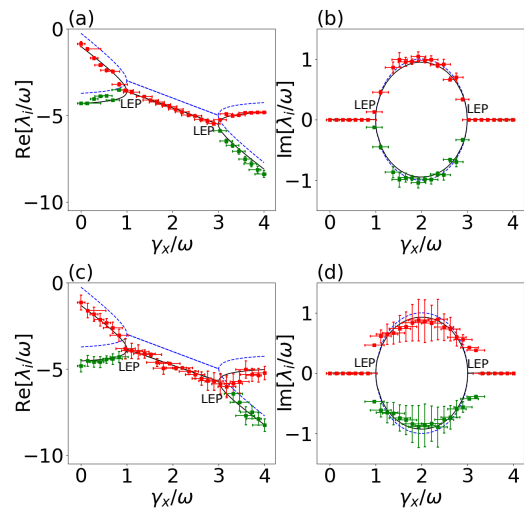


FIG. 1. Spectra of the experimental Liouvillians L (and, thus, \mathcal{L}) reconstructed from single-qubit (a,b) and two-qubit (c,d) measurements performed on an IBM quantum processor [103] (red and green squares) and the corresponding theoretical predictions including white noise (black solid curves) and without it [blue dashed curves obtained from Eq. (13)]. Panels (a,c) show the real part of the eigenvalues λ_i of the Liouvillians L , while (b,d) show their imaginary part. Each measurement was carried out with 20 000 shots and $\omega dt = 1/15$.

Implementing completely positive (CP) maps with unitary gates.—To implement non-Hermitian dynamics using only unitary operations, we purify (coherify) the quantum process by embedding it in a larger Hilbert space, where the joint evolution of the system and its environment is unitary. In particular, starting with the superoperator S , we find its Choi representation $\hat{\chi}$. Depending on the number of nonzero eigenvalues of the Choi matrix, we choose the dimension of the required ancillary system. This approach to implement completely positive maps is well known (see, e.g., Ref. [125]). As we can implement an arbitrary unitary operation on a programmable quantum computer, we use this approach to demonstrate LEPs experimentally with a noisy intermediate-scale quantum (NISQ) processor.

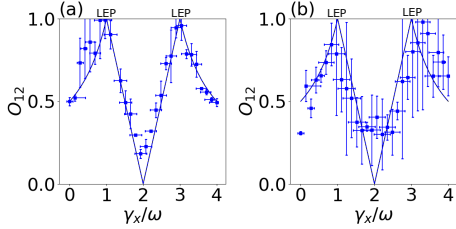


FIG. 2. Overlaps $O_{12} = |\langle \tilde{\sigma}_1 | \tilde{\rho}_2 \rangle|$ of the Liouvillian vectorized eigenmatrices $\langle \tilde{\sigma}_1 |$ and $|\tilde{\rho}_2 \rangle$ measured in our single- (a) and two- (b) qubit experiments on an IBM quantum processor [103] (blue squares) and compared to the corresponding theoretical predictions including white noise (black curves). It is seen that the experimental overlap O_{12} approaches 1 at the LEPs in both panels.

CP maps, are linear maps that preserve the positivity of density matrices. To express a CP map $\mathcal{E}_{\mathcal{H}}$ between the Hilbert spaces \mathcal{H} and \mathcal{K} as a unitary operator we can use the Choi-Jamiolkowski isomorphism [126, 127] between the map and operator $\hat{\chi}$. The associated quantum operation can be expressed as

$$\hat{\rho}_{\text{out}} = \text{tr}_{\mathcal{H}} [\hat{\chi} \hat{\rho}_{\text{in}}^{\text{T}} \otimes \hat{\mathbb{1}}_{\mathcal{K}}], \quad (15)$$

where the operator isomorphic to the map reads $\hat{\chi} = \mathcal{E}_{\mathcal{H}} \otimes \mathcal{I}_{\mathcal{H}}(|\phi\rangle\langle\phi|)$, $\text{tr}_{\mathcal{K}}[\hat{\chi}] = \hat{\mathbb{1}}_{\mathcal{H}}$, and $|\phi\rangle = \sum_{j=1}^{\dim \mathcal{H}} |j\rangle_1 |j\rangle_2$ where, \mathcal{I} is an identity map and $\hat{\mathbb{1}}_{\mathcal{H}}$ denotes the identity operator on \mathcal{H} . Alternatively, a given CP map can be expressed via the Kraus decomposition [125]:

$$\hat{\rho}_{\text{out}} = \mathcal{E}(\hat{\rho}_{\text{in}}) = \sum_l \hat{A}_l \hat{\rho}_{\text{in}} \hat{A}_l^{\dagger}. \quad (16)$$

with $\sum_l \hat{A}_l^{\dagger} \hat{A}_l = \hat{\mathbb{1}}_{\mathcal{H}}$, which can be rewritten, using the elements of the matrix $A_{ki}^{(l)} \equiv \langle k | \hat{A}_l | i \rangle$, as $\sum_{k,l} A_{ki}^{*(l)} A_{kj}^{(l)} = \delta_{ij}$. The number of \hat{A}_l operators corresponds to the number of the nonzero eigenvalues of the $\hat{\chi}$ matrix. In the real case, the $\hat{\chi}$ matrix and the operators \hat{A}_l can be related to each other by the eigenvalues r_l and the eigenstates $|\pi_l\rangle$ of the $\hat{\chi}$ operator,

$$A_{ki}^{(l)} = \sqrt{r_l} \langle k | \langle i | \pi_l \rangle, \quad (17)$$

where $|i\rangle \in \mathcal{H}$ and $|k\rangle \in \mathcal{K}$ are the states in the input and output Hilbert spaces, respectively. Finally,

$$\hat{\rho}_{\text{out}} = \text{tr}_{\text{env}} [\hat{U} \hat{\rho}_{\text{in}} \otimes (|0\rangle\langle 0|)_{\text{env}} \hat{U}^{\dagger}], \quad (18)$$

where $\hat{U} = \sum_l \hat{A}_l \otimes (|l\rangle\langle 0|)_{\text{env}}$ is the unitary operation decomposable into quantum gates.

Implementation complexity.—For the discussed driven lossy qubit model, $l = 0, \dots, 4$ which is the number of the nonzero eigenvalues of the Choi matrix. The simplest single-qubit circuit implementing the CP map applies a unitary operation corresponding to $A^{(l)}$ at random with

probability r_l , as described by Eq. (16). When applied repeatedly to the initial quantum state, the resulting final state approximates the time-evolved quantum state of the simulated system. However, this is not a fully quantum simulation of the quantum dynamics, i.e., we need an external random number generator.

The second simplest experiment is embedded in a two-qubit Hilbert space and utilizes two-qubit unitary operations and a single-qubit environment, $\hat{\rho}_{\text{env}}^{(1)}$, and reads as

$$\hat{\rho}_{\text{out}} \otimes \hat{\rho}_{\text{env}}^{(1)} = \sum_{m=0,2} \hat{A}_m (\hat{\rho}_{\text{in}} \otimes |0\rangle\langle 0|) \hat{A}_m^{\dagger}, \quad (19)$$

where $\hat{A}_m = \sum_{l=0,1} \hat{A}_{l+m} \otimes |l\rangle\langle 0|$, which requires using two random two-qubit operations (labelled as $m = 0, 2$). Finally, a completely coherent quantum three-qubit experiment requires applying a single unitary operation and a two-qubit environment, as described by Eq. (18).

Handling experimental errors.—When working with a programmable quantum computer, we are mostly limited to applying noisy unitary operations and imperfect read-out. There are many approaches towards implementing qubits on quantum computers. Here we focus on transmon qubits, which are nowadays commonly used in superconducting quantum processors. These processors are able to implement sets of elementary instructions containing both single- and two-qubit unitary operations. Not every two qubits in a quantum chip are coupled directly. This requires transpiling a given unitary operation into elementary gates according to a coupling map of a given quantum processor. While the fidelities of two-qubit and single-qubit operations are typically high, the gate errors can accumulate to an unacceptable level. Additionally, if the time required to execute all the gates is comparable to the coherence time T_2 of the applied transmons, then the results are largely affected by decoherence. These all limitations should be taken into account when designing an experiment. It is evident that the experimentally reconstructed dynamics is usually perturbed with respect to the expected one. The effective perturbations in the eigenvalues ($\delta\lambda$) and eigenmatrices ($|\delta\tilde{\rho}_n\rangle$ and $\langle\delta\tilde{\sigma}_n|$) of an experimental Liouvillian $L^{\text{exp}} = L_0 + \delta L$, with the eigenspectrum obtained experimentally, compared to the ideal unperturbed Liouvillian L_0 and its eigenspectrum [denoted with superscript (0)], can be estimated as [122, 128]:

$$\delta\lambda_n \approx \langle\tilde{\sigma}_n^{(0)}|\delta L|\tilde{\rho}_n^{(0)}\rangle, \quad (20)$$

$$|\delta\tilde{\rho}_n\rangle \approx - \sum_{i(i \neq n)} \left(\frac{\langle\tilde{\sigma}_i^{(0)}|\delta L|\tilde{\rho}_n^{(0)}\rangle}{\lambda_i^{(0)} - \lambda_n^{(0)}} \right) |\tilde{\rho}_i^{(0)}\rangle, \quad (21)$$

$$\langle\delta\tilde{\sigma}_n| \approx - \sum_{i(i \neq n)} \left(\frac{\langle\tilde{\sigma}_n^{(0)}|\delta L|\tilde{\rho}_i^{(0)}\rangle}{\lambda_i^{(0)} - \lambda_n^{(0)}} \right) \langle\tilde{\sigma}_i^{(0)}|. \quad (22)$$

Thus, based on these estimations, we can select the most noise-robust experimental strategy. The error bars $\delta\lambda_n$

for the experimental eigenvalues λ_n^{exp} shown in Fig. 1 are calculated by Eq. (20). While the error bars $\delta O_{12}^{\text{exp}}$ for the experimental scalar products O_{12}^{exp} in Fig. are calculated in [122] based on Eqs. (21) and (22). Moreover, the uncertainties of γ_x , as plotted in Figs. 1 and , are estimated in [122].

Experiment.—In our experiments the system $\hat{\rho}_{\text{in}} \equiv \hat{\rho}(t)$ was prepared in one of six input states. Then, the evolution under a given map was applied. Finally, we measure $\hat{\rho}_{\text{out}} \equiv \hat{\rho}(t + dt)$ in the x , y , and z bases to reconstruct L (and, consequently, \mathcal{L}). The results of the experiment, conducted on an IBM quantum processor (i.e., Nairobi) [103] are shown in Figs. 1 and . Measurements were performed for 30 points with 20,000 shots per experiment, and the evolution step was chosen such that $\omega dt = 1/15$. Quantum processors are error-sensitive due to their susceptibility to noise and decoherence. In order to mitigate errors in our system, we used one of the popular correction methods, i.e., dynamic decoupling. The method involves applying a sequence of pulses to each qubit to protect it from ambient noise. The idea behind the method is to repeatedly apply a series of inversion or refocussing pulses that reverse the effect of ambient noise on a qubit. These pulses effectively separate the qubit from its environment and can increase the qubit coherence time. This method is conceptually similar to the spin-echo method.

Our experiments for demonstrating NHH dynamics are challenging even for simple systems due to highly entangling three-qubit operations $\hat{U}^{(3)} = \sum_l \hat{A}_l \otimes |l\rangle\langle 0|$ implemented by quantum circuits. The results of our three-qubit experiments on IBM quantum processors [103] are quite noisy and not shown here. Although our main experimental results, presented in Figs. 1 and , are limited to single- and two-qubit experiments, they show the potential of QPT for revealing and manipulating LEPs.

Conclusions.—We have demonstrated how to engineer

and tune a quantum process to approach and detect LEPs via QPT. The operations for all the experiments are automatically transpiled into a sequence of single- and two-qubit gates, which were physically implemented on a given quantum processor. The physical qubits are selected based on their quality and connectivity, which contribute to the optimal performance of the quantum circuit. To suppress the noise even more, we have explored the state-of-the-art noise-canceling techniques for quantum processors. While we applied experimentally various methods, we found the dynamical decoupling technique to be most useful. Various equivalent QPT methods can be used for revealing LEPs as discussed in the Supplementary Material [122]. However, we observed the least perturbed Liouvillians when applying the QPT method described in the main text. We expect that working with LEPs could lead to developing more robust readout techniques. This could be useful, e.g., in limiting the readout errors in quantum computers. We believe that QPT can become an indispensable tool for precise monitoring and controlling LEP-based quantum devices, including quantum heat engines [78, 79].

Acknowledgements.—The authors thank Anna Kowalska-Kudłaszuk, Grzegorz Chimczak, and Jan Peřina for insightful and useful discussions. We acknowledge the use of IBM Quantum services for this work. The views expressed are those of the authors, and do not reflect the official policy or position of IBM or the IBM Quantum team. This work was supported by the Polish National Science Centre (NCN) under the Maestro Grant No. DEC-2019/34/A/ST2/00081. S.K.O. acknowledges support from Air Force Office of Scientific Research (AFOSR) Multidisciplinary University Research Initiative (MURI) Award on Programmable systems with non-Hermitian quantum dynamics (Award No. FA9550-21-1-0202).

-
- [1] C. M. Bender and S. Boettcher, Real Spectra in Non-Hermitian Hamiltonians having \mathcal{PT} Symmetry, *Phys. Rev. Lett.* **80**, 5243 (1998).
 - [2] C.M. Bender, D. C. Brody, and H. F. Jones, Must a Hamiltonian be Hermitian?, *Am. J. Phys.* **71**, 1095 (2003).
 - [3] C. M. Bender, Making sense of non-Hermitian Hamiltonians, *Rep. Prog. Phys.* **70**, 947 (2007).
 - [4] N. Moiseyev, *Non-Hermitian Quantum Mechanics*, (Cambridge University Press, 2011).
 - [5] R. El-Ganainy, K. G. Makris, M. Khajavikhan, Z. H. Musslimani, S. Rotter, and D. N. Christodoulides, Non-Hermitian physics and \mathcal{PT} symmetry, *Nat. Phys.* **14**, 11 (2018).
 - [6] A. Guo, G. J. Salamo, D. Duchesne, R. Morandotti, M. Volatier-Ravat, V. Aimez, G. A. Siviloglou, and D. N. Christodoulides, Observation of \mathcal{PT} -symmetry breaking in complex optical potentials, *Phys. Rev. Lett.* **103**, 093902 (2009).
 - [7] C. Rüter, K. Makris, R. El-Ganainy, D. N. Christodoulides, M. Segev, and D. Kip, Observation of parity-time symmetry in optics, *Nat. Phys.* **6**, 192 (2010).
 - [8] J. Schindler, A. Li, M.C. Zheng, F. M. Ellis, and T. Kottos, Experimental study of active LRC circuits with \mathcal{PT} symmetries, *Phys. Rev. A* **84**, 040101(R) (2011).
 - [9] H. Benisty *et al.*, Implementation of \mathcal{PT} symmetric devices using plasmonics: Principle and applications, *Opt. Express* **19**, 18004 (2011).
 - [10] M. Kang, F. Liu, and J. Li, Effective spontaneous \mathcal{PT} -symmetry breaking in hybridized metamaterials, *Phys. Rev. A* **87**, 053824 (2013).
 - [11] H. Jing, Ş. K. Özdemir, X.-Y. Lu, J. Zhang, L. Yang, and F. Nori, \mathcal{PT} -symmetric phonon laser, *Phys. Rev. Lett.* **13**, 053604 (2014).
 - [12] Ş. K. Özdemir, S. Rotter, F. Nori, and L. Yang, Parity-time symmetry and exceptional points in photonics, *Nat. Mater.* **18**, 783 (2019).
 - [13] M. Miri and A. Alù, Exceptional points in optics and photonics, *Science* **363**, eaar7709 (2019).

- [14] M. Parto, Y. G. N. Liu, B. Bahari, M. Khajavikhan, and D. N. Christodoulides, Non-Hermitian and topological photonics: Optics at an exceptional point, *Nanophotonics* **10**, 403 (2021).
- [15] A. Regensburger, C. Bersch, M.-A. Miri, G. Onishchukov, D. N. Christodoulides, and U. Peschel, Parity-time synthetic photonic lattices, *Nature (London)* **488**, 167 (2012).
- [16] B. Zhen *et al.*, Spawning rings of exceptional points out of Dirac cones, *Nature (London)* **525**, 354 (2015).
- [17] K. Ding, Z. Q. Zhang, and C. T. Chan, Coalescence of exceptional points and phase diagrams for one-dimensional \mathcal{PT} -symmetric photonic crystals, *Phys. Rev. B* **92**, 235310 (2015).
- [18] A. Cerjan, A. Raman, and S. Fan, Exceptional contours and band structure design in parity-time symmetric photonic crystals, *Phys. Rev. Lett.* **116**, 203902 (2016).
- [19] L. Feng, R. El-Ganainy, and L. Ge, Non-Hermitian photonics based on parity-time symmetry, *Nat. Photon.* **11**, 752 (2017).
- [20] R. El-Ganainy, M. Khajavikhan, D. N. Christodoulides, and Ş. K. Özdemir, The dawn of non-Hermitian optics, *Commun. Phys.* **2**, 1 (2019).
- [21] H. Alaeian and J. A. Dionne, Parity-time-symmetric plasmonic metamaterials, *Phys. Rev. A* **89**, 033829 (2014).
- [22] P.-C. Kuo, N. Lambert, A. Miranowicz, G.-Y. Chen, Y.-N. Chen, and F. Nori, Collectively induced exceptional points of quantum emitters coupled to nanoparticle surface plasmons, *Phys. Rev. A* **101**, 013814 (2020).
- [23] X. Zhu, H. Ramezani, C. Shi, J. Zhu, and X. Zhang, \mathcal{PT} -symmetric acoustics, *Phys. Rev. X* **4**, 031042 (2014).
- [24] R. Fleury, D. L. Sounas, and A. Alu, An invisible acoustic sensor based on parity-time symmetry, *Nat. Commun.* **6**, 5905 (2015).
- [25] K. Ding, G. Ma, M. Xiao, Z. Q. Zhang, and C. T. Chan, Emergence, coalescence, and topological properties of multiple exceptional points and their experimental realization, *Phys. Rev. X* **6**, 021007 (2016).
- [26] H. Lü, Ş. K. Özdemir, L. M. Kuang, F. Nori, and H. Jing, Exceptional Points in Random-Defect Phonon Lasers, *Phys. Rev. Appl.* **8**, 044020 (2017).
- [27] J. Zhang *et al.*, A phonon laser operating at an exceptional point, *Nat. Photon.* **12**, 479 (2018).
- [28] H. Jing *et al.*, Optomechanically-induced transparency in parity-timesymmetric microresonators, *Sci. Rep.* **5**, 9663 (2015).
- [29] D. W. Schönleber, A. Eisfeld, and R. El-Ganainy, Optomechanical interactions in non-Hermitian photonic molecules, *New J. Phys.* **18**, 045014 (2016).
- [30] H. Xu, D. Mason, L. Jiang, and J. G. E. Harris, Topological energy transfer in an optomechanical system with exceptional points, *Nature (London)* **537**, 80 (2016).
- [31] H. Jing, Ş. K. Özdemir, H. Lü, and F. Nori, High-order exceptional points in optomechanics, *Sci. Rep.* **7**, 3386 (2017).
- [32] Z. Zhang *et al.*, Observation of Parity-Time Symmetry in Optically Induced Atomic Lattices, *Phys. Rev. Lett.* **117**, 123601 (2016).
- [33] M. Naghiloo, M. Abbasi, Y. N. Joglekar, and K. W. Murch, Quantum state tomography across the exceptional point in a single dissipative qubit, *Nat. Phys.* **15**, 1232 (2019).
- [34] W. Chen, M. Abbasi, Y. N. Joglekar, and K. W. Murch, Quantum Jumps in the Non-Hermitian Dynamics of a Superconducting Qubit *Phys. Rev. Lett.* **127**, 140504 (2021).
- [35] W. Chen, M. Abbasi, B. Ha, S. Erdamar, Y. N. Joglekar, K. W. Murch, Decoherence Induced Exceptional Points in a Dissipative Superconducting Qubit, *Phys. Rev. Lett.* **128**, 110402 (2022).
- [36] A. Roy, S. Jahani, Q. Guo, A. Dutt, S. Fan, M.-A. Miri, and A. Marandi, Nondissipative non-Hermitian dynamics and exceptional points in coupled optical parametric oscillators, *Optica* **8**, 415 (2021).
- [37] A. Roy, S. Jahani, C. Langrock, M. Fejer, and A. Marandi, Spectral phase transitions in optical parametric oscillators, *Nat. Commun.* **12**, 835 (2021).
- [38] S. Jahani, A. Roy, and A. Marandi, Wavelength-scale optical parametric oscillators, *Optica* **8**, 262 (2021).
- [39] R. Fleury, D. L. Sounas, and A. Alu, Negative refraction and planar focusing based on parity-time symmetric metasurfaces, *Phys. Rev. Lett.* **113**, 023903 (2014).
- [40] Y. Sun, W. Tan, H.-q. Li, J. Li, and H. Chen, Experimental demonstration of a coherent perfect absorber with \mathcal{PT} phase transition, *Phys. Rev. Lett.* **112**, 143903 (2014).
- [41] M. Kang, J. Chen, and Y. D. Chong, Chiral exceptional points in metasurfaces, *Phys. Rev. A* **94**, 033834 (2016).
- [42] S. Xiao, J. Gear, S. Rotter, and J. Li, Effective \mathcal{PT} -symmetric metasurfaces for subwavelength amplified sensing, *New J. Phys.* **18**, 085004 (2016).
- [43] T. Gao *et al.*, Observation of non-Hermitian degeneracies in a chaotic exciton-polariton billiard, *Nature (London)* **526**, 554 (2015).
- [44] P. Peng *et al.*, Anti-parity-time symmetry with flying atoms, *Nat. Phys.* **12**, 1139 (2016).
- [45] L. Ding, K. Shi, Q. Zhang, D. Shen, X. Zhang, and W. Zhang, Experimental Determination of \mathcal{PT} -Symmetric Exceptional Points in a Single Trapped Ion, *Phys. Rev. Lett.* **126**, 083604 (2021).
- [46] L. Feng, Z. J. Wong, R.-M. Ma, Y. Wang, and X. Zhang, Single-mode laser by parity-time symmetry breaking, *Science* **346**, 972 (2014).
- [47] H. Hodaei, M.-A. Miri, M. Heinrich, D. N. Christodoulides, and M. Khajavikhan, Parity-time-symmetric microring lasers, *Science* **346**, 975 (2014).
- [48] B. Peng, Ş. K. Özdemir, S. Rotter, H. Yilmaz, M. Liertzer, F. Monifi, C. M. Bender, F. Nori, and L. Yang, Loss-induced suppression and revival of lasing, *Science* **346**, 328 (2014).
- [49] M. Brandstetter, M. Liertzer, C. Deutsch, P. Klang, J. Schoberl, H. E. Tureci, G. Strasser, K. Unterrainer, and S. Rotter, Reversing the pump dependence of a laser at an exceptional point, *Nat. Commun.* **5**, 4034 (2014).
- [50] I. I. Arkhipov, A. Miranowicz, O. Di Stefano, R. Stassi, S. Savasta, F. Nori, and Ş. K. Özdemir, Scully-Lamb quantum laser model for parity-time-symmetric whispering-gallery microcavities: Gain saturation effects and non-reciprocity, *Phys. Rev. A* **99**, 053806 (2019).
- [51] I. I. Arkhipov, A. Miranowicz, F. Minganti, and F. Nori, Quantum and semiclassical exceptional points of a linear system of coupled cavities with losses and gain within the Scully-Lamb laser theory, *Phys. Rev. A* **101**, 013812 (2020).
- [52] A. Pick, B. Zhen, O. D. Miller, C. W. Hsu, F. Hernandez, A. W. Rodriguez, M. Soljacic, and S. G. Johnson, General theory of spontaneous emission near exceptional points, *Opt. Express* **25**, 12325 (2017).
- [53] W. D. Heiss and H. L. Harney, The chirality of exceptional points, *Eur. Phys. J. D* **17**, 149 (2001).

- [54] C. Dembowski, B. Dietz, H.-D. Gräf, H. L. Harney, A. Heine, W. D. Heiss, and A. Richter, Observation of a Chiral State in a Microwave Cavity, *Phys. Rev. Lett.* **90**, 034101 (2003).
- [55] W. R. Sweeney, C.W. Hsu, S. Rotter, and A. D. Stone, Perfectly Absorbing Exceptional Points and Chiral Absorbers, *Phys. Rev. Lett.* **122**, 093901 (2019).
- [56] Z. Lin, H. Ramezani, T. Eichelkraut, T. Kottos, H. Cao, and D. N. Christodoulides, Unidirectional Invisibility Induced by \mathcal{PT} -Symmetric Periodic Structures, *Phys. Rev. Lett.* **106**, 213901 (2011).
- [57] L. Chang, X. Jiang, S. Hua, C. Yang, J. Wen, L. Jiang, G. Li, G. Wang, and M. Xiao, Parity-time symmetry and variable optical isolation in active-passive-coupled microresonators, *Nat. Photon.* **8**, 524 (2014).
- [58] B. Peng, Ş. K. Özdemir, F. Lei, F. Monifi, M. Gianfreda, G. L. Long, S. Fan, F. Nori, C. Bender, and L. Yang, Parity-time-symmetric whispering-gallery microcavities, *Nat. Phys.* **10**, 394 (2014).
- [59] J. Peřina Jr., A. Luks, J. K. Kalaga, W. Leoński, and A. Miranowicz, Nonclassical light at exceptional points of a quantum \mathcal{PT} -symmetric two-mode system, *Phys. Rev. A* **100**, 053820 (2019).
- [60] R. Huang, Ş. K. Özdemir, J. Q. Liao, F. Minganti, L.-M. Kuang, F. Nori, and H. Jing, Exceptional Photon Blockade: Engineering Photon Blockade with Chiral Exceptional Points, *Laser Photon. Rev.* **16**, 2100430 (2022).
- [61] H. Hodaie, U. H. Absar, S. Wittek, H. Garcia-Gracia, R. El-Ganainy, D. N. Christodoulides, and M. Khajavikhan, Enhanced sensitivity at higher-order exceptional points, *Nature (London)* **548**, 187 (2017).
- [62] I. I. Arkhipov, A. Miranowicz, F. Minganti, and F. Nori, Liouvillian exceptional points of any order in dissipative linear bosonic systems: Coherence functions and switching between \mathcal{PT} and anti- \mathcal{PT} symmetries, *Phys. Rev. A* **102**, 033715 (2020).
- [63] I. I. Arkhipov, F. Minganti, A. Miranowicz, and F. Nori, Generating high-order quantum exceptional points, *Phys. Rev. A* **104**, 012205 (2021).
- [64] E. Lange, A. Kowalewska-Kudłaszyk, G. Chimczak, K. Bartkiewicz, Rotation-time symmetry in bosonic systems and the existence of exceptional points in the absence of \mathcal{PT} -symmetry, *Sc. Rep.* **10**, 19906 (2020).
- [65] J. Wiersig, Enhancing the Sensitivity of Frequency and Energy Splitting Detection by Using Exceptional Points, *Phys. Rev. Lett.* **112**, 203901 (2014).
- [66] N. Zhang, S. Liu, K. Wang, Z. Gu, M. Li, N. Yi, S. Xiao, and Q. Song, Single nanoparticle detection using far-field emission of photonic molecule around the exceptional point, *Sci. Rep.* **5**, 11912 (2015).
- [67] Z.-P. Liu, J. Zhang, Ş. K. Özdemir, B. Peng, H. Jing, X.-Y. Lü, C.-W. Li, L. Yang, F. Nori, and Y.-X. Liu, Metrology with \mathcal{PT} -Symmetric Cavities: Enhanced Sensitivity Near the \mathcal{PT} -Phase Transition, *Phys. Rev. Lett.* **117**, 110802 (2016).
- [68] J. Wiersig, Sensors operating at exceptional points: General theory, *Phys. Rev. A* **93**, 033809 (2016).
- [69] J. Ren, H. Hodaie, G. Harari, A. U. Hassan, W. Chow, M. Soltani, D. Christodoulides, and M. Khajavikhan, Ultra-sensitive micro-scale parity-time-symmetric ring laser gyroscope, *Opt. Lett.* **42**, 1556 (2017).
- [70] W. Chen, Ş. K. Özdemir, G. Zhao, J. Wiersig, and L. Yang, Exceptional points enhance sensing in an optical microcavity, *Nature (London)* **548**, 192 (2017).
- [71] P.-Y. Chen, M. Sakhdari, M. Hajizadegan, Q. Cui, M. M.-C. Cheng, R. El-Ganainy, and A. Alù, Generalized parity-time symmetry condition for enhanced sensor telemetry, *Nat. Electron.* **1**, 297 (2018).
- [72] N. A. Mortensen, P. A. D. Gonçalves, M. Khajavikhan, D. N. Christodoulides, C. Tserkezis, and C. Wolff, Fluctuations and noise-limited sensing near the exceptional point of parity-time-symmetric resonator systems, *Optica* **5**, 1342 (2018).
- [73] M. Zhang, W. Sweeney, C. W. Hsu, L. Yang, A. D. Stone, and L. Jiang, Quantum Noise Theory of Exceptional Point Amplifying Sensors, *Phys. Rev. Lett.* **123**, 180501 (2019).
- [74] S. Yu *et al.*, Experimental Investigation of Quantum \mathcal{PT} -Enhanced Sensor, *Phys. Rev. Lett.* **125**, 240506 (2020).
- [75] J. Wiersig, Robustness of exceptional point-based sensors against parametric noise: The role of Hamiltonian and Liouvillian degeneracies, *Phys. Rev. A* **101**, 053846 (2020).
- [76] F. Minganti, A. Miranowicz, R. Chhajlany, and F. Nori, Quantum exceptional points of non-Hermitian Hamiltonians and Liouvillians: The effects of quantum jumps, *Phys. Rev. A* **100**, 062131 (2019).
- [77] F. Minganti, A. Miranowicz, R. W. Chhajlany, I. I. Arkhipov, and F. Nori, Hybrid-Liouvillian formalism connecting exceptional points of non-Hermitian Hamiltonians and Liouvillians via postselection of quantum trajectories, *Phys. Rev. A* **101**, 062112 (2020).
- [78] J.-W. Zhang *et al.*, Dynamical control of quantum heat engines using exceptional points, *Nat. Commun.* **13**, 6225 (2022).
- [79] J.-T. Bu *et al.*, Enhancement of Quantum Heat Engine by Encircling a Liouvillian Exceptional Point, *Phys. Rev. Lett.* **130**, 110402 (2023).
- [80] C.-Y. Ju, A. Miranowicz, G.-Y. Chen, F. Nori, Non-Hermitian Hamiltonians and no-go theorems in quantum information, *Phys. Rev. A* **100**, 062118 (2019).
- [81] Ch.-Y. Ju, A. Miranowicz, F. Minganti, C.-Ts. Chan, G.-Y. Chen, and F. Nori, Flattening the Curve with Einstein's Quantum Elevator: Hermitization of Non-Hermitian Hamiltonians via the Vielbein Formalism, *Phys. Rev. Research* **4**, 023070 (2022).
- [82] F. Minganti, I. I. Arkhipov, A. Miranowicz, and F. Nori, Continuous dissipative phase transitions with or without symmetry breaking, *New J. Phys.* **23**, 122001 (2021); F. Minganti, I. I. Arkhipov, A. Miranowicz, and F. Nori, Liouvillian spectral collapse in the Scully-Lamb laser model, *Phys. Rev. Res.* **3**, 043197 (2021).
- [83] J. Peřina, Jr., A. Miranowicz, G. Chimczak, and A. Kowalewska-Kudłaszyk, Quantum Liouvillian exceptional and diabolical points for bosonic fields with quadratic Hamiltonians: The Heisenberg-Langevin equation approach, *Quantum* **6**, 883 (2022).
- [84] I. I. Arkhipov, A. Miranowicz, F. Minganti, S. K. Özdemir, and F. Nori, Dynamically encircling an exceptional curve by crossing diabolical points: A programmable multimode switch, *Nat. Comm.* **14**, 2076 (2023).
- [85] I.L. Chuang and M.A. Nielsen, Prescription for experimental determination of the dynamics of a quantum black box, *J. Mod. Opt.* **44**, 2455 (1997).
- [86] J. Poyatos, J. Cirac, and P. Zoller, Complete characterization of a quantum process: The two-bit quantum gate, *Phys. Rev. Lett.* **78**, 390 (1997).
- [87] G. M. D'Ariano and L. Maccone, Measuring Quantum Optical Hamiltonians, *Phys. Rev. Lett.* **80**, 5465 (1998).

- [88] G. M. D'Ariano, M. G. A. Paris, and M. F. Sacchi, Quantum Tomography, *Adv. Imaging Electron Phys.* **128**, 205 (2003).
- [89] *Quantum State Estimation*, edited by M.G.A. Paris and J. Řeháček (Springer, Berlin, 2004), Vol. 649.
- [90] J. Fiurašek and Z. Hradil, Maximum-likelihood estimation of quantum processes, *Phys. Rev. A* **63**, 020101(R) (2001).
- [91] A. M. Childs, I.L. Chuang, and D.W. Leung, Realization of quantum process tomography in NMR, *Phys. Rev. A* **64**, 012314 (2001).
- [92] J. B. Altepeter *et al.*, Ancilla-Assisted Quantum Process Tomography, *Phys. Rev. Lett.* **90**, 193601 (2003).
- [93] F. De Martini, A. Mazzei, M. Ricci, and G. M. D'Ariano, Exploiting quantum parallelism of entanglement for a complete experimental quantum characterization of a single-qubit device, *Phys. Rev. A* **67**, 062307 (2003).
- [94] J. L. O'Brien, G. J. Pryde, A. G. White, T. C. Ralph, and D. Branning, Demonstration of an all-optical quantum controlled-NOT gate, *Nature (London)* **426**, 264 (2003).
- [95] M.W. Mitchell, C.W. Ellenor, S. Schneider, and A.M. Steinberg, Diagnosis, Prescription, and Prognosis of a Bell-State Filter by Quantum Process Tomography, *Phys. Rev. Lett.* **91**, 120402 (2003).
- [96] J. L. O'Brien *et al.*, Quantum process tomography of a controlled-not gate, *Phys. Rev. Lett.* **93**, 080502 (2004).
- [97] M. Mohseni, A. T. Rezakhani, and D. A. Lidar, Quantum Process Tomography: Resource Analysis of Different Strategies, *Phys. Rev. A* **77**, 032322 (2008).
- [98] E. B. Av, Y. Shapira, N. Akerman, and R. Ozeri, Direct reconstruction of the quantum-master-equation dynamics of a trapped-ion qubit *Phys. Rev. A* **101**, 062305 (2020).
- [99] G. O. Samach *et al.*, Lindblad Tomography of a Superconducting Quantum Processor, *Phys. Rev. Applied* **18**, 064056 (2022).
- [100] A. Shukla, M. Sisodia, and A. Pathak, Complete characterization of the directly implementable quantum gates used in the IBM quantum processors, *Phys. Lett. A* **384**, 126387 (2020).
- [101] H.-Y. Ku *et al.*, Detecting quantum non-breaking channels without entanglement, *PRX Quantum* **3**, 020338 (2022).
- [102] M. Asano *et al.*, Distillation of photon entanglement using a plasmonic metamaterial, *Sci. Rep.* **5**, 18313 (2015).
- [103] IBM Quantum Platform, <https://quantum-computing.ibm.com/> (2023).
- [104] M. Howard, J. Twamley, C. Wittmann, T. Gaebel, F. Jelezko, and J. Wrachtrup, Quantum process tomography and Linblad estimation of a solid-state qubit, *New J. Phys.* **8**, 33 (2006).
- [105] F. Minganti, I. I. Arkhipov, A. Miranowicz, and F. Nori, Liouvillian spectral collapse in the Scully-Lamb laser model, *Phys. Rev. Research* **3**, 043197 (2021).
- [106] F. Minganti, I. I. Arkhipov, A. Miranowicz, and F. Nori, Continuous Dissipative Phase Transitions with or without Symmetry Breaking, *New J. Phys.* **23**, 122001 (2021).
- [107] X.-B. Wang, Z.-W. Yu, J.-Z. Hu, A. Miranowicz, and F. Nori, Efficient tomography of quantum optical Gaussian processes probed with a few coherent states, *Phys. Rev. A* **88**, 022101 (2013).
- [108] F. Beaudoin, J. M. Gambetta, and A. Blais, Dissipation and ultrastrong coupling in circuit QED, *Phys. Rev. A* **84**, 043832 (2011).
- [109] A. Settineri, V. Macri, A. Ridolfo, O. Di Stefano, A. F. Kockum, F. Nori, and S. Savasta, Dissipation and thermal noise in hybrid quantum systems in the ultrastrong-coupling regime, *Phys. Rev. A* **98**, 053834 (2018).
- [110] A. Mercurio, S. Abo, F. Mauceri, E. Russo, V. Macri, A. Miranowicz, S. Savasta, and O. Di Stefano, Pure Dephasing of Light-Matter Systems in the Ultrastrong and Deep-Strong Coupling Regimes, *Phys. Rev. Lett.* **130**, 123601 (2023).
- [111] A. F. Kockum, A. Miranowicz, S. De Liberato, S. Savasta, and F. Nori, Ultrastrong coupling between light and matter, *Nat. Rev. Phys.* **1**, 19 (2019).
- [112] H. Breuer and F. Petruccione, *The Theory of Open Quantum Systems* (Oxford University Press, Oxford, 2007).
- [113] S. Haroche and J. M. Raimond, *Exploring the Quantum: Atoms, Cavities, and Photons* (Oxford University Press, Oxford, 2006).
- [114] J. Dalibard, Y. Castin, and K. Mølmer, Wave-Function Approach to Dissipative Processes in Quantum Optics, *Phys. Rev. Lett.* **68**, 580 (1992).
- [115] H. J. Carmichael, Quantum Trajectory Theory for Cascaded Open Systems, *Phys. Rev. Lett.* **70**, 2273 (1993).
- [116] K. Mølmer, Y. Castin, and J. Dalibard, Monte Carlo wavefunction method in quantum optics, *J. Opt. Soc. Am. B* **10**, 524 (1993).
- [117] M. B. Plenio and P. L. Knight, The quantum-jump approach to dissipative dynamics in quantum optics, *Rev. Mod. Phys.* **70**, 101 (1998).
- [118] A. J. Daley, Quantum trajectories and open many-body quantum systems, *Adv. Phys.* **63**, 77 (2014).
- [119] H. J. Carmichael, *Statistical Methods in Quantum Optics 1: Master Equations and Fokker-Planck Equations* (Springer, Berlin, 1999).
- [120] S. Barnett, *Quantum Information* (Oxford University Press, Oxford, 2009).
- [121] H. Wiseman and G. Milburn, *Quantum Measurement and Control* (Cambridge University Press, Cambridge, 2010).
- [122] See the Supplementary Material, which includes Refs. [129, 130], at <http://xxx> for more technical details including presenting various equivalent QPT methods which lead to the same LEPs.
- [123] V. V. Albert and L. Jiang, Symmetries and conserved quantities in Lindblad master equations, *Phys. Rev. A* **89**, 022118 (2014).
- [124] F. Minganti, A. Biella, N. Bartolo, and C. Ciuti, Spectral theory of Liouvillians for dissipative phase transitions, *Phys. Rev. A* **98**, 042118 (2018).
- [125] J. Fiurašek, Extremal equation for optimal completely positive maps, *Phys. Rev. A* **64**, 062310 (2001).
- [126] A. Jamiolkowski, Linear transformations which preserve trace and positive semidefiniteness of operators, *Rep. Math. Phys.* **3**, 275 (1972).
- [127] M.-D. Choi, Completely positive linear maps on complex matrices, *Lin. Alg. Appl.* **10**, 85 (1975).
- [128] D. F. V. James, P. G. Kwiat, W. J. Munro, and A. G. White, Measurement of qubits, *Phys. Rev. A* **64**, 052312 (2001).
- [129] S. Axler, *Linear Algebra Done Right* (Springer, 2015).
- [130] A. Possolo, Simple Guide for Evaluating and Expressing the Uncertainty of NIST Measurement Results, NIST Technical Note 1900 (2015), DOI:10.6028/NIST.TN.1900.

Supplementary Material for “Liouvillian Exceptional Points of Non-Hermitian Systems via Quantum Process Tomography”

In this Supplementary Material, we provide more technical details on our experimental methods. Additionally, we present the measured Liouvillians in comparison to our theoretical simulations including experimental noise.

I. MATRIX REPRESENTATION OF SUPEROPERATORS

To understand the basic idea of quantum Liouvillian exceptional points (LEPs) and their relation to quantum process tomography (QPT), we recall the matrix formalism of superoperators which, in particular, applies to Liouvillians. A general matrix \hat{O} can be formally vectorized (or flattened) with a function \mathcal{F} as

$$\hat{O} = \sum_{m,n} O_{mn} |m\rangle\langle n| \rightarrow |\tilde{O}\rangle = \mathcal{F}(\hat{O}) = \sum_{m,n} O_{mn} |m\rangle \otimes |n^*\rangle, \quad (\text{S1})$$

where $*$ denotes complex conjugate and, for clarity, flattened quantities are henceforth marked by tilde. Thus, a single-qubit matrix $\hat{\rho}$ can be flattened as

$$\hat{\rho} = \begin{pmatrix} \rho_{00} & \rho_{01} \\ \rho_{10} & \rho_{11} \end{pmatrix} \rightarrow |\tilde{\rho}\rangle = \mathcal{F}(\hat{\rho}) = [\rho_{00}, \rho_{10}, \rho_{01}, \rho_{11}]^T, \quad (\text{S2})$$

where T denotes transposition. The inverse function $\mathcal{F}^{-1}(|\tilde{\rho}\rangle)$ gives the standard form of the density matrix $\hat{\rho}$. Arbitrary right-hand-side (RHS) and left-hand-side (LHS) acting superoperators, say $R[\hat{O}_1]$ and $L[\hat{O}_1]$, can be represented by matrices $\tilde{R}[\hat{O}_1]$ and $\tilde{L}[\hat{O}_1]$, defined, respectively, as:

$$\begin{aligned} \tilde{R}[\hat{O}_1]|\tilde{O}\rangle_2 &= (\mathbb{1}_N \otimes \hat{O}_1^T)|\tilde{O}\rangle_2, \\ \tilde{L}[\hat{O}_1]|\tilde{O}\rangle_2 &= (\hat{O}_1 \otimes \mathbb{1}_N)|\tilde{O}\rangle_2, \end{aligned} \quad (\text{S3})$$

where $\mathbb{1}_N$ is the identity operator of dimension $N = \text{size}(\hat{O}_1)$. By applying this convention, the Liouvillian in the Linblad master equation can be represented as

$$\tilde{\mathcal{L}} = -i \left(\hat{H} \otimes \mathbb{1}_N - \mathbb{1}_N \otimes \hat{H}^T \right) + \sum_n \hat{\Gamma}_n \otimes \hat{\Gamma}_n^* - \frac{1}{2} \left(\hat{\Gamma}_n^\dagger \hat{\Gamma}_n \otimes \mathbb{1} - \mathbb{1} \otimes \hat{\Gamma}_n^T \hat{\Gamma}_n^* \right), \quad (\text{S4})$$

or, equivalently,

$$\tilde{\mathcal{L}} = -i \left(\hat{H}_{\text{eff}} \otimes \mathbb{1} - \mathbb{1} \otimes \hat{H}_{\text{eff}}^T \right) + \sum_n \hat{\Gamma}_n \otimes \hat{\Gamma}_n^*, \quad (\text{S5})$$

in terms of the effective Hamiltonian \hat{H}_{eff} defined by:

$$\hat{H}_{\text{eff}} = \hat{H} - \frac{i}{2} \sum_\mu \Gamma_\mu^\dagger \Gamma_\mu. \quad (\text{S6})$$

The last term in Eq. (S5) represents the effect of quantum jumps on the system evolution. And this effect can be decreased or even completely removed by a proper postselection of quantum trajectories, as described by a hybrid Liouvillian formalism [S2].

II. EQUIVALENT QPT METHODS FOR FINDING EXCEPTIONAL POINTS

LEPs can be calculated via the standard superoperator formalism as described in Ref. [S3]. Here we consider three equivalent methods of finding LEPs via QPT methods for a single qubit.

a. Method #1: Formally the simplest approach to find LEPs is via the QPT based on the following 4×4 non-Hermitian input/output projectors ($k, l = 1, \dots, 4$):

$$\hat{\rho}_{\text{in},k}, \hat{\rho}_{\text{out},l} \in \{|0\rangle\langle 0|, |0\rangle\langle 1|, |1\rangle\langle 0|, |1\rangle\langle 1|\}. \quad (\text{S7})$$

By measuring all the elements

$$L_{kl} = \text{tr} \left[\mathcal{L} (\hat{\rho}_{\text{in},k})^\dagger \hat{\rho}_{\text{out},l} \right], \quad (\text{S8})$$

one can reconstruct the 4×4 transformation matrix L , which represents \mathcal{L} . The method, although formally straightforward, it is usually experimentally challenging.

b. Method #2: From an experimental point of view, it is more precise to search for LEPs via the QPT based on 6×6 projectors, i.e., assuming that the input and output states (projections) are the eigenstates of all the Pauli operators ($i, j = x_+, x_-, y_+, y_-, z_+, z_-$):

$$|\text{in}_i\rangle, |\text{out}_j\rangle \in \{|x_+\rangle, |x_-\rangle, |y_+\rangle, |y_-\rangle, |z_+\rangle, |z_-\rangle\}, \quad (\text{S9})$$

where $|x_+\rangle = \frac{1}{\sqrt{2}}(|0\rangle + |1\rangle)$, $|x_-\rangle = \frac{1}{\sqrt{2}}(|0\rangle - |1\rangle)$, $|y_-\rangle = \frac{1}{\sqrt{2}}(|0\rangle + i|1\rangle)$, $|y_+\rangle = \frac{1}{\sqrt{2}}(|0\rangle - i|1\rangle)$, and $|z_+\rangle \equiv |0\rangle$ and $|z_-\rangle \equiv |1\rangle$. These are arguably the most popular projectors used for QST and QPT of photon polarization qubits, but can also be applied to transmon qubits. Thus, for an amplified-dissipative process, described by the Lindblad master equation with a given Liouvillian \mathcal{L} , one can measure all its elements

$$L'_{ij} = \langle \text{out}_j | \mathcal{L} (\hat{\rho} = |\text{in}_i\rangle\langle \text{in}_i|) | \text{out}_j \rangle, \quad (\text{S10})$$

and, thus, we can reconstruct the 6×6 transformation matrix L' , which represents \mathcal{L} .

c. Method #3: LEPs can equivalently be calculated via the QPT for all the Pauli operators ($k = x, y, z$), i.e.,

$$\hat{\sigma}_k = |k_+\rangle\langle k_+| - |k_-\rangle\langle k_-|, \quad (\text{S11})$$

$$\hat{\sigma}_0 = |z_+\rangle\langle z_+| + |z_-\rangle\langle z_-| = \mathbf{1}, \quad (\text{S12})$$

which can be obtained via the projections on their eigenstates, given in Eq. (S9). Thus, by measuring all the elements ($m, n = 0, \dots, 3$):

$$L''_{mn} = \frac{1}{2} \text{tr} [\mathcal{L} (\hat{\sigma}_m) \hat{\sigma}_n], \quad (\text{S13})$$

where $\hat{\sigma}_1 \equiv \hat{\sigma}_x$, $\hat{\sigma}_2 \equiv \hat{\sigma}_y$, and $\hat{\sigma}_3 \equiv \hat{\sigma}_z$, we can reconstruct the 4×4 Liouvillian matrix L'' representing \mathcal{L} .

d. Equivalence of Methods #1, #2, and #3: Let us demonstrate that all the matrices L, L' , and L'' have the same eigenspectra (up to trivial values). The spectral decomposition of L reads $L = UAV$, where A is a diagonal matrix of the singular values of L and the matrices U and V are unitary matrices constructed from the left and right eigenmatrices. It can be verified via direct calculations and using the linearity and the definitions of the Liouvillians L' and L'' that $L = U''L''(U'')^\dagger$, where the respective unitary matrices read

$$U'' = \frac{1}{\sqrt{2}} \begin{pmatrix} 1 & 0 & 0 & 1 \\ 0 & 1 & -i & 0 \\ 0 & 1 & i & 0 \\ 1 & 0 & 0 & -1 \end{pmatrix}. \quad (\text{S14})$$

Hence,

$$L'' = [(U'')^\dagger U] A [V U''] = (U'')^\dagger L U'' \quad (\text{S15})$$

is a spectral decomposition of L'' with the same eigenspectrum as L given by A , but with possibly different left and right eigenmatrices given by unitary matrices $(U'')^\dagger U$ and $V(U'')^\dagger$.

Similarly, we can write a transformation U' for $L'' = U' L' (U')^T$ as

$$U' = \frac{1}{\sqrt{2}} \begin{pmatrix} 1 & 1 & 0 & 0 & 0 & 0 \\ 0 & 0 & 1 & -1 & 0 & 0 \\ 0 & 0 & 0 & 0 & 1 & -1 \\ 1 & -1 & 0 & 0 & 0 & 0 \end{pmatrix}, \quad (\text{S16})$$

where $(U')^T$ and U^T are their respective pseudoinverse matrices. In the next section, by deriving and applying the unitary version of U' , we demonstrate that L'' and L' have equal ranks. We also demonstrate that L'' and L' have the same eigenvalues. Thus, up to the two trivial eigenvalues of L' , the spectra of L, L' , and L'' coincide. This is confirmed by our numerical calculations.

III. DERIVATIONS OF TRANSFORMATION MATRICES FOR EQUIVALENT QPT METHODS

A. Relation between the Liouvillian matrices L and L''

Using the Einstein summation convention, L used in Method #1 can be expressed as $L_{kl} = U_{km} L''_{mn} V_{nl}$, where L'' is given by Method #3. We can derive the expressions for the transformation matrix expressing L_{kl} in terms of the Pauli matrices used in Method #3 as:

$$\begin{aligned} |z_+\rangle\langle z_+| &= \frac{\hat{\sigma}_0 + \hat{\sigma}_z}{2}, & |z_+\rangle\langle z_-| &= \frac{\hat{\sigma}_x + i\hat{\sigma}_y}{2}, \\ |z_-\rangle\langle z_+| &= \frac{\hat{\sigma}_x - i\hat{\sigma}_y}{2}, & |z_-\rangle\langle z_-| &= \frac{\hat{\sigma}_0 - \hat{\sigma}_z}{2}. \end{aligned} \quad (\text{S17})$$

Here, for simplicity, we use the following notation:

$$\hat{X}_0 \equiv \frac{\hat{\sigma}_0 + \hat{\sigma}_z}{2}, \quad \hat{X}_1 \equiv \frac{\hat{\sigma}_x + i\hat{\sigma}_y}{2}, \quad \hat{X}_2 \equiv \frac{\hat{\sigma}_x - i\hat{\sigma}_y}{2}, \quad \hat{X}_3 \equiv \frac{\hat{\sigma}_0 - \hat{\sigma}_z}{2}. \quad (\text{S18})$$

Now, by expanding Eq. (S8) and substituting the input/output projectors, given in Eq. (S17), the matrix elements L_{kl} and L''_{mn} can be related as:

$$\begin{aligned} L_{00} &= \text{tr} \left[\mathcal{L} \left(\hat{X}_0 \right)^\dagger \left(\hat{X}_0 \right) \right] = \frac{1}{2} (L''_{00} + L''_{30} + L''_{03} + L''_{33}), \\ L_{01} &= \text{tr} \left[\mathcal{L} \left(\hat{X}_0 \right)^\dagger \left(\hat{X}_1 \right) \right] = \frac{1}{2} [L''_{01} + L''_{31} + i(L''_{02} + L''_{32})], \\ L_{10} &= \text{tr} \left[\mathcal{L} \left(\hat{X}_1 \right)^\dagger \left(\hat{X}_0 \right) \right] = \frac{1}{2} [L''_{10} + L''_{13} - i(L''_{20} + L''_{23})], \\ L_{02} &= \text{tr} \left[\mathcal{L} \left(\hat{X}_0 \right)^\dagger \left(\hat{X}_2 \right) \right] = \frac{1}{2} [L''_{01} + L''_{31} - i(L''_{02} + L''_{32})], \\ L_{20} &= \text{tr} \left[\mathcal{L} \left(\hat{X}_2 \right)^\dagger \left(\hat{X}_0 \right) \right] = \frac{1}{2} [L''_{10} + L''_{13} + i(L''_{20} + L''_{23})], \\ L_{03} &= \text{tr} \left[\mathcal{L} \left(\hat{X}_0 \right)^\dagger \left(\hat{X}_3 \right) \right] = \frac{1}{2} (L''_{00} + L''_{30} - L''_{03} - L''_{33}), \\ L_{30} &= \text{tr} \left[\mathcal{L} \left(\hat{X}_3 \right)^\dagger \left(\hat{X}_0 \right) \right] = \frac{1}{2} (L''_{00} + L''_{03} - L''_{30} - L''_{33}), \\ L_{11} &= \text{tr} \left[\mathcal{L} \left(\hat{X}_1 \right)^\dagger \left(\hat{X}_1 \right) \right] = \frac{1}{2} [L''_{11} + L''_{22} - i(L''_{21} - L''_{12})], \\ L_{12} &= \text{tr} \left[\mathcal{L} \left(\hat{X}_1 \right)^\dagger \left(\hat{X}_2 \right) \right] = \frac{1}{2} [L''_{11} - L''_{22} - i(L''_{12} + L''_{21})], \\ L_{21} &= \text{tr} \left[\mathcal{L} \left(\hat{X}_2 \right)^\dagger \left(\hat{X}_1 \right) \right] = \frac{1}{2} [L''_{11} - L''_{22} + i(L''_{21} + L''_{12})], \\ L_{13} &= \text{tr} \left[\mathcal{L} \left(\hat{X}_1 \right)^\dagger \left(\hat{X}_3 \right) \right] = \frac{1}{2} [(L''_{10} - L''_{13} - i(L''_{20} - L''_{23}))], \\ L_{31} &= \text{tr} \left[\mathcal{L} \left(\hat{X}_3 \right)^\dagger \left(\hat{X}_1 \right) \right] = \frac{1}{2} [L''_{01} - L''_{31} + i(L''_{02} - L''_{32})], \\ L_{22} &= \text{tr} \left[\mathcal{L} \left(\hat{X}_2 \right)^\dagger \left(\hat{X}_2 \right) \right] = \frac{1}{2} [L''_{11} + L''_{22} + i(L''_{21} - L''_{12})], \\ L_{23} &= \text{tr} \left[\mathcal{L} \left(\hat{X}_2 \right)^\dagger \left(\hat{X}_3 \right) \right] = \frac{1}{2} [L''_{10} - L''_{13} + i(L''_{20} - L''_{23})], \end{aligned}$$

$$\begin{aligned}
L_{32} &= \text{tr} \left[\mathcal{L} \left(\hat{X}_3 \right)^\dagger \left(\hat{X}_2 \right) \right] = \frac{1}{2} [L''_{01} - L''_{31} - i(L''_{02} - L''_{32})], \\
L_{33} &= \text{tr} \left[\mathcal{L} \left(\hat{X}_3 \right)^\dagger \left(\hat{X}_3 \right) \right] = \frac{1}{2} (L''_{00} - L''_{03} - L''_{30} + L''_{33}).
\end{aligned} \tag{S19}$$

For all $k, l = 0, 1..3$ we have

$$L_{kl} = U_{km} L''_{mn} V_{nl}, \tag{S20}$$

where the transformation matrices V and U can be obtained as explained below. For simplicity, consider $k = l = 0$:

$$L_{00} = \frac{1}{2} (L''_{00} + L''_{30} + L''_{03} + L''_{33}) = U_{00} L''_{00} V_{00} + U_{03} L''_{30} V_{00} + U_{00} L''_{03} V_{30} + U_{03} L''_{33} V_{30}. \tag{S21}$$

In this case, we can immediately infer which products vanish, $U_{0m} V_{n0} = 0$, and list the following relations:

$$\begin{aligned}
\because U_{00} V_{00} &= \frac{1}{2} \Rightarrow U_{00} = V_{00} = \frac{1}{\sqrt{2}}, \\
\because U_{03} V_{00} &= \frac{1}{2} \Rightarrow U_{03} = \frac{1}{\sqrt{2}}, \\
\because U_{03} V_{30} &= \frac{1}{2} \Rightarrow V_{30} = \frac{1}{\sqrt{2}},
\end{aligned} \tag{S22}$$

where we apply the symbols \Rightarrow (therefore) and \because (because) to describe our reasoning in a compact form. The remaining relations between the elements of the transformation matrices can be analyzed in the same way, i.e.:

$$\begin{aligned}
L_{01} &= U_{0m} L''_{mn} V_{n1} = U_{00} L''_{01} V_{11} + U_{03} L''_{31} V_{11} + U_{00} L''_{02} V_{21} + U_{03} L''_{32} V_{21} \\
&= \frac{1}{2} [L''_{01} + L''_{31} + i(L''_{02} + L''_{32})], \\
\because U_{00} V_{11} &= \frac{1}{2}, \quad U_{00} V_{21} = \frac{i}{2}, \quad U_{03} V_{11} = \frac{1}{2}, \quad U_{03} V_{21} = \frac{i}{2}, \\
\Rightarrow V_{11} &= \frac{1}{\sqrt{2}}, \quad V_{21} = \frac{i}{\sqrt{2}},
\end{aligned}$$

$$\begin{aligned}
L_{10} &= U_{1m} L''_{mn} V_{n0} = U_{11} L''_{10} V_{00} + U_{11} L''_{13} V_{30} + U_{12} L''_{20} V_{00} + U_{12} L''_{23} V_{30} \\
&= \frac{1}{2} [L''_{10} + L''_{13} - i(L''_{20} + L''_{23})], \\
\because U_{11} V_{00} &= \frac{1}{2}, \quad U_{11} V_{30} = \frac{1}{2}, \quad U_{12} V_{00} = \frac{-i}{2}, \quad U_{12} V_{30} = \frac{-i}{2}, \\
\Rightarrow U_{11} &= \frac{1}{\sqrt{2}}, \quad U_{12} = \frac{-i}{\sqrt{2}},
\end{aligned}$$

$$\begin{aligned}
L_{02} &= U_{0m} L''_{mn} V_{n2} = U_{00} L''_{01} V_{12} + U_{03} L''_{31} V_{12} + U_{00} L''_{02} V_{22} + U_{03} L''_{32} V_{22} \\
&= \frac{1}{2} [L''_{01} + L''_{31} - i(L''_{02} + L''_{32})], \\
\because U_{00} V_{12} &= \frac{1}{2}, \quad U_{03} V_{12} = \frac{1}{2}, \quad U_{00} V_{22} = \frac{-i}{2}, \quad U_{03} V_{22} = \frac{-i}{2}, \\
\Rightarrow V_{12} &= \frac{1}{\sqrt{2}}, \quad V_{22} = \frac{-i}{\sqrt{2}},
\end{aligned}$$

$$\begin{aligned}
L_{20} &= U_{2m} L''_{mn} V_{n0} = U_{21} L''_{10} V_{00} + U_{21} L''_{13} V_{30} + U_{22} L''_{20} V_{00} + U_{22} L''_{23} V_{30} \\
&= \frac{1}{2} [L''_{10} + L''_{13} + i(L''_{20} + L''_{23})], \\
\because U_{21} V_{00} &= \frac{1}{2}, \quad U_{21} V_{30} = \frac{1}{2}, \quad U_{22} V_{00} = \frac{i}{2}, \quad U_{22} V_{30} = \frac{i}{2}, \\
\Rightarrow U_{21} &= \frac{1}{\sqrt{2}}, \quad U_{22} = \frac{i}{\sqrt{2}},
\end{aligned}$$

$$\begin{aligned}
L_{03} &= U_{0m}L''_{mn}V_{n3} = U_{00}L''_{00}V_{03} + U_{03}L''_{30}V_{03} + U_{00}L''_{03}V_{33} + U_{03}L''_{33}V_{33} \\
&= \frac{1}{2}(L''_{00} + L''_{30} - L''_{03} - L''_{33}), \\
\therefore U_{00}V_{03} &= \frac{1}{2}, \quad U_{03}V_{03} = \frac{1}{2}, \quad U_{00}V_{33} = -\frac{1}{2}, \quad U_{03}V_{33} = -\frac{1}{2}, \\
\Rightarrow V_{03} &= \frac{1}{\sqrt{2}}, \quad V_{33} = -\frac{1}{\sqrt{2}},
\end{aligned}$$

$$\begin{aligned}
L_{30} &= U_{3m}L''_{mn}V_{n0} = U_{30}L''_{00}V_{00} + U_{30}L''_{03}V_{30} + U_{33}L''_{30}V_{00} + U_{33}L''_{33}V_{30} \\
&= \frac{1}{2}(L''_{00} + L''_{03} - L''_{30} - L''_{33}), \\
\therefore U_{30}V_{00} &= \frac{1}{2}, \quad U_{30}V_{30} = \frac{1}{2}, \quad U_{33}V_{00} = -\frac{1}{2}, \quad U_{33}V_{30} = -\frac{1}{2}, \\
\Rightarrow U_{30} &= \frac{1}{\sqrt{2}}, \quad U_{33} = -\frac{1}{\sqrt{2}},
\end{aligned}$$

$$\begin{aligned}
L_{11} &= U_{1m}L''_{mn}V_{n1} = U_{11}L''_{11}V_{11} + U_{12}L''_{22}V_{21} + U_{12}L''_{21}V_{11} + U_{11}L''_{12}V_{21} \\
&= \frac{1}{2}[L''_{11} + L''_{22} - i(L''_{21} - L''_{12})], \\
L_{12} &= U_{1m}L''_{mn}V_{n2} = U_{11}L''_{11}V_{12} + U_{12}L''_{22}V_{22} + U_{11}L''_{12}V_{22} + U_{12}L''_{21}V_{12} \\
&= \frac{1}{2}[L''_{11} - L''_{22} - i(L''_{12} + L''_{21})].
\end{aligned} \tag{S23}$$

It can be easily verified that the inferred relations in Eq. (S23) are compatible with

$$\begin{aligned}
L_{21} &= U_{2m}L''_{mn}V_{n1} = U_{21}L''_{11}V_{11} + U_{22}L''_{22}V_{21} + U_{22}L''_{21}V_{11} + U_{21}L''_{12}V_{21} \\
&= \frac{1}{2}[L''_{11} - L''_{22} + i(L''_{21} + L''_{12})],
\end{aligned}$$

$$\begin{aligned}
L_{13} &= U_{1m}L''_{mn}V_{n3} = U_{11}L''_{10}V_{03} + U_{11}L''_{13}V_{33} + U_{12}L''_{20}V_{03} + U_{12}L''_{23}V_{33} \\
&= \frac{1}{2}[L''_{10} - L''_{13} - i(L''_{20} - L''_{23})],
\end{aligned}$$

$$\begin{aligned}
L_{31} &= U_{3m}L''_{mn}V_{n1} = U_{30}L''_{01}V_{11} + U_{33}L''_{31}V_{11} + U_{30}L''_{02}V_{21} + U_{33}L''_{32}V_{21} \\
&= \frac{1}{2}[L''_{01} - L''_{31} + i(L''_{02} - L''_{32})],
\end{aligned}$$

$$\begin{aligned}
L_{22} &= U_{2m}L''_{mn}V_{n2} = U_{21}L''_{11}V_{12} + U_{22}L''_{22}V_{22} + U_{22}L''_{21}V_{12} + U_{21}L''_{12}V_{22} \\
&= \frac{1}{2}[L''_{11} + L''_{22} + i(L''_{21} - L''_{12})],
\end{aligned}$$

$$\begin{aligned}
L_{23} &= U_{2m}L''_{mn}V_{n3} = U_{21}L''_{10}V_{03} + U_{21}L''_{13}V_{33} + U_{22}L''_{20}V_{03} + U_{22}L''_{23}V_{33} \\
&= \frac{1}{2}[L''_{10} - L''_{13} + i(L''_{20} - L''_{23})],
\end{aligned}$$

$$\begin{aligned}
L_{32} &= U_{3m}L''_{mn}V_{n2} = U_{30}L''_{01}V_{12} + U_{33}L''_{31}V_{12} + U_{30}L''_{02}V_{22} + U_{33}L''_{32}V_{22} \\
&= \frac{1}{2}[L''_{01} - L''_{31} - i(L''_{02} - L''_{32})],
\end{aligned}$$

$$\begin{aligned}
L_{33} &= U_{3m} L''_{mn} V_{n3} = U_{30} L''_{00} V_{03} + U_{30} L''_{03} V_{33} + U_{33} L''_{30} V_{03} + U_{33} L''_{33} V_{33} \\
&= \frac{1}{2} (L''_{00} - L''_{03} - L''_{30} + L''_{33}).
\end{aligned} \tag{S24}$$

Thus, we conclude that $U = V^\dagger$ is a unitary matrix given explicitly as

$$U = \begin{pmatrix} \frac{1}{\sqrt{2}} & 0 & 0 & \frac{1}{\sqrt{2}} \\ 0 & \frac{1}{\sqrt{2}} & \frac{-i}{\sqrt{2}} & 0 \\ 0 & \frac{1}{\sqrt{2}} & \frac{i}{\sqrt{2}} & 0 \\ \frac{1}{\sqrt{2}} & 0 & 0 & -\frac{1}{\sqrt{2}} \end{pmatrix}, \tag{S25}$$

which results in

$$L = UL''U^\dagger. \tag{S26}$$

Note that the above-presented reasoning leads to constraints only for the nonzero matrix elements of U . Conversely, all the remaining matrix elements can be set to zero.

B. Relation between the transformation matrices L' and L''

Given L'_{kl} in Method #2 and L'' in Method #3, we can express the relation between the respective matrix representations of a given Liouvillian as

$$L''_{mn} = U'_{mi} L'_{ij} V'_{jn}. \tag{S27}$$

The eigenstates of all the Pauli operators are the input states ($|\text{in}_i\rangle$) and the output projections ($\langle \text{out}_i|$) used in Method #2. Hence, we can express the Liouvillian matrix L' as:

$$\begin{aligned}
L'_{z_+z_+} &= \langle z_+ | \mathcal{L}(|z_+\rangle\langle z_+|) | z_+ \rangle, & L'_{z_+z_-} &= \langle z_- | \mathcal{L}(|z_+\rangle\langle z_+|) | z_- \rangle, \\
L'_{z_-z_+} &= \langle z_+ | \mathcal{L}(|z_-\rangle\langle z_-|) | z_+ \rangle, & L'_{z_-z_-} &= \langle z_- | \mathcal{L}(|z_-\rangle\langle z_-|) | z_- \rangle
\end{aligned} \tag{S28}$$

Using Eq. (S12) we can expand L'' as:

$$\begin{aligned}
L''_{00} &= \frac{1}{2} \text{tr} [\mathcal{L}(\sigma_0) \sigma_0] = \frac{1}{2} \text{tr} [\mathcal{L}(|z_+\rangle\langle z_+| + |z_-\rangle\langle z_-|) (|z_+\rangle\langle z_+| + |z_-\rangle\langle z_-|)] \\
&= \frac{1}{2} [\langle z_+ | \mathcal{L}(|z_+\rangle\langle z_+|) | z_+ \rangle + \langle z_- | \mathcal{L}(|z_+\rangle\langle z_+|) | z_- \rangle + \langle z_+ | \mathcal{L}(|z_-\rangle\langle z_-|) | z_+ \rangle + \langle z_- | \mathcal{L}(|z_-\rangle\langle z_-|) | z_- \rangle] \\
&= \frac{1}{2} [L'_{z_+z_+} + L'_{z_+z_-} + L'_{z_-z_+} + L'_{z_-z_-}], \\
L''_{01} &= \frac{1}{2} \text{tr} [\mathcal{L}(\sigma_0) \hat{\sigma}_x] = \frac{1}{2} \text{tr} [\mathcal{L}(|z_+\rangle\langle z_+| + |z_-\rangle\langle z_-|) (|x_+\rangle\langle x_+| - |x_-\rangle\langle x_-|)] \\
&= \frac{1}{2} [\langle x_+ | \mathcal{L}(|z_+\rangle\langle z_+|) | x_+ \rangle - \langle x_- | \mathcal{L}(|z_+\rangle\langle z_+|) | x_- \rangle + \langle x_+ | \mathcal{L}(|z_-\rangle\langle z_-|) | x_+ \rangle - \langle x_- | \mathcal{L}(|z_-\rangle\langle z_-|) | x_- \rangle] \\
&= \frac{1}{2} [L'_{z_+x_+} - L'_{z_+x_-} + L'_{z_-x_+} - L'_{z_-x_-}].
\end{aligned} \tag{S29}$$

In the same way for the other elements we have:

$$\begin{aligned}
L''_{10} &= \frac{1}{2} \text{tr} [\mathcal{L}(\hat{\sigma}_x) \sigma_0] = \frac{1}{2} [L'_{x_+z_+} - L'_{x_-z_+} + L'_{x_+z_-} - L'_{x_-z_-}], \\
L''_{11} &= \frac{1}{2} \text{tr} [\mathcal{L}(\hat{\sigma}_x) \hat{\sigma}_x] = \frac{1}{2} [L'_{x_+x_+} - L'_{x_+x_-} - L'_{x_-x_+} + L'_{x_-x_-}], \\
L''_{12} &= \frac{1}{2} \text{tr} [\mathcal{L}(\hat{\sigma}_x) \hat{\sigma}_y] = \frac{1}{2} [L'_{x_+y_+} - L'_{x_+y_-} - L'_{x_-y_+} + L'_{x_-y_-}], \\
L''_{21} &= \frac{1}{2} \text{tr} [\mathcal{L}(\hat{\sigma}_y) \hat{\sigma}_x] = \frac{1}{2} [L'_{y_+x_+} - L'_{y_+x_-} - L'_{y_-x_+} + L'_{y_-x_-}],
\end{aligned}$$

$$\begin{aligned}
 L''_{22} &= \frac{1}{2} \text{tr} [\mathcal{L}(\hat{\sigma}_y) \hat{\sigma}_y] = \frac{1}{2} [L'_{y+y+} - L'_{y+y-} - L'_{y-y+} + L'_{y-y-}], \\
 L''_{13} &= \frac{1}{2} \text{tr} [\mathcal{L}(\hat{\sigma}_x) \hat{\sigma}_z] = \frac{1}{2} [L'_{x+z+} - L'_{x+z-} - L'_{x-z+} + L'_{x-z-}], \\
 L''_{31} &= \frac{1}{2} \text{tr} [\mathcal{L}(\hat{\sigma}_z) \hat{\sigma}_x] = \frac{1}{2} [L'_{z+x+} - L'_{z+x-} - L'_{z-x+} + L'_{z-x-}], \\
 L''_{32} &= \frac{1}{2} \text{tr} [\mathcal{L}(\hat{\sigma}_z) \hat{\sigma}_y] = \frac{1}{2} [L'_{z+y+} - L'_{z+y-} - L'_{z-y+} + L'_{z-y-}], \\
 \\
 L''_{23} &= \frac{1}{2} \text{tr} [\mathcal{L}(\hat{\sigma}_y) \hat{\sigma}_z] = \frac{1}{2} [L'_{y+z+} - L'_{y+z-} - L'_{y-z+} + L'_{y-z-}], \\
 L''_{02} &= \frac{1}{2} \text{tr} [\mathcal{L}(\sigma_0) \hat{\sigma}_y] = \frac{1}{2} [L'_{z+y+} - L'_{z+y-} + L'_{z-y+} - L'_{z-y-}], \\
 L''_{20} &= \frac{1}{2} \text{tr} [\mathcal{L}(\hat{\sigma}_y) \sigma_0] = \frac{1}{2} [L'_{y+z+} + L'_{y+z-} - L'_{y-z+} - L'_{y-z-}], \\
 L''_{03} &= \frac{1}{2} \text{tr} [\mathcal{L}(\sigma_0) \hat{\sigma}_z] = \frac{1}{2} [L'_{z+z+} - L'_{z+z-} + L'_{z-z+} - L'_{z-z-}], \\
 \\
 L''_{30} &= \frac{1}{2} \text{tr} [\mathcal{L}(\hat{\sigma}_z) \sigma_0] = \frac{1}{2} [L'_{z+z+} + L'_{z+z-} - L'_{z-z+} - L'_{z-z-}], \\
 L''_{33} &= \frac{1}{2} \text{tr} [\mathcal{L}(\hat{\sigma}_z) \hat{\sigma}_z] = \frac{1}{2} [L'_{z+z+} - L'_{z+z-} - L'_{z-z+} + L'_{z-z-}].
 \end{aligned} \tag{S30}$$

By using (S27) we can find the elements of the unitary matrices U'_{mi} and V'_{jn} starting with

$$L''_{00} = U'_{0z+} L'_{z+z+} V'_{z+0} + U'_{0z+} L'_{z+z-} V'_{z-0} + U'_{0z-} L'_{z-z+} V'_{z+0} + U'_{0z-} L'_{z-z-} V'_{z-0}, \tag{S31}$$

which is equivalent to

$$L''_{00} = \frac{1}{2} [L'_{z+z+} + L'_{z+z-} + L'_{z-z+} + L'_{z-z-}], \tag{S32}$$

as given by (S29). By comparing (S31) with (S32), we obtain:

$$\begin{aligned}
 \because U'_{0z+} V'_{z+0} &= \frac{1}{2} \Rightarrow U'_{0z+} = V'_{z+0} = \frac{1}{\sqrt{2}}, \\
 \because U'_{0z+} V'_{z-0} &= \frac{1}{2} \Rightarrow V'_{z-0} = \frac{1}{\sqrt{2}}, \\
 \because U'_{0z-} V'_{z+0} &= \frac{1}{2} \Rightarrow V'_{01} = \frac{1}{\sqrt{2}}.
 \end{aligned} \tag{S33}$$

In the same way we can find the remaining nonzero matrix elements of S and T as:

$$\begin{aligned}
 L''_{01} &= U'_{0i} L'_{ij} V'_{j1} = U'_{0z+} L'_{z+x+} V'_{x+1} + U'_{0z+} L'_{z+x-} V'_{x-1} + U'_{0z-} L'_{z-x+} V'_{x+1} + U'_{0z-} L'_{z-x-} V'_{x-1} \\
 &= \frac{1}{2} [L'_{z+x+} - L'_{z+x-} + L'_{z-x+} - L'_{z-x-}] \\
 \because U'_{0z+} V'_{x+1} &= \frac{1}{2}, \quad U'_{0z+} V'_{x-1} = -\frac{1}{2}, \quad U'_{0z-} V'_{x+1} = \frac{1}{2}, \quad U'_{0z-} V'_{x-1} = -\frac{1}{2} \\
 \Rightarrow V'_{x+1} &= \frac{1}{\sqrt{2}}, \quad V'_{x-1} = -\frac{1}{\sqrt{2}},
 \end{aligned}$$

$$\begin{aligned}
 L''_{10} &= U'_{1i} L'_{ij} V'_{j0} = U'_{1x+} L'_{x+z+} V'_{z+0} + U'_{1x-} L'_{x-z+} V'_{z+0} + U'_{1x+} L'_{x+z-} V'_{z-0} + U'_{1x-} L'_{x-z-} V'_{z-0} \\
 &= \frac{1}{2} [L'_{x+z+} - L'_{x-z+} + L'_{x+z-} - L'_{x-z-}] \\
 \because U'_{1x+} V'_{z+0} &= \frac{1}{2}, \quad U'_{1x-} V'_{z+0} = -\frac{1}{2}, \quad U'_{1x+} V'_{z-0} = \frac{1}{2}, \quad U'_{1x-} V'_{z-0} = -\frac{1}{2} \\
 \Rightarrow U'_{1x+} &= \frac{1}{\sqrt{2}}, \quad U'_{1x-} = -\frac{1}{\sqrt{2}},
 \end{aligned}$$

$$\begin{aligned}
L''_{11} &= U'_{1i} L'_{ij} V'_{j1} = U'_{1x_+} L'_{x_+x_+} V'_{x_+1} + U'_{1x_+} L'_{x_+x_-} V'_{x_-1} + U'_{1x_-} L'_{x_-x_+} V'_{x_+1} + U'_{1x_-} L'_{x_-x_-} V'_{x_-1} \\
&= \frac{1}{2} [L'_{x_+x_+} - L'_{x_+x_-} - L'_{x_-x_+} + L'_{x_-x_-}] \\
&\Rightarrow U'_{1x_+} V'_{x_+1} = \frac{1}{2}, \quad U'_{1x_+} V'_{x_-1} = -\frac{1}{2}, \quad U'_{1x_-} V'_{x_+1} = -\frac{1}{2}, \quad U'_{1x_-} V'_{x_-1} = \frac{1}{2},
\end{aligned}$$

$$\begin{aligned}
L''_{12} &= U'_{1i} L'_{ij} V'_{j1} = U'_{1x_+} L'_{x_+y_+} V'_{y_+2} + U'_{1x_+} L'_{x_+y_-} V'_{y_-2} + U'_{1x_-} L'_{x_-y_+} V'_{y_+2} + U'_{1x_-} L'_{x_-y_-} V'_{y_-2} \\
&= \frac{1}{2} [L'_{x_+y_+} - L'_{x_+y_-} - L'_{x_-y_+} + L'_{x_-y_-}] \\
&\because U'_{1x_+} V'_{y_+2} = \frac{1}{2}, \quad U'_{1x_+} V'_{y_-2} = -\frac{1}{2}, \quad U'_{1x_-} V'_{y_+2} = -\frac{1}{2}, \quad U'_{1x_-} V'_{y_-2} = \frac{1}{2} \\
&\Rightarrow V'_{y_+2} = \frac{1}{\sqrt{2}}, \quad V'_{y_-2} = -\frac{1}{\sqrt{2}},
\end{aligned}$$

$$\begin{aligned}
L''_{21} &= U'_{2i} L'_{ij} V'_{j1} = U'_{2y_+} L'_{y_+x_+} V'_{x_+1} + U'_{2y_+} L'_{y_+x_-} V'_{x_-1} + U'_{2y_-} L'_{y_-x_+} V'_{x_+1} + U'_{2y_-} L'_{y_-x_-} V'_{x_-1} \\
&= \frac{1}{2} [L'_{y_+x_+} - L'_{y_+x_-} - L'_{y_-x_+} + L'_{y_-x_-}] \\
&\because U'_{2y_+} V'_{x_+1} = \frac{1}{2}, \quad U'_{2y_+} V'_{x_-1} = -\frac{1}{2}, \quad U'_{2y_-} V'_{x_+1} = -\frac{1}{2}, \quad U'_{2y_-} V'_{x_-1} = \frac{1}{2} \\
&\Rightarrow V'_{x_+1} = \frac{1}{\sqrt{2}}, \quad U'_{2y_+} = \frac{1}{\sqrt{2}}, \quad U'_{2y_-} = -\frac{1}{\sqrt{2}},
\end{aligned}$$

$$\begin{aligned}
L''_{22} &= U'_{2i} L'_{ij} V'_{j2} = U'_{2y_+} L'_{y_+y_+} V'_{y_+2} + U'_{2y_+} L'_{y_+y_-} V'_{y_-2} + U'_{2y_-} L'_{y_-y_+} V'_{y_+2} + U'_{2y_-} L'_{y_-y_-} V'_{y_-2} \\
&= \frac{1}{2} [L'_{y_+y_+} - L'_{y_+y_-} - L'_{y_-y_+} + L'_{y_-y_-}] \\
&\Rightarrow U'_{2y_+} V'_{y_+2} = \frac{1}{2}, \quad U'_{2y_+} V'_{y_-2} = -\frac{1}{2}, \quad U'_{2y_-} V'_{y_+2} = -\frac{1}{2}, \quad U'_{2y_-} V'_{y_-2} = \frac{1}{2},
\end{aligned}$$

$$\begin{aligned}
L''_{13} &= U'_{1i} L'_{ij} V'_{j3} = U'_{1x_+} L'_{x_+z_+} V'_{z_+3} + U'_{1x_+} L'_{x_+z_-} V'_{z_-3} + U'_{1x_-} L'_{x_-z_+} V'_{z_+3} + U'_{1x_-} L'_{x_-z_-} V'_{z_-3} \\
&= \frac{1}{2} [L'_{x_+z_+} - L'_{x_+z_-} - L'_{x_-z_+} + L'_{x_-z_-}] \\
&\because U'_{1x_+} V'_{z_+3} = \frac{1}{2}, \quad U'_{1x_+} V'_{z_-3} = -\frac{1}{2}, \quad U'_{1x_-} V'_{z_+3} = -\frac{1}{2}, \quad U'_{1x_-} V'_{z_-3} = \frac{1}{2} \\
&\Rightarrow V'_{z_+3} = \frac{1}{\sqrt{2}}, \quad V'_{z_-3} = -\frac{1}{\sqrt{2}},
\end{aligned}$$

$$\begin{aligned}
L''_{31} &= U'_{3i} L'_{ij} V'_{j1} = U'_{3z_+} L'_{z_+x_+} V'_{x_+1} + U'_{3z_+} L'_{z_+x_-} V'_{x_-1} + U'_{3z_-} L'_{z_-x_+} V'_{x_+1} + U'_{3z_-} L'_{z_-x_-} V'_{x_-1} \\
&= \frac{1}{2} [L'_{z_+x_+} - L'_{z_+x_-} - L'_{z_-x_+} + L'_{z_-x_-}] \\
&\because U'_{3z_+} V'_{x_+1} = \frac{1}{2}, \quad U'_{3z_+} V'_{x_-1} = -\frac{1}{2}, \quad U'_{3z_-} V'_{x_+1} = -\frac{1}{2}, \quad U'_{3z_-} V'_{x_-1} = \frac{1}{2} \\
&\Rightarrow U'_{3z_+} = \frac{1}{\sqrt{2}}, \quad U'_{3z_-} = -\frac{1}{\sqrt{2}},
\end{aligned}$$

$$\begin{aligned}
L''_{32} &= U'_{3i} L'_{ij} V'_{j2} = U'_{3z_+} L'_{z_+y_+} V'_{y_+2} + U'_{3z_+} L'_{z_+y_-} V'_{y_-2} + U'_{3z_-} L'_{z_-y_+} V'_{y_+2} + U'_{3z_-} L'_{z_-y_-} V'_{y_-2} \\
&\because U'_{3z_-} V'_{y_-2} = \frac{1}{2} \\
&\Rightarrow V'_{y_+2} = \frac{1}{\sqrt{2}}, \quad V'_{y_-2} = -\frac{1}{\sqrt{2}}, \quad V'_{y_+2} = \frac{1}{\sqrt{2}},
\end{aligned}$$

$$\begin{aligned}
L''_{23} &= U'_{2i} L'_{ij} V'_{j3} = U'_{2y_+} L'_{y_+z_+} V'_{z_+3} + U'_{2y_+} L'_{y_+z_-} V'_{z_-3} + U'_{2y_-} L'_{y_-z_+} V'_{z_+3} + U'_{2y_-} L'_{y_-z_-} V'_{z_-3} \\
L''_{23} &= \frac{1}{2} [L'_{y_+z_+} - L'_{y_+z_-} - L'_{y_-z_+} + L'_{y_-z_-}] \\
&\because U'_{2y_+} V'_{z_+3} = \frac{1}{2}, \quad U'_{2y_+} V'_{z_-3} = -\frac{1}{2}, \quad U'_{2y_-} V'_{z_+3} = -\frac{1}{2}, \quad U'_{2y_-} V'_{z_-3} = \frac{1}{2} \\
&\Rightarrow V'_{z_+3} = \frac{1}{\sqrt{2}}, \quad V'_{z_-3} = -\frac{1}{\sqrt{2}}, \quad U'_{2y_-} = -\frac{1}{\sqrt{2}},
\end{aligned}$$

$$\begin{aligned}
L''_{02} &= U'_{0i} L'_{ij} V'_{j2} = U'_{0z_+} L'_{z_+y_+} V'_{y_+2} + U'_{0z_+} L'_{z_+y_-} V'_{y_-2} + U'_{0z_-} L'_{z_-y_+} V'_{y_+2} + U'_{0z_-} L'_{z_-y_-} V'_{y_-2} \\
L''_{02} &= \frac{1}{2} [L'_{z_+y_+} - L'_{z_+y_-} + L'_{z_-y_+} - L'_{z_-y_-}] \\
&\because U'_{0z_+} V'_{y_+2} = \frac{1}{2}, \quad U'_{0z_+} V'_{y_-2} = -\frac{1}{2}, \quad U'_{0z_-} V'_{y_+2} = \frac{1}{2}, \quad U'_{0z_-} V'_{y_-2} = -\frac{1}{2} \\
&\Rightarrow V'_{y_-2} = -\frac{1}{\sqrt{2}}, \quad V'_{y_+2} = \frac{1}{\sqrt{2}},
\end{aligned}$$

$$\begin{aligned}
L''_{20} &= U'_{2i} L'_{ij} V'_{j0} = U'_{2y_+} L'_{y_+z_+} V'_{z_+0} + U'_{2y_+} L'_{y_+z_-} V'_{z_-0} + U'_{2y_-} L'_{y_-z_+} V'_{z_+0} + U'_{2y_-} L'_{y_-z_-} V'_{z_-0} \\
L''_{20} &= \frac{1}{2} [L'_{y_+z_+} + L'_{y_+z_-} - L'_{y_-z_+} - L'_{y_-z_-}] \\
&\because U'_{2y_+} V'_{z_+0} = \frac{1}{2}, \quad U'_{2y_+} V'_{z_-0} = \frac{1}{2}, \quad U'_{2y_-} V'_{z_+0} = -\frac{1}{2}, \quad U'_{2y_-} V'_{z_-0} = -\frac{1}{2} \\
&\Rightarrow U'_{2y_+} = \frac{1}{\sqrt{2}}, \quad U'_{2y_-} = -\frac{1}{\sqrt{2}},
\end{aligned}$$

$$\begin{aligned}
L''_{03} &= U'_{0i} L'_{ij} V'_{j3} = U'_{0z_+} L'_{z_+z_+} V'_{z_+3} + U'_{0z_+} L'_{z_+z_-} V'_{z_-3} + U'_{0z_-} L'_{z_-z_+} V'_{z_+3} + U'_{0z_-} L'_{z_-z_-} V'_{z_-3} \\
L''_{03} &= \frac{1}{2} [L'_{z_+z_+} - L'_{z_+z_-} + L'_{z_-z_+} - L'_{z_-z_-}] \\
&\Rightarrow U'_{0z_+} V'_{z_+3} = \frac{1}{2}, \quad U'_{0z_+} V'_{z_-3} = -\frac{1}{2}, \quad U'_{0z_-} V'_{z_+3} = \frac{1}{2}, \quad U'_{0z_-} V'_{z_-3} = -\frac{1}{2},
\end{aligned}$$

$$\begin{aligned}
L''_{30} &= U'_{3i} L'_{ij} V'_{j0} = U'_{3z_+} L'_{z_+z_+} V'_{z_+0} + U'_{3z_+} L'_{z_+z_-} V'_{z_-0} + U'_{3z_-} L'_{z_-z_+} V'_{z_+0} + U'_{3z_-} L'_{z_-z_-} V'_{z_-0} \\
L''_{30} &= \frac{1}{2} [L'_{z_+z_+} + L'_{z_+z_-} - L'_{z_-z_+} - L'_{z_-z_-}] \\
&\Rightarrow U'_{3z_+} V'_{z_+0} = \frac{1}{2}, \quad U'_{3z_+} V'_{z_-0} = \frac{1}{2}, \quad U'_{3z_-} V'_{z_+0} = -\frac{1}{2}, \quad U'_{3z_-} V'_{z_-0} = -\frac{1}{2}
\end{aligned}$$

$$\begin{aligned}
L''_{33} &= U'_{3i} L'_{ij} V'_{j3} = U'_{3z_+} L'_{z_+z_+} V'_{z_+3} + U'_{3z_+} L'_{z_+z_-} V'_{z_-3} + U'_{3z_-} L'_{z_-z_+} V'_{z_+3} + U'_{3z_-} L'_{z_-z_-} V'_{z_-3} \\
&= \frac{1}{2} [L'_{z_+z_+} - L'_{z_+z_-} - L'_{z_-z_+} + L'_{z_-z_-}] \\
&\Rightarrow U'_{3z_+} V'_{z_+3} = \frac{1}{2}, \quad U'_{3z_+} V'_{z_-3} = -\frac{1}{2}, \quad U'_{3z_-} V'_{z_+3} = -\frac{1}{2}, \quad U'_{3z_-} V'_{z_-3} = \frac{1}{2}
\end{aligned} \tag{S34}$$

Now, we can collect all the matrix elements of U' and V' as:

$$U' = \begin{pmatrix} \frac{1}{\sqrt{2}} & \frac{1}{\sqrt{2}} & 0 & 0 & 0 & 0 \\ 0 & 0 & \frac{1}{\sqrt{2}} & -\frac{1}{\sqrt{2}} & 0 & 0 \\ 0 & 0 & 0 & 0 & \frac{1}{\sqrt{2}} & -\frac{1}{\sqrt{2}} \\ \frac{1}{\sqrt{2}} & -\frac{1}{\sqrt{2}} & 0 & 0 & 0 & 0 \end{pmatrix}, \quad V' = \begin{pmatrix} \frac{1}{\sqrt{2}} & 0 & 0 & \frac{1}{\sqrt{2}} \\ \frac{1}{\sqrt{2}} & 0 & 0 & -\frac{1}{\sqrt{2}} \\ 0 & \frac{1}{\sqrt{2}} & 0 & 0 \\ 0 & -\frac{1}{\sqrt{2}} & 0 & 0 \\ 0 & 0 & \frac{1}{\sqrt{2}} & 0 \\ 0 & 0 & -\frac{1}{\sqrt{2}} & 0 \end{pmatrix}. \tag{S35}$$

10

It is clear that $U' = (V')^T$ and $U'(U')^T = \mathbb{1}_4$ and $U'^T U = \mathbb{1}_6$, where the identity matrices have dimensions 4 and 6, respectively. Now, we can rewrite (S27) as

$$L'' = U' L' (U')^T. \quad (\text{S36})$$

To demonstrate that L' and L'' have a common set of eigenvalues consider an eigenstate $|\tilde{\rho}''\rangle$ of L'' corresponding to an eigenvalue λ , i.e.,

$$L'' |\tilde{\rho}''\rangle = \lambda |\tilde{\rho}''\rangle. \quad (\text{S37})$$

Now, let us apply $(U')^T$ to the LHS of this equation to arrive at

$$\begin{aligned} U'^T L'' |\tilde{\rho}''\rangle &= U'^T \lambda |\tilde{\rho}''\rangle, \\ U'^T L'' U' (U'^T |\tilde{\rho}''\rangle) &= \lambda (U'^T |\tilde{\rho}''\rangle), \\ L' |\tilde{\rho}'\rangle &= \lambda |\tilde{\rho}'\rangle, \end{aligned} \quad (\text{S38})$$

where we used $L'' = U' L' U'^T \Rightarrow L' = U'^T L'' U'$ and $U' U'^T = U'^T U' = \mathbb{1}_6$. The same procedure can be repeated starting with

$$L' |\tilde{\rho}'\rangle = \lambda |\tilde{\rho}'\rangle, \quad (\text{S39})$$

and arriving at

$$L'' (U' |\tilde{\rho}'\rangle) = \lambda (U' |\tilde{\rho}'\rangle). \quad (\text{S40})$$

Hence, L' has the same eigenvalues as L'' , but different eigenmatrices. Moreover, the rank of L' and L'' is at most 4.

C. More properties of L'

To convert the matrix $(U')^T$ to a unitary matrix, we expand it by adding two columns in a way that the columns form an orthonormal set of vectors, i.e.,

$$(\bar{U}')^T = \begin{pmatrix} \frac{1}{\sqrt{2}} & 0 & 0 & \frac{1}{\sqrt{2}} & 0 & 0 \\ \frac{1}{\sqrt{2}} & 0 & 0 & -\frac{1}{\sqrt{2}} & 0 & 0 \\ 0 & \frac{1}{\sqrt{2}} & 0 & 0 & \frac{1}{\sqrt{2}} & 0 \\ 0 & -\frac{1}{\sqrt{2}} & 0 & 0 & \frac{1}{\sqrt{2}} & 0 \\ 0 & 0 & \frac{1}{\sqrt{2}} & 0 & 0 & \frac{1}{\sqrt{2}} \\ 0 & 0 & -\frac{1}{\sqrt{2}} & 0 & 0 & \frac{1}{\sqrt{2}} \end{pmatrix}. \quad (\text{S41})$$

This unitary matrix $(\bar{U}')^T$ can be used to express L' in a form containing a 4×4 block equivalent to L'' , i.e.,

$$\bar{U}' L' (\bar{U}')^T = \left(\begin{array}{c|c} L'' & B \\ \hline B^\dagger & C \end{array} \right), \quad B^\dagger = \begin{pmatrix} B_{00} & B_{10} & B_{20} & B_{30} \\ B_{01} & B_{11} & B_{21} & B_{31} \end{pmatrix}, \quad C = \begin{pmatrix} C_{00} & C_{01} \\ C_{10} & C_{11} \end{pmatrix}, \quad (\text{S42})$$

where

$$\begin{aligned} B_{00} &= \frac{1}{2} [L'_{z_+x_-} + L'_{z_+x_+} + L'_{z_-x_-} + L'_{z_-x_+}], & B_{01} &= \frac{1}{2} [L'_{z_+y_+} + L'_{z_+y_-} + L'_{z_-y_+} + L'_{z_-y_-}], \\ B_{10} &= \frac{1}{2} [L'_{x_+x_-} + L'_{x_+x_+} - L'_{x_-x_-} - L'_{x_-x_+}], & B_{11} &= \frac{1}{2} [L'_{x_+y_+} + L'_{x_+y_-} - L'_{x_-y_+} - L'_{x_-y_-}], \\ B_{20} &= \frac{1}{2} [L'_{y_+x_-} + L'_{y_+x_+} - L'_{y_-x_-} - L'_{y_-x_+}], & B_{21} &= \frac{1}{2} [L'_{y_+y_+} + L'_{y_+y_-} - L'_{y_-y_+} - L'_{y_-y_-}], \\ B_{30} &= \frac{1}{2} [L'_{z_+x_-} + L'_{z_+x_+} - L'_{z_-x_-} - L'_{z_-x_+}], & B_{31} &= \frac{1}{2} [L'_{z_+y_+} + L'_{z_+y_-} - L'_{z_-y_+} - L'_{z_-y_-}], \\ C_{00} &= \frac{1}{2} [L'_{x_-x_-} + L'_{x_-x_+} + L'_{x_+x_-} + L'_{x_+x_+}], & C_{01} &= \frac{1}{2} [L'_{x_-y_+} + L'_{x_-y_-} + L'_{x_+y_+} + L'_{x_+y_-}], \\ C_{10} &= \frac{1}{2} [L'_{y_+x_-} + L'_{y_+x_+} + L'_{y_-x_-} + L'_{y_-x_+}], & C_{11} &= \frac{1}{2} [L'_{y_+y_+} + L'_{y_+y_-} + L'_{y_-y_+} + L'_{y_-y_-}]. \end{aligned} \quad (\text{S43})$$

Now, we are able to use the unitary matrix

$$D = \begin{pmatrix} \frac{\sqrt{3}}{3} & 0 & 0 & 0 & 0 & \frac{\sqrt{6}}{3} \\ 0 & 1 & 0 & 0 & 0 & 0 \\ 0 & 0 & 1 & 0 & 0 & 0 \\ 0 & 0 & 0 & 1 & 0 & 0 \\ \frac{\sqrt{3}}{3} & 0 & 0 & 0 & -\frac{\sqrt{2}}{2} & -\frac{\sqrt{6}}{6} \\ \frac{\sqrt{3}}{3} & 0 & 0 & 0 & \frac{\sqrt{2}}{2} & -\frac{\sqrt{6}}{6} \end{pmatrix},$$

to rearrange the elements of $\bar{U}'L'(\bar{U}')^T$ without chaining its spectrum as

$$D^\dagger \bar{U}'L'(\bar{U}')^T D = \begin{pmatrix} 3L_{00} & \sqrt{3}L_{01} & \sqrt{3}L_{02} & \sqrt{3}L_{03} & 0 & 0 \\ \sqrt{3}L_{10} & L_{11} & L_{12} & L_{13} & 0 & 0 \\ \sqrt{3}L_{20} & L_{21} & L_{22} & L_{23} & 0 & 0 \\ \sqrt{3}L_{30} & L_{31} & L_{32} & L_{33} & 0 & 0 \\ 0 & 0 & 0 & 0 & 0 & 0 \\ 0 & 0 & 0 & 0 & 0 & 0 \end{pmatrix}. \quad (\text{S44})$$

It is evident that L' is a rank-4 matrix. By subtracting the null space from Eq. (S44) can be rewritten as

$$\tilde{L}' = D^\dagger \bar{U}'L'(\bar{U}')^T D = \begin{pmatrix} 3L_{00} & \sqrt{3}L_{01} & \sqrt{3}L_{02} & \sqrt{3}L_{03} \\ \sqrt{3}L_{10} & L_{11} & L_{12} & L_{13} \\ \sqrt{3}L_{20} & L_{21} & L_{22} & L_{23} \\ \sqrt{3}L_{30} & L_{31} & L_{32} & L_{33} \end{pmatrix}. \quad (\text{S45})$$

Note that

$$\det(\tilde{L}') = 3 \det(L''). \quad (\text{S46})$$

It is straightforward to show that matrices L' , \tilde{L}' , and L'' have the same rank. This is evident by obtaining L'' dividing both the first row and column of \tilde{L}' by $\sqrt{3}$, which are, rank-conserving operations. The rank of L' is the same as that of \tilde{L}' , as implied by the rank-nullity theorem [S4].

IV. ESTIMATION OF ERRORS IN THE EIGENSPECTRA OF EXPERIMENTAL LIOUVILLIANS

Here, we estimate, based on the derivation of Ref. [S5], how much experimental (or numerical) perturbations can affect the eigenspectra of an Liouvillian superoperator. Let us consider an experimental Liouvillian L^{exp} , with the eigenspectra,

$$\begin{aligned} L^{\text{exp}}|\tilde{\rho}_n^{\text{exp}}\rangle &= \lambda_n^{\text{exp}}|\tilde{\rho}_n^{\text{exp}}\rangle, \\ \langle \tilde{\sigma}_n^{\text{exp}}|L^{\text{exp}} &= \lambda_n^{\text{exp}}\langle \tilde{\sigma}_n^{\text{exp}}|, \end{aligned} \quad (\text{S47})$$

which slightly differ from the spectra of an ideal Liouvillian L_0 ,

$$\begin{aligned} L_0|\tilde{\rho}_n^{(0)}\rangle &= \lambda_n^{(0)}|\tilde{\rho}_n^{(0)}\rangle, \\ \langle \tilde{\sigma}_n^{(0)}|L_0 &= \lambda_n^{(0)}\langle \tilde{\sigma}_n^{(0)}|. \end{aligned} \quad (\text{S48})$$

So, one can write

$$L^{\text{exp}} = L_0 + \delta L, \quad (\text{S49})$$

assuming that δL is a small perturbation. Note that the completeness relation, $\sum_n |\tilde{\rho}_n^{(0)}\rangle\langle \tilde{\sigma}_n^{(0)}| = \mathbf{1}_4$, and the orthonormality condition, $\langle \tilde{\sigma}_n^{(0)}|\tilde{\rho}_m^{(0)}\rangle = \delta_{nm}$, are satisfied for L_0 , and analogously for the corresponding eigenmatrices of L^{exp} . Thus, if the Liouvillians are diagonalizable (i.e., a way from their LEPs), we have

$$f(L_0) = \sum_i f(\lambda_i^{(0)})|\tilde{\rho}_i^{(0)}\rangle\langle \tilde{\sigma}_i^{(0)}|, \quad (\text{S50})$$

$$f(L^{\text{exp}}) = \sum_i f(\lambda_i^{\text{exp}})|\tilde{\rho}_i^{\text{exp}}\rangle\langle \tilde{\sigma}_i^{\text{exp}}|. \quad (\text{S51})$$

for any well-behaved functions f of the Liouvillians. Assuming small perturbations in L and in related quantities, we consider their power-series expansions:

$$\begin{aligned} L^{\text{exp}} &= L_0 + \epsilon L_1 + \dots, \\ \lambda_n^{\text{exp}} &= \lambda_n^{(0)} + \epsilon \lambda_n^{(1)} + \dots, \\ |\tilde{\rho}_n^{\text{exp}}\rangle &= |\tilde{\rho}_n^{(0)}\rangle + \epsilon |\tilde{\rho}_n^{(1)}\rangle + \dots, \\ \langle \tilde{\sigma}_n^{\text{exp}} | &= \langle \tilde{\sigma}_n^{(0)} | + \epsilon \langle \tilde{\sigma}_n^{(1)} | + \dots, \end{aligned} \quad (\text{S52})$$

in some perturbation parameter ϵ . For simplicity, hereafter, we omit all the terms with higher powers of ϵ . So, we can assume that $\delta L \approx \epsilon L_1$. By inserting these expansions into Eq. (S47), one instantly obtains Eq. (S48) for all the terms independent of ϵ . Moreover, by collecting all the terms proportional to ϵ in these equations, one obtains:

$$F_n^{(0)} |\tilde{\rho}_n^{(1)}\rangle = -F_n^{(1)} |\tilde{\rho}_n^{(0)}\rangle, \quad (\text{S53})$$

$$\langle \tilde{\sigma}_n^{(1)} | F_n^{(0)} = -F_n^{(1)} \langle \tilde{\sigma}_n^{(0)} |, \quad (\text{S54})$$

where $F_n^{(k)} = L_k - \lambda_n^{(k)} \mathbb{1}_4$ for $k = 0, 1$. Multiplying Eq. (S53) by $\langle \tilde{\sigma}_n |$ from the LHS, one obtains $\lambda_n^{(1)} = \langle \tilde{\sigma}_n^{(0)} | L_1 | \tilde{\rho}_n^{(0)} \rangle$, or, equivalently,

$$\begin{aligned} \delta \lambda &\equiv \lambda_n^{\text{exp}} - \lambda_n^{(0)} \approx \epsilon \lambda_n^{(1)} = \langle \tilde{\sigma}_n^{(0)} | (\epsilon L_1) | \tilde{\rho}_n^{(0)} \rangle, \\ &\approx \langle \tilde{\sigma}_n^{(0)} | \delta L | \tilde{\rho}_n^{(0)} \rangle. \end{aligned} \quad (\text{S55})$$

By applying Eq. (S50), with $f(L_0) = F_n^{(0)}$, to Eq. (S53), one obtains

$$|\tilde{\rho}_n^{(1)}\rangle \approx - \sum_{i (i \neq n)} \left(\frac{\langle \tilde{\sigma}_i^{(0)} | L_1 | \tilde{\rho}_i^{(0)} \rangle}{\lambda_i^{(0)} - \lambda_n^{(0)}} \right) |\tilde{\rho}_i^{(0)}\rangle, \quad (\text{S56})$$

which leads to

$$|\delta \tilde{\rho}_n\rangle \equiv |\tilde{\rho}_n^{\text{exp}}\rangle - |\tilde{\rho}_n^{(0)}\rangle \approx |\delta \tilde{\rho}_n^{(1)}\rangle = \epsilon |\tilde{\rho}_n^{(1)}\rangle. \quad (\text{S57})$$

Analogously, by using Eq. (S54), one arrives at

$$\langle \tilde{\sigma}_n^{(1)} | = - \sum_{i (i \neq n)} \left(\frac{\langle \tilde{\sigma}_n^{(0)} | L_1 | \tilde{\rho}_i^{(0)} \rangle}{\lambda_i^{(0)} - \lambda_n^{(0)}} \right) \langle \tilde{\sigma}_i^{(0)} |, \quad (\text{S58})$$

which leads to

$$\langle \delta \tilde{\sigma}_n | \equiv \langle \delta \tilde{\sigma}_n^{\text{exp}} | - \langle \delta \tilde{\sigma}_n^{(0)} | \approx \langle \delta \tilde{\sigma}_n^{(1)} | \equiv \epsilon \langle \tilde{\sigma}_n^{(1)} |, \quad (\text{S59})$$

as derived in [S5].

Thus, the error bars O_{12}^{exp} of the scalar products (overlaps) $O_{12}^{\text{exp}} = |\langle \tilde{\sigma}_1^{\text{exp}} | \tilde{\rho}_2^{\text{exp}} \rangle|$ of the experimental eigenmatrices $\langle \tilde{\sigma}_1^{\text{exp}} |$ and $|\tilde{\rho}_1^{\text{exp}}\rangle$, which are shown in Fig. 2 in the main text, are obtained as

$$\delta O_{12}^{\text{exp}} = |\langle \tilde{\sigma}_1^{\text{exp}} | \tilde{\rho}_2^{\text{exp}} \rangle - \langle \tilde{\sigma}_1^{(0)} | \tilde{\rho}_2^{(0)} \rangle| = |\langle \delta \tilde{\sigma}_1 | \tilde{\rho}_2^{(0)} \rangle + \langle \tilde{\sigma}_1^{(0)} | \delta \tilde{\rho}_2 \rangle + \langle \delta \tilde{\sigma}_1 | \delta \tilde{\rho}_2 \rangle|. \quad (\text{S60})$$

Note that these error bars are affected by the phase factors from the overlaps, which can be arbitrary and depend on the applied diagonalization method. Thus, to avoid this phase dependence, one can redefine $\delta O_{12}^{\text{exp}}$ as:

$$\delta \bar{O}_{12}^{\text{exp}} = \left[|\langle \delta \tilde{\sigma}_1 | \tilde{\rho}_2^{(0)} \rangle|^2 + |\langle \tilde{\sigma}_1^{(0)} | \delta \tilde{\rho}_2 \rangle|^2 + |\langle \delta \tilde{\sigma}_1 | \delta \tilde{\rho}_2 \rangle|^2 \right]^{1/2}. \quad (\text{S61})$$

These error bars are depicted in Fig. S1, and can be compared with those in Fig. 2 in the main text. Note that the point at $\gamma_x = 0$ in Fig. 2(b) is fully consistent with our theoretical prediction using this redefined error bar, $\delta \bar{S}^{\text{exp}}$, but it is not the case for δS^{exp} .

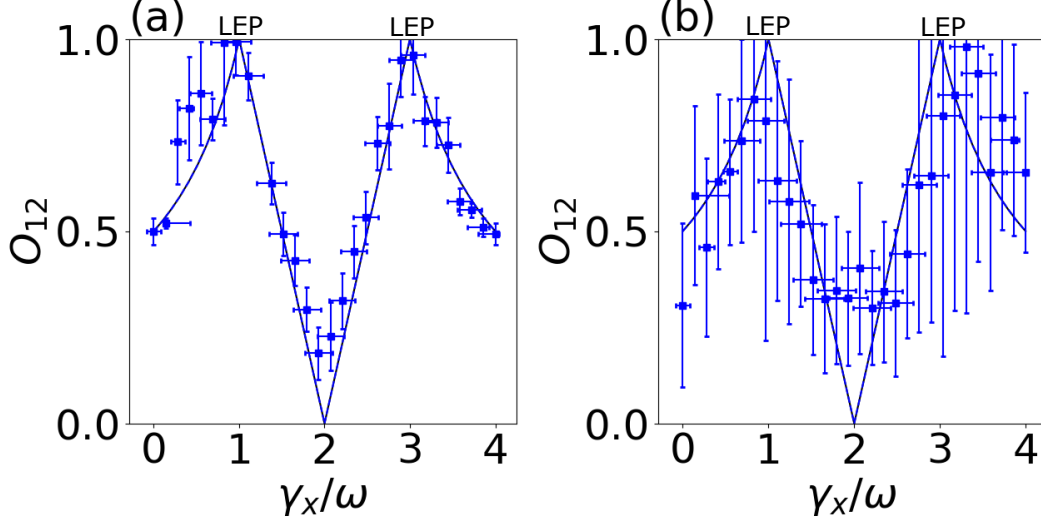


FIG. S1. Overlaps $O_{12} = |\langle \tilde{\sigma}_1 | \tilde{\rho}_2 \rangle|$ of the Liouvillian vectorized eigenmatrices $\langle \tilde{\sigma}_1 |$ and $|\tilde{\rho}_2\rangle$ measured in our single- (a) and two- (b) qubit experiments on an IBM quantum processor (blue squares) and compared to the corresponding theoretical predictions including white noise (black curves). Same as Fig. 2 in the main text, but the error bars $\delta \bar{O}_{12}^{\text{exp}}$ are given here by Eq. (S61).

V. ANALYTICAL FORMULAS FOR A LOSSY DRIVEN QUBIT

Here we show analytical results on the QPT of the lossy driven qubit model analyzed in the main text.

Case 1: Assuming $\gamma_- = 0$, we have

$$L' = \frac{\omega}{4} \begin{pmatrix} -4 & 4 & -1 & 1 & 0 & 0 \\ 4 & -4 & 1 & -1 & 0 & 0 \\ 1 & -1 & -2x & 2x & 0 & 0 \\ -1 & 1 & 2x & -2x & 0 & 0 \\ 0 & 0 & 0 & 0 & -y_2 & y_2 \\ 0 & 0 & 0 & 0 & y_2 & -y_2 \end{pmatrix}, \quad (\text{S62})$$

where $x = \gamma/\omega$ and $y_k = 2(x+k)$. The eigenvalues of L' are:

$$\begin{aligned} \lambda'_1 &= -2\omega(2+x), \\ \lambda'_2 &= -\omega(2+x-z), \\ \lambda'_3 &= -\omega(2+x+z), \end{aligned} \quad (\text{S63})$$

where $z = \sqrt{x^2 - 4x + 3}$, while the other three eigenvalues are zero. The corresponding eigenmatrices are:

$$\begin{aligned} |\tilde{\rho}'_1\rangle &= [0, 0, 0, 0, -1, 1]^T, \\ |\tilde{\rho}'_2\rangle &= [2-x-z, -2+x+z, -1, 1, 0, 0]^T, \\ |\tilde{\rho}'_3\rangle &= [2-x+z, -2+x-z, -1, 1, 0, 0]^T. \end{aligned} \quad (\text{S64})$$

Analogously, we find

$$L'' = \omega \begin{pmatrix} 0 & 0 & 0 & 0 \\ 0 & -4 & -1 & 0 \\ 0 & 1 & -2x & 0 \\ 0 & 0 & 0 & -y_2 \end{pmatrix}, \quad (\text{S65})$$

for which the *nonzero* eigenvalues of L'' are the same as those of L' : $\lambda'_k = \lambda''_k$ ($k = 1, 2, 3$), but their eigenmatrices:

$$\begin{aligned} |\tilde{\rho}''_1\rangle &= [0, 0, 0, 1]^T, \\ |\tilde{\rho}''_2\rangle &= [0, -2 + x + z, 1, 0]^T, \\ |\tilde{\rho}''_3\rangle &= [0, -2 + x - z, 1, 0]^T, \end{aligned} \quad (\text{S66})$$

are, in general, different from those of the corresponding ρ'_k .

Case 2: Assuming $\gamma_- = \omega$, we have

$$L' = \frac{\omega}{4} \begin{pmatrix} -9 & 9 & -2 & 2 & 2 & -2 \\ 9 & -9 & 2 & -2 & 2 & -2 \\ 2 & -2 & -4x-1 & 4x+1 & 2 & -2 \\ -2 & 2 & 4x+1 & -4x-1 & 2 & -2 \\ 0 & 0 & 0 & 0 & -2y_2 & 2y_2 \\ 0 & 0 & 0 & 0 & 2y_3 & -2y_3 \end{pmatrix}, \quad (\text{S67})$$

having the nonzero eigenvalues equal to:

$$\begin{aligned} \lambda'_1 &= -\omega(2x+5), \\ \lambda'_2 &= -\frac{\omega}{2}(2x+5+2z), \\ \lambda'_3 &= -\frac{\omega}{2}(2x+5-2z), \end{aligned} \quad (\text{S68})$$

and the corresponding eigenmatrices:

$$\begin{aligned} |\tilde{\rho}'_1\rangle &= \left[\frac{-1}{2(x+2)}, \frac{-1}{2(x+2)}, \frac{-1}{2(x+2)}, \frac{-1}{2(x+2)}, -\left(\frac{x+3}{x+2}\right), 1 \right]^T, \\ |\tilde{\rho}'_2\rangle &= [2-x-z, -2+x+z, -1, 1, 0, 0]^T, \\ |\tilde{\rho}'_3\rangle &= [2-x+z, -2+x-z, -1, 1, 0, 0]^T. \end{aligned} \quad (\text{S69})$$

Analogously, we find

$$L'' = \frac{\omega}{2} \begin{pmatrix} 0 & 0 & -2 & 0 \\ 0 & -4x-1 & 0 & 2 \\ 0 & 0 & -4x-10 & 0 \\ 0 & -2 & 0 & -9 \end{pmatrix}. \quad (\text{S70})$$

As in the case 1, the *nonzero* eigenvalues of L'' are the same as those of L' : $\lambda'_k = \lambda''_k$ ($k = 1, 2, 3$), but their eigenmatrices are different as:

$$\begin{aligned} |\tilde{\rho}''_1\rangle &= \left[\frac{1}{2x+5}, 0, 1, 1 \right]^T, \\ |\tilde{\rho}''_2\rangle &= [0, -2+x+z, 0, 1]^T, \\ |\tilde{\rho}''_3\rangle &= [0, -2+x-z, 0, 1]^T. \end{aligned} \quad (\text{S71})$$

VI. EXAMPLES OF RECONSTRUCTED LIOUVILLIANS INCLUDING EXPERIMENTAL ERRORS

Examples of quantum circuits and calibration data for the quantum processors are shown in Fig. S2. Our experiments were implemented on a seven-qubit IBM processor (*ibm_nairobi*) [S1] and we used the Qiskit Runtime environment, which provides a controllable error mitigation and suppression to perform our experiment. Note that, we also performed experiments on several other quantum processors from IBM, which we selected based on their coupling maps. However, *ibm_nairobi* resulted in the best results compared to our theoretical predictions and the lowest experimental errors.

The theoretical and reconstructed process matrices S , at the first LEP in Figs. 1(a) and 1(b) in the main text, are shown in Fig. S3 for a single-qubit experiment. Analogously, Fig. S4 shows S for the two-qubit experiment for the first LEP in Figs. 1(c) and 1(d).

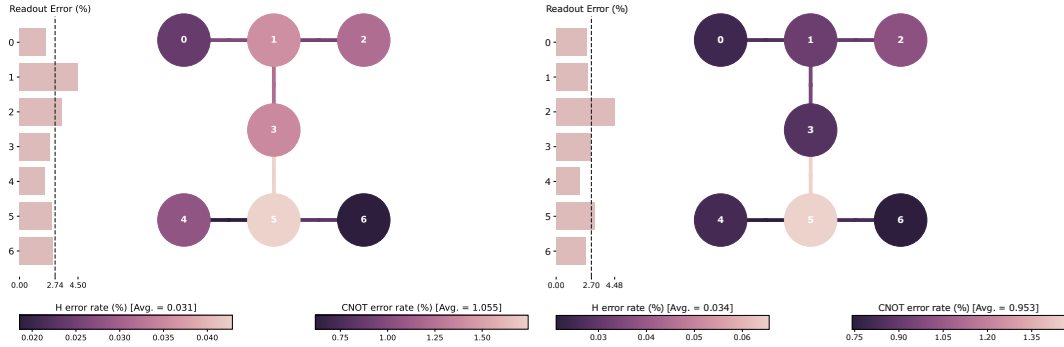


FIG. S2. Examples of the calibration data of the seven-qubit IBM quantum processor (i.e., *ibm_nairobi*) for (a) single- and (b) two-qubit experiments, as completed on 18 and 22 April, 2023, respectively. Source: [S1]. In the single-qubit case, we applied the Qiskit optimization level 1, which enables a dynamical decoupling error suppression, and the resilience level 1, which enables readout error mitigation. In the two-qubit experiments, we used the optimization level 3 and the resilience level 1. Moreover, we experimentally tested different qubits to find that the best results were obtained for: Qubit #0 in the single-qubit experiment and Qubits #4 and #5 for the two-qubit experiments. The number of shots used in both experiments are set to 20 000. Here, H stands for the Hadamard gate. See Table VI for more experimental characteristics of chosen qubits and gates.

Qubit	$\bar{T}_1(\mu s)$	$\bar{T}_2(\mu s)$	Frequency (GHz)	Anharmonicity (GHz)	Single-qubit gate error	CNOT error	Basic gates
#5	109.41 ± 14.12	75.92 ± 7.4	5.18	-0.34	2.98×10^{-4}	6.5×10^{-3}	$I, R_Z, X, \sqrt{X}, \text{CNOT}$
#4	154.72 ± 23.15	20.34 ± 0.6	5.29	-0.34	2.68×10^{-4}	—	I, R_Z, X, \sqrt{X}
#0	125.58 ± 14.89	32.63 ± 2	5.26	-0.34	2.27×10^{-4}	—	I, R_Z, X, \sqrt{X}

TABLE I. Calibration data of the *ibm_nairobi* superconducting processor used for our experiments with 1 and 2 qubits. Here, R_z is a single-qubit rotation around the z -axis for various angles, while \bar{T}_1 and \bar{T}_2 are, respectively, the relaxation and decoherence times of a given qubit averaged for a few days (i.e., 14–16.04.2023). Qubit numbers # n refer to those in Fig. S2. Source: [S1].

VII. ERROR BARS IN γ/ω

In our experiments, we intended to prepare quantum circuits to be initially in pure states $|\psi(\gamma)\rangle$, where the dependence on γ is given by the simulated quantum model. However, due to random errors, the prepared states are not exactly the intended pure states. Instead, we observe that the curves associated with the prepared input states fit the experimental data best, if we assume the input state to be

$$\rho = (1 - w)|\psi(\gamma)\rangle\langle\psi(\gamma)| + \frac{w}{d}\mathbb{1}_d, \tag{S72}$$

where d is the dimension of the Hilbert space and w stands for the level of white noise. On the other hand, there are infinitely many ways to decompose unity or to express the noisy input ρ in a way that is compatible with our observations. In particular, for a given γ , the associated noisy state ρ can be expressed as

$$\rho = \int_{\gamma-\gamma_L}^{\gamma+\gamma_R} p(\gamma + \gamma')|\psi(\gamma + \gamma')\rangle\langle\psi(\gamma + \gamma')|d\gamma', \tag{S73}$$

where $p(\gamma)$ is a semipositive function defined on $[\gamma - \gamma_L, \gamma + \gamma_R]$, such that ρ is normalized. To simplify the notation, let us set $\gamma = 0$ and $\omega = 1$ in our model. Both expressions for ρ should result in the same fidelity with respect to the target input state $|\psi(\gamma)\rangle$, i.e.,

$$\int_{-\gamma_L}^{\gamma_R} P(\gamma')|\langle\psi(\gamma)|\psi(\gamma')\rangle|^2d\gamma' = 1 - w(1 - 1/d) \tag{S74}$$

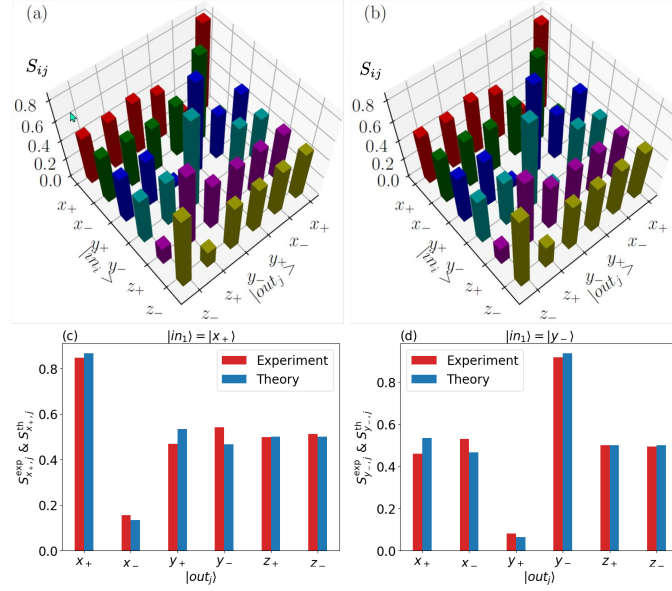


FIG. S3. Theoretical (a) and experimental (b) matrix elements $S_{ij} = L'_{ij}dt + \mathbb{1}$, corresponding to the Liouvillian elements L'_{ij} , for our single-qubit experiment performed for $\omega dt = 1/15$ and $\gamma/\omega = 0.96$. These matrices correspond to the first (left) LEP shown in Figs. 1(a) and 1(b) in the main text. Comparison of the cross-sections of figures (a) and (b) for chosen input states: $|x_+\rangle$ (c) and $|y_-\rangle$ (d).

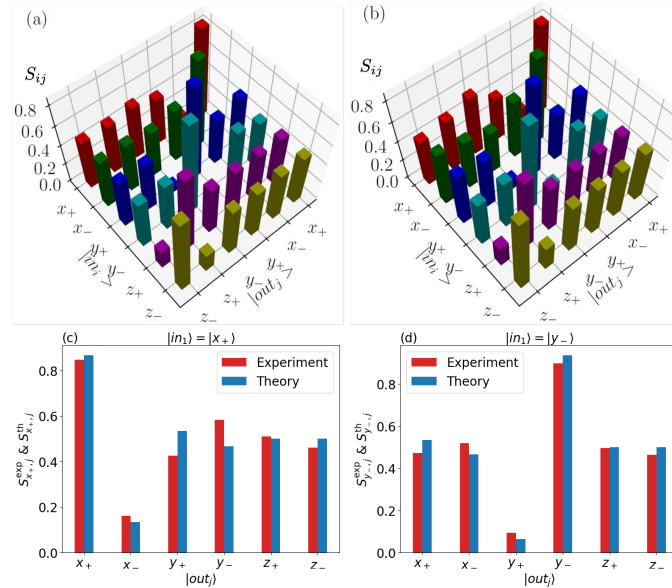


FIG. S4. Same as in Fig. S3, but for our two-qubit experiment. These matrices correspond to the first LEP shown in Figs. 1(c) and 1(d) in the main text.

Let the integrand vanish for $\gamma \geq \gamma_R$ and $\gamma \leq -\gamma_L$:

$$p(\gamma')|\langle\psi(\gamma)|\psi(\gamma')\rangle|^2 = 0 \quad \Rightarrow \quad p(\gamma_R) = p(-\gamma_L) = 0. \quad (\text{S75})$$

Let $p(\gamma)$ reach its maximum at $\gamma = 0$, which can be interpreted as preparing the target state with a maximum likelihood. If we assume that p is a triangular distribution, we arrive at

$$\int_{-\gamma_L}^0 (a_L\gamma' + b)|\langle\psi(\gamma)|\psi(\gamma')\rangle|^2 d\gamma' + \int_0^{\gamma_R} (a_R\gamma' + b)|\langle\psi(\gamma)|\psi(\gamma')\rangle|^2 d\gamma' = 1 - w(1 - 1/d), \quad (\text{S76})$$

where $a_L = \frac{b}{\gamma_L}$, $a_R = \frac{-b}{\gamma_R}$, and $P(0) = b$. We find b from the normalization condition and $\gamma_{L,R}$ are found numerically from

$$b \int_{-\gamma_L}^{\gamma_R} |\langle\psi(\gamma)|\psi(\gamma')\rangle|^2 d\gamma' + \int_{-\gamma_L}^0 a_L |\langle\psi(\gamma)|\psi(\gamma')\rangle|^2 \gamma' d\gamma' + \int_0^{\gamma_R} a_R |\langle\psi(\gamma)|\psi(\gamma')\rangle|^2 \gamma' d\gamma' = 1 - w(1 - 1/d). \quad (\text{S77})$$

In this way, we estimated the maximum uncertainty in setting γ . In general, we end up with $\gamma_L \neq \gamma_R$, which corresponds to asymmetric uncertainties. We estimate the left and right uncertainties (error bars for γ), respectively, as for two independent triangular distributions to be $P_L\gamma_L/\sqrt{6}$ and $P_R\gamma_R/\sqrt{6}$ [S6], where

$$P_L = \int_{-\gamma_L}^0 p(\gamma') d\gamma' \quad \text{and} \quad P_R = \int_0^{\gamma_R} p(\gamma') d\gamma'. \quad (\text{S78})$$

[S1] IBM Quantum Platform, <https://quantum-computing.ibm.com>
[S2] F. Minganti, A. Miranowicz, R. W. Chhajlany, I. I. Arkhipov, and F. Nori, Hybrid-Liouvillian formalism connecting exceptional points of non-Hermitian Hamiltonians and Liouvillians via postselection of quantum trajectories, *Phys. Rev. A* **101**, 062112 (2020).
[S3] F. Minganti, A. Miranowicz, R. Chhajlany, and F. Nori, Quantum exceptional points of non-Hermitian Hamiltonians and Liouvillians: The effects of quantum jumps, *Phys. Rev. A* **100**, 062131 (2019).
[S4] S. Axler, *Linear Algebra Done Right* (Springer, 2015).
[S5] D. F. V. James, P. G. Kwiat, W. J. Munro, and A. G. White, Measurement of qubits, *Phys. Rev. A* **64**, 052312 (2001).
[S6] A. Possolo, Simple Guide for Evaluating and Expressing the Uncertainty of NIST Measurement Results, NIST Technical Note 1900 (2015), DOI:10.6028/NIST.TN.1900.

Chapter 6

Conclusion

In this thesis, I discussed quantum correlations in the dissipative quantum systems based on various approaches that we used in our research articles.

In Chapter 1, I discussed the results of article [P1], in which we studied quantum correlations for the Werner and generalized Werner states (GWSs) as two-qubit quantum systems that contain environmental noise (i.e., white noise). We showed that it is experimentally feasible to demonstrate the hierarchy of quantum correlations such as quantum entanglement, EPR steering, and Bell nonlocality without the need for full quantum state tomography (QST) for some classes of states, including the Werner states and GWSs. As far as we know, all previous demonstrations of such hierarchies relied on the application of complete QST. Finally, we reported an experiment revealing the hierarchy of these quantum correlations for the Werner states without QST.

Photon blockade (PB) and photon-induced tunneling (PIT) are two nonclassical phenomena that I discussed in Chapter 2 based on article [P2]. Specifically, we studied a novel type of hybrid photon-phonon blockade in a hybrid mode of a proposed dissipative system. We found such parameter regimes to observe a strong hybrid photon-phonon blockade, which is, however, not accompanied by the photon or phonon blockade effects in separate modes. In this article, we used two approaches to study the dynamics of our system, i.e., those based on the standard master equation and a non-Hermitian Hamiltonian (NHH). In both approaches, we calculated the steady-state solution of the system to obtain the second-order correlation function of the system. The blockade in a hybrid mode is explained by the destructive interference of both photonic and phononic modes at the balanced linear coupler. Our study explored how photons and phonons interact and how this can lead to a new type of blockade in the hybrid photon-phonon mode. We

also observed different types of the blockade and tunneling effects in the photon, phonon, and hybrid modes that occur because of a nonlinearity induced in the system or a destructive interference. Moreover, we introduced two setups to measure the second-order correlation function in the hybrid mode, which can inspire more research on quantum engineering with hybrid modes of photons and phonons.

Nonlinearity is the key quantum resource to induce and observe PB and PIT in dissipative quantum systems. In Chapter 3, I discussed the results of article [P3], in which we showed that it is possible to observe unconventional single- and multi-photon blockade effects in a linear quantum system that dissipates into a nonlinear reservoir. To study the dynamics of our system interacting with a squeezed reservoir, we introduced a more general form of the standard master equation containing a two-photon process in addition to a one-photon process as in the standard master equation. Our results showed that the roles of the Kerr nonlinear interaction and two-photon dissipation are interchanged in the steady states of our systems. The results also showed that it is possible to observe two-PB just according to refined criteria. We showed that by preparing the cavity in squeezed coherent states and displaced squeezed thermal states, it is also possible to obtain similar results in some specific squeezing parameter regimes as expected. Furthermore, we discussed the nonclassicality of the studied effects and states.

In Chapter 4, I discussed open quantum light-matter systems in the ultrastrong-coupling (USC) and deep-strong-coupling (DSC) regimes, based on the results of article [P4]. In this article, we mainly studied pure dephasing of two well-known models of light-matter interactions: the quantum Rabi model and the Hopfield model according to adopted gauge. Our results showed the importance of gauge consideration for the noise Hamiltonian that describes pure dephasing in these two models. To calculate the pure dephasing rate in these two models, we used a master equation in a dressed basis. We highlighted the importance of using a correct description of pure dephasing rate by comparing how it behaves with or without the gauge transformation in the USC and DSC regimes.

Quantum exceptional points, including their experimental generation and detection, were discussed in Chapter 5 based on my article [P5], which includes both theoretical and experimental results. Non-Hermiticity arises in open quantum systems due to their interaction with environment leading to dissipation and/or incoherent gain. Unlike Hermitian systems, non-Hermitian ones can have both real eigenvalues (for PT-symmetrical systems) or complex eigenvalues (for systems with

broken PT-symmetry), which lead to novel phenomena including the occurrence exceptional points.

A general experimental method, proposed by us in [P5], involves the generation and control of Liouvillian exceptional points (LEPs) through quantum dissipative engineering. Subsequently, we demonstrated that LEPs can be revealed using quantum process tomography. As an illustration, the method has been applied on an IBMQ processor to simulate the dissipative dynamics of a single superconducting qubit at and in the vicinity of LEPs.

In conclusion, this thesis delves into novel quantum effects and advances the control methods of quantum correlations in dissipative systems through innovative theoretical and experimental approaches. I aspire for my work to serve as an inspiration for future research in the exploration of dissipative quantum systems, uncovering novel phenomena under specific conditions.

In my upcoming research, I aim to explore two key areas: non-Hermitian dynamics in quantum systems and the development of robust theoretical models for scaling up the number of qubits in superconducting circuits.

Appendix A

List of publications

Publications included in the dissertation:

- [P1] Shilan Abo, Jan Soubusta, Katerina Jiráková, Karol Bartkiewicz, Antonin Černoch, Karel Lemr, and Adam Miranowicz,
Experimental hierarchy of two-qubit quantum correlations without state tomography,
Scientific Reports **13**, 8564 (2023),
e-print arXiv:2302.10159,
DOI: 10.1038/s41598-023-35015-9
Keywords: [Bell nonlocality], [quantum steering], [quantum entanglement], [noise robustness], [linear optics], [quantum dissipative engineering], [experiment].
- [P2] Shilan Abo, Grzegorz Chimczak, Anna Kowalewska-Kudłaszyk, Jan Peřina Jr., Ravindra Chhajlany, and Adam Miranowicz:
Hybrid photon-phonon blockade,
Scientific Reports **12**, 17655 (2022),
e-print arXiv:2207.09388,
DOI: 10.1038/s41598-022-21267-4
Keywords: [photon blockade], [phonon blockade], [photon-induced tunneling], [quantum temporal correlations], [photon antibunching], [quantum dissipative engineering], [circuit QED], [quantum optomechanics].
- [P3] Anna Kowalewska-Kudłaszyk, Shilan Abo, Grzegorz Chimczak, Jan Peřina Jr., Franco Nori, and Adam Miranowicz,
Two-photon blockade and photon-induced tunneling generated by squeezing,

Physical Review A **100**, 053857 (2019),

e-print arXiv:1908.08414,

DOI: 10.1103/PhysRevA.100.053857

Keywords: [photon blockade], [photon-induced tunneling], [quantum temporal correlations], [squeezing of light], [squeezed-mode reservoir], [photon antibunching], [quantum dissipative engineering].

- [P4] Alberto Mercurio, Shilan Abo, Fabio Mauceri, Enrico Russo, Vincenzo Macri, Adam Miranowicz, Salvatore Savasta, and Omar Di Stefano: Pure Dephasing of Light-Matter Systems in the Ultrastrong and Deep-Strong Coupling Regimes, Physical Review Letters **130**, 123601 (2023), e-print arXiv:2205.05352, DOI: 10.1103/PhysRevLett.130.123601
Keywords: [ultrastrong coupling], [deep-strong coupling], [generalized master equation], [quantum Rabi model], [Hopfield model], [Coulomb gauge], [dipole gauge], [quantum dissipative engineering].
- [P5] Shilan Abo, Patrycja Tulewicz, Karol Bartkiewicz, Sahin K. Özdemir, and Adam Miranowicz, Liouvillian Exceptional Points of Non-Hermitian Systems via Quantum Process Tomography, e-print arXiv:2401.14993, DOI: 10.48550/arXiv.2401.14993
Keywords: [Liouvillian exceptional points], [quantum process tomography], [quantum dissipative engineering], [IBMQ], [experiment].

Appendix B

Statements about the contributions to the publications

For the publications [P1, P2, P4, P5], I attach the statements of all the co-authors specifying her/his individual contribution to the work with the declaration that she/he is aware that the publication will be included in my doctoral thesis.

For the publication [P3], which has six authors, I have attached the statements of five authors, i.e., all the co-authors from Adam Mickiewicz University and Prof. Peřina from Palacký University.

My contribution to the publications [P1]–[P5] is described in Chapters 1–5, i.e., in the commentaries preceding each publication and, additionally, in some publications (i.e., [P1,P2]).


June 5, 2023

Statement about the contribution to the publication


We hereby declare that we are aware that the work:

Experimental hierarchy of two-qubit quantum correlations without state tomography, Sci Rep 13, 8564 (2023), Shilan Abo, Jan Soubusta, Kateina Jiráková, Karol Bartkiewicz, Antonín Černoč, Karel Lemr, Adam Miranowicz, of which we are co-author, has been included in the doctoral thesis of Shilan Abo.

The main idea of the manuscript was conceived by Adam Miranowicz; Shilan Abo and Jan Soubusta performed numerical and analytical calculations; the concept of linear-optical implementation was devised by Karol Bartkiewicz; the experiment was designed, performed, and raw-data processed by Antonín Černoč and Karel Lemr. All the authors were involved in writing and discussing the manuscript.




Antonín Černoč




Jan Soubusta



K. Bartkiewicz
KAROL BARTKIEWICZ



KATEŘINA JIRÁKOVÁ



Karel Lemr



A. Miranowicz



Institute of Spintronics and Quantum Information, Faculty of Physics
Adam Mickiewicz University
ul. Uniwersytetu Poznańskiego 2, 61-614 Poznań, Poland

Poznań, 28.01.2023

Statement about the contribution to the publication

We hereby declare that we are aware that the work:

on *Hybrid photon-phonon blockade*

by Shilan Abo, Grzegorz Chimczak, Anna Kowalewska-Kudłaszyk,
Jan Peřina Jr., Ravindra Chhajlany, and Adam Miranowicz,
published in *Scientific Reports* 12, 17655 (2022),

of which we are co-authors, has been included in the doctoral thesis of Shilan Abo.

The work was supervised by Adam Miranowicz and Ravindra Chhajlany. Adam Miranowicz conceived the original idea. Shilan Abo performed all numerical and analytical calculations, which were double-checked by Grzegorz Chimczak and Anna Kowalewska-Kudłaszyk. The paper was written by Shilan Abo with contributions from all coauthors. Shilan Abo made significant contributions to the interpretation of the obtained results. Moreover, all authors actively participated in revising and discussing the manuscript.

Jan Peřina

A. Kudłaszyk

A. Miranowicz

R. W. Chhajlany

Grzegorz Chimczak



Institute of Spintronics and Quantum Information, Faculty of Physics
Adam Mickiewicz University
ul. Uniwersytetu Poznańskiego 2, 61-614 Poznań, Poland

Poznań, 28.01.2023

Statement about the contribution to the publication

We hereby declare that we are aware that the work:

on *Two-photon blockade and photon-induced tunneling generated by squeezing*,
by Anna Kowalewska-Kudłaszyk, Shilan Abo, Grzegorz Chimczak,
Jan Peřina Jr., Franco Nori, and Adam Miranowicz,
published in Physical Review A **100**, 053857 (2019),

of which we are co-authors, has been included in the doctoral thesis of Shilan Abo.

Adam Miranowicz conceived the original idea and supervised the work. Anna Kowalewska-Kudłaszyk and Shilan Abo performed all the numerical and analytical calculations, as well as they wrote the paper with input from all the authors. Shilan Abo made significant contributions to the interpretation of the obtained results. All authors actively participated in revising and discussing the manuscript.

Jan Peřina

A. Miranowicz

A. Kudłaszyk

Grzegorz Chimczak



Università
degli Studi di
Messina

DIPARTIMENTO DI SCIENZE
MATEMATICHE E INFORMATICHE,
SCIENZE FISICHE E SCIENZE DELLA TERRA

Statement about the contribution to the publication

We hereby declare that we are aware that the work:

Pure Dephasing of Light-Matter Systems in the Ultrastrong and Deep-Strong Coupling Regimes, Physical Review Letters, **10.1103** (2023), Alberto Mercurio, Shilan Abo, Fabio Mauceri, Enrico Russo, Vincenzo Macrì, Adam Miranowicz, Salvatore Savasta, and Omar Di Stefano, of which we are co-author, has been included in the doctoral thesis of Shilan Abo.

The main idea of the manuscript was conceived by Salvatore Savasta and Omar Di Stefano. Alberto Mercurio and Shilan Abo performed numerical and analytical calculations, plots and contributed to the interpretation of the results.

These two authors contributed equally to the work; All the authors were also involved in writing and discussing the manuscript.

Messina, 29/05/2023

Prof. Salvatore Savasta

Prof. Omar Di Stefano



Institute of Spintronics and Quantum Information, Faculty of Physics
Adam Mickiewicz University
ul. Uniwersytetu Poznańskiego 2, 61-614 Poznań, Poland

Poznań, 28.01.2023

Statement about the contribution to the publication

We hereby declare that we are aware that the work:

on *Liouvillian Exceptional Points of Non-Hermitian Systems via Quantum Process Tomography*,
by Shilan Abo, Patrycja Tulewicz, Karol Bartkiewicz, Şahin K. Özdemir, and Adam Miranowicz,
arXiv:2401.14993 (2024), DOI:10.48550/arXiv.2401.14993,

of which we are co-authors, has been included in the doctoral thesis of Shilan Abo.

Adam Miranowicz originated and oversaw the initial concept of the project, while Shilan Abo and Patrycja Tulewicz executed experiments on IBMQ processors under the guidance of Karol Bartkiewicz. Shilan Abo conducted both analytical and numerical calculations, inclusive of data postprocessing, with thorough validation by other contributors. The first version of the paper was written by Shilan Abo and subsequently refined through collaborative revision by all authors. The importance of this research area has been highlighted in the paper by Şahin Özdemir. The entire team actively engaged in discussions pertaining to the manuscript, including the interpretation of the experimental results and their minor deviations from theory.

A. Miranowicz

Patrycja Tulewicz

Ş. Özdemir

K. Bartkiewicz

Appendix C

Abbreviations

1PB	single-photon blockade
2MS	two-measurement scenario (in steering protocols)
2PB	two-photon blockade
2PT	two-photon tunneling
3MS	three-measurement scenario (in steering protocols)
3PT	three-photon tunneling
BS	beam splitter
CHSH	Clauser-Horne-Shimony-Holt (e.g., inequality)
CP map	completely positive map
DSC	deep-strong coupling
DSTS	displaced squeezed thermal state
EP	exceptional point or entanglement potential
EPR	Einstein, Podolsky, and Rosen
FEF	fully entangled fraction
GWS	generalized Werner state
HBT	Hanbury Brown and Twiss
HEP	Hamiltonian exceptional point
JC	Jaynes-Cummings (e.g. model)
LEP	Liouvillian exceptional point
LIGO	Laser Interferometer Gravitational-wave Observatory
multi-PB	multi-photon blockade
NHH	non-Hermitian Hamiltonian
NPB	nonstandard photon blockade
OpenQASM	Open Quantum Assembly Language
PAB	photon antibunching
PB	photon blockade
PIT	photon-induced tunneling
PT	parity-time (e.g., symmetry)
QD	quantum drum
QED	quantum electrodynamics
QEP	quantum exceptional point
QPT	quantum process tomography
QRM	quantum Rabi model
QST	quantum state tomography
RWA	rotating-wave approximation
SC	strong coupling
SCS	squeezed coherent state
SMR	superconducting microwave resonator
SV	squeezing variance
TLS	two-level system
UPB	unconventional photon blockade
USC	ultra-strong coupling